# Biophysical strategies to inhibit bacterial amyloid formation and undermine biofilm infections

Alissa Bleem

A dissertation

submitted in partial fulfillment of the

requirements for the degree of

Doctor of Philosophy

University of Washington

2019

Reading Committee:

Valerie Daggett, Chair

James Bryers

Douglas Fowler

Matthew Parsek

Program Authorized to Offer Degree:

Bioengineering

University of Washington

## Abstract

Biophysical strategies to inhibit bacterial amyloid formation and undermine biofilm infections

Alissa Bleem

Chairs of the Supervisory Committee:
Valerie Daggett, Professor
Bioengineering
James D. Bryers, Professor
Bioengineerg

When bacteria dwell in biofilms on the surface of an implanted medical device or surgical site, cells co-associate using a self-produced extracellular matrix (EM), which acts as a layer of protection against antibiotic infiltration. The EM is comprised of polysaccharides, DNA, and proteins including amyloid fibrils. Extracellular deposition of amyloid has long been associated with protein misfolding and neurodegenerative diseases, but a growing body of research demonstrates that bacteria have adopted amyloid fibrils as a functional scaffold to reinforce the biofilm. Consequently, these functional amyloids represent a novel target to interrupt biofilm formation and address the problems of biofilm-associated infection and resistance. The pathway to amyloid formation in the EM is characterized by specific physicochemical motifs; therefore, peptides engineered to bind these motifs should inhibit fibril formation and disrupt biofilm development. Here, the mechanism of amyloid formation is analyzed in both Gram positive and Gram negative bacteria, peptide design approaches are introduced to inhibit amyloid formation, and the results are translated to clinically relevant models.

# TABLE OF CONTENTS

# LIST OF FIGURES

# LIST OF TABLES

# ACKNOWLEDGEMENTS

The author would like to thank Dr. Valerie Daggett and Dr. James Bryers for mentorship throughout her graduate career, as well as Dr. Douglas Fowler and Dr. Matthew Parsek for service on the supervisory committee. She is also grateful to Dr. Daniel Otzen, Dr. Morten Dueholm, Dr. Brian Vad, Janni Nielsen, and affiliated lab members for mentorship during her research stay at Aarhus University. Additional appreciations are due to Dr. Gene Hopping, Dr. Clare-Louise Towse, Dr. Neal Beeman, Dr. Ruying Chen, Dr. Billanna Hwang, Dr. Matthew Chapman, Dr. Lynette Cegelski, Dr. Blaise Boles, Dr. Swaine Chen, Matthew Childers, Dylan Shea, Thomas Hady, Ian Dryg, Zak Wescoe, Robyn Francisco, Elizabeth Leber, Ivan Vulovic, William Walker, and Nathan Maris for helpful discussions, practical instruction, and donation of materials. Finally, the author would like to thank the Department of Bioengineering for providing administrative support, as well as the National Science Foundation, National Institutes of Health, and Danish Council for Independent Research for financial support and computational resources.

# DEDICATION

To J.D.S., for igniting the passion, leading by example, and

reminding me to find serenity in the mountains.

And to mom, for doing it first.

# Chapter 1. Introduction

## 1.1 Biofilm Infection: A Global Healthcare Burden

Each year, approximately 35 million adults receive inpatient care in America's hospitals. More than half of the patient-days spent in hospitals involve treatment with invasive medical devices, and 7 million inpatient stays were attributed to surgeries in 2014[1,2]. All of these patients are at risk for healthcare-associated infections (HAI), the most common adverse event in healthcare delivery worldwide and a significant contributor to mortality and financial losses. In the United States in 2014, approximately one in 25 patients contracted an infection during the course of hospitalization, and the frequency of HAI in developing countries is expected to be at least three times higher than that in the United States[3,4]. Pneumonia and surgical site infections are the most common, followed by gastrointestinal infection, urinary tract infection (UTI), and primary bloodstream infection. A variety of pathogens are implicated in HAI, and their distribution is dependent on the site of colonization. For example, *Staphylococcus aureus* dominates surgical site infections, *Pseudomonas aeruginosa* is a common culprit in pneumonia, and *Escherichia coli* tends to thrive in UTI[5].

Because microbial infections typically occur on surfaces – including surgical wounds, prosthetic heart valves, pacemakers, cerebrospinal fluid shunts, urinary and intravascular catheters, ocular prostheses, and intrauterine contraceptive devices – approximately 60% of HAIs are associated with biofilm formation[6,7]. Biofilms are surface-associated, spatially structured bacterial communities, and the high density of these environments enables specialized intercellular communication via quorum sensing[8]. Microbes in biofilms also produce an extracellular matrix (EM) comprised of proteins, polysaccharides, and extracellular DNA (eDNA) to mediate attachment and immobilize constituent bacteria. This EM promotes unique nutrient exchange pathways, enables adaptive stress responses, allows differentiation of highly protected "persister" cells, and shields constituent microorganisms from the host immune system[9,10]. Finally, the EM protects biofilm-associated bacteria from exogenous compounds, reducing their susceptibility to antibiotics by several orders of magnitude compared to free-swimming microbes[11–13]. Sub-lethal doses of antibiotics can actually enhance biofilm formation, and the spread of resistance genes is accelerated when biofilm communities are subjected to antibiotic stress[14–16]. These factors likely

contribute to the fact that a growing number of pathogens exhibit resistance to a broad range of antibiotics, with resistant bacteria now implicated in at least 14% of all HAI in the United States[17,18].

Unfortunately, the recent increases in antibiotic resistance accompany an overall decline in antimicrobial drug development. Since their discovery in the 1930s, the deployment of virtually every antibiotic has been followed by the emergence of clinically significant resistance[19]. Only two new classes of synthetic antibiotics (floroquinolones and oxazolidinones) have been introduced in the past 50 years, and a lack of promising leads has necessitated reexamination of natural products that were previously deemed unworthy of development[20]. In the planktonic or free-swimming state, bacteria exhibit high growth rates, so they are quite susceptible to mechanisms of antibiotic clearance including inhibition of nucleic acid synthesis (fluoroquniolones), interference with protein synthesis (aminoglycosides), or disruption of the cell wall (β-lactams). Conversely, in the dense, nutrient-limited biofilm environment, cells are forced to transition to a state of low growth and activity. These bacteria lack the typical functions targeted by antibiotics – DNA replication, cell wall synthesis, and protein translation – so they can acquire resistance[21]. Therefore, a deeper understanding of biofilm development and specific contributors to intractability is required to effectively combat HAI, and efforts to develop new antimicrobials should focus on specific mechanisms of bacterial virulence rather than simply killing cells. Such antivirulence therapies should "disarm" pathogens by decreasing tissue damage, facilitating clearance by the host immune system, and lowering selective pressure for resistance mutations[19]. Successful applications of this approach include limiting bacterial toxin function and delivery[22,23], disrupting quorum sensing to prevent transcription of virulence-associated genes[24], and targeting adhesion[25]. Few of these therapies have been tested against biofilms, however, where the EM presents additional complexities for transport and signaling.

## 1.2 Amyloids and Their Role in Biofilm Development

Due to the heterogeneous nature of biofilms, multiple mechanisms likely contribute to resistance. The EM plays an essential role by limiting not only the transport of antimicrobial compounds but also important cellular metabolites. Thus, antimicrobials may react with or adsorb to components of the EM, rendering them inactive, while compounds that effectively diffuse

through the biofilm are likely to encounter cells with a resistant phenotype[15,26]. The structural scaffold of the EM is also crucial for maintaining cell signaling and resistance to mechanical stress[27,28]. Mature biofilm architectures result from the physicochemical contributions of each of the three materials that comprise the EM: hydrated polysaccharides, eDNA, and proteins. Proteins in the EM take on a variety of roles, but a growing body of research seeks to understand the role of amyloid fibrils in this complex biological material.

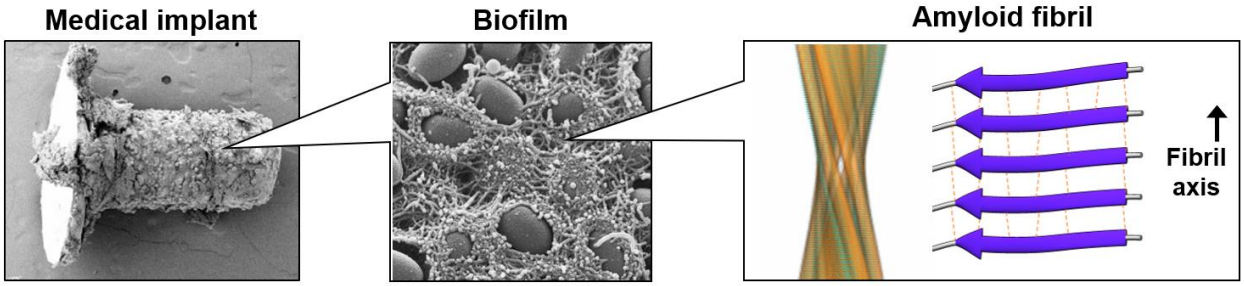


**Figure 1.1. Amyloid fibrils as a structural scaffold in the biofilm EM.** A variety of pathogens form biofilms on medical devices. Within the biofilm, bacteria produce amyloid fibrils, rigid protein structures characterized by the alignment of β-sheets perpendicular to the fibril axis. Images adapted with permission[29,30].

### 1.2.1 *Characteristics of Amyloids and Historical Emphasis on Human Disease*

Protein folding is an immensely complex process, driven by external factors such as temperature, ionic strength, and molecular crowding as well as intrinsic factors determining the conformational propensities of both the main chain and side chains. Fortunately, intrinsic kinetic barriers to aggregation are normally quite high, and organisms have evolved additional regulatory mechanisms to protect themselves from the dangers of unfolding and loss of function[31]. However, aging, stress, mutations, and high local protein concentrations can lower these kinetic barriers, enabling conversion to amyloid fibrils with thermodynamic stabilities greater than those of their native counterparts[32]. Amyloid fibrils are insoluble, β-sheet-rich protein aggregates formed by the aggregation of soluble, monomeric precursors. The fibrils are characterized by a rigid "cross-β-sheet" structure in which β-strands run perpendicular to the fibril axis and van der Waals interactions between side chains promote interstrand hydrogen bonding parallel to the fibril[33–35] (**Figure 1.1**). This composition is chemically robust, preventing dissociation by denaturants, high temperatures, proteases, and physical forces. Indeed, amyloid fibrils display remarkable material

properties, with an ultimate strength of 0.6 ± 0.4 GPa, comparable to that of steel, and a Young's modulus of 3.3 ± 0.4 GPa, similar to that of silk[36,37].

Extracellular deposition of amyloid has long been associated with protein misfolding and neurodegenerative conditions such as Alzheimer's disease, and to date there are 37 proteins or peptides associated with amyloid formation in diverse human diseases[38]. In amyloid-associated diseases, the soluble forms of these proteins and peptides undergo conformational changes that trigger their aggregation. Some pathologies, such as transthyretin amyloidosis, involve the dissociation of protein complexes into their constituent monomers, followed by conversion of monomers to an aggregation-prone state[39,40]. In other cases, such as Parkinson's disease, destabilization of intrinsically disordered α-synuclein monomers is sufficient to trigger amyloidosis[41,42]. Misfolded aggregates then increase in size to form oligomers and protofibrils, resulting in cell death and eventual precipitation of insoluble amyloid fibrils[43–45]. The clinical manifestations of these events are threefold (**Figure 1.2**). First, conversion of native monomers to the toxic or fibrillar state depletes the pool of biologically active protein or peptide, resulting in a loss of function. Second, oligomeric aggregates of unfolded protein cause cellular damage *en route* to the amyloid fibril state[46–50]. Amyloid oligomers are non-covalently associated and they exhibit greater toxicity than either monomers or fibrils, likely due to the display of unique conformational attributes that are independent of sequence[51–55]. These intermediates therefore represent an appealing therapeutic target for compounds that can remove or neutralize the toxic oligomeric species. The third major clinical manifestation of amyloid diseases results from extracellular deposition of amyloid fibrils, which form characteristic plaques in the brain and other tissues in the later stages of disease. By the time amyloid plaques form, most of the cellular damage by toxic oligomers has already transpired, and disruption of these plaques can cause further cytotoxicity through the disassociation into toxic soluble oligomers[56]. Therapeutic efforts have shifted accordingly in recent years to focus on neutralization of oligomers and application before any detectable symptoms, but much progress remains to be made before these interventions exhibit significant clinical success[38].

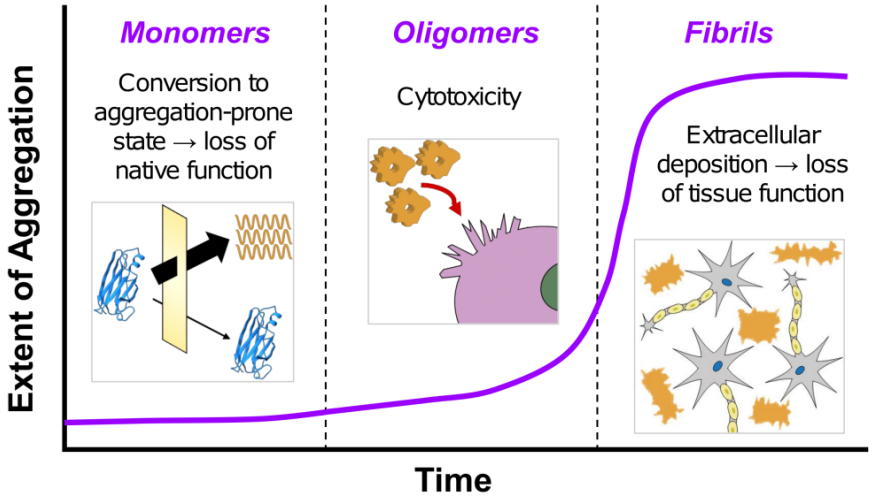


**Figure 1.2. Amyloid proteins aggregate over time, and each phase of aggregation produces pathogenic consequences in mammalian disease.** First, conversion of native monomers to aggregation-prone conformations results in a loss of native function. Second, oligomeric intermediates form membrane pores and may generate reactive oxygen species, resulting in host cell death. Finally, extracellular fibril deposits can lead to a loss of function in tissues and organs.

### 1.2.2 *Functional Bacterial Amyloids*

Amyloid fibrils are known to display impressive material properties, including high deformation resistance, elasticity, and persistence under extreme conditions. Recent research suggests that many bacteria take advantage of these properties by producing extracellular amyloid fibrils that reinforce the biofilm and resist dispersion by chemical or mechanical agents (**Figure 1.1**)[57,58]. These fibrils are biochemically similar to those formed in mammalian disease, but unlike pathological amyloids, bacterial amyloids are intentionally produced to play a functional role. The conservation of the amyloid fold through millions of years of evolution likely relies on amyloids' universal characteristics – such as backbone hydrogen bonding – rather than specific side chain chemistries[59]. Additionally, amyloid fibrils polymerize in the absence of an energy source, so they serve as a metabolically advantageous molecular scaffold despite the limited resources of the EM environment[60].

A number of pathogenic bacteria produce functional amyloid proteins, and these have significant implications for EM stabilization and virulence. In Gram-positive *Staphylococcus* biofilms, small peptides called phenol soluble modulins (PSMs) polymerize to form β-sheet-rich protein aggregates[61]. In their fibril form, PSMs impart structural stabilization to *S. aureus* biofilms, promoting resistance to various dispersion agents including Proteinase K, DNAse, and Dispersin

B[62]. Similarly, the Bap protein of *S. aureus* has been shown to self-assemble into amyloid-like aggregates upon proteolytic release from the peptidoglyclan layer[63]. In Gram-negative bacteria, functional amyloids share several common characteristics. Curli are the major proteinaceous component of *E. coli* biofilms[60], while Fap fibrils play an important role in aggregative biofilm phenotypes in many *Pseudomonas* species[64]. Both Fap and curli are expressed in a highly regulated fashion, and the synthesis of fibrils depends on the coordination of several tightly packed genes. These functional amyloid operons encode the amyloid subunits as well as a "nucleator" protein that contains an amyloidogenic domain to serve as a template for rapid fibril polymerization on the exterior of the cell[65]. The remaining proteins in the expression system serve as outer membrane pores for translocation of amyloid monomers, chaperones to guide monomers through the periplasm, or additional processors and regulators[64,66–70]. Detailed properties of the functional amyloids found in *P. aeruginosa*, *S. aureus*, and *E. coli* are presented in **Chapter 2**, **Chapter 5**, and **Chapter 6**, respectively. Other bacterial amyloids include microcin E492 in *Klebsiella pneumoniae*[71], TasA in *Bacillus subtilis*[72], paracrystalline sheaths in the archaea *Methanosaeta thermophila*[73], and chaplins in the spore-forming filamentous bacterium *Streptomyces coelicolor*[74], among others[75].

### 1.2.3 *Amyloid Fibrils as a Target for Combatting Biofilm Formation*

Despite their conservation and widespread presence throughout the bacterial kingdoms, functional bacterial amyloids have only come into focus in the last decade as potential targets for anti-biofilm compounds. They operate exclusively in the extracellular space, so their production is not a requirement for cellular growth. Instead, functional amyloids represent an attractive means to disarm bacterial pathogens, making infectious biofilms more susceptible to clearance while avoiding the potential for resistance. In addition to their role as biofilm matrix scaffolds, functional bacterial amyloids are known to promote antibiotic resistance and act as a reservoir for small molecules involved in quorum sensing[76,77]. Thus, therapeutic strategies designed to inhibit amyloid formation could theoretically suppress multiple virulence mechanisms involved in biofilm-associated infection. Existing compounds designed to target bacterial amyloids are rather limited, however. Some anti-biofilm efficacy has been demonstrated through screening of known bioactive molecules that bind amyloid, such as ring-fused 2-pyridones and epigallocatechin gallate (EGCG), but systemic administration of these compounds is somewhat impractical and may result in

significant mammalian cell cytotoxicity at the concentrations used[77–80]. In this Dissertation, peptide-based amyloid inhibitors are presented as an ideal alternative to small molecules. With the proper constraints, the selection of amino acids can vary while keeping peptide backbone structure relatively constant, which creates opportunities for modular design and grafting to other molecules. Additionally, the set of possible chemical motifs and geometries is greatly expanded in peptide systems compared to small molecules, enabling greater specificity. Computational approaches are required to narrow the sequence and structural space for effective design of such peptides, however, and these are reviewed in the next section.

## 1.3 Computational Methods to Probe Mechanisms of Amyloid Formation

Amyloid fibrils are incredibly recalcitrant, with the ability to maintain their robust cross-β structure under a variety of chemical and physical assaults. Bacteria have taken advantage of these properties and developed systems for the secretion of amyloid precursors into the extracellular space, where they polymerize to form fibrils that support the biofilm EM and contribute to biofilm virulence. Since the mature fibrils are resistant to degradation, the amyloid polymerization process itself must be studied in more detail to identify sequences and/or structures that arise on the pathway to fibril formation, and then these motifs can be exploited as targets for anti-biofilm therapeutics. Modern computational methods provide high-throughput means to identify such motifs and guide the selection of promising inhibitors.

### 1.3.1 *Analysis of Amyloid Sequence*

Bacteria present an advantage from a design standpoint, since the genomes of most pathogenic species are sequenced and publicly available. Accordingly, a variety of modeling methods have been developed to predict amyloid propensity based exclusively on amino acid sequence information. These include the WALTZ algorithm[81], which uses data from known amyloid segments[82] to generate a position-specific scoring matrix and predict amyloid-forming sequences, and the FISH Amyloid machine learning method[83], which was trained on several datasets of hexapeptides with amyloidogenic properties. Other methods include additional information such as intrinsic disorder, *in vivo* experiments, and physicochemical properties of the individual amino acids[84–87]. The ZipperDB database predicts fibril-forming segments by threading

putative sequences onto the backbone of a known amyloid fibril (NNQQNY peptide) and then evaluating the energetic fit with the RosettaDesign program[88,89].

The first portion of this Dissertation analyzes the mechanisms of amyloid formation in a model system, *P. aeruginosa*. Computational predictions from FISH and ZipperDB are integrated with experimental testing to identify drivers of amyloid formation in the sequence of the FapC protein, which then informs the design of anti-amyloid peptide inhibitors. Sequence-based approaches are advantageous because they can quickly identify key "hot spots" as candidates for mutation or binding by designed peptides. However, with the partial exception of ZipperDB, sequence-based methods fail to take the structure or dynamics of the amyloid target into account, thereby neglecting the effect of native secondary structure on stability and amyloid propensity.

### 1.3.2 *Analysis of Amyloid Structure and Dynamics*

Amyloid proteins and peptides are not sufficiently defined by a single, static fibril structure. Although certain computational methods utilize structures of known amyloid fibrils to predict aggregation potential, these strategies encourage the construction of inhibitors that bind the very entity we seek to prevent. The 3D profile method in ZipperDB, for example, assumes amyloid-forming proteins and peptides conform to the same fibril structure used to generate its predictions[82]. In order to bind and sequester bacterial amyloids before they form fibrils, however, design approaches must combine pre-fibrillar structural information with knowledge of sequence propensities. Molecular dynamics (MD) simulations represent an excellent tool to inform inhibitory peptide design in this manner, due to the conformational heterogeneity afforded by dynamic analysis[90]. MD uses a potential energy function, or force field, to simulate protein motion according to classical mechanics[91]. MD data contains sufficient resolution to identify functionally relevant conformations as well as transitions between them, thereby filling the "gaps" that arise in experimental studies of amyloid aggregation[90]. In this manner, MD simulations can identify amyloid-specific structural motifs, which may then be exploited as binding sites for inhibitors[45,92–94]. Subsequently, inhibitor designs can be informed by datasets generated from MD (*e.g.*, libraries for intrinsic conformational propensities of individual amino acids)[95–98].

A large section of this Dissertation concerns the development and testing of peptide designs for their ability to inhibit bacterial amyloid formation in three pathological biofilms – *S. aureus*, *E. coli*, and *P. aeruginosa*. The design approach, based on unique "α-sheet" structural motifs

observed in MD simulations, targets pre-amyloid oligomers formed on the pathway to fibril formation and represents a promising new avenue to combat biofilm infections.

## 1.4 Overview of Chapters

Functional amyloid fibrils represent a novel target to interrupt biofilm formation and address the problems of biofilm-associated infection and resistance. If the pathway to amyloid formation in the EM is characterized by specific physicochemical motifs, peptides engineered to bind these motifs should inhibit fibrillation and suppress biofilm formation. This Dissertation analyses the mechanism of amyloid formation in both Gram positive and Gram negative bacteria, develops peptide designs to inhibit amyloid formation in these systems, and translates the results to clinically relevant models.

In *P. aeruginosa*, functional amyloid fibrils are composed primarily of a subunit known as FapC. In **Chapter 2**, a sequence-based approach is employed to computationally predict amyloid-forming motifs in this protein, which then serves as the basis for redesign of the sequence and experimental validation. Sequence regions with high evolutionary conservation tend to coincide with regions of high amyloid propensity, and mutation of amyloidogenic motifs to a designed, non-amyloidogenic motif suppresses fibrillation. These insights expand understanding of the mechanism of amyloid polymerization in *P. aeruginosa*, paving the way for development of new, sequence-specific amyloid inhibitors in **Chapter 3**.

Also in **Chapter 3**, α-sheet secondary structure is introduced as a structure-specific target for amyloid suppression in biofilms. Molecular dynamics (MD) studies suggest that the soluble, oligomeric forms of mammalian amyloid proteins adopt a novel structure, termed "α-sheet", as they aggregate. This led to the design of complementary, synthetic α-sheet peptides to inhibit amyloidogenesis. **Chapter 3** describes the computational basis for the design of these inhibitors, including simulations of the *E. coli* functional amyloid, CsgA. Subsequently, **Chapter 4** details the experimental characteristics of synthetic α-sheet peptides, including spectral properties, practical considerations for their synthesis, and unique physical and chemical traits that make them desirable as pharmaceutics.

Next, synthetic α-sheet peptides are deployed as inhibitors of functional amyloid formation in three different bacterial systems: *S. aureus*, *E. coli*, and *P. aeruginosa*. In **Chapter 5**, synthetic α-sheet peptide designs are applied to *S. aureus* biofilms, where they inhibit amyloid formation in

the EM. The peptides also inhibit aggregation of pure, synthetic phenol soluble modulin α1 (PSMα1), a major component of functional amyloids in *S. aureus*. **Chapter 6** examines the role of α-sheet in uropathogenic *E. coli* via a combination of biophysical tests with the major amyloid subunit, CsgA, and *in situ* tests with biofilms. Once again, synthetic α-sheet peptides inhibit amyloid formation, and the implications of this are extended to associations with the immune system and antibiotic therapy. In **Chapter 7**, synthetic α-sheet peptides are further developed as a component of anti-infective biomaterials. In a surface decoration approach, polydopamine coating facilitates attachment of synthetic α-sheet peptides directly at the surface of biomedical implant materials. These functional materials are shown to improve anti-fouling performance in a variety of biofilm assays. Finally, **Chapter 8** provides preliminary evidence of a role for α-sheet in *P. aeruginosa* and also identifies further opportunities for the engineering of peptide designs and anti-infective material coatings.

# Chapter 2. Sequence Analysis of Functional Amyloid in *P. aeruginosa*

## 2.1 Summary

In *P. aeruginosa* biofilms, functional amyloids are comprised primarily of a subunit called FapC. Despite its strong sequence conservation among pseudomonads, the mechanism of FapC fibril formation remains largely unexplored. The FapC sequence was examined in greater detail though a combination of bioinformatics and protein engineering. Sequence regions with high evolutionary conservation tended to coincide with regions of high amyloid propensity, and mutation of amyloidogenic motifs to a designed, non-amyloidogenic motif suppressed fibrillation. These findings clarify mechanisms of amyloid polymerization in *P. aeruginosa* and provide insight for development of new amyloid inhibitors.

## 2.2 Background and Motivation

*P. aeruginosa* is one of the most prominent causes of healthcare-associated infections (HAIs) due to its unique arsenal of virulence factors, resistance to a range of antibiotics, and its ability to form biofilms[18,99,100]. Infections with *P. aeruginosa* often manifest in the form of ventilator associated pneumonia (VAP), which demonstrates mortality rates as high as 30% in patients with comorbidities[101]. The plastic endotracheal tube readily provides a colonization site for *P. aeruginosa*, and aerosolization of the mature biofilm by mechanical ventilation or tracheal suctioning can lead to VAP[102]. Mucoid, biofilm-associated *P. aeruginosa* is also found in chronic lung infections of patients with cystic fibrosis[103]. In these cases, the EM of the biofilm is characterized by a large quantity of alginate exopolysaccharide, which allows the infection to persist and leads to poor patient prognoses[104]. In addition to alginate, *P. aeruginosa* synthesizes Psl and Pel, and all of these exopolysaccharide components confer fitness advantages to the biofilm by acting as structural scaffolds, initiating attachment, promoting intercellular interactions, and shielding microbes from host immune cells and antibiotics[11,26,27,105–107]. eDNA, another important macromolecule in the *P. aeruginosa* biofilm matrix, also plays a variety of roles in supporting the biofilm and can interact with other elements to influence development[108,109]. Proteins constitute the third, highly diverse group of polymers in the *P. aeruginosa* EM. These range from appendages

on individual cells, such as flagella and type IV pili, to secreted adhesins like CdrA[110,111]. Recently, amyloid fibers were identified as an additional proteinaceous EM component with important roles in mechanical stability, hydrophobicity, and quorum sensing[76,112]. These functional amyloids are highly conserved and impressively stable under denaturing or reducing conditions, and thus represent a promising avenue for disruption of biofilm physiology[64,113].

In *P. aeruginosa*, the production of functional amyloids is controlled by a single six-gene operon known as *fap*[64]. Wild-type *P. aeruginosa* PAO1 expresses *fap* constitutively, with peak promoter activity occurring during the exponential growth phase, but laboratory growth conditions limit the strain's ability to produce large quantities of functional amyloid. Conversely, overexpression of the *fap* operon in *P. aeruginosa* PAO1 leads to highly aggregative phenotypes with five to six times more biofilm than the wild-type strain, and similar effects are observed for overexpression of *fap* in *E. coli*[64,114] (**Figure 2.1 A**). The expression of *fap* is also tightly linked to a variety of other pathways generally associated with a biofilm mode of growth, including increased alginate production (AlgD, AlgE), increased Pel exopolysaccharide production (PelC), loss of motility, and decreased virulence (cAMP, Vfr)[115]. The mature form of the major amyloid subunit, FapC, consists of 316 amino acid residues without its 24-residue signal peptide, and it includes three imperfect sequence repeats (R1, R2, R3) separated by two "linker" regions (L1, L2)[114] (**Figure 2.1 B-D**). The three repeats are highly conserved among pseudomonads and related genera, with 56 ± 25% average residue conservation observed among 65 strains[116]. As such, the current model of FapC fibril formation designates the repeat regions as drivers of amyloid polymerization that ultimately constitute the core of the mature fibril. Analogous to the curli amyloids found in *E. coli*[117], the *fap* system also includes a nucleator protein FapB, which demonstrates 38% sequence identity to FapC (*P. aeruginosa* PAO1) and is believed to serve as a template for rapid fibril polymerization on the exterior of the cell. Small amounts of FapB are also found in mature fibrils, so it may play an additional role in modulating physicochemical properties of the fibrils[116]. The remaining proteins encoded by the *fap* operon serve as outer membrane pores for translocation of amyloid precursors (FapF)[118], chaperones to guide monomers through the periplasm (FapA), or auxiliary regulators and proteases (FapE, FapD)[114].

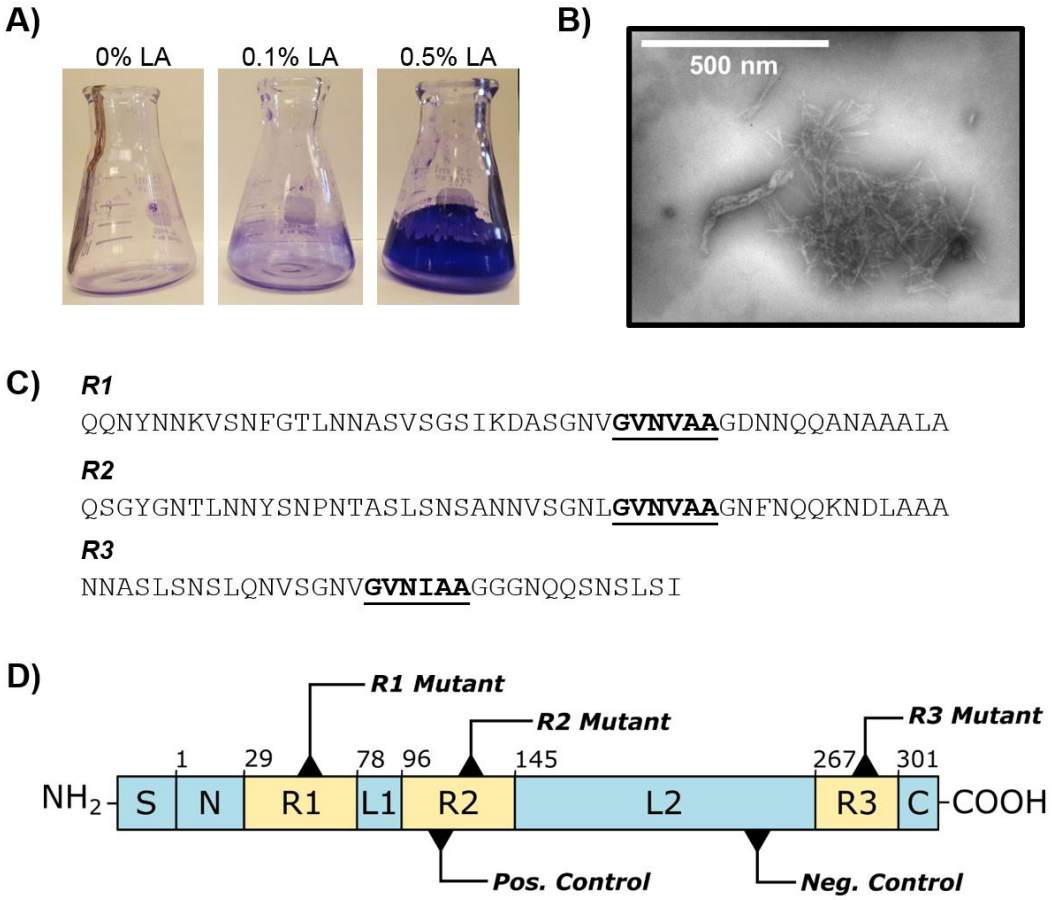


**Figure 2.1. The FapC protein from *P. aeruginosa* PAO1. A)** Tunable expression of the *fap* operon in an L-arabinose (LA; values are %w/v) inducible vector demonstrates enhanced aggregation and biofilm formation (see vector construction methods in **Appendix C.1**). **B)** The major amyloid subunit FapC aggregates to form amyloid fibrils. **C)** The FapC sequence is characterized by three conserved repeats – R1, R2, and R3 – each of which contains a "GVNXAA" motif indicated by bold/underlined text. **D)** Schematic of the PAO1 FapC sequence, including mutation sites for each of the protein variants used in this study. S = signal peptide, N = N-terminal region (residues 1-28), R1-R3 = repeat regions (residues 29-77, 96-144, 267-300); L1-L2 = linker regions (residues 78-95, 145-266); C = C-terminal region (residues 301-316). The first residue of each region is indicated above its corresponding box. The R1, R2, and R3 mutants incorporate GVNXAA→KFDDTK substitution in each of the three repeats, and the triple mutant incorporates this substitution in all three repeats. The negative control (AQGAKD→KFDDTK) consists of mutation in L2, and the positive control (SANNVS→GVNVAA) inserts a second amyloidogenic hexapeptide in R2.

Despite prior characterization of Fap proteins under sessile growth conditions, their mechanisms of fibrillation remain largely unexplored. In this chapter, the FapC sequence is examined in greater detail though a combination of bioinformatics and protein engineering[119]. Sequence analysis of the repeat regions predicts that a specific, conserved hexapeptide motif – GVNXAA – is responsible for a significant amyloidogenic effect in each of the three repeats.

Mutation of the amyloidogenic motif to a highly soluble, non-amyloidogenic hexapeptide changes fibrillation kinetics compared to wild-type FapC in a direction consistent with computational predictions. These effects are pH-dependent, and the third sequence repeat, R3, strongly influences fibril formation. The investigation presented in this Chapter reveals important mechanistic details of FapC fibril formation, with implications for new strategies to inhibit functional amyloid formation that are introduced in **Chapter 3**.

## 2.3 Results

### 2.3.1 *Amyloid-Prone Segments of FapC Coincide with Conserved Regions*

The rapid polymerization of FapC *in vitro* precludes its structural characterization by traditional means, such as NMR or X-ray crystallography, but a combination of evolutionary sequence analyses and bioinformatics tools helped identify potential "hot spots" for aggregation. The three repeat regions of the FapC sequence are highly conserved among pseudomonads, and therefore we hypothesized that these regions are critical for the macromolecular assembly of amyloid fibrils. A variety of bioinformatics tools has been developed to predict aggregation propensity and solubility of proteins[120], and we applied two of these algorithms to examine the repeat sequences of FapC from *P. aeruginosa* PAO1 (**Figure 2.2 A,B**). Both programs apply a sliding-window approach to analyze query sequences in hexapeptide increments.

ZipperDB, which uses structural alignment via the 3D profile method and Rosetta-based scoring to compute fibrillation propensities, predicts fibril formation in hexapeptides with Rosetta energies below -23 kcal/mol[82,89]. In PAO1 FapC, these segments tend to arise in the center of each repeat, with the greatest fibrillation propensity occurring in R3 (**Figure 2.2 A**). Similarly, FISH Amyloid, a machine learning approach that classifies sequences based on co-occurrence of query residues with those of known amyloidogenic hexapeptides[83], also predicts higher amyloidogenicity in the center of each repeat, with a notable spike in R3 (**Figure 2.2 B**). The hexapeptide with the greatest predicted fibrillation propensity in each repeat follows the same amino acid motif: GVNXAA, where X = Val in R1 and R2 and X = Ile in R3. Importantly, these amyloidogenic motifs coincide with regions of high sequence conservation among pseudomonads. Clustal Omega[121] was used to align 31 *Pseudomonas* FapC sequences originally compiled by Dueholm and coworkers[116], and then the sequence identity of each hexapeptide motif was

compared to its counterpart in the *P. aeruginosa* PAO1 FapC sequence. The R1 hexapeptide site averaged 85.5% identity; the R2 site averaged 75.6% identity; and the R3 site averaged 78.9% identity to PAO1 FapC. Notably, the Gly and Asn residues at positions 1 and 3 were 100% conserved in all repeats across all analyzed sequences (**Appendix A, Table A.1**).

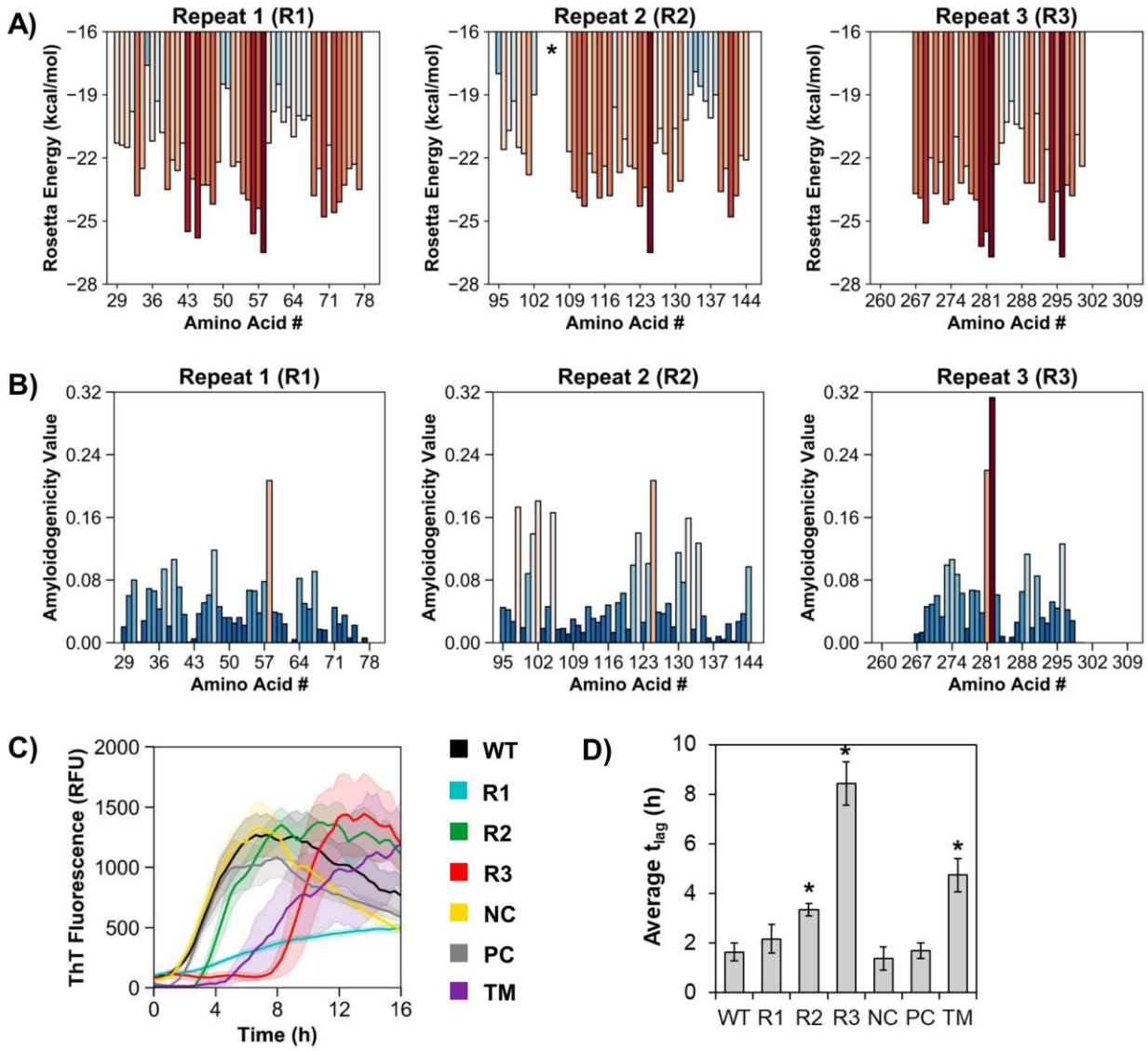


**Figure 2.2. Mutation of conserved GVNXAA motifs modulates aggregation kinetics in a direction consistent with computational predictions. A)** ZipperDB and **B)** FISH Amyloid algorithms were used to predict amyloidogenic regions within each of the three FapC repeats, R1-R3. Red colored bars indicate high amyloidogenicity, while blue colored bars indicate low amyloidogenicity. R1 spans residues 29-77, R2 spans residues 95-144, and R3 spans residues 267-300. GVNXAA motifs initiate at the following sties: R1 = residue 59; R2 = residue 126; R3 = residue 283. The asterisk in ZipperDB output for R2 indicates no data for residues 104-109 because residue Pro109 is incompatible with the 3D profile method. Amino acid numbering schemes in this figure are based on PAO1 FapC without its signal peptide. **C)** Protein variants were expressed and purified, diluted into 10 mM Tris buffer (pH 7.5), and allowed to aggregate with shaking at 37°C.

ThT fluorescence indicates amyloid fibril formation. **D)** Lag times define the amount of time elapsed prior to onset of fibril formation in each of the FapC variants. Asterisks indicate significant increase ($p < 0.001$, two-tailed Student's t-test) in lag time compared to WT. Error bands/bars in **(C)** and **(D)** indicate one standard deviation from the mean of at least three replicates.

### 2.3.2 *Redesigned Amyloidogenic Segments Modulate FapC Aggregation Kinetics*

To further probe the significance of predicted amyloidogenic regions in PAO1 FapC, the conserved hexapeptide motif, GVNXAA, was mutated to a hexapeptide with very low amyloid propensity. To select a low-amyloid hexapeptide, candidate sequences were first determined using peptide microarrays displaying segments from the *Pseudomonas sp*. UK4 FapC protein, a shorter sequence (226 residues in the mature protein versus 316 for PAO1 FapC) that is more amenable to high-throughput analysis but retains the triple repeat structure found in *P. aeruginosa* PAO1 FapC. Solutions of fluorescent-labeled UK4 FapC were applied to cellulose arrays of 384 immobilized peptide spots, each of which displays a 14-residue peptide. 107 of these spots were dedicated to the UK4 FapC sequence. Each spot moves two residues forward in the sequence compared to its predecessor, generating 12-residue overlaps between successive spots that facilitate high resolution analysis of protein self-association[122]. Fluorescence measurements indicated low levels of self-association for a charged region around residues 23-56 (numbering based on the first position of the mature protein, highlighted with orange in **Appendix B, Figure B.1 A**). Hexapeptide sequences from this region were subsequently analyzed for amyloid propensity in ZipperDB (**Appendix B, Figure B.1 B**) and FISH Amyloid, and generic aggregation potential was evaluated using the AGGRESCAN server[84]. The hexapeptide KFDDTK was ultimately selected as the ideal substitution for GVNXAA in PAO1 FapC, with a Rosetta energy of -17.7 kcal/mol and a FISH amyloidogenicity value of 0.025. A total of six mutant proteins were generated (**Figure 1C**): GVNXAA→KFDDTK substitution in each of the three repeats (R1, R2, R3); a triple mutant with substitution in all three repeats (TM); AQGAKD→KFDDTK as a negative control in linker region 1 (NC); and SANNVS→GVNVAA to insert a second amyloidogenic hexapeptide in R2, 9 residues upstream of GVNVAA (PC). All mutant proteins and wild-type (WT) PAO1 FapC were recombinantly expressed in *E. coli* using pET30a+ vectors and a C-terminal His tag for purification.

The aggregation kinetics of PAO1 FapC WT and its associated mutants were compared using a fluorescence assay. Briefly, each protein was desalted from a stock solution containing 8

M urea (which keeps the protein monomeric under storage conditions) into buffer and diluted to a final concentration of 0.2 mg/mL. Samples were incubated with shaking in a plate reader at 37°C, and Thioflavin T (ThT), a compound known to fluoresce in the presence of β-sheet-rich amyloid fibrils[123], enabled monitoring of protein fibril formation in real time. Conversion from random coil to β-sheet secondary structure was verified by circular dichroism spectroscopy (CD) (**Figure 2.3 A**) and the presence of amyloid fibrils was confirmed by transmission electron microscopy (TEM) (**Figure 2.3 B**). Fibril conformation was additionally validated by Fourier transform infrared spectroscopy (FTIR), where recombinant FapC fibrils were compared to Fap fibril extracts from *P. aeruginosa*. The high content of antiparallel β-sheets in amyloid fibrils leads to a characteristic high frequency band in the 1620-1630 $cm^{-1}$ region[124], and the FapC variants displayed a characteristic band at ~1625 $cm^{-1}$ (**Figure 2.3 C**).

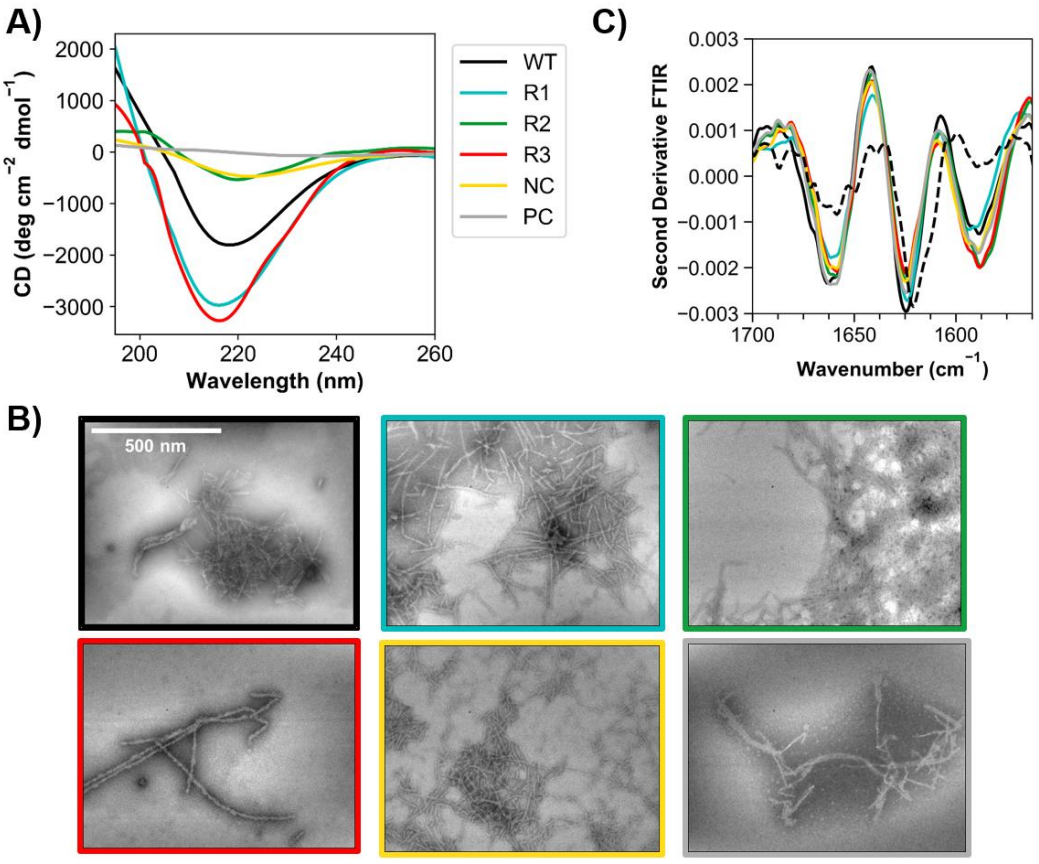


**Figure 2.3. Comparison of engineered FapC mutants. A)** Conversion to β-sheet secondary structure was verified by CD for FapC WT and five mutants. The positive control, PC, has a null signal because the sample consisted almost entirely of insoluble fibrils. **B)** The presence of amyloid fibrils was also confirmed by TEM (border colors match the legend in "A", and scale applies to all images). **C)** FTIR comparison of recombinant FapC fibrils (solid lines) compared Fap fibril extracts

(dashed lines) from *P. aeruginosa* PAO1 pFap. Second derivitave minimum at ~1625 cm-1 indicates β-sheet structure. Line coloring in **(C)** is the same as in **(A)**, but with black dashed line added to indicate PAO1 fibril extracts.

As shown in **Figure 2.2 C**, FapC WT polymerized rapidly, with essentially no lag time before ThT fluorescence increased. The three GVNXAA→KFDDTK mutants, however, displayed markedly different kinetics compared to the wild-type. Substitutions in R2 and R3 delayed the onset of fibril formation, and mutation in R1 substantially slowed the rate of fibril formation, i.e. the slope of the transition region from low to high ThT fluorescence (**Figure 2.2 C**). Interestingly, the combined effect of three hexapeptide mutations did not entirely suppress fibril formation in the triple mutant (TM). Rather, the aggregation kinetics of TM reflected a blend of the three single mutants, R1, R2, and R3; the lag time for TM extended, like R3, but its rate of fibril formation also slowed, like R1. It was not uncommon to see a decay in ThT signal intensity from the plateau reached after the transition region; this is frequently observed for amyloid proteins and while no definitive explanation for its occurrence has been provided, it may be caused by slow isomerization of ThT or bundling of the initially formed fibrils rather than reflecting conformational transitions at the level of the individual molecule. Therefore we like others chose to disregard it in our analysis of the data[123].

**Table 2.1. ZipperDB analysis of FapC mutants.** RE = Rosetta energy. Values in italics indicate no change from wild-type; values in bold indicate change from wild-type.

| | Average RE, full sequence (kcal/mol) | Average RE in R1 (kcal/mol) | Average RE in R2 (kcal/mol) | Average RE in R3 (kcal/mol) | Change from WT, full sequence (kcal/mol) | Change from WT, within repeat (kcal/mol) |
|---|---|---|---|---|---|---|
| FapC WT | *-21.84* | *-21.96* | *-21.59* | *-22.93* | – | – |
| FapC R1 | **-21.72** | **-21.23** | *-21.59* | *-22.93* | **+0.12** | **+0.73** |
| FapC R2 | **-21.71** | *-21.96* | **-20.65** | *-22.93* | **+0.13** | **+0.94** |
| FapC R3 | **-21.69** | *-21.96* | *-21.59* | **-21.58** | **+0.14** | **+1.35** |
| FapC NC | **-21.79** | *-21.96* | *-21.59* | *-22.93* | **+0.05** | – |
| FapC PC | **-21.84** | *-21.96* | **-21.82** | *-22.93* | **-0.004** | **-0.23** |
| FapC TM | **-21.44** | **-21.23** | **-20.65** | **-21.58** | **+0.40** | – |

Overall, the most significant changes resulted from GVNIAA→KFDDTK mutation in R3. This mutation induces a remarkable increase in the lag time, $t_{lag}$, from 1.6 h in the wild-type to 8.4 h in the R3 mutant (**Figure 2.2 D**). Analysis of the mutant sequences in ZipperDB supports this

observation; mutations in the R3 region are predicted to have a greater energetic impact than mutations in R1 or R2 (**Table 2.1**). Additionally, the negative and positive control mutants NC and PC fibrillated with behavior similar to WT, indicating that the influence of mutations is site-specific. The NC and PC mutants display modest changes in Rosetta energy compared to WT (**Table 2.1**), but the magnitude of these changes is much smaller than that of the GVNXAA mutants, which serves as a salutary reminder of the importance of context. These observations support the hypothesis that conserved GVNXAA motifs shape the kinetics of amyloid formation in PAO1 FapC.

### 2.3.3 *FapC Fibril Formation Depends on pH.*

*P. aeruginosa* dwells in a wide variety of natural habitats, including soil, water, plants, animals, and sewage. The pH of these environments spans a broad range from 4.5 to 9.5, which necessitates adaptation according to extracellular conditions[125]. In the hospital environment, *P. aeruginosa* encounters both acidic conditions (e.g. the airway of cystic fibrosis patients) and alkaline conditions (e.g. chronic wounds)[126,127]. To explore the influence of pH on PAO1 FapC fibril formation *in vitro*, desalted protein stocks were diluted into pH-adjusted buffer and aggregation was monitored in a plate reader using ThT fluorescence. Three pH values were evaluated to account for three clinical scenarios – pH 6.5 for the cystic fibrosis airway, pH 7.5 for normal physiological conditions, and pH 8.5 for chronic wounds – along with two additional "extreme" pH values at 5.5 and 9.5. ThT becomes inactivated by hydroxylation at pH > 8, so the pH 8.5 and 9.5 samples were incubated without ThT[128]. At the end of the assay (48 h), the pH of these samples was shifted back to 6.5 and then ThT was added to obtain endpoint fluorescence measurements. In the case of FapC WT, the extent of fibril formation did not change significantly between pH 5.5-9.5 (**Figure 2.4 A**), and the lag time remained quite short (~1 h) for pH values < 8 (**Appendix B, Figure B.2 A**). Like WT, aggregation kinetics of the R3 mutant were relatively similar to one another at pH 5.5-7.5 (**Appendix B, Figure B.2 B**). However, the extent of fibril formation was substantially reduced at pH 8.5 and 9.5 (**Figure 2.4 A**). These observations were confirmed by CD spectroscopy, which demonstrated conversion from random coil to β-sheet structure in FapC WT but not the R3 mutant at pH 9.5 (**Figure 2.4 B**). These results further support the role of conserved GVNXAA motifs in promoting amyloid formation under a variety of

conditions, and they underscore the importance of amino acid charge composition at the mutation site.

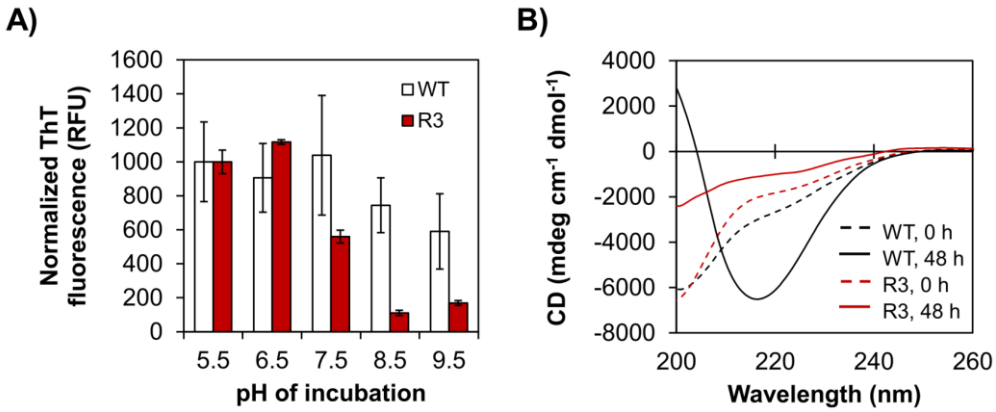


**Figure 2.4. FapC fibril formation depends on pH. A)** FapC WT and FapC R3 mutant were incubated with shaking at 37°C in 10 mM Tris buffer, pH 5.5, 6.5, 7.5, 8.5, or 9.5. After 48h, the ThT fluorescence of all samples was measured on a plate reader (high pH samples were incubated without ThT and adjusted to pH 6.5 prior to measurement). These endpoint measurements indicated a high degree of fibril formation for WT, regardless of pH, but R3 fibril formation was more pH-dependent. Error bars represent the standard deviation from the mean of three replicates. **B)** CD spectra for pH 9.5 at t = 0 h (dashed lines) and 48 h (solid lines) indicate secondary structure conversion from random coil to β-sheet in FapC WT (black) but not the R3 mutant (red).

### 2.3.4 *Sequence Repeat R3 is Essential for Robust Fibril Formation*

The markedly reduced aggregation propensity of the R3 mutant prompted further investigation of the role of R3 in amyloid fibril formation and stability. First, we hypothesized that delayed aggregation of the R3 mutant would enhance its susceptibility to known amyloid inhibitors. Next, we compared the stability of R3 fibrils to their WT counterparts using a novel dissociation approach with formic acid.

Epigallotcatechin-3-gallate (EGCG) is a widely studied antimicrobial that disrupts biofilm stability, interferes with quorum sensing, and increases susceptibility to antibiotics[129,130]. EGCG also inhibits PAO1 FapC amyloid formation by stabilizing pre-fibrillar oligomers, and it structurally remodels existing fibrils in vitro through the formation of non-amyloid aggregates[77]. To investigate the effect of EGCG on fibril formation of FapC WT and R3, desalted protein stocks were diluted in Tris buffer with various concentrations of EGCG. Samples were aliquoted into 96-well plates and incubated with shaking in a plate reader at 37°C, where fibril formation was monitored by ThT fluorescence (**Figure 2.5 A,B**). Without EGCG, FapC WT and R3 aggregated in a similar fashion to previous experiments, albeit at a slower rate due to decreased protein

concentration and gentler shaking (see Methods). As expected, the introduction of EGCG substantially inhibited the extent of amyloid formation in both FapC WT and R3, but the R3 mutant responded with greater sensitivity; an EGCG:protein molar ratio of 30:1 was required to fully suppress fibril formation in FapC WT, while a molar ratio of 5:1 was sufficient to elicit the same effect in R3 within the 25 hour observation window. Some evidence of aggregation eventually emerged in the 5:1 R3 sample after ~30 hours' incubation.

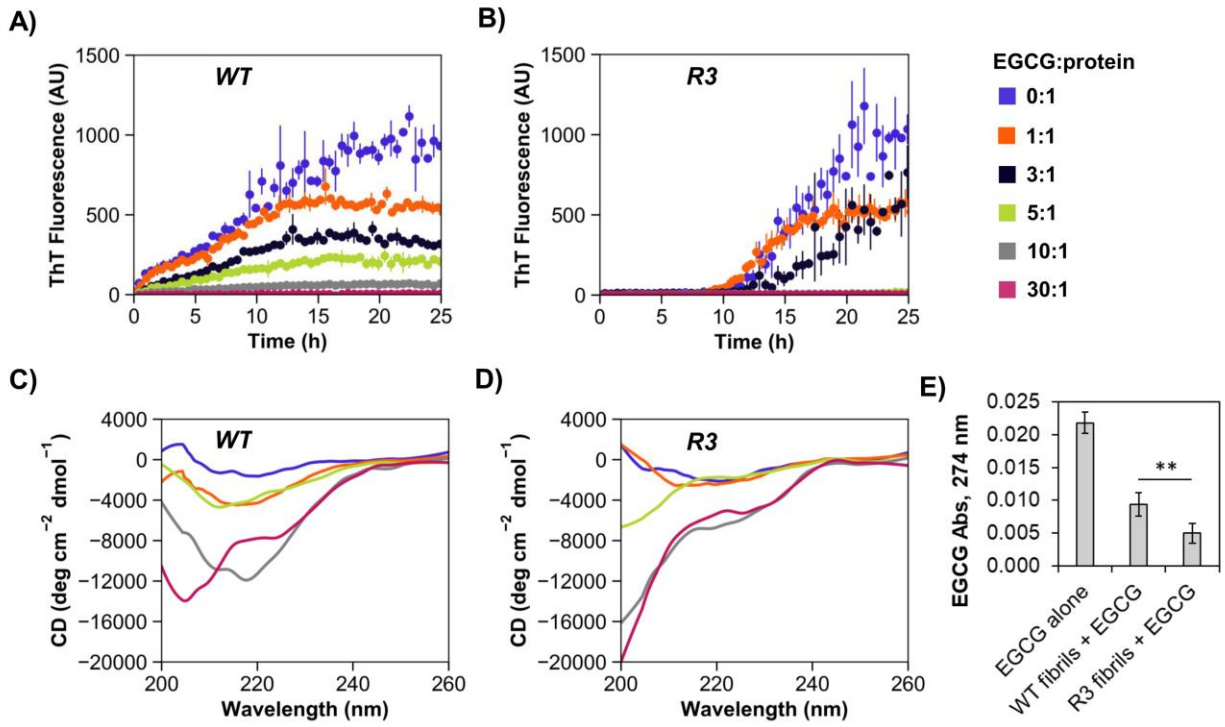


**Figure 2.5. FapC R3 is more susceptible to inhibition by the small molecule EGCG. A)** FapC WT and **B)** FapC R3 mutant were incubated at ~3 μM with shaking in 10 mM Tris buffer, pH 7.5. Various EGCG:protein molar ratios were tested (blue = 0:1, orange = 1:1, black = 3:1, green = 5:1, gray = 10:1, magenta = 30:1). In all cases, EGCG exerted some inhibitory effect on FapC fibril formation, but the effect was much more pronounced for the R3 mutant protein than WT. At the end of the assay, samples were analyzed further by CD. **C)** For FapC WT, only the samples with an EGCG:protein molar ratio of 30:1 remained unstructured throughout the 45 hour incubation; all other samples converted to β-sheet-rich signals at ~220 nm. **D)** For FapC R3, random coil content persisted down to an EGCG:protein ratio of 1:1, indicating much greater susceptibility to inhibition by EGCG. Error bars in **(A)** and **(B)** represent the standard deviation from the mean of three replicates. **E)** FapC WT and R3 fibrils were incubated with 15 μM EGCG overnight, and then fibrils were removed from solution by centrifugation. Analysis of the supernatants by UV-Vis spectrometry demonstrated that R3 fibrils bound more EGCG than WT fibrils ($p$ = 0.003, two-tailed Student's t-test). Error bars indicate standard deviation from the mean of three measurements.

Independent tests show that EGCG can displace ThT from its fibril binding sites or serve as a quencher, which may bias fluorescence assays[131,132]. Therefore, we chose to validate the impact of EGCG by structurally evaluating endpoint samples with CD spectroscopy (**Figure 2.5 C,D**). Prefibrillar, soluble FapC is mostly random coil (unstructured), and these types of signals were observed for samples incubated with high concentrations of EGCG. In the case of FapC WT, only the samples with an EGCG:protein molar ratio of 30:1 remained unstructured throughout the 45 hour incubation; all other samples converted to β-sheet-rich fibrils with signals at ~220 nm. Conversely, unstructured content persisted in FapC R3 down to an EGCG:protein ratio of 1:1, indicating much greater susceptibility to inhibition by EGCG. For both proteins, weakening of the β-sheet signal at low EGCG concentrations was attributed to visible fibril precipitation. We also performed a simple spin-down assay to assess the binding of EGCG to WT and R3 fibrils. Fibrils were prepared in 10 mM Tris buffer, pH 7.5, and then washed and resuspended either in buffer alone or buffer + 15 μM EGCG. The suspensions were incubated at room temperature overnight and then insoluble fibrils were removed by centrifugation. The supernatants were analyzed by UV-Vis spectrometry to assess the quantity of unbound EGCG remaining in solution (**Figure 2.5 E**). In accord with its increased EGCG susceptibility, R3 fibrils bound significantly more EGCG than WT fibrils. Finally, to address the possibility of a nonspecific, colloidal inhibition effect[133,134], we used Dynamic Light Scattering (DLS) and Nanoparticle Tracking Analysis (NTA) to analyze EGCG samples at a range of concentrations. Some particles were observed at a concentration of 90 μM EGCG (i.e. the 30:1 molar ratio used in inhibition experiments), but not in more dilute samples. Thus, colloidal effects may play a role in inhibiting FapC fibril formation, but only when EGCG is applied at very high concentrations.

The notable differences in aggregation kinetics and susceptibility to inhibitors between FapC WT and R3 prompted further examination of the fibrils themselves. Treatment of amyloids with concentrated formic acid (FA) is an established technique to solubilize mature fibrils[135], particularly functional amyloids which require much higher concentrations of FA than pathological amyloids to be solubilized[64] (and Line F.B. Christiansen and D.E.O., unpublished results). We extended these methods to investigate the stability of FapC fibrils. Samples of FapC WT and R3 were incubated in 96-well plates under the same conditions as the ThT aggregation assays, but with no ThT present. After 48 hours, fibril solutions were withdrawn from the plates and subjected to a series of centrifugation and wash steps to remove soluble or loosely adhered

protein. The fibrils were then incubated with increasing concentrations of FA (25% - 100%) for ten minutes prior to freeze drying and resuspension in water. The solubility of each sample was determined by SDS-PAGE, where the intensity of the FapC monomer band corresponded to the fraction of protein dissolved by FA (**Figure 2.6 A**). Visible aggregates were present in samples treated with low concentrations of FA, but solutions with 100% FA treatment appeared completely soluble and were used as the reference bands for intensity normalization. In accordance with its relatively slow polymerization and greater susceptibility to inhibition by EGCG, the R3 mutant generated fibrils that easily dissolved and therefore displayed more soluble protein on gels than FapC WT (**Figure 2.6 B**). The midpoint of dissolution (i.e. the concentration of FA at which 50% of fibrils dissolved) was estimated using least-squares regression (**2.6.8**; **Appendix B, Figure B.3**) at 54% FA for the R3 mutant and 80% FA for FapC WT, demonstrating that WT fibrils are more stable. These results further underscore the importance of the R3 repeat, and the GVNIAA sequence in particular, in reinforcing the intractable structure of native FapC fibrils.

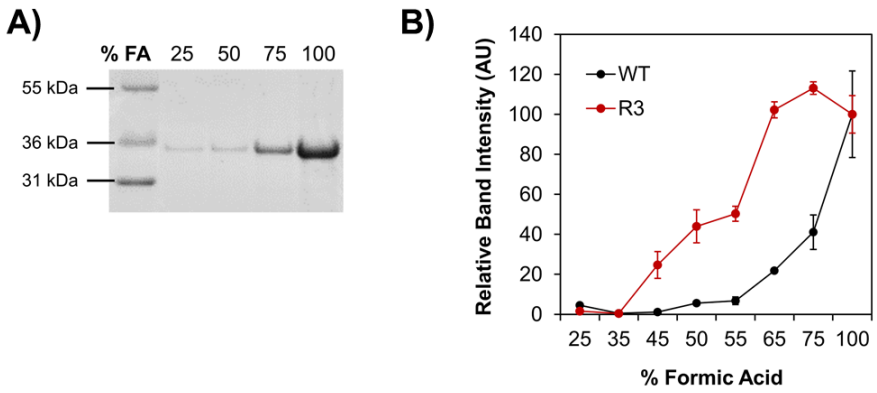


**Figure 2.6. Fibrils produced by the R3 mutant are less stable than those from FapC WT.** FapC WT and R3 were indubated under the same conditions as ThT assays, harvested, and incubated with increasing concentrations of FA. Treated samples were lyophilized and resuspended for analysis by SDS-PAGE; **A)** shows an example gel for FapC WT. **B)** Bands corresponding to FapC monomers were more pronounced for R3 (red) than WT (black), indicating that R3 mutant fibrils dissociated more easily. Error bars indicate the standard deviation from the mean of two samples.

### 2.3.5 *Small Oligomers Originate Through a Conserved Disulfide Bond*

The distinct kinetic behavior observed in the R3 mutant, as well as the other engineered proteins, inspired investigation of the molecular species formed on the pathway to amyloid formation. When FapC WT samples incubated quiescently for 1 h at room temperature, dimers and tetramers appeared on SDS-PAGE gels (**Figure 2.7 A**). We hypothesized that two conserved

cysteines near the end of the FapC sequence, which comprise a CXXC motif, may form an intermolecular disulfide bridge to initiate dimer formation and subsequent assembly of tetramers and higher-order species. Dimers were proven to arise via the disulfide bond by a simple chemical reduction test, in which reduced (β-mercaptoethanol) FapC WT samples ran as monomers on SDS-PAGE gels while non-reduced samples retained the dimer and tetramer species. Next, we tracked changes in the populations of soluble species throughout the fibril formation process. FapC WT was incubated in a 96-well plate under the same conditions as **Figure 2.2 C**, and samples were periodically withdrawn for analysis by size exclusion chromatography (SEC). Solutions were spun down to remove insoluble material prior to injection, and the resulting chromatograms revealed the presence of distinct dimer and tetramer species in addition to the main monomer peak, particularly at early time points (**Figure 2.7 B**). Interestingly, the purified dimer species aggregated on its own, but with slower kinetics than the monomer (**Figure 2.8 A**). This suggests a primary nucleation mechanism, in which some or all of the initial FapC monomer passes through small oligomeric states on the pathway to amyloid formation. However, these results could not establish whether the dimeric and tetrameric states serve as compulsory precursors to FapC amyloid assembly.

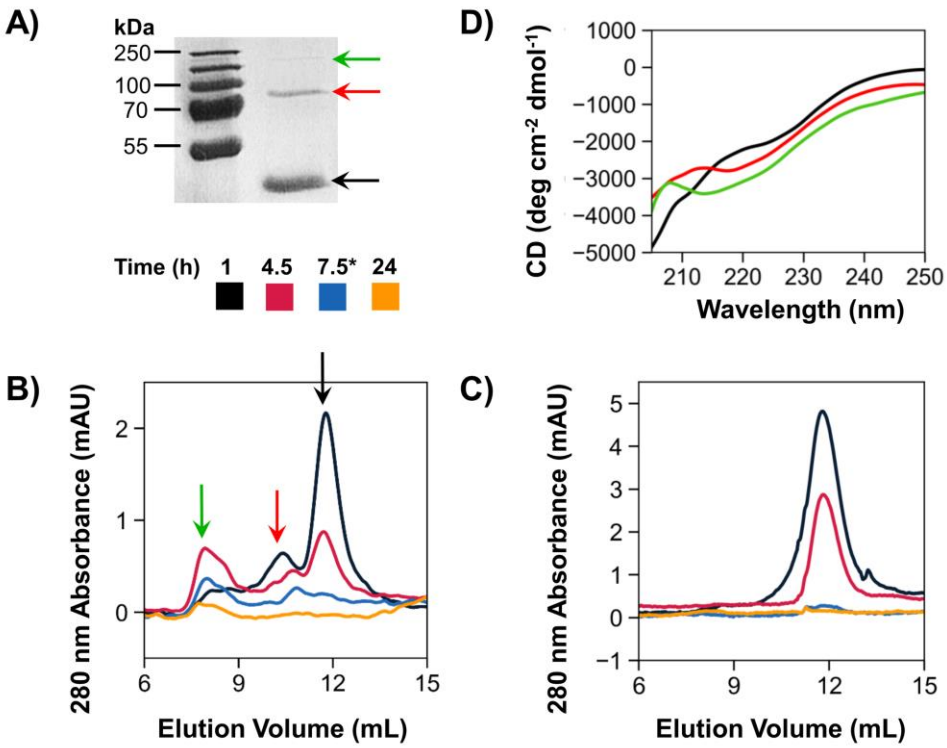


**Figure 2.7. Small oligomers originate through a conserved disulfide bond. A)** After 1 h incubation at room temperature, FapC WT began to convert from monomeric (black arrow) to dimeric (red arrow) and tetrameric (green arrow) species. To assess the influence of disulfide bonding on small oligomer species, **B)** FapC WT and **C)** the ΔCys (C304S/C307G) mutant were incubated with shaking at 37°C, and samples were periodically withdrawn for analysis by SEC. Peaks corresponding to monomeric, dimeric, and tetrameric species elute at approximately 12, 10.5, and 8 mL, respectively, and arrows indicate the same species as in **(A)**. *The third sample was withdrawn at 7.5 h for WT, but at 12 h for ΔCys. **D)** SEC elution fractions were pooled, concentrated, and adjusted to 0.1 mg/mL prior to measurement by CD. Monomers (black), dimers (red), and tetramers (green) all displayed spectra dominated by random-coil signal. Fibrils produced by the R3 mutant are less stable than those from FapC WT.

To assess whether dimer formation through the disulfide bond is required for polymerization, FapC was mutated to remove its two cysteine residues (FapC ΔCys, with mutations C304S and C307G). The mutant protein was expressed in *E. coli*, purified, and desalted in the same manner as FapC WT. Non-reducing SDS-PAGE confirmed that FapC ΔCys lacks the ability to form dimers (**Figure 2.8 B**). However, ThT assays and CD spectra of endpoint samples failed to reveal any substantial differences in the rate, extent, or structure of amyloid formed by FapC ΔCys compared to WT (**Figure 2.8 C,D**). Furthermore, SEC chromatograms of matched ΔCys samples exhibited only a single peak for the monomeric species, which depleted over time (**Figure 2.7 C**); no dimers, tetramers, or other higher order species were observed. Taken together,

these results imply that disulfide bonding is not a prerequisite for amyloid formation in FapC. Additionally, FapC WT precursors isolated by fraction collection were dominated by random-coil CD signal in all three species (monomer, dimer, tetramer; **Figure 2.7 D**), indicating that most conversion to β-sheet structure occurs in larger oligomers formed later in the aggregation process.

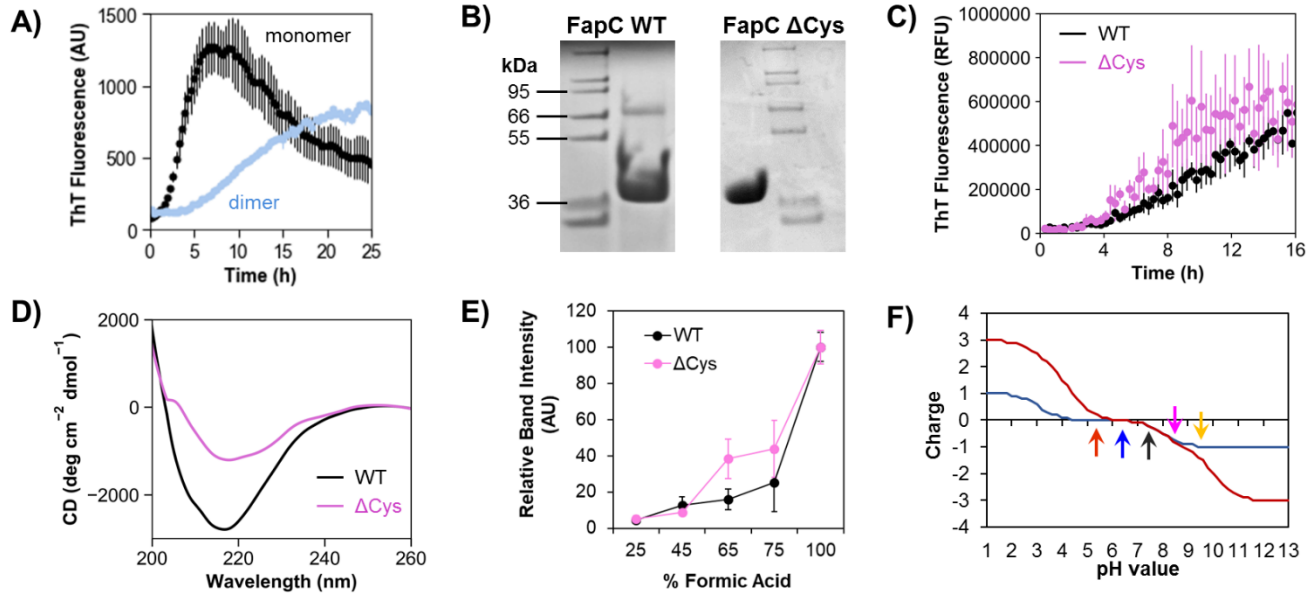


**Figure 2.8. Analysis of disulfide formation and charge states in FapC. A)** Isolated fractions of the FapC WT dimer species were pooled and concentrated to 0.5 mg/mL, and then aggregation of the dimer was tracked using ThT fluorescence. Dimer (0.5 mg/mL) is shown in blue and monomer (0.2 mg/mL) is shown in black). **B)** SDS-PAGE of purified FapC WT and ΔCys demonstrates the lack of disulfide-mediated dimers in ΔCys. Note that FapC runs slightly higher than its molecular weight of ~32 kDa; this is typical behavior for this protein on polyacrylamide gels. **C)** ThT assay to compare fibrillation profiles of FapC WT (black) and FapC ΔCys (pink). Error bars in **(A)** and **(B)** indicate standard deviation from the mean of three replicates. **D)** CD spectra for endpoint samples of FapC WT (black) and FapC ΔCys (pink) indicate conversion to β-sheet secondary structure. **E)** Formic acid treatment of WT fibrils (black) versus ΔCys fibrils (pink) demonstrates that disulfide bonding capability leads to a moderate increase in fibril stability. **F)** pH versus predicted charge state within the R3 repeat segment (residues 267-300) of FapC. Blue line = wild-type R3 sequence; red line = GVNIAA→KFDDTK mutated R3 sequence. Arrow colors correspond to pH values tested in Figure 3: red = pH 5.5, blue = pH 6.5, black = pH 7.5, pink = pH 8.5, and yellow = pH 9.5. Charges were predicted using the ThermoFisher Peptide Analyzing Tool.

## 2.4 Discussion

The *P. aeruginosa* FapC protein contains specific sequence motifs that drive amyloid formation. Analyses revealed sequence regions with high levels of both evolutionary conservation and amyloid propensity, which facilitated biophysical study of these regions with protein

engineering. Mutation of highly conserved segments to corresponding segments with much lower aggregation propensity confirmed the role of evolution in maintaining FapC amyloidogenicity. Modification of just six amino acid residues substantially altered the aggregation kinetics of mutant proteins compared to their wild-type counterparts, and the observed effects were site-specific. The third sequence repeat was especially sensitive to mutation, underscoring the importance of this conserved region in promoting amyloid assembly. Sequence analysis also identified a highly conserved disulfide motif that facilitates the development of soluble oligomers, but these species are not required for fibril formation.

The repeat mutants developed in this study draw important connections between computational predictions and experimental outcomes for the PAO1 FapC protein. FapC is large compared to most amyloids, and its dynamic nature has eluded structural characterization by traditional means such as NMR or X-ray crystallography. Therefore, we focused only on physicochemical characteristics and known relationships between the PAO1 sequence and its evolutionary relatives. These data were surprisingly rich and, coupled with prediction tools, allowed us to engineer the FapC protein in a way that revealed much about its mechanisms of fibril formation. All three of the site-specific mutants in this study (GVNXAA→KFDDTK) polymerized with uniquely delayed kinetics, demonstrating that the GVNXAA motif fulfills its predicted role as a highly conserved "driver" of amyloid formation in FapC. The extent of delay varied among the three mutants, with more profound effects observed in R3 than R2 and R1. Several kinetic models have been generated to fit ThT aggregation data, and these can help elucidate the dominant reaction mechanism in each case[136–139]. Generally, fibril formation kinetics are the result of up to four contributing microscopic processes: primary nucleation (association of individual monomers, mostly during the lag phase), elongation (addition of monomers to existing aggregates), secondary nucleation (association of monomers catalyzed by an existing fibril surface), and fragmentation (breaking of fibrils generates new ends for elongation). When secondary nucleation dominates the initial stages of fibril formation, existing fibrils are able to self-replicate, resulting in aggregation curves with very long and flat lag phases followed by an exponential increase in the rate of polymerization[138]. Primary nucleation, by contrast, requires the association of multiple monomers and occurs much more slowly. The R1 mutant, with its slower growth rate, likely undergoes less secondary nucleation than the other mutants or the WT protein. R2 and R3 display a flat lag followed by a rapid exponential phase, indicating strong secondary

nucleation effects and/or fragmentation. The length of the lag phase is most strongly influenced by the amplification of primary nuclei through their proliferation by secondary processes[137], so the especially long lag in R3 may reflect a delay in this cooperative activity.

Analysis in ZipperDB revealed that discrepancies between the mutants also depend on the predicted energetic impact of each mutation. The wild-type R3 segment has the lowest Rosetta energy (and, therefore, highest amyloid propensity) of the three repeats, so introduction of the KFDDTK mutation in this region induces the greatest reduction in overall amyloid propensity (**Table 2.1**). Substitution of all three GVNXAA motifs in the TM mutant also delayed the rate and onset of amyloid formation, but TM was still able to form fibrils. This reflects the complexities of FapC polymerization – while important, the presence of GVNXAA motifs is not the only property required to induce amyloid formation. Predictions identified several other sequence segments with high amyloid propensity, so these regions may compensate for the loss of GVNXAA in the triple mutant. All of the mutants ultimately formed amyloid fibrils with properties matching those of native (biofilm-purified) fibrils, so the mutations reported here successfully modulated aggregation kinetics without generating off-pathway aggregates. Mutants derived through this approach could serve as novel tools to study fibril formation in a variety of amyloid proteins, particularly those with little or no structural information. Moreover, mutations to reduce the amyloid propensity of FapC's third repeat increased its susceptibility to exogenous inhibitors. In theory, compounds designed to target R3, or the GVNIAA hexapeptide site specifically (e.g. peptides or peptide mimetics), could serve as effective inhibitors of fibril formation and biofilm establishment *in vivo*.

A second conserved sequence region, a CXXC motif near the C-terminus of FapC, forges a disulfide linkage between two monomers and promotes the formation of early, on-pathway oligomeric species. Despite CXXC conservation among pseudomonads, disulfide formation is not a requirement for amyloid formation in FapC, and pre-fibrillar oligomers larger than dimeric and tetrameric species are likely involved. It is also possible that the disulfide bond persists throughout amyloid assembly and provides additional molecular reinforcement in mature fibrils. Faint dimer bands were visible by SDS-PAGE for urea-purified FapC WT stocks, so the ability to dimerize even under harsh or denaturing conditions indicates that FapC readily forms disulfide contacts. Even FA-treated FapC displayed faint dimer bands on SDS-PAGE gels, suggesting that dimers were either retained in the fibrils or re-formed from monomers sometime during the treatment with

FA. In dissolution experiments with FA, fibrils with disulfide bonds intact (FapC WT) were moderately more stable than those without disulfide bonding capability (FapC ΔCys) (**Figure 2.8 E**). *In vivo*, FapC disulfide bonds may be far more essential, with potential involvement in preventing proteolysis, imparting stability, or encouraging fibril formation[140,141]. Indeed, evolutionary sequence analysis revealed that only *P. putida* strains consistently lacked the CXXC motif and, intriguingly, previous attempts to isolate amyloid fibrils from *P. putida* failed due to fibril instability and inefficient separation from contaminants[114].

The range of pH experienced by bacteria *in vivo* depends not only on the growth medium but also a variety of other factors, such as access to fermentable sugars, oxygen availability, and the size of the biofilm. Amyloid fibrils, including those from FapC, are highly resistant to acidic conditions[142], so increased fibril formation at low pH values could help provide a denser mesh of protective protein to shield the biofilm from harsh conditions. The EM of *Pseudomonas* is highly complex, however, so interactions between FapC and other matrix components – particularly charged macromolecules such as the exopolysaccharides Pel, Psl, and alginate, as well as extracellular DNA – must be considered to fully elucidate the effect of pH on aggregation *in vivo*. The examination of FapC behavior at a variety of pH values was designed to mimic variable biofilm conditions, and low pH values ($\leq$ 7.5) resulted in a greater extent of fibril formation, especially in the R3 mutant. Charge state analysis of the R3 repeat (residues 267-300) reveals that mutation of GVNIAA to KFDDTK increases charge sensitivity to pH above and below the isoelectric point (**Figure 2.8 F**). For example, at pH 9.5, the wild-type R3 segment has a predicted net charge of -1 while the mutated R3 segment has a predicted net charge of -1.5. This is in accord with the insertion of charged residues. However, charge state values assume that all residues have pKa values equivalent to those of the isolated residues, so the influence of pH and charge may become more pronounced as FapC associates with itself and neighboring monomers during the course of fibril formation.

## 2.5 Conclusions

Recent advances in prediction tools have enabled accurate prediction of intrinsic aggregation propensity based on specific mutations in mammalian amyloid proteins[143,144], but this chapter details the first extension of this approach to the relatively unexplored realm of bacterial amyloids. This study identified segments in the *P. aeruginosa* FapC sequence that are implicated

in amyloid fibril formation. Mutation of important segments helped elucidate mechanisms of aggregation in these complex proteins, establishing new targets for therapeutic exploitation. These insights are highly valuable in the development of antibiotic alternatives for combating biofilm and ultimately reducing the burden of hospital-acquired infections.

## 2.6 Materials and Methods

### 2.6.1 *Sequence Analysis*

The FASTA sequence for PAO1 FapC (without the 24-residue signal peptide) was imported from the UniProtKB database (ID Q9I2F0). The sequence was then analyzed for amyloid "hot spots" in ZipperDB (http://services.mbi.ucla.edu/zipperdb/) with threshold -23 kcal/mol and FISH Amyloid (http://www.comprec.pwr.wroc.pl/fish/) with threshold 0.19. Predicted hot spots were compared to conserved regions among 31 *Pseudomonas* FapC homologs using sequence alignment in Clustal Omega[121].

### 2.6.2 *Peptide Microarrays*

Printed peptide libraries were designed to assess the self-recognition of UK4 FapC. Each array contained 384 peptide spots, each 14 residues in length. 107 of these spots were employed to display residues 25-250 in the UK4 FapC sequence (NCBI entry EEP64551.1, excluding the 24-residue signal peptide), advancing stepwise two residues through the FapC sequence with each spot and thus overlapping the previous spot by 12 residues. Peptides were synthesized in parallel using a ResPep SL synthesis robot (Intavis AG, Cologne, Germany) equipped with a Celluspot synthesis module and printed using a slide spotting robot (Intavis AG). Coupling reagents were freshly prepared every 48 h. Synthesis was based on standard Fmoc peptide synthesis using reagents from Sigma-Aldrich (St. Louis, MO) and Iris (Marktredwitz, Germany) and performed on acid-soluble Fmoc-β-Alanine etherified cellulose disks. N-terminal Fmoc protection was removed by adding 2 µL and 4 µL 20% Piperidine in N-Methyl Pyrrolidone (NMP) for 5 and 10 min. Two couplings (each 40 min) using Oxyma/N,N′-Diisopropylcarbodiimide/Amino Acid in the relation (1.1/1.5/1.0) in at least 5-fold excess followed by two washing steps (100 µL and 300 µL NMP) and 4 µL capping solution (5% Acetic Anhydride in NMP) achieved peptide elongation by one amino acid. The subsequent peptide work-up was performed manually on all peptides in

parallel after transfer of the cellulose disks into 96 deep-well blocks. Peptide side-chain deprotection was achieved with 150 µL deprotection solution (trifluoroacetic acid (TFA)/triisopropylsilane (TIPS)/water/DCM: 80%, 3%, 5%, 12%) for 2 h. Disks were then solubilized overnight in 250 µL of cellulose solvation solution (TFA/trifluoromethansulfonic acid/TIPS/water: 88.5%, 4%, 2.5%, 5%) under strong agitation. 750 µL diethyl ether (DE, -20°C) was added to the dissolved cellulose-peptide conjugates and the mixture was briefly agitated and kept at -20°C for 1 h. Precipitated conjugates were pelleted by centrifugation at 2000 xg for 30 min at 4°C. After removal of the supernatant the pellet was additionally washed twice with 750 µL fresh DE (-20°C). After the final washing step, residual ether was evaporated and 250 µL of dimethyl sulfoxide (DMSO) was added to re-solvate the cellulose-peptide conjugates. The cellulose-peptide conjugate stock solutions were stored at -20°C. Prior to printing 80 µL of the stocks were transferred to a 384-well plate and mixed with 20 µL SSC buffer (150 µM NaCl; 15 µM Na3C6H5O7; pH 7.0). 50 nL of each peptide was contact printed on coated glass slides with a slide spotting robot (Intavis AG) and dried overnight.

Recombinant UK4 FapC was expressed in *E. coli* BL21 (DE3), purified with Ni-NTA beads, and labeled with AlexaFluor® 546 (A546; Thermo Fisher, Waltham, MA) according to manufacturer protocols. Prior to protein application, peptide microarrays were blocked overnight at 4°C with PBS-T (phosphate buffered saline + 0.05% Tween-20) containing 3% w/v whey protein. A546-labeled protein was then added to the array at a concentration of 0.05 mg/mL and incubated for six hours at room temperature on a roller. After incubation, each array was washed with TBS-T for 15 min. The washed arrays were left to dry for approximately 5 minutes and then the fluorescence of each spot was measured using a Typhoon Trio scanner (GE Life Sciences, Pittsburgh, PA). Spots were quantified using the ImageJ Protein Array Analyzer[145].

### 2.6.3 *Expression and Purification of Recombinant FapC*

A synthetic gene corresponding to the wild-type FapC protein from *P. aeruginosa* PAO1 was designed and synthesized by GenScript (Piscataway, NJ). The gene was then cloned into the pET30a(+) vector, which added a C-terminal 6x His tag for purification. All FapC mutants were constructed by GenScript using this plasmid as template, with the exception of FapC TM which was generated in-house using restriction enzyme cloning (synthetic TM gene from Genscript) and FapC ΔCys which was constructed in-house using site directed mutagenesis (**Appendix A, Table**

**A.3**). Mutation in FapC ΔCys (C304S and C307G) and insertion of the synthetic TM gene was verified by Sanger sequencing (Genewiz, South Plainfield, NJ). Plasmids were transformed into *E. coli* BL21 (DE3) cells and protein expression was carried out in 2 L baffled shake flasks at 37°C and 165 rpm (LB medium supplemented with 4 mM MgSO4, 1% v/v glycerol, and 50 μg/mL kanamycin). Cultures grew to an OD600nm of 0.6-0.8 prior to induction with 1 mM IPTG. After 3-4 hours of additional growth, cells were harvested by centrifugation at 4000 xg for 20 minutes. Cell pellets were re-suspended in 30 mL denaturing buffer (8M Urea, 20 mM sodium phosphate, 500 mM NaCl, pH 7.8) and lysed overnight with stirring at 4°C. Insoluble material was removed by centrifugation at 14,000 xg for 30 minutes and the supernatant was incubated with Ni-NTA beads for ≥ 4 h at 4°C. The beads were then washed twice with denaturing buffer, once with denaturing buffer plus 15 mM imidazole, and twice with denaturing buffer plus 30 mM imidazole. Finally, protein was eluted with denaturing buffer plus 300 mM imidazole. Protein purity was assessed by SDS-PAGE (15% acrylamide-bis, MES-Tris running buffer) and eluents were stored at -20°C to prevent urea-induced carbamylation. Immediately prior to use, protein eluents were thawed and desalted according to the PD-10 desalting column protocol (GE Life Sciences) into 10 mM Tris, pH 7.5, and kept on ice. Protein concentration was determined by absorption at 280 nm (extinction coefficients calculated with ExPAsy ProtParam[146]). Desalted proteins were of high concentration and purity, so they were not purified further prior to aggregation assays.

### 2.6.4 *FapC Amyloid Formation Assays*

The buffer in all aggregation assays was 10 mM Tris, pH 7.5, plus 20 μM ThT. As necessary, pH adjustments were made using 6 M HCl or 6 M NaOH, and all buffers were filtered through a 0.2 μm membrane before use. In the case of inhibition experiments, EGCG (Cayman Chemical, Ann Arbor, Michigan) was freshly prepared as a 20 mg/mL stock and added to the buffer to a final concentration of 3, 9, 15, 30, or 90 μM. To start the assay, desalted protein stocks were added to black-walled 96-well plates and diluted with appropriate buffer such that the final concentration of protein was 0.2 mg/mL (except for EGCG inhibition assays, where it was 0.1 mg/mL) and the final volume was 100 μL per well. A sterile 3 mm borosilicate glass bead was added to each well to facilitate mixing and the plate was covered with an adhesive seal. ThT fluorescence was monitored in a Tecan (Männedorf, Switzerland) plate reader at 37°C with excitation at 448 nm and emission at 485 nm. For each measurement, 60 s of orbital shaking at

180 rpm was applied before a 5 s settling time, and then 10 single reads were averaged for each well. In the case of EGCG and ΔCys experiments, settling time was extended to 5 min. All experiments consisted of at least three replicates per condition, and plots display data points from every 0.5-0.7 h for clarity. Samples for CD, FTIR, and SEC were treated identically and added to the same plate to ensure matched conditions. Values for the lag time ($t_{lag}$) and rate of maximum fibril formation were calculated according to the methods of Morris, et al.[147].

### 2.6.5 *Spectroscopy*

Samples for CD were diluted fresh from desalted protein stocks (0 h samples) or removed from microtiter plates (endpoint, fibrillated samples). SEC elution fractions were pooled, concentrated with Amicon® Ultra centrifugal filter units (Sigma-Aldrich), and adjusted to 0.1 mg/mL prior to measurement. CD spectra were recorded on a J-810 spectropolarimeter (Jasco Spectroscopic Co. Ltd., Tokyo, Japan) using a 1 mm quartz cuvette and the following settings: wavelength 260-200 nm, 0.5 nm data pitch, 1 s integration time, 2 nm bandwidth, 25°C, and 4-6 accumulations. Only data points with detector voltages below 600 V were used. All spectra were corrected by a blank spectrum of relevant buffer and smoothed with a Savitsky-Golay filter at window size 25-65 and polynomial order 2. FTIR spectroscopy was performed on a Tensor 27 FTIR spectrophotometer (Bruker, Billerica, MA) with a deuterated tri-glycine sulfate mid-infrared detector and a Golden Gate single reflection diamond attenuated total reflectance (ATR) cell (Specac, Kent, UK). Fibril samples were dried on the ATR crystal with a stream of nitrogen and spectra were collected from 4000-600 cm-1. Spectra were baseline corrected and atmospheric compensation was performed with OPUS 5.5 software (Bruker). Signals in the amide I region (~1550 – 1700 cm-1) were normalized and identified by second derivative analysis in Python. For FTIR analysis of fibrils from *P. aeruginosa* PAO1 biofilms, fibrils were collected from a *fap* overexpressing strain (**Appendix A, Table A.2**) as previously described[114].

### 2.6.6 *EGCG Particle Analysis*

EGCG stock was prepared by dissolving lyophilized stock powder in PBS to a concentration of 20 mg/mL. This stock was then diluted in 10 mM Tris, pH 7.5 to a concentration of 1, 3, 9, 30, or 90 μM and immediately used for analysis. DLS measurements were performed in triplicate on a Zetasizer Nano Series instrument (Malvern, Salisbury, UK) using 1 mL for each

sample. NTA measurements were performed on a NanoSight NS300 (Malvern) at 23°C, camera level 11, and a detection threshold of 3.

### 2.6.7 *SEC*

Samples for SEC were FapC WT and ΔCys, fibrillated under identical conditions and in the same plate as the corresponding ThT assays. At each time point, three well volumes (300 μL total) per condition were removed from the plate and transferred to a 1.5 mL Eppendorf tube. Tubes were flash-frozen for storage. Immediately prior to SEC analysis, each sample was thawed on ice and then centrifuged at >12,000 rpm for at least 10 minutes to remove insoluble material. Supernatant (250 μL) was loaded onto a Superdex 200 Increase 10/300 GL column (GE Life Sciences) equilibrated in 10 mM Tris, pH 7.5. Fractions of 0.75 mL were collected at a flow rate of 0.75 mL/min and chromatography traces were collected with a UV cell at 280 nm (ÄKTA Pure system; GE Life Sciences).

### 2.6.8 *Formic Acid Treatment*

FapC WT, R3, and ΔCys were incubated at 0.2 mg/mL in Tris buffer, under the same conditions as the ThT aggregation assays but with 200 μL of solution per well. After 48 hours, fibril solutions were removed from wells and transferred to Eppendorf tubes. Fibrils were isolated by centrifugation at 20,000 xg for 10 min and the concentration of FapC remaining in the supernatant was measured by NanoDrop™ (Thermo Fisher). Fibrils were then washed twice in filtered water, resuspended to a concentration of 1 mg/mL, and divided among a series of new Eppendorf tubes. The tubes were centrifuged again and each fibril pellet was resuspended in different concentrations of formic acid in water (range = 25-100% formic acid) such that the final concentration of protein was 0.5 mg/mL. Samples were incubated for 10 minutes, frozen, and lyophilized overnight. For SDS-PAGE analysis, each dried protein film was resuspended in water and mixed with non-reducing sample buffer. Samples were heated for 5 min at 95° and then loaded into lanes of 15% acrylamide-bis gels. Gels ran at 100V for 90 minutes in MOPS-Tris running buffer, stained for 30 min in Coomassie Brilliant Blue R-250, and destained overnight prior to imaging on an Azure c300 imaging system (Azure Biosystems, Dublin, CA). Relative band intensities were determined using ImageJ software[148]. Two gels were run for each condition to ensure reproducibility. The midpoint of dissolution ($x_o$, the concentration of FA at which 50% of

fibrils dissolved) was estimated with a least-squares regression script in Python using the following equation:

$$y = \frac{c}{e^{-k(x-x_o)}} + y_o \quad (2.1)$$

where $c$ is the maximum band intensity; $k$ is the steepness of the sigmoidal curve; and $x$ and $y$ are the percentage of FA and the relative band intensity, respectively.

# Chapter 3. Application of Computational Tools for Anti-amyloid Peptide Design

## 3.1 Summary

Recent advances in next-generation sequencing and high-performance computing have massively expanded the known protein sequence and dynamic space, enabling analyses that were previously inaccessible due to high experimental or computational costs. These data are now being combined with experimentally derived constraints to identify and predict interactions within proteins as well as between proteins and a variety of binding partners. For the design of functional amyloid inhibitors, this process took two forms – both of which generated *de novo* peptides intended to bind amyloids and prevent their polymerization into fibrils. First, a structure-fitting approach in Rosetta utilized information from *P. aeruginosa* sequence analysis to design synthetic peptides to "cap" the end of a growing amyloid fibril, thereby preventing further polymerization. Second, MD simulations identified a unique secondary structure termed "α-sheet" in the soluble, pre-fibrillar forms of mammalian amyloid proteins and peptides. Synthetic α-sheet peptides were then designed to recapitulate the α-sheet structure observed in amyloid targets, with the goal of exploiting structural similarity to bind and sequester the pre-fibrillar species.

## 3.2 Fibril Cap Designs: Rosetta

### 3.2.1 *Background and Motivation*

The studies presented in Chapter 2 provided detailed new insights to the mechanisms of fibril formation in the *P. aeruginosa* FapC amyloid subunit. In addition to filling a knowledge gap in biophysical understanding of this protein, identification of amyloid-prone "hot spots" in the sequence provided new opportunities for inhibitor design. The three repeat regions of FapC each contain the highly conserved hexapeptide sequence GVNXAA (where X = Val in R1 and R2 and X = Ile in R3), and mutation of this amyloidogenic segment to a non-amyloidogenic segment elicited profound changes in polymerization kinetics and fibril stability. Mutation of the native FapC protein is not a viable therapeutic strategy to disrupt *P. aeruginosa* biofilm formation in the clinic, however. Instead, exogenous compounds must be introduced – either as a surface coating

on medical implants, or through systemic administration – that can bind GVNXAA and thereby interfere with the amyloid formation process *in vivo*. In addition to tight target binding, the design of inhibitors is constrained by practical considerations such as degradation of the compound. Peptides comprised of D-amino acids represent the optimal solution to both of these concerns. The combination of 20 different amino acids affords enormous chemical variability in the selection of ideal binders, and D-enantiomers of the canonical amino acids retain critical functional groups while exhibiting increased resistance to enzymatic degradation compared to their L-counterparts[149]. Furthermore, polypeptide chains can be generated on a variety of scales, including the relatively small hexapeptide length required to align with GVNXAA targets.

### 3.2.2 *Design Approach*

Guided by the aforementioned design constraints, candidate peptide binders were generated with the Rosetta program[150]. The assumption that FapC forms "steric zipper" amyloid fibrils served as a key assumption in this workflow. In the steric zipper model, two self-complementary β-sheets constitute the spine of an amyloid fibril through tight interdigitation of side chains, hydrogen bonding, and exclusion of solvent[34]. Very short peptide segments can form steric zippers *in vitro*, with as few as six amino acid residues in each β-strand[151]. In Chapter 2, this information was applied to determine the amyloid formation propensity of all possible hexapeptides in FapC via the 3D profile method[82], and GVNVAA segments were identified as segments with high likelihood to form steric zippers. To generate a model of the target fibril structure, the GVNVAA sequence was threaded onto the crystal structure of the known steric zipper, NNQQNY (Protein Data Bank ID 1YJO)[34], in ZipperDB. The resulting extended L-peptide model was repacked and minimized with the Rosetta relax protocol[152].

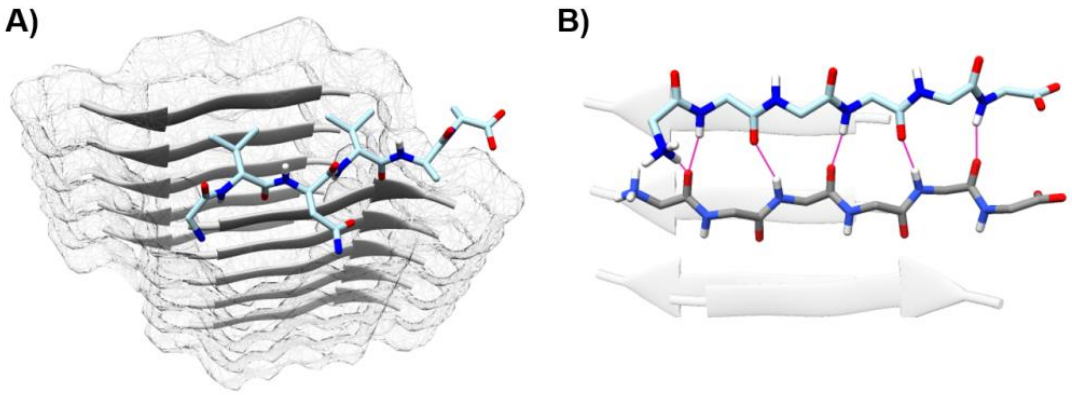


**Figure 3.1. Manual assembly of initial pose for the all-L zipper target and all-D capping peptide. A)** Top view shows the all-L GVNVAA repeating zipper in silver (with transparent surface) and the all-D GVNVAA peptide manually positioned as a "cap" at the end of the fibril. **B)** The capping peptide (blue) was aligned with the adjacent fibril strand (silver) to promote hydrogen bonding (bonds drawn in magenta).

Next, protocols were carried out to design D-peptides that could "cap" the end of the GVNVAA fibril and, in theory, block its further polymerization[153]. An in-house protein manipulation tool called Wrangler (Jenny Ferina, unpublished work, Daggett lab) was used to construct a D-peptide with the same sequence and backbone angles as the GVNVAA zipper target, and this D-peptide was manually positioned in a favorable hydrogen-bonding position at the terminus of the all-L fibril model (**Figure 3.1**). The FlexPepDock refinement mode algorithm[154] was then applied to select favorable backbone conformations for the capping D-peptide while keeping the all-L fibril model fixed. FlexPepDock operates in three steps: (1) prepacking of the input structure side chains to remove internal clashes in the steric zipper and the capping peptide; (2) fast, low resolution of the rigid body orientation and backbone degrees of freedom of the D-peptide; and (3) Monte-Carlo search with energy minimization to first optimize the rigid body orientation between zipper and D-peptide and then optimize the peptide backbone for the new orientation. Candidate structures (1000 total) were scored according to several criteria, each of which represents a different contribution to the energy of the peptide-fibril complex[155] (**Figure 3.2**). Lower scores indicate lower energy and more favorable binding between the D-peptide and the L-fibril. The large number of candidate peptide conformations was reduced to 181 representative clusters by grouping according to backbone RMSD; each cluster contained a given structure and all its neighbors within a cluster radius of 2 Å. As shown in **Figure 3.3 A**, lower cluster numbers tended to have lower scores (e.g., only 3 of the 100 best-scoring designs fell

outside Cluster 0), low-numbered clusters contained far more structures than in high-numbered clusters (e.g., Cluster 0 contained over 400 structures, while Cluster 10 contained only 11 structures). Representative structures for each of the top three clusters are shown in **Figure 3.3 B**.

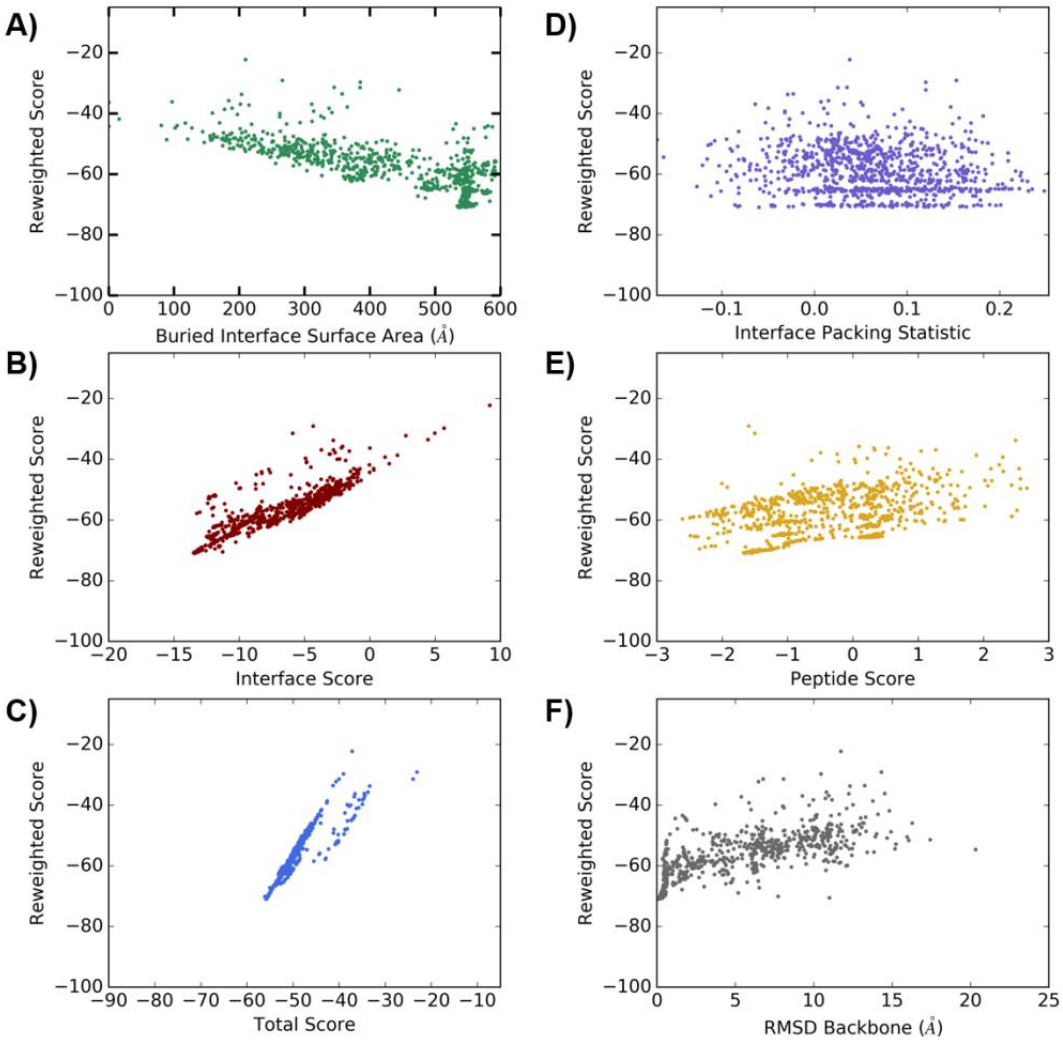


**Figure 3.2. Scoring of 1000 candidate backbone structures with FlexPepDock.** Reweighted score as a function of **A)** buried interface surface area (Å$^2$) between the fibril and the capping peptide, **B)** interface score (sum over energy contributed by interface residues of both partners), **C)** total score (total score of the complex), **D)** interface packing statistic, **E)** peptide score (sum over energy contributed by the peptide to the total score; consists of the internal peptide energy and the interface energy), and **F)** backbone RMSD (Å) between output model and initial structure. Reweighted score give double weight to interface residues and triple weight to peptide residues, and lower values indicate lower (more favorable) energy of docking.

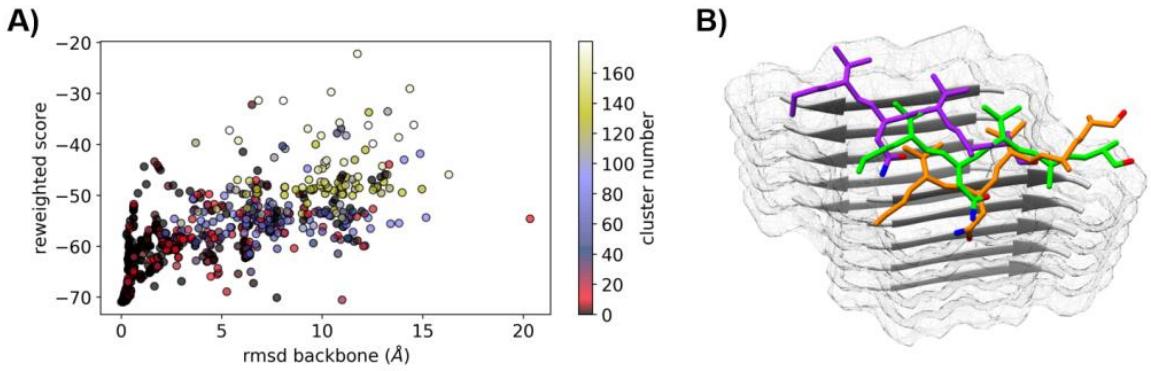


**Figure 3.3. Clustering candidate backbone structures. A)** The large number of candidate peptide conformations was reduced to 181 representative clusters by grouping according to backbone RMSD; each cluster contained a given structure and all its neighbors within a cluster radius of 2 Å. **B)** All-L steric zipper model docked with representative all-D peptides from cluster 0 (orange), 1 (green), and 2 (purple).

For the final step in the design process, side chain chemistries of the capping D-peptide were varied while keeping backbone conformation fixed. The top backbone conformations from Clusters 0, 1, and 2 were used as starting points for this step (rankings based on lowest reweighted score, where interface residues are given double weight and peptide residues are given triple weight). The FixBB Rosetta algorithm finds the lowest energy set of side chains and rotamers by optimizing a potential consisting of terms for electrostatics, hydrogen bonding, implicit solvation, and torsions[156]. Two rounds of side chain iteration were performed; in the first, any amino acid was allowed, and in the second, mutations were forced (i.e. the D-peptide sequence could not contain G, V, N, V, A, or A in the same sequence position as the steric zipper). 500 candidate D-peptide sequences were generated for each round, and candidates were further ranked based on their change in binding energy, $\Delta E_{binding}$, according to Equation 3.1:

$$\Delta E_{binding} = E_{complex} - [E_{fibril} + E_{peptide}] \quad (3.1)$$

where $E_{complex}$ is the score of the relaxed peptide-fibril complex, $E_{fibril}$ is the score of the relaxed GVNVAA steric zipper fibril (-42.79), and $E_{peptide}$ is the peptide-specific component of the score of the relaxed peptide-fibril complex.

Increasing the length of the fibril, *i.e.* adding another GVNVAA segment to the existing steric zipper, results in a predicted value of $\Delta E_{binding}$= -7.37. The best D-peptide capping designs generated are listed in **Table 3.1**, and they are all predicted to bind more favorably to the GVNVAA steric zipper. The lowest-energy design, GVYVKS ($\Delta E_{binding}$= -17.58), utilized the

backbone structure from Cluster 0 and has 50% sequence identity to the fibril target. When amino acid identity was restricted, the lowest-energy design was SYVIKN ($\Delta E_{binding}$= -14.73), which utilized the backbone structure from Cluster 1. These two D-peptide capping designs, along with two additional low-energy candidates, were selected for testing in the experimental phase of this study.

**Table 3.1. Energy scores for all-D capping peptides designed in Rosetta and selected for experimental testing.**

| Sequence (D-AA) | Total Score ($E_{complex}$) | Peptide Score ($E_{peptide}$) | $\Delta E_{binding}$ |
|---|---|---|---|
| GVYVKS | -63.62 | -3.26 | -17.58 |
| SYVIKN | -57.70 | -0.18 | -14.73 |
| GYNVKS | -60.36 | -0.98 | -16.60 |
| STVIKN | -58.31 | -1.30 | -14.22 |

D-AA = D-amino acids; $\Delta E_{binding}$is defined by Eq. 3.1.

### 3.2.3 *Experimental Testing*

The four capping peptide designs listed in Error! Reference source not found.**1** were synthesized by Genscript (Nanjing, China) using all D-amino acids. The target hexapeptide, all-L GVNVAA, was synthesized separately in-house with solid phase peptide synthesis on Rink amide resin and purified by reverse-phase high performance liquid chromatography (RP-HPLC) on a Shimadzu Prominence chromatograph (Shimadzu; Kyoto, Japan). All peptides included N-terminal acetylation and C-terminal amidation to promote solubility. First, GVNVAA was evaluated for its ability to form amyloid fibrils on its own in solution. The small size of this hexapeptide prevented its aggregation at low concentrations, but it eventually formed short, amyloid-like fibrils after two days' incubation without shaking at 5 mg/mL in PBS at 37°C (**Figure 3.4**, red arrows). However, because of their small size, assembly of these fibrils was quite difficult to track with ThT fluorescence. Inhibition testing for the all-D capping peptide designs was therefore restricted to the full-length target, PAO1 FapC, which is known to form robust amyloid fibers and has been described extensively in **Chapter 2**.

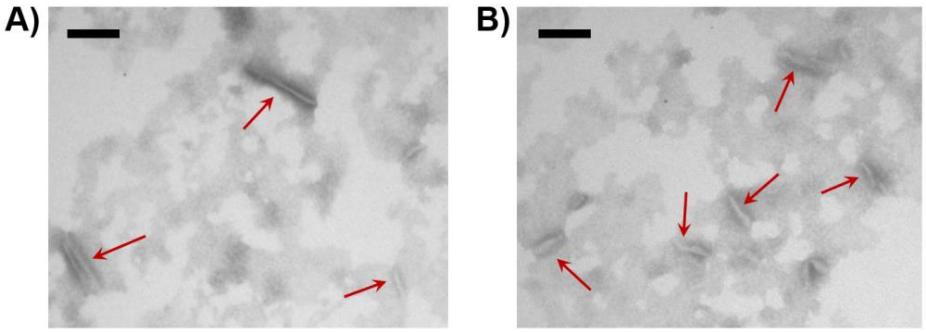


**Figure 3.4. Aggregation of the GVNVAA peptide. A,B)** TEM imaging demonstrated formation of short amyloid fibrils when Ac-GVNVAA-$NH_2$ was incubated at 5 mg/mL in PBS. Red arrows indicate fibrils and scale bars = 130 nm.

To assess whether designed capping peptides would inhibit amyloid fibril formation *in vitro*, PAO1 FapC was recombinantly expressed as described in **Section 2.6.3**. Urea-denatured FapC stocks were buffer exchanged in 10 mM Tris, pH 7.5 and added to black-walled 96-well plates such that the final concentration of protein was 0.05 mg/mL. All-D capping peptides were reconstituted in Tris buffer and added to wells with FapC such that the final concentration of peptide was 0.1 mg/mL (2:1 peptide:protein mass ratio; or ~45:1 peptide:protein molar ratio). All solutions contained 20 μM ThT, the final volume of each well was 100 μL, and all samples were tested in triplicate. A sterile 3 mm borosilicate glass bead was added to each well to facilitate mixing and the plate was covered with an adhesive seal. FapC aggregation was monitored by ThT fluorescence using a Tecan (Männedorf) plate reader at 37°C (excitation 448 nm, emission 485 nm). Readings were taken every 1.7 min after a 60 s shake and 5 s settling time.

As shown in **Figure 3.5 A**, the conditions of this experiment (*i.e.*, elevated temperature and agitation) encouraged rapid fibril formation by FapC and provided ample target sites for capping by the designed peptides. However, little inhibition was observed, even with over 40-fold molar excess of capping peptide. Aggregation curves for FapC with GYNVKS and STVIKN displayed no significant differences when compared to those for FapC alone. SYVIKN appeared to actually increase fibril formation, as evidenced by a more rapid increase of ThT fluorescence than FapC alone. The FapC + SYVIKN samples also exhibited a decay of fluorescence after the peak at ~8 h, which may indicate slow isomerization of ThT or bundling of the initially formed fibrils. SYVIKN was the only peptide that aggregated significantly on its own (**Figure 3.5 A**, inset), so this undesirable characteristic may have contributed to the unusual kinetics when it was combined in excess with FapC. Only the lowest-scoring design, GVYVKS, demonstrated ~25% inhibition

when added to FapC at a 2:1 mass ratio (**Figure 3.5 A**, purple). The lower ThT fluorescence plateau values for this case indicated that GVYVKS may have been able to access some of the GVNVAA sites in the growing FapC fibril and thereby shift the equilibrium toward fewer fibrils in solution compared to peptide-free controls.

Additional tests were carried out in biofilm cultures to determine whether the mild inhibition by GVYVKS *in vitro* would translate to a more complex, clinically relevant system. Biofilms of two *P. aeruginosa* PAO1 strains were cultivated in the presence of designed capping peptides (0.33 mg/mL, ~470 μM) in LB broth (Lennox formulation) in sterile 96 well microtiter plates. PAO1 pFap carries a plasmid for overexpression of the *fap* operon, which induces the production of large quantities of amyloid; PAO1 Δ*fap* is a chromosomal deletion strain that cannot express amyloid fibrils[114] (**Appendix A, Table A.2**). After 40 h of growth at 37°C, biofilms were rinsed gently and stained with ThT to provide a proxy for amyloid formation in the EM. Fluorescence values are plotted as a percentage of the peptide-free PAO1 pFap control (red dotted line) in **Figure 3.5 B**. As expected, the *fap* deletion strain formed biofilms with significantly lower ThT fluorescence values than the pfap overexpression strain, but none of the peptide-treated pfap biofilms displayed significantly lower ThT fluorescence than peptide-free controls. This lack of inhibition, even at rather high doses of peptide, suggested that perhaps the fibril-capping approach was not an appropriate method for disrupting amyloid formation in the EM of *P. aeruginosa* biofilms.

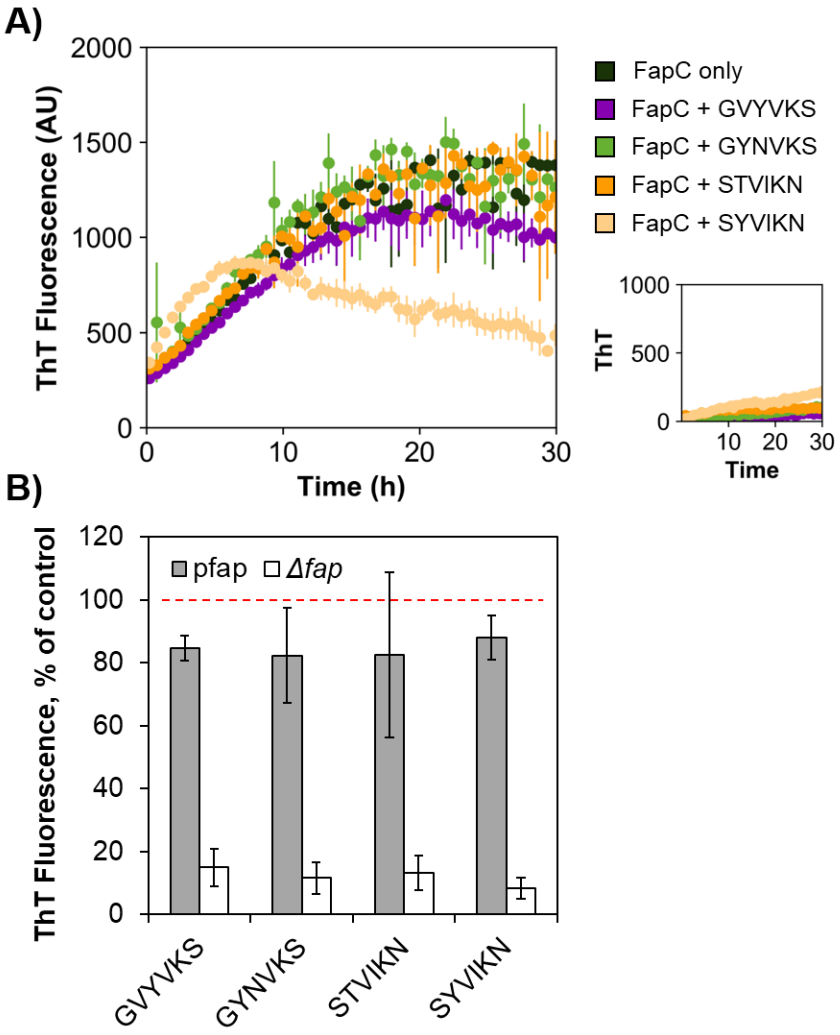


**Figure 3.5. Inhibition tests with all-D capping peptide designs. A)** Capping peptides were combined with recombinant PAO1 FapC at a mass ratio of 2:1 (molar ratio 45:1) in 10 mM Tris buffer, pH 7.5, and amyloid formation was tracked by ThT fluorescence in a plate reader. Aggregation of the capping peptides alone was monitored separately (inset). Only GVYVKS displayed significant inhibition of FapC fibril formation under these conditions. **B**) Biofilms of *P. aeruginosa* PAO1 pFap and PAO1 Δ*fap* were cultivated in the presence of designed capping peptides for 40 h at 37°C, and then they were stained with ThT to provide a proxy measurement of amyloid formation in the EM. Fluorescence values are plotted as a percentage of the peptide-free PAO1 pFap control (red dotted line). The *fap* deletion strain formed biofilms with much lower EM amyloid content than the pFap overexpression strain, but none of the peptide-treated pFap biofilms displayed a significant difference in fluorescence compared to control biofilms. Error bars in **(A)** and **(B)** indicate the standard deviation from the mean of three replicates.

### 3.2.4 *Conclusions*

In **Chapter 2**, bioinformatics studies identified the most amyloidogenic segments of the *P. aeruginosa* FapC protein. A highly conserved, highly amyloidogenic segment – GVNVAA – was

identified as a promising target for inhibitors designed to specifically recognize this sequence. Consequently, a Rosetta-based modeling approach was carried out *in silico* to engineer small peptides to bind the GVNVAA sequence. Peptides consisted of six all-D-amino acid residues and were designed to act as "caps" on the growing end of an amyloid fibril, thereby interfering with FapC fibril assembly. A high-throughput computational approach generated hundreds of designs, which were clustered and scored according to the free energy of binding between a hypothetical GVNVAA fibril and the capping peptide monomer. Four of the top-scoring peptides were then synthesized for experimental testing. Unfortunately, however, none of these peptides performed well *in vitro* (with recombinant FapC) or *in situ* (in biofilms).

The lack of substantial inhibition by capping peptides can be attributed to three key design assumptions. First, the GVNVAA fibril target model was constructed by simple threading of the GVNVAA sequence onto a crystal structure of a different sequence (NNQQNY). Though this approach may prove sufficient for some scenarios, it relies strongly on the assumption that all amyloidogenic hexapeptides form repeating steric zippers with the same geometry as NNQQNY. FapC capping peptide designs would be better informed by experimentally derived structural information for their specific target (*i.e.*, GVNVAA). The GVNVAA hexapeptide forms short amyloid fibrils in solution (**Figure 3.4**), so these macromolecules could be characterized with structure determination techniques such as NMR, X-ray crystallography, or Cryo EM. Such experiments may reveal unique properties of GVNVAA with implications for fibrillation of full-length FapC, and these could be exploited by capping peptides with specialized geometries or chemical properties. A second limitation arises from the fact that structure-based modeling tools like Rosetta rely almost entirely on static structures. The capping peptide designs presented here were constructed with a stationary GVNVAA fibril target model, and their backbones were fixed during optimization of side chain chemistries. Neither of these scenarios accurately captures protein motion *in vivo* and may therefore fail to account for important interactions between the two species. Finally, attempts to block fibril extension target only elongation and secondary nucleation mechanisms, not primary nucleation. As discussed in **Section 2.4**, primary nucleation occurs early in the aggregation phase and involves the coalescence of monomers, while secondary nucleation generates new aggregates due to the presence of existing aggregates[139]. Kinetic analyses of FapC and other bacterial amyloids like CsgA[157,158] indicate that primary nucleation is an important driver of functional amyloid aggregation *in vitro*. Therefore, further emphasis must be

placed on the initial conformational changes that shift monomers into an aggregation-competent state to promote primary nucleation.

Even though hundreds of capping peptide designs were predicted to dock successfully to a highly amyloidogenic portion of FapC *in silico*, these lacked efficacy as disruptors of amyloid formation in experiments with recombinant protein and bacteria. The design process suffered from reliance on poorly substantiated assumptions, and more detail is needed to adequately inform structure-based designs. Since polymerization of functional bacterial amyloids involves primary nucleation mechanisms, the transition from monomeric precursors to oligomeric intermediates requires consideration. This step is difficult to characterize experimentally, but MD simulations can provide critical dynamic information about the conformational changes involved. Efforts to apply the results of such simulations toward design of amyloid inhibitors are described in the next section.

## 3.3 Designs to Mimic α-sheet Oligomers: Molecular Dynamics

### 3.3.1 *The α-sheet Hypothesis*

The Rosetta-based design approach described in **Section 3.2** above suffers from a central disadvantage: it relies on static structures. Amyloid formation is a dynamic process, however, characterized by structural adaptations and drastic increases in size of the macromolecule. Aggregation into oligomeric species and ultimately mature fibrils requires initial conformational changes in native amyloid monomers[159], and static approaches are severely limited in their ability to capture these transitions. Conversely, MD simulations analyze protein dynamics and conformational heterogeneity at atomic resolution, providing rich detail to inform design[90]. The conformational ensembles generated by simulation also serve as a better reference for experimental studies, since experimental measurements represent an average over the entire ensemble[160]. Over the past two decades, the Daggett group has developed a MD package, *in lucem* molecular mechanics (*il*mm), for simulation of biomolecules[161]. This platform utilizes the ENCAD force field and F3C water model[162,163], and users may manipulate the configuration of each simulation according to a variety of adjustable parameters.

MD simulations have been applied to study the conformational landscape of a variety of unrelated amyloid proteins and peptides. In so doing, a novel secondary structure termed "α-sheet"

was identified, and it was populated during MD simulations at amyloidogenic conditions irrespective of native secondary structure[45,92–94]. Pauling and Corey originally modeled α-sheet structure in 1951 as a possible fit for x-ray diffraction data[164], but it was rejected – correctly – in favor of β-sheet structure for natively folded proteins. The α-sheet is similar to the more conventional β-sheet backbone, but it is typified by the regular alternation of consecutive residue dihedral (φ and ψ) angles in the $\alpha_L$ and $\alpha_R$ helical conformations, resulting in the polar alignment of carbonyl groups on one side of the sheet and amide protons on the other[54] (**Figure 3.6**). Observations from MD indicate that the emergence of even a small, localized region of α-sheet structure can trigger conversion of neighboring residues (Armen *et al.*[45] and M. C. Childers, unpublished results). Partial charges from the polarized α-sheet backbone also build up a dipole moment across the molecule, which facilitates addition of further strands[93] (**Figure 3.6 A**). In this manner, α-sheet may serve as an initiator of aggregation in amyloid diseases, with only a simple peptide-plane flip required to convert the α-sheet structure into a β-sheet and ultimately a mature amyloid fibril. Rotation of the backbone from α- to β-conformation occurs via a "crank-shaft" motion, so side chain positions remain fixed while backbone groups reorganize.

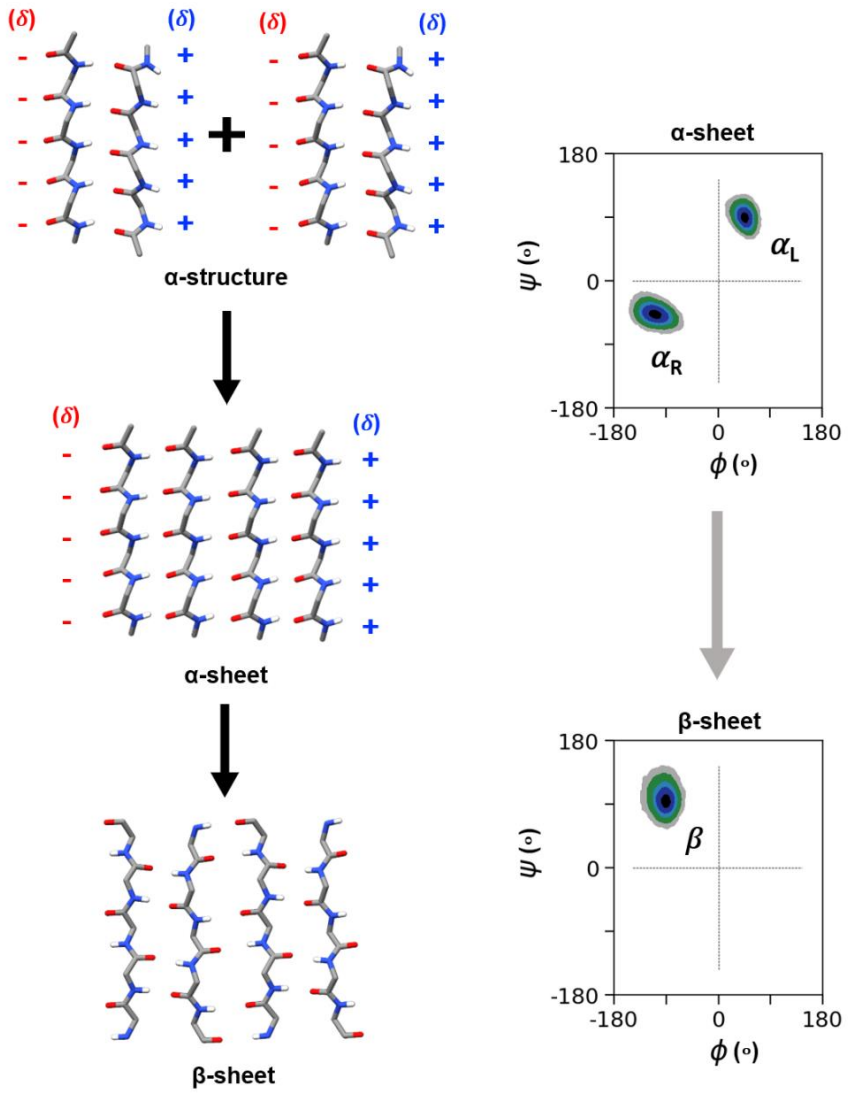


**Figure 3.6. Model for α-sheet-mediated amyloid assembly.** (top) α-sheet secondary structure is characterized by the alignment of carbonyl groups on one side of the sheet and amide protons on the other, which results from the alternation of sequential residue dihedral angles (φ, ψ) between $\alpha_L$ and $\alpha_R$ helical conformations. Accumulation of partial charges (δ) on either side of the interface (red for negative charges; blue for positive charges) facilitates assembly of additional sheets, followed by peptide-plane flipping into β-sheet secondary structure (bottom) and eventually mature amyloid fibrils.

### 3.3.2 *MD Simulations of the Functional Bacterial Amyloid CsgA*

Extensive MD simulations have been conducted to study the emergence α-sheet in mammalian amyloid protein and peptides, but the lack of structures for functional bacterial amyloids has hindered similar characterization. In *E. coli*, the major subunit of amyloid curli fibers is a 151-residue protein called CsgA. The structure of monomeric CsgA has not been

experimentally determined, due to its transient nature and propensity to aggregate. However, unlike disease-related amyloids, functional amyloids are beneficial and therefore conserved through millions of years of bacterial evolution. Collections of sequence homologs reflect this evolutionary process, and patterns of sequence covariation among residues can provide information about tertiary contacts. These contacts can then be combined with experimental data (NMR) as constraints to build a structural model[165] . Tian *et al.* applied these theories to generate a model structure for CsgA using two evolutionary contact prediction methods – PSICOV[166] and EVCOUPLING[167]. Multiple sequence alignment of CsgA and its homologous proteins was performed with HHBlits[168] (390 entries), and the resulting tertiary contacts were combined with chemical shifts derived from ssNMR studies of curli amyloid fibrils[169]. Monte Carlo simulations designed to find low-energy conformations (ProFASi[170]) consistently resulted in β-helical structures, with each of CsgA's homologous sequence repeats, R1-R5, aligned in a parallel fashion (**Figure 3.7 A**). Later iterations of CsgA modeling with different packages (e.g. Robetta) converged on the same tertiary fold[171]. In general, these types of models tend to be over-structured, and it is unlikely that CsgA forms a β-helix with such robust structure *in vivo.* Nevertheless, the CsgA model from Tian *et al*. merited analysis in MD because it represents the only predicted structure of this functional bacterial amyloid. Since the model combines sequence information with intramolecular chemical shifts based on fibrils, it can be considered a monomeric, yet structured CsgA subunit. This is in fact the precise type of model sought for our analyses, since conversion to α-sheet typically requires consistent contacts between structured strands[45].

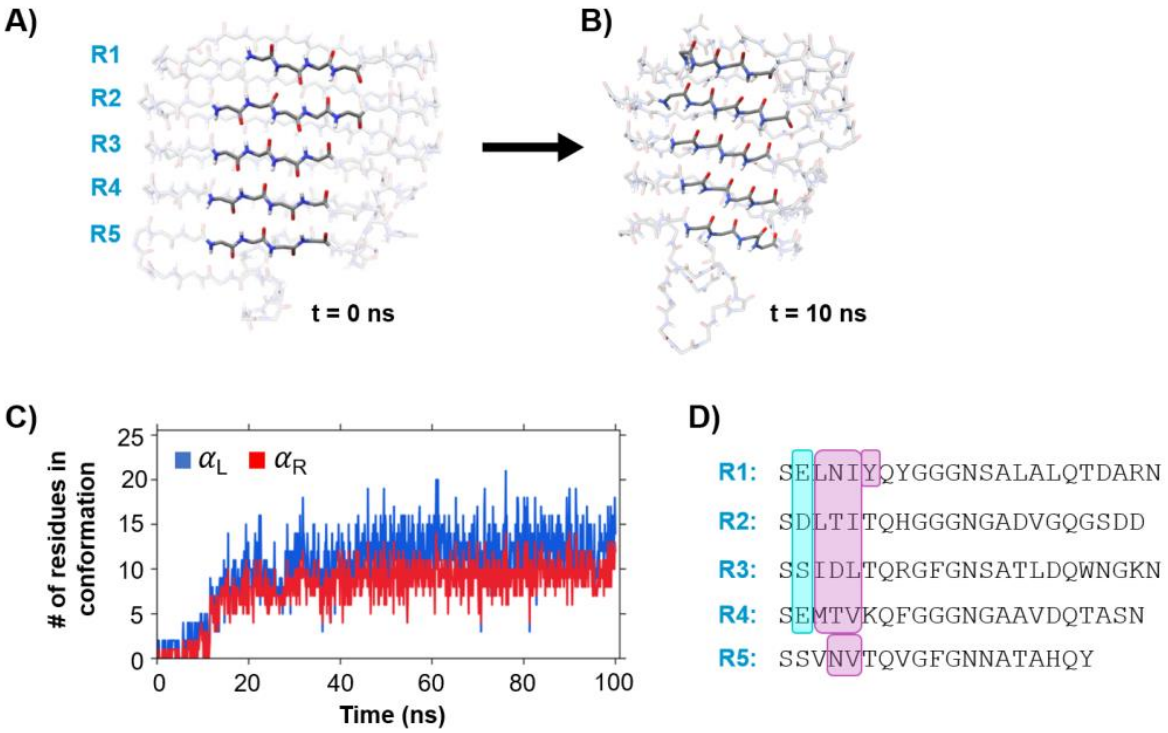


**Figure 3.7. MD simulations of CsgA reveal conversion to α-sheet structure. A)** The model CsgA structure generated by sequence variation (Tian et al.) takes the form of a β-helix. Conserved repeat sequences, labeled R1-R5, form each of the five turns in the helix. **B)** When simulated at low pH and 310 K, one side of the CsgA helix rapidly converted to α-sheet structure (this occurred within the first 10 ns of simulation for Run 1, as shown). **C)** At equilibrium,

To corroborate the α-sheet hypothesis in *E. coli* biofilms, MD simulations were executed for the right-handed CsgA β-helix model. All simulations were performed using the *il*mm simulation package and ENCAD forcefield according to previously described protocols[162,163,172]. A total of 6 simulations were performed – three at neutral pH (positive charge on Lys and Arg residues; negative charge on Asp and Glu residues) for 40 ns each, and three at low pH (neutral charge on Asp and Glu residues; positive charge on Lys, Arg, and His residues) for 100 ns each. Hydrogen atoms were added to the starting structures and minimized separately prior to minimization of the whole structure *in vacuo* for 1000 steps. The protein was then solvated in a water box (density 0.993 g/cm$^3$ at 310 K) with edges at least 10 A away from all protein atoms. Water molecules alone were minimized for 1000 steps, simulated with MD for 500 steps, and minimized again for 500 steps; then the protein was minimized for 500 steps. After this preparation, atoms were assigned velocities according to a Maxwellian distribution and allowed to move according to Newton's equations of motion. Velocities of the atoms were adjusted until the

system reached the desired temperature of 310 K (37°C). A 2 fs timestep was used for both preparation and simulation, and structures were saved every 1 ps for analysis. After simulation, trajectories were analyzed to calculate the backbone angles (φ, ψ) of each residue at each timestep. This information was then applied to detect formation of α-strand secondary structure. The minimum α-strand motif required for detection consisted of three sequential residues in alternating $\alpha_L/\alpha_R/\alpha_L$ or $\alpha_R/\alpha_L/\alpha_R$ conformation, with angles defined as (φ, ψ) = (45°, 92°) for $\alpha_L$ and (φ, ψ) = (-87°, -49°) for $\alpha_R$[93]. A tolerance of 30° about the central angle was employed to set a limit on qualified residues.

**Figure 3.7 C** depicts α-strand conformations as a function of time for CsgA simulated at low pH. Under these conditions, one face of the CsgA β-helix consistently converted to α-sheet structure (**Figure 3.7 B; Appendix B, Figure B.4 A**), while some transient α-strand formation occurred at neutral pH. The conversion to α-sheet structure occurred quickly, within the first 20 ns of all three low pH simulations (**Figure 3.7 C**; **Appendix B, Figure B.4 B**). This is in accordance with the role of CsgA as a functional amyloid protein; unlike mammalian amyloids, it is intended to aggregate rapidly, so α-sheet must arise early in the folding process. At equilibrium, approximately 25 residues in each simulation were part of an α-strand, as defined above. Additionally, α-sheets tended to arise predominantly on one face of the CsgA β-helix, which may aid the addition of more monomers *in vivo*. In one run, however (Run 1), a small portion of the "back" side of the helix began to convert to α-sheet after 80 ns of simulation, increasing the total number of α-strand residues to ~40 (**Appendix B, Figure B.4 B)**. The residues involved in triggering α-sheet formation were quite consistent; in all three low pH simulations, the first residue to undergo a peptide-plane flip from β to $\alpha_R$ or $\alpha_L$ conformation was found at position 2 in one of the repeats, R1-R4 (**Figure 3.7 D**, blue highlight). These residues are vertically aligned along the axis of the helix, so conversion of one residue often encouraged propagation of α-sheet structure between strands and then across each strand (**Figure 3.7 D**, purple highlight). Interestingly, three of the four "triggering" residues (Glu 24, Asp 47, Glu 92) are protonated at low pH, but not at neutral pH, which may help explain the rapid and stable onset of α-sheet structure in low pH simulations.

The development of α-sheet structure in MD simulations of CsgA provided promising evidence of a role for α-sheet in curli. To further establish the mechanisms of this phenomenon *in vitro*, molecules capable of recognizing α-sheet were required. The design of these recognition

compounds is described in the next section, and their application in experiments with recombinant CsgA is discussed in **Chapter 6**.

### 3.3.3 *Computational Design of Synthetic α-sheet Peptides*

Based on results from MD simulations of mammalian proteins, it was proposed that α-sheet structure is universally adopted during amyloidogenesis and associated with oligomer toxicity[54]. To test this hypothesis, peptides were designed *in silico* to adopt stable, monomeric α-sheet structure complementary to the structure observed in MD simulations[173]. Synthetic reconstruction of the α-sheet backbone was achieved by alternating L- and D-amino acids, which naturally prefer the $\alpha_R$ and $\alpha_L$ conformations, respectively (**Figure 3.8 A**). The design process was further informed by conformational propensity and rotamer libraries for each of the L- and D-amino acids[95–98,174,175]. The resulting synthetic α-sheet peptide designs are hairpins consisting of two α-strands of seven residues each, with amino acids alternating sequentially between L-conformation and D-conformation in each of the strands. The α-strands are connected by a five residue turn comprised of all L-amino acids, giving the peptide its hairpin shape and locking in α-sheet structure (**Figure 3.8 B**). Selection of specific side chain chemistries discourages addition of subsequent α-strands by sterically inhibiting hydrogen bonding with the exposed face[92]. Finally, the tail of each strand consists of a Gly and an Arg residue, followed by acetyl and amide caps at the N- and C-terminus, respectively, to promote solubility. Sequences for the synthetic α-sheet peptide designs referenced in this Dissertation are listed in **Table 4.2**.

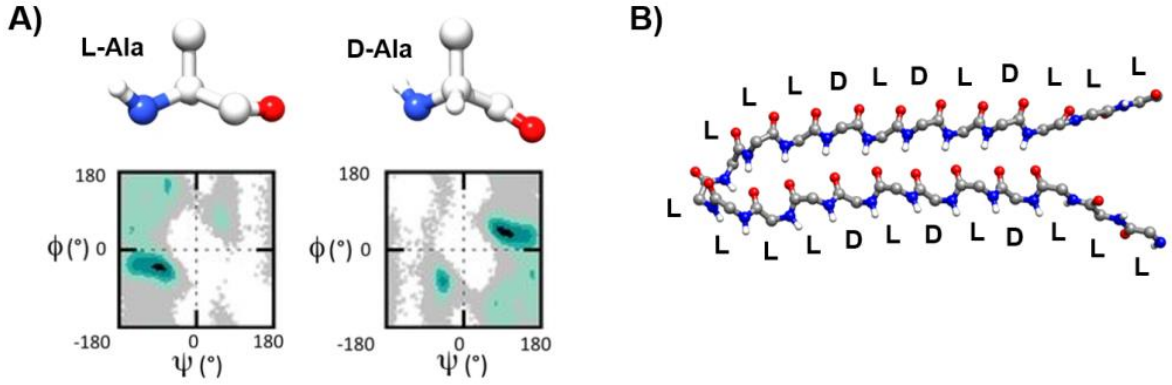


**Figure 3.8. Construction of synthetic α-sheet peptides. A)** Intrinsic conformational propensities for L- and D-amino acids (Ala shown) were calculated from 100 ns simulations of GGXGG host-guest pentapeptides, with X as one of the 20 L-amino acids or cognate D-amino acids. The chiral inversion of L- and D-Ala are shown by differential positioning of the backbone atoms (top) as well as Ramachandran plots of each residue with data collected from the entire simulation (bottom).

L-Ala favors the $\alpha_R$ conformation, while D-Ala prefers angles in the $\alpha_L$ region. **B)** Synthetic α-sheet peptide designs take advantage of these differences in conformational preference to recapitulate α-sheet structure observed in MD simulations of amyloidogenic proteins and peptides. Synthetic α-sheet structure is achieved by alternating L- and D-amino acids along the strands while maintaining all-L-amino acids in the turn; the resulting peptide forms an α-sheet hairpin.

Following static optimization of the design sequences, MD simulation was utilized once again to assess peptide stability and retention of the desired α-sheet structure. Stable, well-structured candidate designs were then synthesized, characterized, and tested for their ability to inhibit amyloid formation in a variety of systems. Experimental characterization of synthetic α-sheet peptides, including their unique biophysical properties, is described in **Chapter 4**. Synthetic α-sheet peptides are designed to be complementary to the α-sheet structures observed in MD, so binding between these two species should sequester the intermediate species and thereby prohibit aggregation (**Figure 3.9**). In mammalian systems, this results in neutralization of toxicity associated with soluble amyloid oligomers. In bacterial systems, which are the focus of this Dissertation, synthetic α-sheet peptides prevent formation of functional amyloid fibers which in turn promotes biofilm dispersion (**Chapter 5**, **Chapter 6**, and **Chapter 7**).

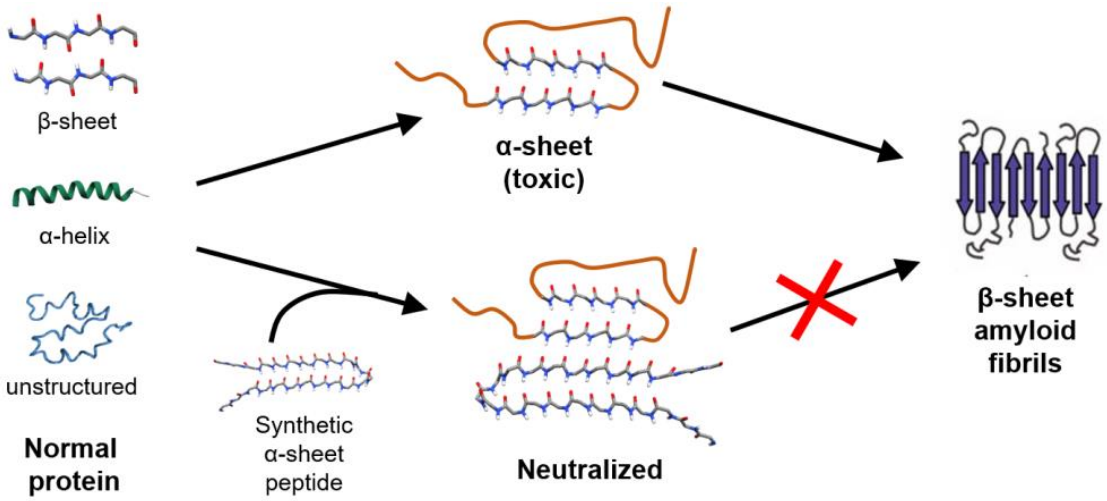


**Figure 3.9. Schematic of proposed amyloid inhibition by synthetic α-sheet peptides.** Amyloidogenic proteins and peptides form α-sheet structure in MD simulations, regardless of native secondary structure. Synthetic α-sheet hairpin peptides were designed to complement the α-sheet structure observed in MD. Recognition of complementary α-sheet structure between the peptides and their targets sequesters amyloid oligomers to neutralize toxicity and inhibit aggregation.

# Chapter 4. Experimental Characterization and Development of Synthetic α-sheet Peptide Designs

## 4.1 Synthetic α-sheet Peptide Designs

As described in **Section 3.3**, analysis of MD trajectories identified α-sheet secondary structure in a variety of unrelated amyloid proteins and peptides when they were simulated under amyloidogenic conditions. This structure displays a unique backbone conformation typified by the alternation of sequential residue dihedral angles between the $\alpha_R$ and $\alpha_L$ helical conformations. Synthetic, hairpin shaped peptides were designed *in silico* to adopt α-sheet structure complementary to the α-sheet structure observed in MD simulations of amyloidogenic proteins. These peptides typically contain 23 amino acid residues (**Table 4.2**). Seven alternating L/D amino acids generate two α-strands on either side of the hairpin, as L-amino acids favor $\alpha_R$ conformations and D-amino acids favor $\alpha_L$ conformations. Five L-amino acids comprise the hairpin turn to lock in α-sheet structure. Two L-amino acid residues (usually Arg and Gly) form the ends of each strand to promote solubility. Finally, a C-terminal amide group is added by the solid resin substrate, and an N-terminal acetyl group is added by acetylation upon completion of peptide assembly. **Figure 4.1** depicts the sequence of the "template" α-sheet peptide design, AP90 (Alternating Peptide #90), as well as its structural model generated *in silico*. AP90 served as the basis for the design of all other synthetic α-sheet peptides, and **Table 4.2** provides a list of these additional sequences along with their specific properties.

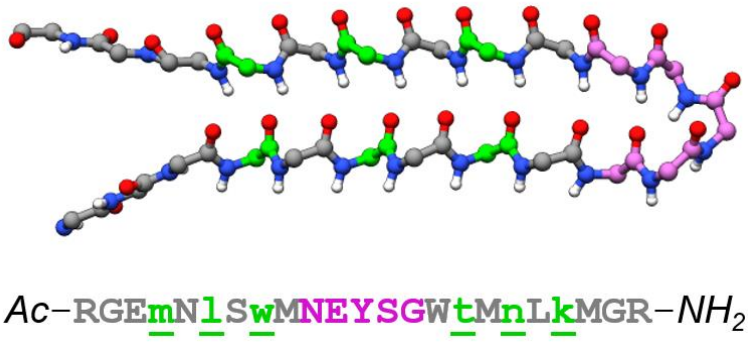


**Figure 4.1. Sequence and structural model of AP90, the template α-sheet peptide design.** AP90 consists of 23 amino acids and forms an α-sheet hairpin. D-amino acids are colored green and underlined in the sequence; L-amino acids in the turn (Asn10-Gly14) are colored pink; and other L-amino acids are colored gray. The sequence also includes N-terminal acetyl (Ac) and C-terminal amide ($NH_2$) groups, which are not shown in the structure.

In addition to their amenability to high-throughput design and inherently modular character, peptides present several advantages that make them attractive as therapeutics for amyloid-associated biofilm infection and amyloid disease. Because of their smaller size, peptides penetrate tissue more effectively than larger proteins, but they are large enough to exhibit increased affinity and specificity when compared to small organic molecules[176]. Peptides also exhibit lower immunogenicity than antibodies or proteins, and they can be easily stored at room temperature[177]. Proteins and antibodies require recombinant technology for production, but peptides are chemically synthesized, resulting in lower production costs and higher activity per unit mass[178]. One drawback of peptide-based therapeutics is their susceptibility to proteolytic cleavage *in vivo*, but the synthetic α-sheet peptides presented here utilize D-amino acids and chemical modifications at the termini (N-terminal acetylation and C-terminal amidation) to circumvent this problem[149,179–182].

To date, over 20 synthetic α-sheet peptides originally designed *in silico* have been synthesized and tested for their ability to inhibit amyloid formation in biofilms. As discussed in **Chapter 5**, **Chapter 6**, and **Chapter 7**, these peptides specifically prevent the formation of functional amyloid fibers in the EM, and the effect translates to four different bacterial biofilm systems: *S. aureus*, *S. mutans*, *E. coli*, and *P. aeruginosa*. Though the details are not presented in this Dissertation, synthetic α-sheet peptides also inhibit aggregation and neutralize toxicity of soluble oligomers in three different mammalian disease targets: β-amyloid (Aβ; Alzheimer's disease), amylin (Type II diabetes), and transthyretin (systemic amyloidosis)[173,183,184]. This Chapter provides a perspective on the physicochemical characteristics of these *de novo* designed peptides, with emphasis on the unique properties of α-sheet secondary structure that may lend therapeutic advantages when compared to other, canonical structures.

**Table 4.2. Peptide design sequences.** [a] "AP" refers to "Alternating Peptide", indicating alternating L- and D- amino acid templating. "P" refers to "Peptide", indicating a lack of templating. [b] All peptides are N- and C-terminally acetylated and amidated, respectively, except for P1, which has a free N-terminus. Lowercase, underlined letters denote D-amino acids. Disulfide-bonded cysteines are shown in red. Homodimeric α-sheet hairpins consist of two identical monomers as indicated by "**2x**", while the heterodimeric α-sheet hairpin AP195/AP199 consists of one AP195 monomer and one AP199 monomer.

| Name[a] | Sequence[b] | Description | Source |
|---|---|---|---|
| AP90 | Ac-RGEmNlSwMNEYSGWtMnLkMGR-$NH_2$ | α-sheet hairpin; "template" design | Hopping *et al*., 2014 |
| AP407 | Ac-RGEmNlCwMNEYSGWcMnLkMGR-NH2 | α-sheet hairpin; intramolecular disulfide bond between C | This work |
| AP401 | Ac-rGeMnLsWmneysGwTmNlKmGr-$NH_2$ | α-sheet hairpin; chiral inversion in strands and turn | This work |
| AP5 | Ac-RGNwNeSkMNEYSGWmLmLtMGR-$NH_2$ | α-sheet hairpin | Kellock *et al*., 2016 |
| AP193 | **2x** Ac-RGEmNyFwMNEYYGWtMnCkMGR-$NH_2$ | homodimeric α-sheet hairpin | Hopping *et al*., 2014 |
| AP195 | **2x** Ac-RGNwNeSkMNEYSGWmLmCtMGR-$NH_2$ | homodimeric α-sheet hairpin; AP5 analogue | This work |
| AP199 | **2x** Ac-RGEmNlSwMNEYSGWtMnCkMGR-$NH_2$ | homodimeric α-sheet hairpin; AP90 analogue | This work |
| AP195/199 | **1x** AP195 + **1x** AP199 | heterodimeric α-sheet hairpin | This work |
| P1 | Ac-KLKpLLTSENTL-$NH_2$ | unstructured (random coil) control | Hopping *et al*., 2014 |
| P411 | SWTWEpNKWTWK-$NH_2$ | β-sheet hairpin control | Cochran *et al.*, 2001 |
| P90 | Ac-RGEMNLSWMNEYSGWTMNLKMGR-$NH_2$ | all-L structural isomer of AP90 | Maris *et al.*, 2018 |

## 4.2 Spectral Properties of Synthetic α-sheet Peptides

Structurally, the presence of an alternating L/D-amino acid motif influences the inhibitory efficacy of synthetic α-sheet peptides by enforcing a polar α-sheet backbone configuration and encouraging complementarity between the designed peptide and its amyloidogenic target. MD simulations indicate that some of the α-sheet peptides designed *in silico* retain α-sheet backbone structure more persistently than others, but experimental validation of these predictions was required prior to testing in amyloid systems. To this end, several techniques were applied to assess peptide structure, including nuclear magnetic resonance (NMR), circular dichroism spectroscopy (CD), and Fourier transform infrared spectroscopy (FTIR).

### 4.2.1 *Circular Dichroism Spectroscopy (CD)*

Since its development in the 1960s, CD spectroscopy has since been used to characterize a wide variety of proteins and peptides, including amyloids[185–187]. The technique measures the differential absorption of left- and right-handed polarized light as a function of wavelength in optically active chiral molecules. In the far-UV region (180-250 nm), protein CD spectra are

dominated by electronic transitions within amide groups due to the abundance of peptide bonds[187,188]. These transitions are influenced by the geometry of the polypeptide backbone, so CD spectra indicate the presence of specific backbone dihedral angles (φ, ψ), which in turn can be used to elucidate secondary structure. Due to its repeating nature, the α-helix produces highly reproducible CD spectra, with minima at 208 and 222 nm and a maximum at 193 nm[189] (**Figure 4.2**, purple line). Spectra for β-sheet display more diversity, due to parallel/antiparallel orientations and strand twisting, but generally these structures produce negative peaks at ~220 nm and positive peaks at ~195-200 nm[187,190] (**Figure 4.2**, green line). Disordered proteins (also called "unstructured" or "random-coil") have low ellipticity above 210 nm, but their spectra drop off steeply toward a single minimum at ~195-200 nm[191] (**Figure 4.2**, black line). As discussed in **Section 3.3.1**, α-sheet is not a conventional secondary structure. In synthetic α-sheet peptides like AP90, the alternating chirality of residues in the strands of the hairpin leads to cancellation of CD signal, and the resulting spectrum is featureless save for some negative ellipticity in the disordered region (~195-200 nm) caused by all-L-amino acid stretches in the turn and termini (**Figure 4.2**, red line).

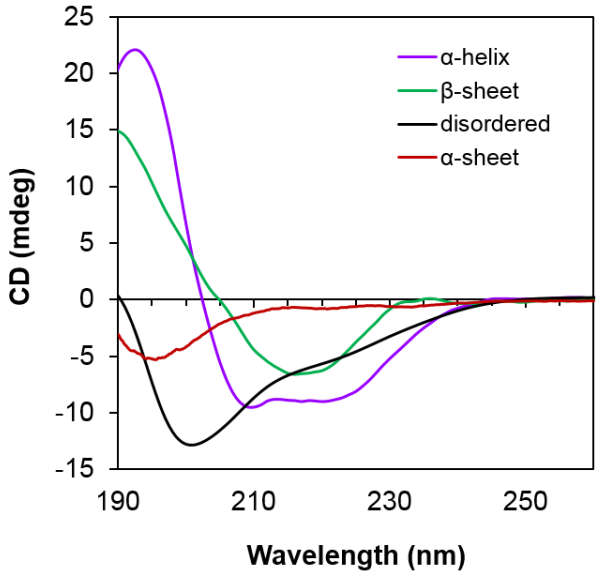


**Figure 4.2. Example CD spectra for four important secondary structures.** α-helical conformations (purple line) produce negative peaks at 208 and 222 nm, and a positive peak at 193 nm. β-sheets (green line) display a minimum signal at ~220 nm and a maximum signal at ~190 nm. Disordered or unstructured proteins (black line) have low ellipticity at higher wavelengths, but the signal descends steeply to a minimum at ~200 nm. Alternation of chirality in the α-sheet backbone results in signal cancellation and produces mostly featureless spectra (red line); here, the spectrum for AP90 displays some negative ellipticity in the disordered region (~190-200 nm) due to stretches of all-L-amino acids in the peptide turn and tails. Data for α-helix and β-sheet spectra were taken

from entries CD0000117000 and CD0000118000, respectively, in the Protein CD Databank[192]; the disordered ("random-coil") spectrum was collected for monomeric PAO1 FapC[119].

After synthesis and purification, CD served as an important analytical tool to assess the quality of synthetic α-sheet peptides. According to the alternating chirality of its backbone, the template design AP90 produced a relatively featureless CD spectrum (**Figure 4.2**, red line). This spectrum confirmed that the peptide in solution behaved according to the structural constraints set forth *in silico*. CD spectra were subsequently collected for additional synthetic α-sheet peptide designs (**Figure 4.3**), using the AP90 spectrum (**Figure 4.3 A**) as a reference for proper backbone configuration. AP407 is a variant of AP90 with an intramolecular disulfide bond across the hairpin to improve stability, and as expected its CD spectrum resembled that of AP90 (**Figure 4.3 B**). The AP401 design displayed similar spectral features by CD, except that the its signal became slightly positive in the unstructured region (200-220 nm; **Figure 4.3 C**). AP401 has the same sequence as AP90 but with reversed chirality in the strands and turn (**Table 4.2**), so the D-amino acids gave rise to an approximate mirror image CD spectrum relative to AP90. AP5, which retains the L/D templating of AP90 but has a scrambled sequence, displays characteristic α-sheet CD spectra despite rearrangement of the amino acids (**Figure 4.3 D**). This supports the idea that backbone geometry, more than side chain chemistry, influences α-sheet stability. AP195, AP193, and AP199 are all homodimeric α-sheet peptides, consisting of two identical α-sheet hairpins linked by an intermolecular disulfide bond through the Cys residues. In accordance with the increased α-sheet surface area in these designs, their CD spectra appeared even more flattened compared to the monomeric peptides (**Figure 4.3 E-G**). The heterodimer, AP195/199, produced similar effects (**Figure 4.3 H**). Several peptides were also employed as structural controls. The unstructured peptide, P1, contains D-amino acids but displayed a characteristically disordered CD spectrum (**Figure 4.4 A**). P411 is a β-sheet hairpin that includes a D-Pro residue; its spectrum was obscured by the Cotton effect (interaction of Trp-Trp residues across the sheet; **Figure 4.4 B**), but further characterization of this peptide elsewhere confirmed its β-sheet structure[193]. Finally, the P90 control shares 100% sequence identity with AP90, but it is constructed entirely of L-amino acids and therefore lacks α-sheet secondary structure. In fact, P90 is quite insoluble and forms a weak β-sheet signal by CD (**Figure 4.4 C**; the weak signal resulted from precipitation of large amounts of peptide). The remarkable biochemical differences between these two structural isomers (AP90 and P90) are examined further in **Section 4.3**.

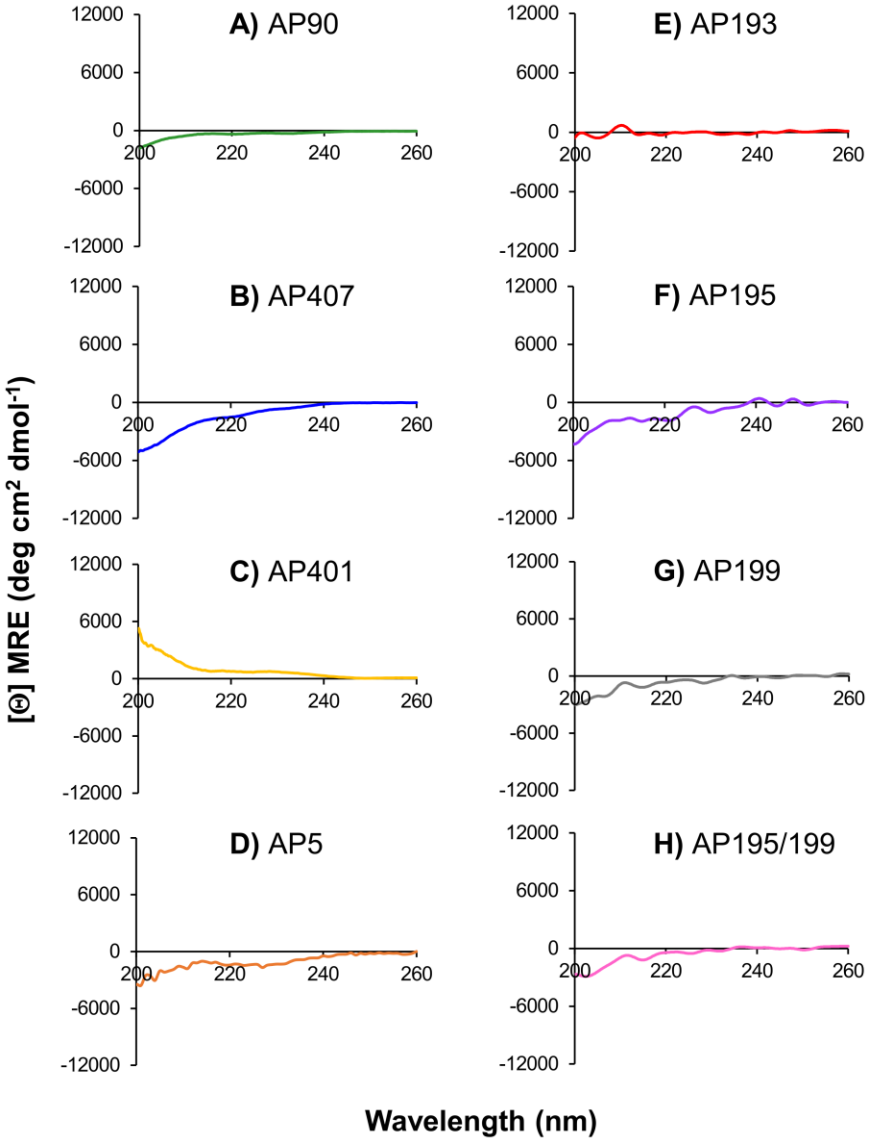


**Figure 4.3. CD spectra for synthetic α-sheet peptides.** Spectra for monomeric α-sheet peptides **A)** AP90, **B)** AP407, **C)** AP401, and **D)** AP5, and dimeric α-sheet peptides **E)** AP193, **F)** AP195, **G)** AP199, and **H)** AP195/199. Peptides were dissolved to a concentration of 100 μM in phosphate buffer (monomers) or 10 μM in water (dimers) and spectra were gathered at 25°C. Data were background subtracted and smoothed before plotting. [Θ] MRE = mean residue ellipticity, which accounts for variabilities in peptide concentration and size.

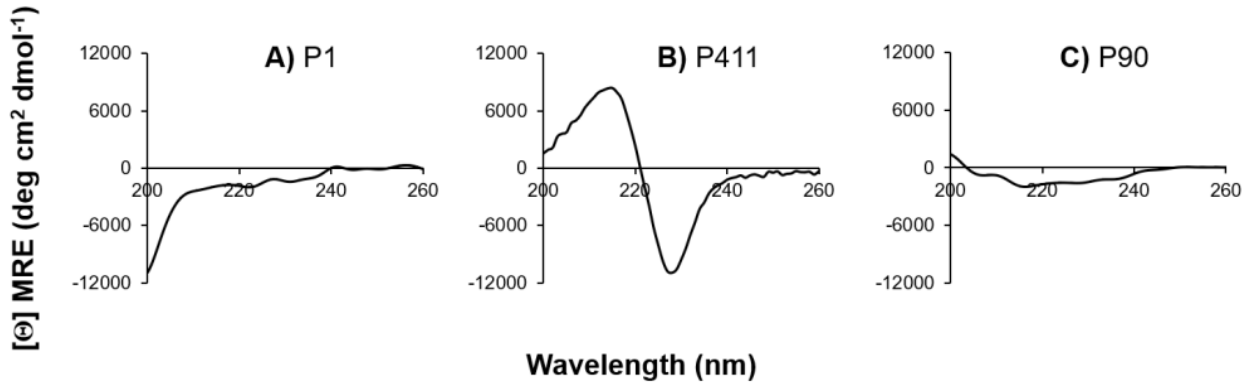


**Figure 4.4. CD spectra for synthetic peptide controls that lack α-sheet structure. A)** P1 displays a random coil (disordered) spectrum. **B)** P411 is a β-sheet hairpin, but identification of this secondary structure with CD is hindered by the Cotton effect[193]. **C)** P90 is the all-L isomer of AP90, and it displays a weak β-sheet spectrum (stronger signals were unattainable due to insolubility of the peptide). Peptides were dissolved to a concentration of 30 μM (P1), 100 μM (P411), or 45 μM (P90) in phosphate buffer and spectra were gathered at 25°C. Data were background subtracted and smoothed before plotting. [Θ] MRE = mean residue ellipticity, which accounts for variabilities in peptide concentration and size.

Together, these CD spectroscopy results confirm the presence of α-sheet structure in *de novo* designed α-sheet peptides and establish a spectroscopic signature for alternating backbone chirality. CD spectra from synthetic peptides also serve as reference spectra for the detection of α-sheet structure in amyloidogenic proteins and peptides as they aggregate. This application of CD spectroscopy is discussed in **Section 5.3.2** and **Section 6.3.2** for the amyloids PSMα1 and CsgA, respectively.

### 4.2.2 *FTIR and NMR*

FTIR and NMR spectroscopy can reveal information about protein secondary structure (and tertiary structure, in the case of NMR). Neither of these techniques was applied directly to characterize α-sheet peptides as part of this Dissertation, but other studies in the Daggett group included extensive characterization of α-sheet with FTIR and NMR, so they are discussed briefly in **Appendix C.2**.

## 4.3 Chemical and Physical Variability in Structural Isomers of Synthetic α-sheet Peptides

The alternating L/D- templated "benchmark" design, AP90, displays remarkably different chemical and structural behavior compared to its all-L structural isomer, P90. While AP90 is highly soluble in aqueous solutions, inhibits aggregation, and displays α-sheet structure as indicated by CD and FTIR spectroscopy, P90 lacks substantial solubility and displays β-structure in the same analyses. A series of experiments was conducted to highlight the substantial structural and chemical disparities between these two sequentially identical designs.

Traditional prediction metrics such as the Hopp-Woods hydrophilicity scale, which utilizes individual amino acid transfer free energies (**Appendix B, Figure B.5**), suggest that the AP90/P90 sequence should have poor solubility. Other than five charged residues primarily clustered around the N- and C-termini, the peptide's 18 remaining amino acids are either neutrally hydrophilic or hydrophobic. However, AP90 was very soluble (>25 mg/mL) in water and its turbidity in water was indistinguishable from pure water alone (**Figure 4.5 A**), suggesting that the solubility of AP90 depends on factors other than side chain hydrophilicity. Further analysis of AP90 in water with light microscopy (**Figure 4.5 B**) could not discern any notable particulate matter in the solution to indicate insoluble character. Additionally, when AP90 was dissolved to a concentration of 350 μM and filtered through a 0.2 μm cellulose–acetate membrane to remove large particulates, the concentration of peptide still measured ~300 μM as determined by the aromatic side chain absorbance at 280 nm, indicating the high solubility of the dissolved peptide. Finally, analysis by atomic force microscopy (AFM) revealed no significant buildup of aggregated or solid material on the imaging surface (**Figure 4.5 C**).

Conversely, P90 displayed very different physical characteristics compared to those of its L/D-templated counterpart, despite its sole modifications being the chiral reversal of six D-amino acids. As a result of this alteration, P90 was completely insoluble in aqueous solutions, accurately reflecting its low Hopp–Woods hydrophilicity score. Its average turbidity value of 0.0618 AU was 41% higher than that of AP90 and pure water (**Figure 4.5 A**). Light microscopy images of P90 in solution at 200x revealed glassy, insoluble deposits of peptide film scattered throughout the sample (**Figure 4.5 B**). Imaging by AFM also clearly captured these large, nonspecific peptide aggregates (**Figure 4.5 C**). Filtration through a 0.2 μm cellulose–acetate membrane trapped these fragments, and no peptide absorbance signal was detected at 280 nm in the filtrate. In a final attempt to

improve the solubility of P90, it was dissolved in dimethyl sulfoxide (DMSO) prior to dilution in PBS, but this induced the formation of an insoluble gel. The turbidity and other properties of P90 are independent of whether the N- and C-termini were capped.

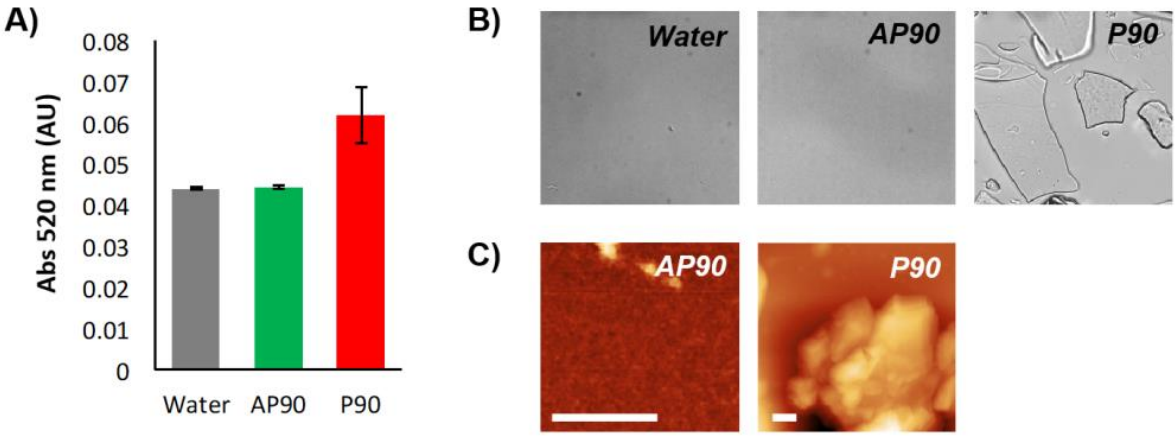


**Figure 4.5. Physical properties of structural isomers AP90 and P90 in aqueous solutions. A)** Each peptide was dissolved in filtered water to a concentration of 1 mg/mL, sonicated to break up any remaining solids, and analyzed for the absorbance of 420 nm light. Though raw absorbance was somewhat low because of the lack of color in all solutions, the P90 solution had an absorbance significantly higher than that of either AP90 or pure water. **B)** The same solutions were imaged by light microscopy at 200x magnification. Neither AP90 nor water had any insoluble solids other than some small dust particles, while the P90 solution contained large pieces of insoluble peptide film. **C)** P90 formed a viscous gel upon being solubilized in dimethyl sulfoxide and diluted with phosphate-buffered saline. AFM analysis of this gel revealed large, nonspecific aggregates of insoluble peptide material. AP90, in contrast, produced no discernible aggregates (pieces of dust located and shown for reference). Scale bars in **(C)** indicate 200 nm.

Since the amino acid sequences of AP90 and P90 are identical, it was hypothesized that their starkly dissimilar physical profiles resulted from differences in secondary structure. The use of alternating L- and D-amino acids in the strands forces AP90 to adopt the alternating $\alpha_R/\alpha_L$ local structure that defines α-sheet, and these minor changes in conformation strongly influence the solubility of the peptide. Calculations of *in vacuo* dipole moments yielded a highly polar value of 85 D for AP90, while P90 gave a value of 11 D as a β-hairpin and 15 D as an extended strand[194]. The large disparity between these two values supports the idea that polar α-sheet structure is responsible for the enhanced solubility of AP90. As discussed in **Section 4.2**, this idea is further substantiated by spectroscopic determination of the peptide secondary structures (CD spectra for AP90 and P90 are depicted in **Figure 4.3 A** and **Figure 4.4 C**, respectively). FTIR analyses also revealed striking differences between the two peptides. AP90 exhibits strong absorbance at 1675 and 1640 $cm^{-1}$, corresponding to predictions for α-sheet from density functional calculations for

amide I vibrations[195]. In contrast, P90 produces a strong band at 1620 $cm^{-1}$ consistent with β-sheet structure[173,184].

Together, these fundamental studies confirm that chirality of individual amino acids can dramatically affect behavior. AP90 and P90 differ in chirality at only six positions, but they vary significantly in terms of their chemical and physical behavior. The introduction of α-strand motifs through swapping chirality at specific positions in the sequence enforces a conformation with a molecular dipole that provides heightened solubility in an otherwise hydrophobic molecule. This has profound implications for application of synthetic α-sheet peptides peptides as anti-biofilm therapeutics, as solubility is required for recognition and sequestration of α-sheet-containing targets in the EM.

## 4.4 Dimeric α-sheet Peptide Designs

Synthetic α-sheet peptides contain unique secondary structure that lends desirable physical properties for their deployment as amyloid inhibitors. Other studies in the Daggett group have demonstrated the efficacy of these peptides in preventing amyloid fibril formation and neutralizing toxicity in mammalian systems[173,183,184,194], and these findings are translated to bacterial amyloids in **Chapter 5** and **Chapter 6** of this Dissertation. To date, published work with synthetic α-sheet peptides has focused on derivatives of AP90 – that is, monomeric peptides. However, the α-sheet-rich oligomers formed on the pathway to amyloid formation are much larger than a single peptide; SEC separation of Aβ oligomers indicates sizes ranging from hexamers to dodecamers[183,196], over 20 times the molecular weight of AP90, and bacterial amyloid oligomers are likely even larger based on the mass of their constituent monomers. Furthermore, a molar excess of monomeric α-sheet peptide is typically required to achieve an inhibitory effect *in vitro*. These two observations led to the hypothesis that increasing the availability of α-sheet surface area would increase inhibitory potency.

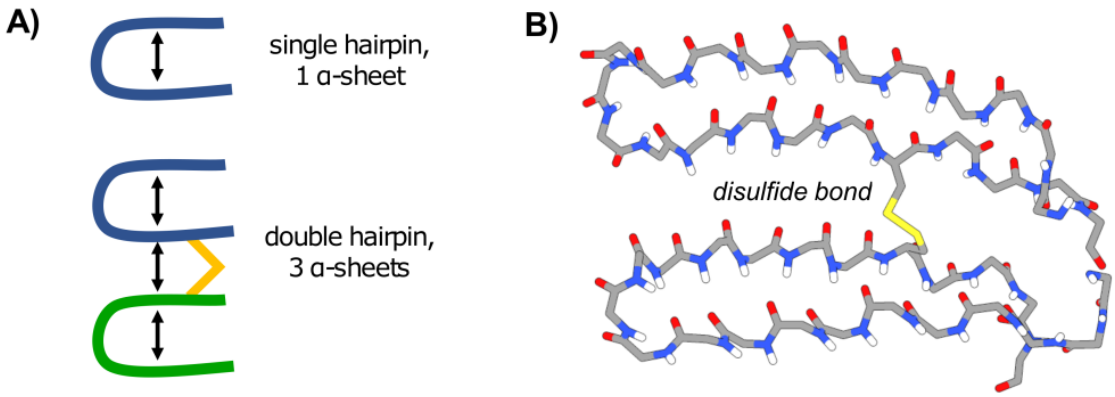


**Figure 4.6. Dimeric α-sheet peptide designs. A)** Design theory based on availability of α-sheet surface area. Monomeric peptides consist of one hairpin, so they can only form one α-sheet. Dimerization of two peptides via a disulfide bond (yellow) can generate up to three α-sheets, depending on the orientation of the two hairpins. **B)** AP193 is a heterodimeric α-sheet peptide linked by a disulfide bond between Cys19 in each hairpin. As predicted by the design theory, AP193 can achieve triple-α-sheet structure in MD simulations at 298 K.

Monomeric α-sheet peptides form a single hairpin, or one α-sheet. Dimerization of two peptides could, in theory, increase the number of α-sheets from one to three, thereby increasing potency by either (i) increasing avidity or (ii) surpassing the amount of therapeutically active surface area presented by two separate monomers (**Figure 4.6 A**). To this end, a series of dimeric α-sheet peptides was designed *in silico* using previously designed monomers as a basis. Each dimeric peptide consists of two α-sheet monomers linked by a disulfide bond through a pair of Cys residues at position 19 (**Figure 4.6 B**). The peptides were initially synthesized and purified as monomers, then oxidized to produce dimers. This process generated three homodimers (AP193, AP195, AP199) and one heterodimer (AP195/199); the sequences of the constituent monomers are provided in **Table 4.2**. AP193 is a dimer constructed of a previously designed monomer[173]; AP195 and AP199 mirror the AP5 and AP90 sequences, respectively, with the exception of Leu→Cys mutations at position 19 to form the disulfide. The heterodimer, AP195/199, is constructed of one AP195 monomer and one AP199 monomer. Oxidation of Cys residues required slightly alkaline pH and extensive dilution of the peptide solution; without these experimental considerations, the dimeric designs failed to oxidize completely. Addition of organic solvent (isopropyl alcohol; see **Section 4.5.2**) was also required to promote peptide solubility throughout the oxidation reaction, particularly for the slightly hydrophobic AP193 design. Peptides were purified by RP-HPLC after oxidation to isolate the dimer product, and under the conditions described above, all homodimers eluted as a single pure peak with very little monomer remaining. Indeed, oxidation of AP193

produced 0.46 mg of pure dimer per 1 mg of pure monomer – a 92% molar yield. In the case of the AP195/199 heterodimer, oxidation of equal masses of AP195 and AP199 monomer resulted in three products, which were present in approximately equimolar concentrations according to their peak size in RP-HPLC chromatograms (**Appendix B, Figure B.6**; peak 1 = AP199 homodimer, peak 2 = AP195/199 heterodimer, peak 3 = AP195 homodimer). The yield of the desired heterodimer product was therefore lower in this case (~33% of the starting mass), but no peaks corresponding to monomeric peptide were observed, indicating good oxidation efficiency.

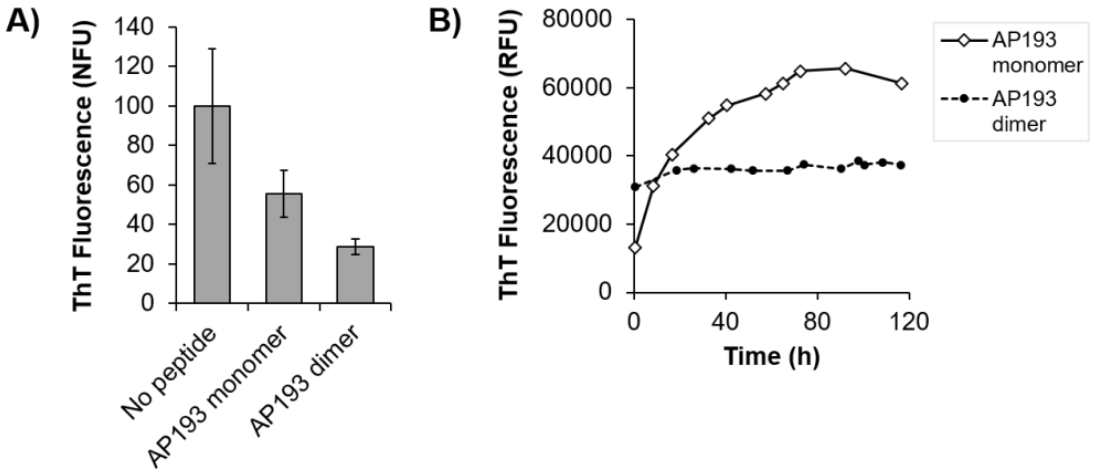


**Figure 4.7. Comparisons between monomeric and dimeric AP193. A)** *E. coli* UTI89 biofilms were cultivated in the presence of AP193 monomer (16 μM) or AP193 dimer (8 μM) and the amyloid content of the EM was evaluated with a ThT fluorescence assay (see methods, **Section 6.6.2**). Both forms of the peptide inhibited amyloid formation in these biofilms, but dimeric AP193 exhibited greater potency than the same molar dose of monomer. Error bars indicate standard deviation from the mean. **B)** Monomeric AP193 aggregates to form non-fibrillar, insoluble deposits in aqueous solution. AP193 dimer exhibits higher initial ThT fluorescence than AP193 monomer due to the conformation of the hairpins, but it does not aggregate. Aggregation was carried out in 50 mM potassium phosphate buffer with 20 μM ThT and 15 μM (monomer) or 5 μM (dimer) peptide.

As expected based on the design and performance of monomeric α-sheet peptides, all dimeric peptides produced featureless CD spectra characteristic of α-sheet (**Figure 4.3 E-H**). In fact, these spectra were even more flattened than their monomeric counterparts, presumably due to the increase in α-sheet surface area per molecule. Dimeric peptides also exhibited improved potency compared to the same molar dose of monomer, in accordance with the design hypothesis. First, in uropathogenic *E. coli* biofilms, AP193 dimer suppressed curli amyloid formation almost 30% more than the equivalent dose of AP193 monomer (**Figure 4.7 A**), a finding that motivated the use of mostly dimeric α-sheet peptides in the biofilm studies presented in **Chapter 6**.

Additionally, in ThT aggregation assays with CsgA (the major constituent of curli amyloid fibers), AP193 inhibited amyloid formation only when it was applied in its dimeric form (**Figure 6.5 C**). Similar findings were obtained in experiments with Aβ (Dylan Shea; data not shown). Indeed, due to the hydrophobic nature of the AP193 amino acid side chains (**Table 4.2**), monomeric AP193 aggregates in solution to form insoluble, non-fibrillar deposits, rendering it inactive (**Figure 4.7 B**). Conversely, the dimeric form of AP193 does not aggregate (**Figure 4.7 B**). Akin to the improved solubility of AP90 compared to P90, dimerization of AP193 may increase its dipole moment and prevent nonspecific aggregation. Unlike AP90, AP193 dimer binds significant ThT in solution (**Figure 4.7 B**), but the signal does not increase over time. The relatively high fluorescence was therefore attributed to promiscuous interactions of the ThT molecule with crevices in the peptide brought on by its dimerization, as observed in related studies[197].

In agreement with predictions from intuitive design *in silico*, dimerization of synthetic α-sheet peptides increases α-sheet surface area and results in a corresponding increase in inhibitory potency. The precise molecular mechanisms behind this phenomenon can be elucidated by comparing MD simulations of dimeric peptides to those of constituent monomers (**Figure 4.6 B**; **Section 8.3**), but the proof of principle established here enabled the use of dimeric α-sheet peptides in more complex systems (**Chapter 5** and **Chapter 6**), and the oxidation methodology could be further combined with rational design to generate novel α-sheet geometries for future applications.

## 4.5 Materials and Methods

### 4.5.1 *Synthesis, Purification, and Analytical Chemistry*

All synthetic α-sheet peptides were assembled manually by solid phase peptide synthesis using fluorenylmethyloxycarbonyl (Fmoc) chemistry[198]. Fmoc-protected Rink amide MBHA resin (Peptides International; Louisville, KY) was first allowed to swell in dimethylformamide (DMF; Alfa Aesar; Haverhill, MA) for two hours. Next, Fmoc-protected amino acids (Peptides International) were coupled to the resin in a cyclical fashion: excess 50% (v/v) piperidine (Sigma-Aldrich) in DMF was applied with stirring for two 1-minute intervals to remove the terminal Fmoc protecting group, followed by thorough flow-washing with more DMF. Each amino acid, dissolved in 0.5 M 2-(1H-benzotriazol-1-yl)-1,1,3,3-tetramethyluronium hexafluorophosphate (HBTU; Peptides International) in DMF and activated with N,N-diisopropylethylamine (DIEA; Sigma),

was then applied in fourfold molar excess to the resin and allowed to react for 10 minutes with intermittent stirring. Coupling efficiency was qualitatively measured by ninhydrin test (Aapptec, Louisville, KY). Upon passing the test (i.e. little to no free amine), the resin was flow-washed with DMF and the cycle was repeated. N-terminal acetylation was accomplished by the addition of acetic anhydride/DMF/DIEA (4.5:5:0.5). The resin was washed five times with dichloromethane (DCM; VWR; Radnor, PA) and methanol (50/50), rinsed with pure DCM, and then dried under a stream of nitrogen. Peptides were cleaved from the resin and side chain deprotected by TFA/TIPS/H2O (95:2.5:2.5) for 15 min on ice and 105 min at room temperature. TFA was evaporated by nitrogen stream, and then the peptide was precipitated with cold ether. The slurry was gravity-filtered through a glass frit and the resulting solids were dissolved in a solution of water/acetonitrile/TFA (55:45:0.047). Crude peptides were purified to >98% by RP-HPLC (Shimadzu) using 5 μM C12 or C18 100 Å columns (Phenomenex; Torrance, CA) and a gradient of acetonitrile in water with TFA. Masses were confirmed by electrospray mass spectrometry on a Bruker Esquire Ion Trap mass spectrometer. Pure peptides were lyophilized and stored at -20°C until use.

### 4.5.2 *Oxidation of Disulfide Bonds*

In the case of AP407, an intramolecular disulfide bond was designed to lend stability to the peptide hairpin and enforce α-sheet structure. Oxidation of this disulfide bond was carried out in two steps. First, cleavage of the peptide from its synthesis resin was performed under reducing conditions (TFA:thioanisole:anisole:ethanedithiol at ratio 90:5:2:3) to prevent disulfide formation during the cleavage[199]. Crude, lyophilized peptide was then oxidized by dissolving in 10% v/v isopropyl alcohol (IPA), diluting to ~1 mg/mL in 100 mM ammonium carbonate buffer (pH ~10), and aerating by stirring at 300 rpm for 24 h at room termperature. The resulting oxidized mixture was purified by RP-HPLC in the same manner as other peptides, with a 5 μM C12 column (Phenomenex).

In the case of AP193, AP195, and AP199, two monomers were linked together via their Cys residues to form a homodimer. For the AP195/199 heterodimer, equal masses of monomeric AP195 and AP199 were combined and oxidation resulted in three products: homodimeric AP195, homodimeric AP199, and heterodimeric AP195-199. In all cases, oxidation was carried out by dissolving purified, monomeric peptide in IPA and diluting to 0.1 mg/mL in 100 mM ammonium

carbonate buffer (pH ~10). The amount of IPA varied according to the solubility of the peptide (30% v/v for AP193, and 5% v/v for AP195 and AP199). Peptides were oxidized by air at room temperature with stirring for 24 h prior to a second round of RP-HPLC purification and verification of the oxidation via mass spectrometry as in **Section 4.5.1**. All peptides were lyophilized after purification and stored at -20°C until use.

### 4.5.3 *Determination of Physical Properties*

For solubility measurements, dry peptide stocks of AP90 and P90 were dissolved to a concentration of 1 mg/mL in filtered deionized (DI) water, vortexed, and sonicated for 30 min to break up any large solids. Remaining solids were evenly distributed in solution by repipetting. 100 μL of each peptide solution was aliquoted in triplicate into a clear 96 well plate along with filtered DI water as a blank. Solution turbidity was then evaluated by absorbance measurements at 420 nm on an Ensight plate reader (PerkinElmer; Waltham, MA).

Light microscopy images of peptide samples (prepared as above) were collected at 200X on a Zeiss Axio Observer (Carl Zeiss AG; Oberkochen, Germany) inverted fluorescent microscope. For AFM, P90 was first dissolved in DMSO to a concentration of 4 mg/mL and then it was diluted to 1 mg/mL by adding PBS to the tube, forming a viscous, insoluble gel. The gel was applied to a mica chip and incubated for 36 hours at 4˚C. Finally, the surface was rinsed three times with distilled water and air-dried. The sample was then evaluated using a Bruker Scanasyst-Air tip (Billerica, MA) on a Veeco Scanning Probe Microscope (Plainview, NY).

### 4.5.4 *Spectroscopy*

CD spectra were taken on a Jasco J-720 spectrophotometer in 1 mm quartz cuvettes using peptide samples in buffer (10 mM sodium phosphate) or water with the relevant solvent blank subtracted. All α-sheet peptides were diluted to between 10–50 μM (verified by NanoDrop) prior to measurements, except for P90 which due to its insoluble character could only be evaluated as a suspension at a nominal concentration of 45 μM. The spectrophotometer settings and post processing methods were identical to those in **Section 2.6.5**. FTIR spectroscopy was carried out in a separate study[173] using a Spectrum 100 instrument (PerkinElmer).

# Chapter 5. Role of α-sheet Structure in *S. aureus* Biofilms

## 5.1 Summary

MD studies suggest that amyloidogenic proteins and peptides adopt a non-standard structure, termed "α-sheet", as they aggregate into soluble oligomeric species. This led to the design of complementary α-sheet peptides as anti-α-sheet inhibitors; these designs exhibit unique physicochemical properties and they inhibit amyloidogenesis in mammalian disease-associated systems through preferential binding of soluble oligomers. The findings in this Chapter demonstrate that synthetic α-sheet peptides also inhibit amyloid formation in *S. aureus* biofilms. Furthermore, they inhibit aggregation of pure, synthetic phenol soluble modulin α1 (PSMα1), a major component of *S. aureus* functional amyloids. As it aggregates, PSMα1 adopts α-helix then α-sheet secondary structure and finally forms β-sheet fibrils. The binding of synthetic peptides coincides with the formation of α-sheet. Together, the results presented in this Chapter illustrate an effective new approach to destabilize the extracellular matrix and interrupt biofilm formation in *S. aureus*.

## 5.2 Background and Motivation

Methicillin-resistant *Staphylococcus aureus* (MRSA) is the second-most common cause of nosocomial infections due to its versatility and virulence[18]. Unlike most other pathogens, *S. aureus* is routinely implicated in nearly every type of HAI, with infections ranging from skin and soft tissue infections (SSTI) to endocarditis, pneumonia, and osteomyletis[200]. Strikingly, more than half of *S. aureus* isolates in U.S. hospitals from 2011-2014 were classified as MRSA strains because they exhibited resistance to oxacillin, methicillin, or cefoxitin[18]. Methicillin resistance is carried by the *mecA* gene, located on a moble genetic element known as the staphylococcal cassette chromosome (SCC*mec*). Observations of resistance in the mid-20$^{th}$ century initially traced to a single clone, but by 2002 five major healthcare-associated MRSA (HA-MRSA) clones had emerged worldwide[201]. Since the mid-1990s, increases in the incidence of MRSA infection have been attributed to development of new, community-associated MRSA (CA-MRSA) clones. The CA-MRSA strains display altered genotypes, and they often affect a different patient population and cause unique clinical syndromes[200]. However, CA-MRSA isolates have become increasingly

capable of crossing into the hospital environment, and this remains a major area of concern for monitoring and management[202].

The broad adaptability of MRSA to changing environments is often attributed to its ability to form biofilms. Since staphylococci are part of the normal skin flora, they act as opportunistic pathogens in a variety of common medical procedures, such as incision or introduction of an implanted device. When *S. aureus* forms a biofilm on a medical device or wound, cells associate with surfaces and each other using a self-produced extracellular matrix (EM) composed of proteins, polysaccharides, and genetic material. Staphylococcal biofilm maturation often requires an adhesive polysaccharide called polysaccharide intercellular adhesin (PIA), also known as poly-N-acetyl glucosamine (PNAG), whose production depends on the *ica* gene locus[203,204]. MRSA isolates in particular, however, may not require PIA to form biofilms. Instead, these strains exhibit increased release of eDNA and expression of extracellular proteins such as fibrinogen adhesins, protein A, and accumulation-associated protein[205–207].

In recent years, another protein component of the *S. aureus* EM has drawn attention as a key determinant in pathogenicity. Phenol-soluble modulins (PSMs) constitute a class of amphipathic, α-helical peptide toxins that promote virulence by inducing inflammation, lysing erythrocytes, recruiting and lysing neutrophils, and killing competing bacteria[208–210]. *S. aureus* secretes up to eight types of PSMs (**Figure 5.1 A**). The α-type PSMs contain 21-26 amino acids and include PSMα1-4 (encoded on the *psmα* operon) and δ-toxin (encoded by *hld* in the Agr system). The two β-type peptides, PSMβ1 and PSMβ2, are each 44 amino acids long and encoded on the *psmβ* operon[208,211]. PSM-mec is an additional α-type PSM encoded on the *mec* mobile genetic element that confers methicillin resistance to *S. aureus*[212]. Increased production of all types of PSMs is associated with MRSA infection, particularly for skin and soft tissue sites[213–215]. PSMs also promote biofilm formation. Their amphipathic nature lends surfactant-like activity, facilitating development of characteristic biofilm channel structures and – at high concentrations – dispersing the biofilm to colonize other locations in the body[216,217]. Interestingly, PSMs can also form amyloid-like fibers that lend structural support to the biofilm EM. Biofilms imbued with PSM amyloid fibers are resistant to dispersal by matrix degrading enzymes, and fibers isolated from these cultures share morphological traits with those of mammalian amyloids[62] (**Figure 5.1 B**). In consonance with their multifaceted role in *S. aureus* biofilm development, individual PSMs exhibit varying degrees of amyloid formation. Only PSMα1 and PSMα4 convert to β-sheet

amyloid structures *in vitro*[218], a property which is reflected by their high abundance in fibrils isolated from biofilm cultures[62]. PSMα3, conversely, is highly cytotoxic but not prone to β-sheet fibril formation[218].

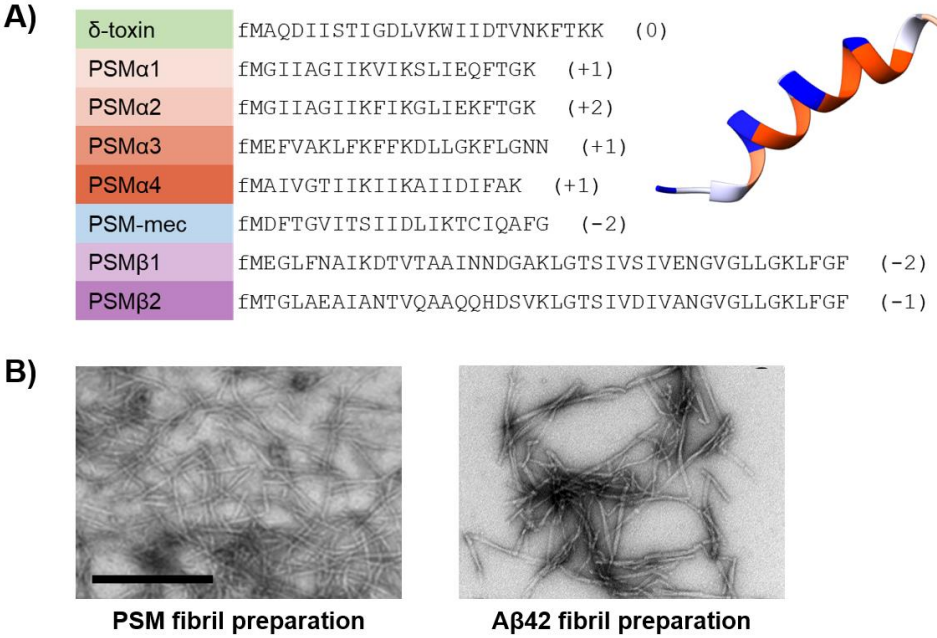


**Figure 5.1.** Phenol soluble modulins (PSMs) are small α-helical peptide toxins with diverse roles in *S. aureus*. **A)** Amino acid sequences of the eight PSMs, with peptide charges shown in parentheses. All PSMs are formylated at the N-terminus. A solution NMR structure for PSMα1 (PDB ID 5KHB) is shown at right, with residues colored to highlight its amphipathy (blue: hydrophilic, white: neutral, orange: hydrophobic; scale based on Kyte-Doolittle hydrophobicity). **B)** PSM amyloid fibrils from *S. aureus* SH1000 biofilms share morphological characteristics with Aβ42 amyloid fibrils from human cerebral cortices. Scale bar = 250 nm. Figures adapted from Schwartz *et al.* and Rostagno & Ghiso with permission[62,219].

Given the increasing threat of antibiotic resistance, new strategies are greatly needed to combat *S. aureus* biofilm infections. PSMs represent an ideal target for therapeutic intervention with synthetic α-sheet peptides because PSM amyloid fiber assembly requires conversion from soluble, monomeric α-helical structure to insoluble β-sheet structure. The findings of this Chapter establish that the transition between the two endpoint states is typified by the emergence of α-sheet secondary structure in PSM oligomers, and that synthetic α-sheet peptides therefore inhibit amyloid assembly *in vitro* and *in situ*. This is the first study demonstrating the efficacy of these peptides outside of a mammalian amyloid system, supporting the generality of the α-sheet hypothesis.

## 5.3 Results

### 5.3.1 *Designed α-sheet Peptides Inhibit Amyloid Formation in* S. aureus *Biofilms*

Two *S. aureus* strains were employed in this study: SH1000 WT, a *rsbU*$^+$ *agr*$^+$ laboratory strain, and MN8, a clinical strain isolated from the human urogenital tract (**Appendix A, Table A.2**). To test whether synthetic α-sheet peptides inhibited *S. aureus* amyloid formation, 80 μM of α-sheet (AP90, AP401, AP407) or control (P1, P411) peptides were added to the growth medium prior to inoculation. After 24 h of growth in microtiter plates, biofilms of each strain were rinsed and incubated with ThT, and the resulting fluorescence signals served as a proxy for the extent of fibril formation in the EM. The synthetic α-sheet peptides AP90, AP401, and AP407 caused a significant reduction in biofilm amyloid content (**Figure 5.2 A**), particularly for the MN8 clinical isolate. The disulfide-linked peptide design, AP407, performed especially well, resulting in 46 and 56% inhibition in the MN8 and SH1000 WT strains, respectively. In contrast, control peptides designed to adopt random coil (P1) or β-hairpin (P411) structure did not exhibit a significant effect. ThT fluorescence values also decreased in a dose-dependent manner when *S. aureus* MN8 biofilms were grown with increasing concentrations of AP90 in the culture medium (**Figure 5.2 B**). These results suggested that inhibition was specifically associated with the presence of α-sheet structure. To validate these observations, *S. aureus* SH1000 WT biofilms were examined with transmission electron microscopy (TEM). Amyloid-like fibrils were clearly visible in the spaces around cells grown without peptide, but biofilms cultivated in the presence of AP90 were relatively free of amyloid deposits (**Figure 5.2 C**).

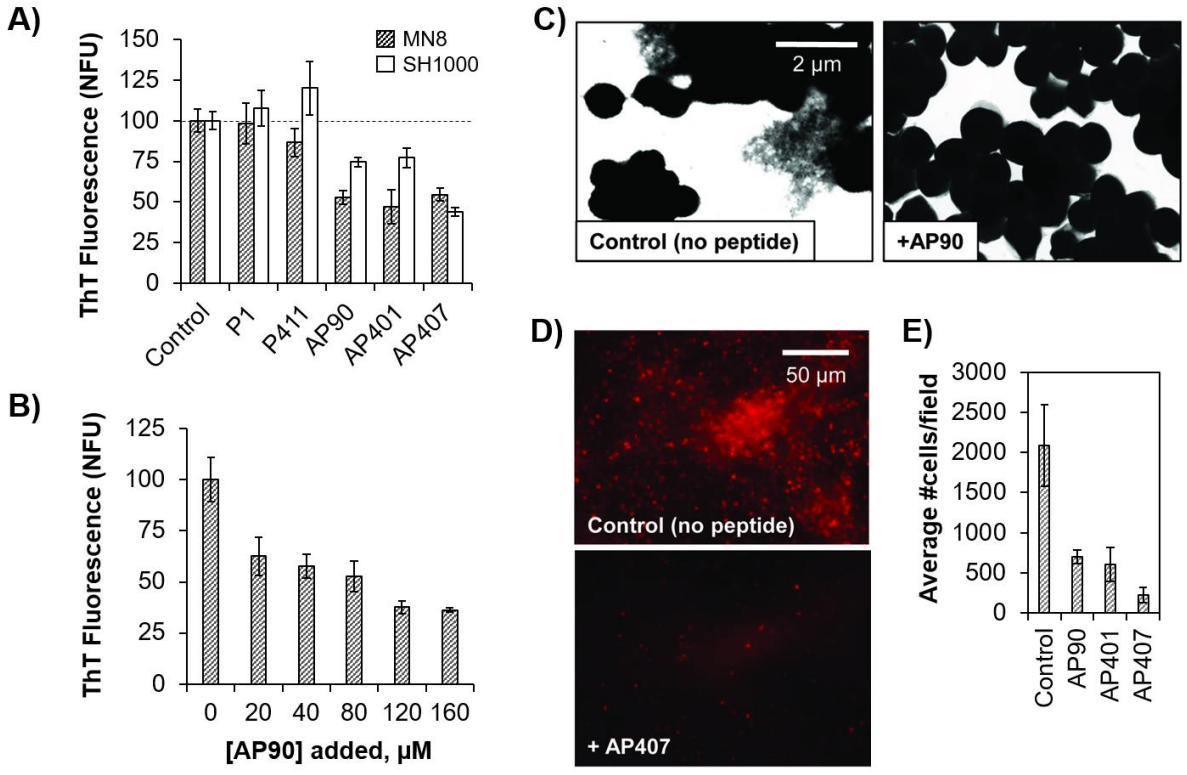


**Figure 5.2. A)** A panel of synthetic α-sheet peptides (AP90, AP401, and AP407), as well as the random coil (P1) and β-hairpin (P411) controls, was tested against two *S. aureus* strains, MN8 (hashed bars) and SH1000 (white bars). ThT fluorescence values indicate the extent of amyloid formation in the EM and are shown as the percent of peptide-free control conditions. **B)** Dose-response curve for AP90 against *S. aureus* MN8 biofilms. **C)** In *S. aureus* SH1000 biofilms, PSM amyloid fibrils were visible as deposits in spaces between cells (left), but addition of AP90 (80 μM) eliminated these extracellular fibril deposits (right). **D)** *S. aureus* MN8-mCherry biofilms were grown on glass substrates for 24 h and then cells were washed and fixed. Synthetic α-sheet peptides (80 μM; AP407 shown as example) caused cells to detach during the wash step. **E)** The average number of cells per field was determined for triplicate images like those in **(D)**. Error bars in **(A)** and **(B)** represent the standard error of the mean for experiments performed in triplicate; error bars in **(E)** represent the standard deviation of the mean of three images.

To determine whether inhibition of amyloid triggered a corresponding decrease in biofilm integrity, peptides were added to cultures of fluorescent (mCherry) *S. aureus* MN8. After 24 h growth on glass slides, biofilms were gently rinsed with pipetted saline to remove unattached biomass and the remaining attached cells were fixed and imaged. A robust biofilm formed on the glass at the bottom of each well in LB medium alone (**Figure 5.2 D,E**). In contrast, biofilms were substantially disrupted in the presence of α-sheet compounds, indicating that suppression of PSM amyloid formation weakens the EM of *S. aureus* biofilms and compromises mechanical stability.

### 5.3.2 *Amyloid Formation by PSMα1 is Characterized by Structural Changes*

To clarify the mechanism of inhibition of synthetic α-sheet peptides, we began by characterizing the structural transitions of a synthetic PSM peptide, PSMα1, as it aggregated to form amyloid fibrils in solution. Solutions of PSMα1 (30 μM, 1.3% v/v HFIP, potassium phosphate buffer, pH 5.5) were incubated at 37 °C and CD spectra were periodically collected to determine the conformational species populated during aggregation (**Figure 5.3 A,B**). Simultaneously, the aggregation of matched PSMα1 samples was tracked by ThT fluorescence in a microtiter plate (**Figure 5.3 C**). At the beginning of the time course, the PSMα1 peptide displayed a characteristic α-helical spectrum by CD, with minima at ~208 and 222 nm. With time, however, the α-helical content decreased, as evidenced by progressive loss of these minima. As discussed above, α-sheet structure gives rise to a featureless CD spectrum (**Figure 4.2**); PSMα1 samples analyzed at 130 h displayed similarly featureless spectra (**Figure 5.3 A,B**). Notably, this "flattened" spectrum coincided with the onset of fibril formation at ~130 h. By the end of the aggregation time course, CD spectra were dominated by β-sheet signals with minima at ~220 nm, indicating conversion to amyloid fibrils. This was confirmed Atomic Force Microscopy (AFM), which revealed fibrils measuring ~10 nm in diameter and 0.1–4.0 μm in length (**Figure 5.3 D**).

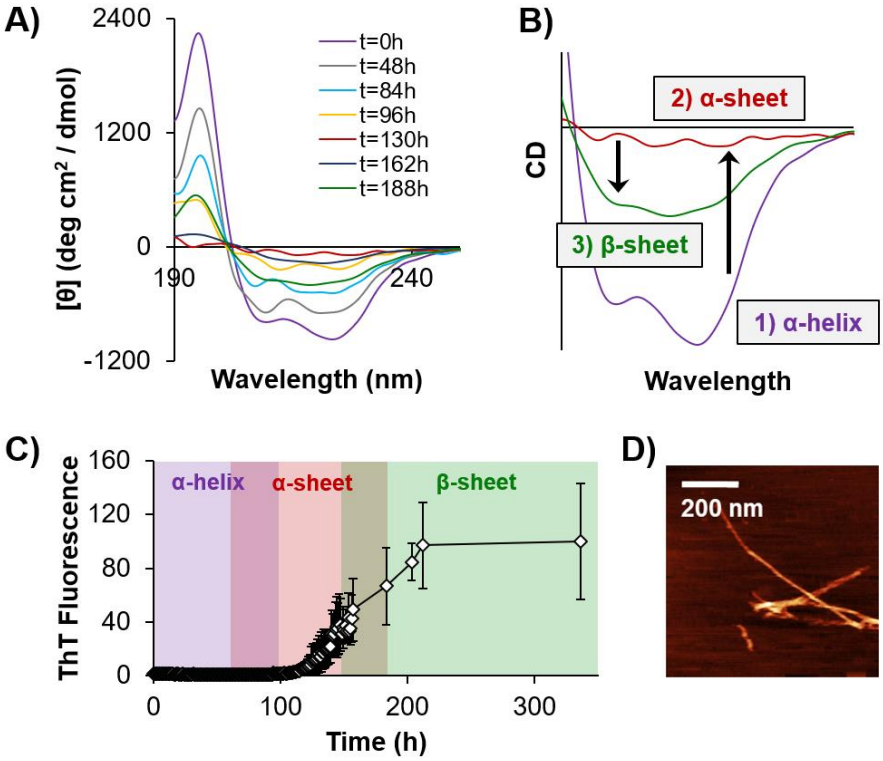


**Figure 5.3. A)** CD spectra of PSMα1 samples (30 μM, 1.3% HFIP, 50 mM potassium phosphate buffer, pH 5.5) were taken periodically during aggregation. At early time points (t = 0, 48, 84 h), negative peaks at ~208 and ~220 nm represent α-helical secondary structure. At intermediate time points (t = 130 h), featureless spectra indicate formation of α-sheet, and by the end of the time course (t = 188 h) a negative peak at ~218 nm signals the presence of β-structure. **B)** Close-up view of characteristic CD spectra for α-helix (0 h, purple), α-sheet (red, 130 h), and β-sheet (green, 188 h). **C)** Aggregation of synthetic PSMα1 peptide (30 μM, same conditions as for CD) was tracked over time by ThT fluorescence in a microtiter plate. Error bars in **(C)** represent the standard deviation of the mean of four samples.

### 5.3.3 *Synthetic α-sheet Peptides Inhibit PSMα1 Amyloid Formation by Selective Binding*

The emergence of α-sheet structure in prefibrillar PSMα1 suggested that synthetic α-sheet peptides should inhibit aggregation of PSMα1 *in vitro*. Designed peptide inhibitors were co-incubated with freshly prepared samples of synthetic PSMα1 (30 μM, 0.34% v/v DMSO, ddH2O, pH 5) and aggregation was monitored by ThT fluorescence. In accordance with observations *in situ*, addition of AP90 at a 4:1 molar ratio inhibited PSMα1 amyloid formation by 81 ± 5%, while the random coil peptide P1 had little effect (**Figure 5.4A**). Similar inhibitory effects were obtained whether the peptides were incubated in aqueous solutions or bacterial growth medium.

The mechanism of inhibition was further assessed by binding assays between synthetic α-sheet peptides and PSMα1. Agarose beads were functionalized with a slightly hydrophobic AP90

derivative, AP193, and then solutions of fresh (soluble and monomeric), pre-incubated (oligomeric), or post-incubated (fibrillar) PSMα1 were applied to the beads. After incubation, the beads were washed several times and bound PSMα1 was eluted with denaturing buffer (GndHCl). CD spectroscopy indicated enrichment of α-sheet structure in PSMα1 near the end of the aggregation "lag phase", which occurred between 45 and 50 h for DMSO-solubilized PSMα1 (**Figure 5.4 B**). (PSMα1 is hydrophobic, so it requires an organic solvent like DMSO or HFIP to go into solution, and the aggregation kinetics of PSMα1 are considerably slower in HFIP than DMSO). As shown in **Figure 5.4 C**, AP193-functionalized beads preferentially bound pre-incubated PSMα1 (48 h) over helical PSMα1 (0 and 24 h). Additionally, binding constants were determined by biolayer interferometry (BLI), which analyzes interference patterns based on adsorption of samples to a biosensor tip. For this study, AP90 was immobilized on the tip, and then the association and dissociation of PSMα1 was measured at various time points during aggregation. In agreement with the agarose bead-binding experiments, PSMα1 samples from the end of the lag phase displayed the highest binding affinity ($K_D$ = 0.9–6.8 μM, **Figure 5.4 D**), and the binding affinity dropped by two orders of magnitude to 104 μM as PSMα1 converted to β-sheet (~150 h).

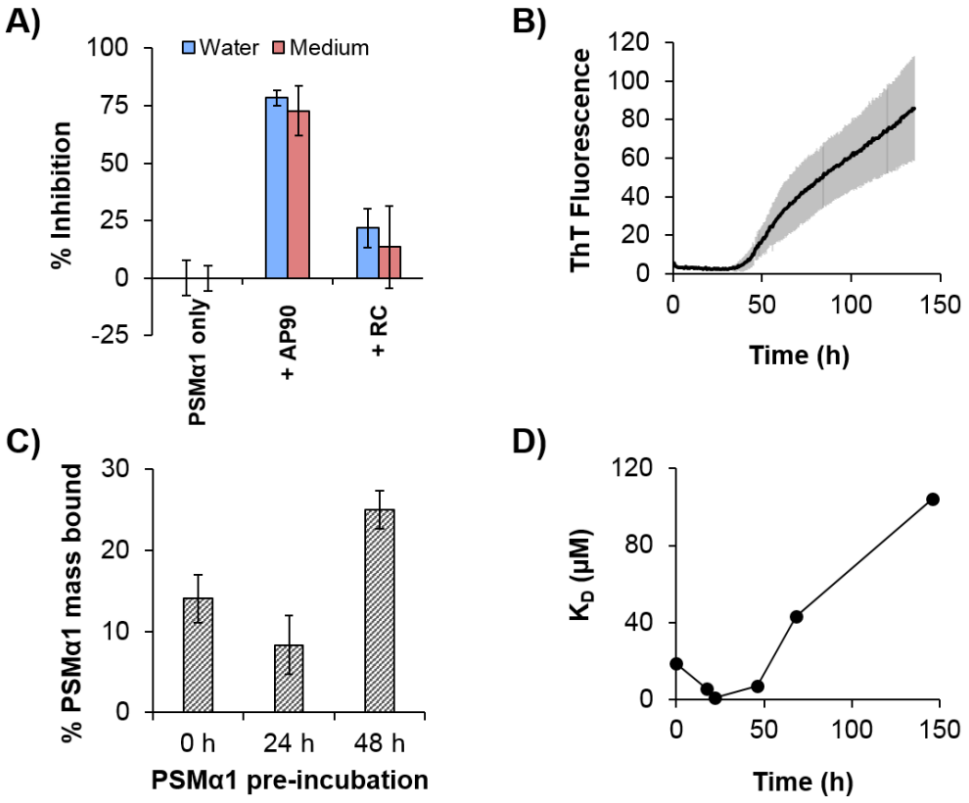


**Figure 5.4. A)** Synthetic PSMα1 peptide (30 μM) was allowed to aggregate alone and in the presence of AP90 or P1 (1:4 molar ratio) for 200 h. Two solvent conditions were tested: water (blue) and LB medium (red). Aggregation was monitored by ThT fluorescence. Inhibition values for each peptide are reported as a percentage of the peptide-free control samples (0% inhibition). Error bars represent the standard error of the mean of 3–6 replicates. **B)** Synthetic PSMα1 peptides were incubated in water as in **(A)**, and matched samples were removed periodically from the plate for binding assessment. **C)** In the resin-based assay, AP193-functionalized beads preferentially bound α-sheet rich PSMα1 (48 h) over earlier time points (0 and 24 h). **D)** In BLI, the equilibrium dissociation constant, KD, indicates preferential binding between AP90 and α-sheet-rich PSMα1 (~48 h) as opposed to α-helical monomer (~0 h) or β-sheet fibril (~150 h).

## 5.4 Discussion

PSMs play significant and varied roles in the biofilm matrix in *S. aureus*. In their soluble, α-helical form, these small peptides act as surfactants to disperse the biofilm and promote downstream colonization. On the other hand, PSMs can aggregate to form functional amyloid fibrils that stabilize biofilms and provide resistance to disruption, which is critical to the virulence of medical device-associated infections. Through these two modes of action, *S. aureus* communities take advantage of the unique properties of PSMs to thrive under a variety of

conditions within the host. In this Chapter, we have demonstrated a novel application of synthetic α-sheet peptides to suppress amyloid formation in the *S. aureus* biofilm matrix. The peptides inhibited amyloid formation in both a laboratory strain of *S. aureus* (SH1000), as well as a human urogenital isolate (MN8), and the effect was dose-dependent. Inhibition was accompanied by a weakening of biofilm attachment or the biofilm matrix, presumably through disruption of the PSM fibrillar scaffold[62]. Interestingly, while ThT fluorescence indicated that the AP90 design only inhibited amyloid formation by ~30% in *S. aureus* SH1000 biofilms, no amyloid fibrils were visible when these biofilms were imaged by TEM. This suggests that ThT may bind to other species in addition to the amyloid fibrils, or that smaller ThT-binding protofibrils may be present but not visible in the TEM images.

As a simple bridge between the inhibition studies *in situ* and *in vitro*, aggregation of synthetic PSMα1 was investigated in two different solvent conditions – water and LB medium. The lag phase was eliminated in the LB medium, suggesting that the growth medium accelerated aggregation (**Appendix B, Figure B.7 A**). Indeed, components of the medium gave rise to higher ThT fluorescence even after correcting for their high fluorescence in the absence of PSMα1 (**Appendix B, Figure B.7 B**). This presents a variety of possibilities including that LB components interact with the fibrils and bind or trap ThT, that they differentially bind ThT when PSMα1 is present, or that they affect the fluorescence yield. Nevertheless, despite the influence of complex media components, the inhibition by AP90 persisted. These observations reinforce our hypothesis that specific interactions between PSMs and designed α-sheet inhibitors lead to a reduction of amyloid fibril content in *S. aureus* biofilm cultures. It is possible that other staphylococcal matrix components may accelerate aggregation *in vivo*, as shown for extracellular DNA[220], but they are not required for amyloid formation. Additionally, extracellular Bap proteins may act as another functional amyloid in *S. aureus*[63], so future studies could benefit from inclusion of these in their analysis.

To better map the process of conversion, PSMα1 conformational behavior was investigated in aqueous solution. Independent of PSMα1 concentration, the aggregation reactions ultimately resulted in fibrils ~10 nm in diameter and 0.1–4.0 μm in length (**Figure 5.3 D**). These measurements align well with those of mammalian amyloid fibers, which also typically span 10 nm in diameter (with a range of 5–25 nm) and up to 10 μm in length[36]. The AFM images of PSMα1 fibrils confirm that their size and morphology are indeed amyloid-like. Given that mature fibrils

contain cross-β-structure, it is often assumed that intermediate species generated on the pathway to amyloid formation must also contain β-structure. However, it has been shown in several amyloid systems that these intermediate species lack β-structure[221–223]. These findings are in accord with our CD results for PSMα1, as it converted from soluble monomers to insoluble fibrils, progressing from α-helix→α-sheet→β-sheet fibrils. Correspondingly, synthetic α-sheet peptides target the intermediate α-sheet structure of PSMα1 and inhibit amyloid fibril formation *in vitro*, supporting a recent study showing that PSMα1 has a high aggregation propensity compared to the other α-PSMs[218]. We observed entry and exit from α-sheet occurring just prior to the onset of a steep increase in ThT binding, with mixed populations before and after with α-helix and β-sheet, respectively. The end of the lag phase of aggregation was also associated with preferential binding of α-sheet-rich PSMα1 samples to beads functionalized with AP193, as well as the increased binding affinity observed by biolayer interferometry.

Only PSMα3 fibrils have been studied with X-ray crystallography, and interestingly these structures exhibit stacked α-helices, not β-sheets[224]. This challenges the long-held dogma that amyloid is necessarily cross β-sheet. While fascinating, it's not clear how general this finding is for PSM peptides in particular or amyloid proteins in general. CD measurements from Marinelli et al.[218] indicate maintenance of α-helical structure in PSMα3 for up to 25 days of aggregation, while their CD measurements of PSMα1 agree with our finding that PSMα1 undergoes a transition from α-helix→β-sheet during aggregation. Furthermore, PSMα1 and PSMα3 have low sequence identity (7 residues in common). Others have noted α-helical supernatant and β-sheet pellets within a single sample[62], which could confound structural studies. Given the complicated conformational equilibria and sensitivity to concentration, incubation time and solution conditions, as well as the lack of continuity in the conditions and timing of the various experiments, making direct links between structure, aggregation and toxicity is difficult.

The functional amyloid of *S. aureus* represents an interesting and complicated system with many components and opportunities for regulation, and further research into the details of individual components as well as more holistic approaches are warranted. Together, the CD, column-binding, inhibition assays, and biolayer interferometry experiments presented here reinforce our hypotheses that amyloid formation by PSMα1 is characterized by formation of α-sheet structures and that the interaction between synthetic α-sheet peptides and PSMα1 is structure-

specific. By removing the structural reinforcement of biofilm EM afforded by amyloid fibrils, these peptides may help mitigate problems with antibiotic transport and associated resistance.

## 5.5 Conclusions

The prevalence of PSMs in drug-resistant infections, combined with their ability to influence biofilm development, makes them an attractive target for therapeutic intervention. However, no efforts to date have attempted to inhibit PSM amyloid formation. This Chapter demonstrates a novel approach to suppress amyloid formation in the *S. aureus* biofilm matrix using synthetic α-sheet peptides. The results presented here support the hypothesis that α-sheet secondary structure is a hallmark of amyloid formation, independent of source, sequence or structure. This is the first study demonstrating the efficacy of synthetic α-sheet peptides outside of a mammalian amyloid system, but their inhibitory effect persists, even in the complex matrix of mature biofilms. Therefore, this study provides a foundation for extension of the α-sheet hypothesis and its associated therapeutic implications to other amyloid-producing biofilm systems.

## 5.6 Materials and Methods

### 5.6.1 *Peptide Screening in Biofilms*

Overnight cultures of *S. aureus* were spun down and re-suspended in fresh LB medium (Lennox formulation) to an optical density of 0.1 (600 nm). Peptides were synthesized and purified according to the methods described in **Section 4.5.1**. Lyophilized peptide stocks were reconstituted in sterile water immediately before use, and their concentration was determined by NanoDrop™ (Thermo Fisher). Diluted *S. aureus* cultures were mixed with reconstituted peptides (or sterile water, in the case of controls) and aliquoted in quadruplicate into wells of a clear 48-well plate (plasma-treated polystyrene; Corning, Inc.). The final concentration of peptide in each well was 80 μM, unless otherwise noted. Plates were covered and incubated at 37 °C for 24 h with gentle rocking. Medium and planktonic cells were then removed from wells using a vacuum and the remaining adherent biofilms were rinsed once with PBS. ThT (22 μM in PBS) was added to each well and allowed to stain the biofilms for 4 h at room temperature. The solution was removed from the wells and PBS was added with vigorous pipetting to detach biofilms. Plates were shaken at high speed for 1 min on a plate shaker to detach any remaining biofilm material and homogenize

the samples, which were then transferred to a 96-well black-walled plate. ThT fluorescence was measured at 438/495 nm excitation/emission on a plate reader (PerkinElmer). Fluorescence measurements were corrected by subtracting the background intensity of identical samples without ThT.

### 5.6.2 *Microscopy*

For fluorescence microscopy studies, *S. aureus* MN8 + mCherry overnight cultures were diluted to an optical density of 0.1 (600 nm) and combined with synthetic α-sheet peptides as described above; the final concentration of peptide was 80 μM. Biofilms were grown in sixteen-well chambered coverglass plates (Thermo Fisher) and analyzed on an Axio Observer (Carl Zeiss AG) inverted microscope after gentle PBS washing and fixing with 4% paraformaldehyde. For each condition, 4–6 images (field size = 0.074 $mm^2$) were collected. Cell counts were performed in ImageJ[148] by adjusting the color threshold and using the particle analysis feature. For AFM studies, the synthetic PSMα1 peptides were prepared to concentrations of 44 and 437 μM (as described below, DMSO solubilization) and incubated at 37 °C. The resulting amyloid fibrils were applied directly to freshly cleaved mica and incubated for 2 h. Samples were rinsed five times with ddH2O and allowed to dry prior to imaging on an ICON atomic force microscope (Bruker) using tapping mode and a ScanAsyst silicon tip. Images were analyzed using Gwyddion software (Czech Metrology Institute). For TEM, biofilms were grown in 48-well plates as described above. After 24 h of growth, biofilms were rinsed with PBS, scraped from the sides of the plate, spotted onto formvar-coated copper grids, stained with 2% uranyl acetate for 2 min, and imaged on a JEOL-1230 microscope (JEOL USA; Peabody, MA) with an AMT XR80 camera (Advanced Micrsocopy Techniques; Woburn, MA).

### 5.6.3 *Preparation of PSMα1 Peptide*

Lyophilized peptide stocks of synthetic PSMα1 (fMGIIAGIIKVIKSLIEQFTGK, where f denotes formylation; Ontores Biotechnologies, Hangzhou, China) were prepared as described previously[62] to eliminate aggregates from lyophilization prior to assay. Briefly, dry PSMα1 peptide was dissolved to a concentration of 10 mg/mL in a 1:1 mixture of TFA and HFIP. Ice-cold HFIP was then added to dilute PSMs to 1 mg/mL and the sample was sonicated for 10 min. Solvent TFA/HFIP was removed by air stream and then speedvac at room temperature before storage at

−20 °C. Prior to assay, PSMα1 aliquots were subjected to a secondary HFIP treatment. The peptide was dissolved in ice cold HFIP to a concentration of 10 mg/mL, vortexed, sonicated for 5 min, and incubated for 25 min on ice. The peptide was then dried to a film using a stream of air and vacuum (Savant SpeedVac concentrator) at room temperature. PSMα1 is very hydrophobic and requires a small amount of organic solvent for solubilization. At this point either DMSO or HFIP was utilized to dissolve the peptide film. DMSO was used for the bulk of the experiments but it has strong UV absorption, precluding its use for CD.

### 5.6.4 *PSMα1 Aggregation Tracking by CD Spectroscopy*

An HFIP-treated film of PSMα1 (0.1 mg) was solubilized with HFIP (20 µL) and diluted to 30 µM in potassium phosphate buffer (50 mM $KH_2PO_4$, pH 5.5) with and without 22 µM ThT, resulting in 1.3% v/v HFIP in the diluted samples. To determine the timing of CD measurements, PSMα1 polymerization was monitored over time. 150 µL samples with and without ThT were aliquoted into individual wells of a black-walled 96-well plate (Corning) and the plate was incubated at 37 °C inside the plate reader. ThT fluorescence was measured every hour after shaking. ThT-free samples were periodically withdrawn from the plate for CD measurements at 37 °C on a Jasco J-715 spectrophotometer with 1 mm quartz cuvettes. All spectra were smoothed (Savitsky–Golay method, convolution width 25, polynomial order 2) and deconvoluted (FWHM 10–15 $cm^{-1}$) in Jasco Spectra Analysis software.

### 5.6.5 *PSMα1 Fibrillization Assay with Added Inhibitors*

To solubilize PSMs for the aggregation assay, filtered DMSO was added to a treated film of PSMα1 to achieve a 20 mg/mL solution. Samples were then further diluted by addition of 22 µM ThT in ddH2O or LB medium/components with and without added synthetic α-sheet peptides (1:4 molar ratio of PSMα1:inhibitor) resulting in a final concentration of 30 µM PSMα1, 22 µM ThT, and 0.34% DMSO in all cases. LB medium components were formulated as three separate solutions: 10 g/L peptone, 5 g/L yeast extract, and 85 mM NaCl. 50 µL samples were aliquoted into 384-well black-walled plates (BrandTech; Essex, CT) and incubated in a plate reader at 37 °C, where ThT fluorescence was measured every 30–60 min.

### 5.6.6 *Immobilization and Solution Binding*

Synthetic α-sheet peptides were immobilized on Pierce Amino Link agarose beads in a Pierce spin column (Thermo Fisher) according to manufacturer protocols. Briefly, AP193 was dissolved to a concentration of 250 μM in PBS + 25% v/v DMSO + 50 mM $NaCNBH_3$ and allowed to couple to the aldehyde-functionalized resin overnight at 4 °C. Residual active sites were blocked with 1 M Tris HCl + 50 mM $NaCNBH_3$ for 4 h at 25 °C. Meanwhile, PSMα1 samples were prepared in Section 5.6.6 and incubated at 37 °C. After 0, 24, and 48 h, a sample of 200 μL PSMα1 was removed from the microtiter plate and added to a prepared spin column, where samples bound to the peptide-functionalized resin beads for 2 h at 25 °C. The solution was then collected by centrifugation (flow-through, FT). The beads were re-suspended in 300 μL PBS, vortexed to obtain a uniform slurry, and then the solution was collected by centrifugation (wash 1, W1). This wash step was performed a total of seven times, until no remaining protein was detected in the eluent. FT and the washes (W1-W7) were analyzed with the NanoOrange® Protein Quantitation Kit (Thermo Fisher). The masses of the eluents were summed and subtracted from the mass of PSMα1 applied to the column, providing a rough estimate of the bound material. This approach was necessary because elution of bound PSMα1 with GndHCl obscures protein quantification, and unfortunately, the inability to quantify the GndHCl bound fractions prevents confirmation of the mass balance.

### 5.6.7 *Biolayer Interferometry (BLI)*

All BLI experiments were performed on a BLItz biosensor system (ForteBio; Fremont, CA) using aminopropylsilane (APS) sensors. Sensors were hydrated in ddH2O + 22 μM ThT for 10 min prior to use; ThT was included to mirror the conditions of the corresponding aggregation curves. AP90 (180 μM dissolved in ddH2O + 22 μM ThT) was loaded onto the APS tip, a baseline was established in ddH2O + 22 μM ThT, and then the association of PSMα1 (50 μM prepped with DMSO + ddH2O + 22 μM ThT, as in the fibrillization assay) at various pre-incubation times was monitored over a period of 3 min. Dissociation was subsequently measured in ddH2O + 22 μM ThT, and the equilibrium dissociation constant ($K_D$) was calculated using BLItz analysis software.

# Chapter 6. Preventing Biofilm Formation in Uropathogenic *E. coli* with Synthetic α-sheet Peptides

## 6.1 Summary

Although *S. aureus* accounts for a large number of HAI and remains a major threat to compromised patients, concerns are even greater for Gram-negative pathogens. In fact, the World Health Organization released a "Priority Pathogens List" in February 2017 to guide research and development of new antibiotics, and all three of the "Priority 1 – Critical" bacteria on this list were classified as Gram-negative[225]. Uropathogenic *E. coli* (UPEC) account for the largest proportion of all HAI. These microbes are well-established biofilm formers with the ability to produce extracellular amyloid fibrils known as curli. Despite extensive characterization of the fibrils themselves and their associated secretion system, mechanistic details of curli assembly *in vivo* remain unclear. We hypothesize that populations of transient α-sheet oligomers exist within UPEC biofilms and that these structures can serve as targets for synthetic α-sheet peptides to suppress fibril formation in the EM. This Chapter describes the role of α-sheet secondary structure in curli formation, establishes synthetic α-sheet peptides as inhibitors of UPEC biofilms, and demonstrates the role of these peptides in infection clearance. These findings are extended further in **Chapter 7**, which discusses conjugation of synthetic α-sheet peptides to medical implant materials.

## 6.2 Background and Motivation

Short- and long-term medical device implantation increases the risk of infection, particularly for individuals who are already compromised by injury or illness. Thus, most HAI are associated with the very devices required to provide life-sustaining care. Catheter-associated urinary tract infections (CAUTI) account for nearly 40% of all HAI and resulted in an estimated $1.7 billion economic burden in the United States in 2016[18,226]. The complicated nature of these infections, compounded by their association with other risk factors, makes them the most common source of secondary sepsis in hospitalized patients[227]. Uropathogenic *E. coli* (UPEC) are the primary causative agents of CAUTI[18]. Urethral catheters inoculate these organisms into the bladder and promote colonization by providing a surface for bacterial adhesion and mucosal irritation[228]. After initial attachment via pili and other adhesins, *E. coli* multiply and undergo morphological

changes to form biofilms, which promote epithelial damage and ultimately lead to renal or even systemic infection[227,229]. Biofilm formation complicates the treatment of CAUTI because *E. coli* produce a robust EM when they colonize an implanted device. Current treatments to eliminate biofilm-associated CAUTI typically involve intense antibiotic administration, but these approaches can result in long-term disruption of the host microbiota as well as emergence of multi-drug resistant organisms[230]. Thus, new antimicrobial strategies should aim to "disarm" the infection by targeting biofilm-specific aspects of virulence.

In biofilms, *E. coli* produce an EM comprised primarily of cellulose and adhesive amyloid fibers called curli that stabilize the EM scaffold and facilitate adhesion to inert surfaces as well as neighboring cells[60]. The curli-specific genes are encoded in two divergently transcribed operons – *csgBAC* and *csgDEFG* – and their expression is subject to highly complex and extensive regulation[66,231]. The major amyloid subunit, CsgA, is a 13 kDa protein consisting of five imperfect sequence repeats, among which the residues serine, glutamine, and asparagine are highly conserved[232]. The assembly of functional amyloids is assisted by a "nucleator" protein, CsgB, which contains an amyloidogenic domain to template rapid fibril polymerization on the exterior of the cell[65]. The remaining proteins in the curli expression system serve as outer membrane pores for translocation of amyloid monomers (CsgG), chaperones to prevent premature polymerization of CsgA in the periplasm (CsgC), or additional processors and regulators (CsgD-F)[66–68,158,233–236] (**Figure 6.1**). As fully assembled amyloid fibrils, curli play a crucial role in uropathogenesis, where they enable adhesion and colonization, activate the host immune response, and can become involved in sepsis[237–240]. Indeed, the *csgA* gene, which encodes the major curlin subunit, is highly conserved among clinical UPEC isolates[241–244]. Thus, curli represent an essential component of CAUTI biofilm virulence as well as an excellent target for therapeutic intervention.

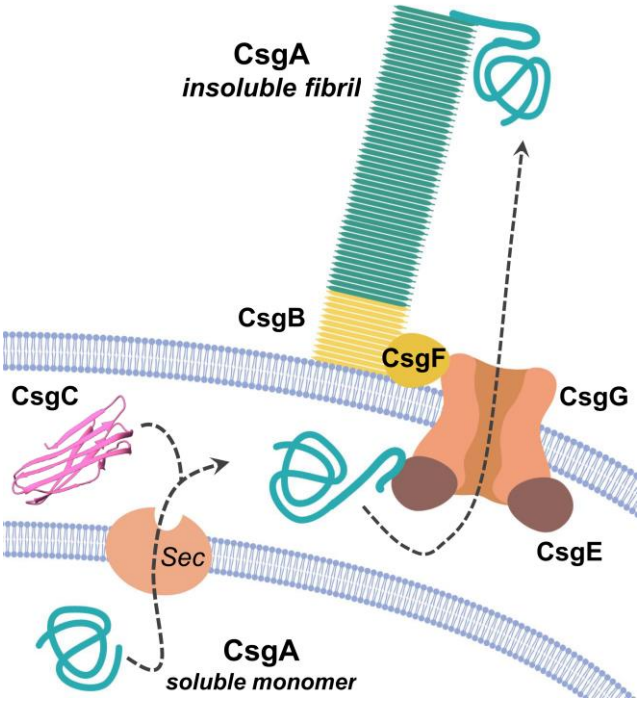


**Figure 6.1. UPEC produce curli through a coordinated system of proteins.** The major curli subunit, CsgA, begins as a soluble monomer in the cytoplasm prior to its export and cleavage by general secretory (Sec) system. In the periplasm, CsgA interacts with chaperone CsgC and is then exported to the extracellular space by CsgE and CsgG. There, CsgB serves as a template for rapid amyloid fiber formation by CsgA, and CsgF anchors the fibril complex.

Curli and other amyloids are characterized by the aggregation of soluble, monomeric proteins into insoluble, β-sheet-rich fibrils. In human amyloid diseases such as Alzheimer's and Parkinson's, amyloid-related toxicity is linked to the soluble oligomers formed during aggregation, while the mature fibrils remain relatively inert[245]. As discussed in detail in **Chapter 4**, MD simulations and biophysical experiments suggest that the soluble, oligomeric species formed on the pathway to amyloid formation contain a unique secondary structure, termed α-sheet. Synthetic peptides designed to adopt α-sheet structure complementary to the proposed α-sheet structure observed in MD inhibit the aggregation of three different mammalian disease targets by preferentially binding the toxic soluble oligomers[173,183,184]. These synthetic α-sheet peptides also exhibit anti-biofilm activity against two different Gram positive bacteria: *S. aureus* (see **Chapter 5**) and *Streptococcus mutans*, an oral microbe involved in the formation of dental caries[246]. It was therefore proposed that α-sheet secondary structure is universally adopted during amyloidogenesis and associated with toxicity.

In this Chapter, the α-sheet hypothesis is extended to a clinically important Gram negative bacterium, uropathogenic *E. coli*. The presence of α-sheet structure is established in curli by tracking the structural features of CsgA as it aggregates. Additionally, synthetic α-sheet peptides are shown to inhibit amyloid formation in CsgA alone as well as biofilm cultures, providing a novel strategy to enhance antibiotic efficacy and immune clearance against UPEC. The results presented here identify a previously undiscovered aspect of curli fiber formation, which in turn is exploited to generate novel antimicrobials focused on this specific aspect of UPEC biofilm recalcitrance.

## 6.3 Results

### 6.3.1 *Synthetic α-sheet Peptides Inhibit Biofilm Formation by Specifically Targeting Curli*

In UPEC biofilms, curli monomers aggregate to form large, β-sheet-rich amyloid fibrils upon reaching the extracellular space. It was hypothesized that populations of transient α-sheet oligomers arise during this transition, and that these structures serve as targets for synthetic α-sheet peptides to suppress fibril formation. To test this hypothesis *in situ*, biofilms of the cystitis UPEC isolate UTI89 were cultivated in YESCA broth with 4% DMSO at 26°C, conditions which are known to elicit increased curli biogenesis[247]. Varying doses of synthetic α-sheet peptide (AP193, AP195, AP195/199, or AP5) or unstructured control peptide (P1) were also added to the cultures at the time of inoculation. AP5 is a 23-residue, monomeric α-sheet hairpin. AP195 and AP193 are homodimers consisting of two identical α-sheet hairpins, and AP195/199 is a heterodimer consisting of one AP195 monomer and one AP199 monomer (**Figure 4.3**; **Table 4.2**). All dimers are covalently linked through a single disulfide bond between Cys19 residues. After 48 hours of growth, biofilms were rinsed, homogenized, and stained with the amyloid dye ThT, which fluoresces upon binding β-sheet structure and serves as a proxy for amyloid fibril content[123]. ThT binds non-specifically with the bacterial cell surface, so biofilms of a UTI89 Δ*csgA* knockout strain were cultivated in the same experiment to provide an estimate of non-specific ThT fluorescence. This non-specific signal was subtracted from UTI89 WT signals to produce the corrected fluorescence values shown in **Figure 6.2 A,B**.

In curliated UTI89 wild-type (WT) biofilms, all synthetic α-sheet peptides induced a dose-dependent reduction in ThT fluorescence, indicating suppression of EM amyloid formation

(**Figure 6.2A**). UTI89 WT biofilms were also cultivated in the presence of an unstructured peptide, P1, which retains a mixture of L- and D-amino acids but lacks α-sheet secondary structure (**Table 4.2**). Amyloid content remained unaffected regardless of the concentration of P1 applied, indicating the importance of α-sheet structure in the mechanism of inhibition (**Figure 6.2B**). This was confirmed by transmission electron microscopy (TEM), which revealed elimination of curli structures for biofilms grown the presence of α-sheet peptides (**Figure 6.3**). Furthermore, RT-qPCR found no significant difference in *csgA* expression for biofilms grown in the presence of AP193 compared to peptide-free controls (**Appendix B, Figure B.9**). Synthetic α-sheet peptides did not suppress biofilm growth or demonstrate appreciable toxicity; rather, the reduction in EM amyloid content shifted a considerable proportion of bacteria from the biofilm state to the planktonic state (**Figure 6.4**). Peptide-treated biofilms thus displayed a more dispersed and soluble phenotype, with far less biomass adhered to glass slides after a gentle washing step (green-fluorescent *E. coli* UTI89 SLC-719, **Figure 6.2C,D**).

To extend the applicability of synthetic α-sheet peptides beyond the well-characterized UTI89 system, we obtained several UPEC isolates from pediatric patients who had presented with urinary tract infections. PCR confirmed the presence of the *csgA* gene in all isolates, but only those that exhibited curliated, "rdar" colony morphotypes[248] on YESCA + Congo Red agar were selected for further characterization (**Appendix B, Figure B.10**). As in the UTI89 WT system, AP193 and AP195 caused a significant decrease in ThT fluorescence of the gentamicin/ciprofloxacin-resistant strain GERB319 (**Figure 6.2E**), highlighting the broad antimicrobial utility of synthetic α-sheet peptides irrespective of bacterial resistance profile.

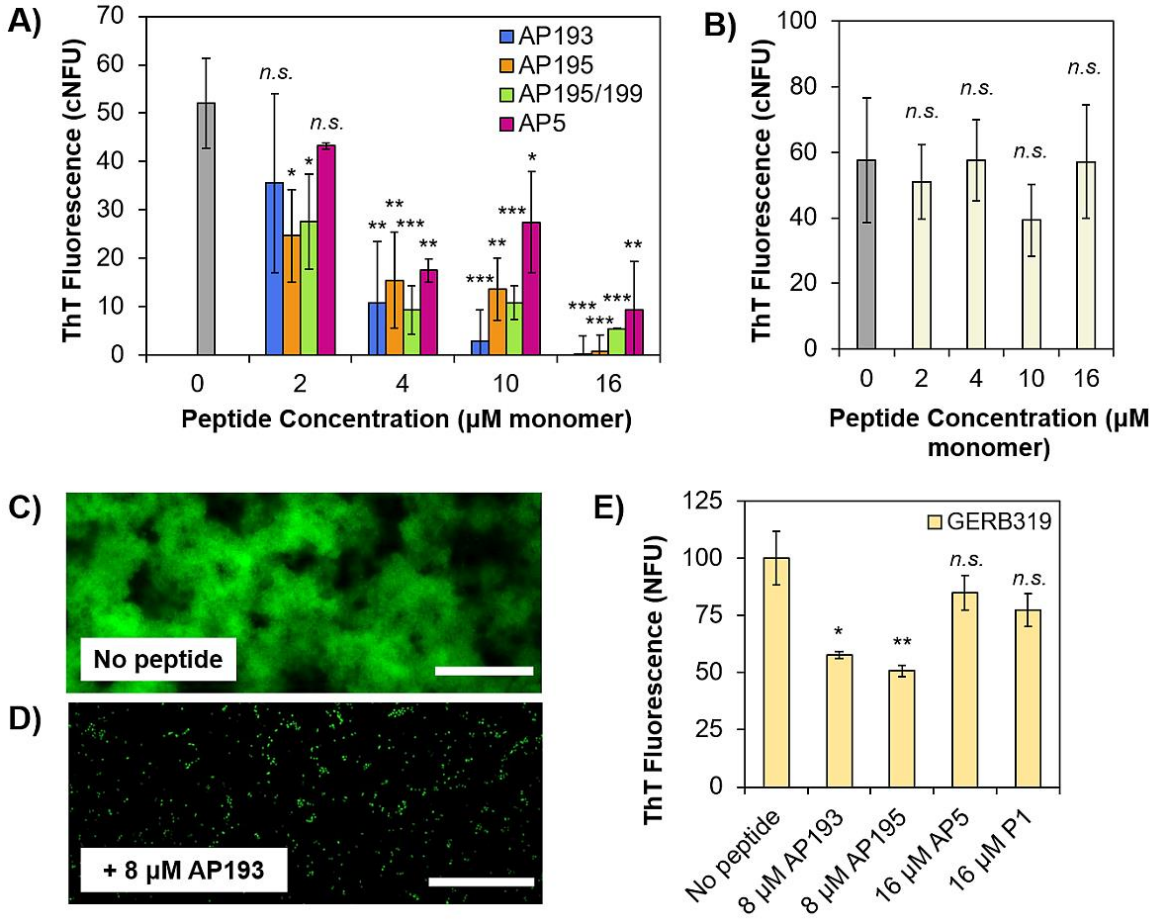


**Figure 6.2. Synthetic α-sheet peptides inhibit curli formation in biofilms. A)** AP193, AP195, AP195/199, and AP5 caused a dose-dependent reduction in EM amyloid content in UTI89 WT biofilms, as measured by ThT fluorescence. Concentrations are listed as monomer equivalents, *e.g.* 2 μM monomeric peptide (AP5) is equivalent to 1 μM dimeric peptide (AP193, AP195, AP195/199). cNFU = corrected, normalized fluorescence units, where normalized signals were corrected by the nonspecific ThT fluorescence of UTI89 Δ*csgA* biofilms. **B)** The unstructured control peptide P1 had no effect when applied at the same concentrations as synthetic α-sheet peptides. **C-D)** Green fluorescent (UTI89 SLC-719) biofilms exhibited far less adhesion to glass slides when grown in the presence of 8 μM AP193 (scale bars = 50 μm). **E)** Synthetic α-sheet peptides also decreased the ThT fluorescence of GERB319 biofilms, a clinical UTI isolate with resistance to gentamicin and ciprofloxacin. Error bars represent the standard deviation from the mean of at least three replicates.

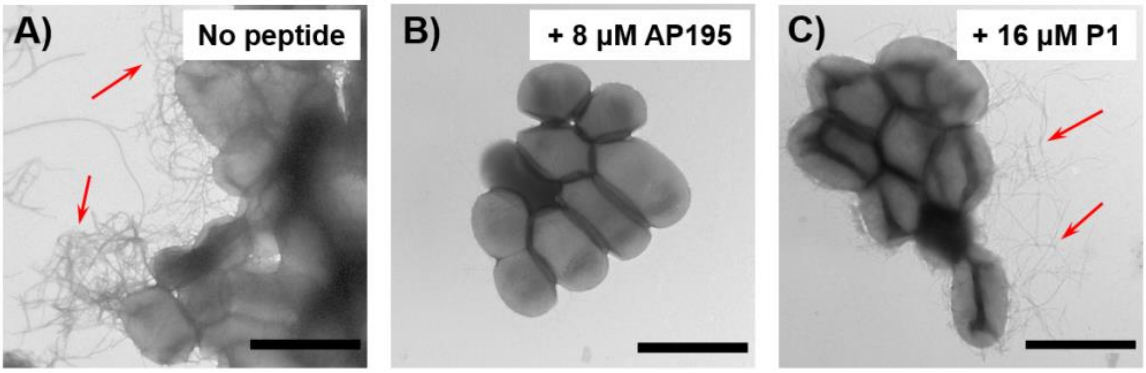


**Figure 6.3. TEM imaging of UTI89 WT biofilms.** Biofilms grown **(A)** without peptide or **(C)** with 16 µM unstructured control, P1, displayed extensive curli formation (red arrows), but **(B)** no amyloid fibrils were visible in biofilms grown in the presence of 8 µM AP195. Scale bars = 2 µm.

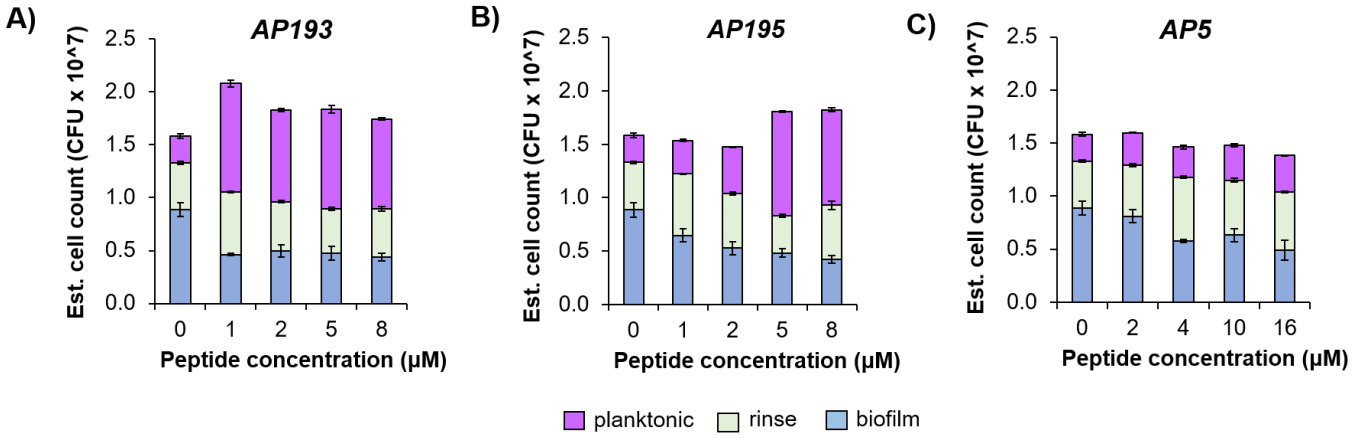


**Figure 6.4. Estimation of bacterial cell counts in ThT assays with UTI89 WT biofilms.** Peptides do not affect growth, they just shift bacteria from the biofilm state to the planktonic state. **A)** AP193, **B)** AP195, **C)** AP5.

### 6.3.2 *CsgA Passes Through α-sheet Secondary Structure on the Pathway to Amyloid Formation*

Synthetic α-sheet peptides dramatically reduced biofilm formation by inhibiting assembly of curli amyloid fibrils in UTI89 WT, but they did not affect growth or development of UTI89 Δ*csgA* biofilms. The mechanism of inhibition was thus attributed to specific interactions between the synthetic α-sheet peptides and the major curli substituent CsgA. The emergence of α-sheet structure is proposed to result from aggregation-inducing conformational changes in the CsgA protein, with α-sheet persisting throughout the accumulation of soluble oligomers before its

replacement by β-sheet structure in the fibrils. To assess this hypothesis, kinetic studies of CsgA aggregation *in vitro* were coupled with periodic measurements by CD spectroscopy, which uses polarized light to estimate secondary structure of proteins[190]. The α-sheet secondary structure displays a unique spectral signature by CD, where alternation of subsequent residues between $\alpha_L$ and $\alpha_R$ backbone conformation leads to a nearly flat spectrum, produced by cancellation of the alternately polarized light[249] (**Figure 4.3**).

Purified, recombinant CsgA was desalted into potassium phosphate buffer (KPi, pH 6.2) and diluted to a final concentration of 0.2 mg/mL (~14 μM). Samples were aliquotted into 96 well plates and incubated quiescently at 25°C. Plates were removed for periodic measurements in a plate reader, where the fluorescence of ThT tracked amyloid fibril formation. Samples without ThT were also incubated in the same plate, and these were removed at given time points for CD spectra measurements. Under these conditions, CsgA aggregated with sigmoidal kinetics (**Figure 6.5 A**). A lag period of approximately 40 h was followed by a rapid increase in ThT fluorescence, corresponding to the accumulation of amyloid fibrils. Fibril formation continued until reaching a plateau in ThT fluorescence, typically around 150 h of incubation. These three phases of the aggregation process corresponded to unique secondary structure characteristics in the CsgA protein, as measured by CD. At the beginning of the assay, CsgA was highly soluble, with low ThT fluorescence values and mostly random-coil secondary structure (**Figure 6.5 A,B**, purple lines). Near the inflection point between the lag and the exponential increase in ThT fluorescence, CsgA samples became enriched in α-sheet secondary structure (**Figure 6.5 A,B**, red lines). Finally, at the end of the assay when ThT fluorescence had reached a plateau, CsgA exhibited β-sheet structure by CD and insoluble amyloid fibrils were visible to the naked eye (**Figure 6.5 A,B**, green lines).

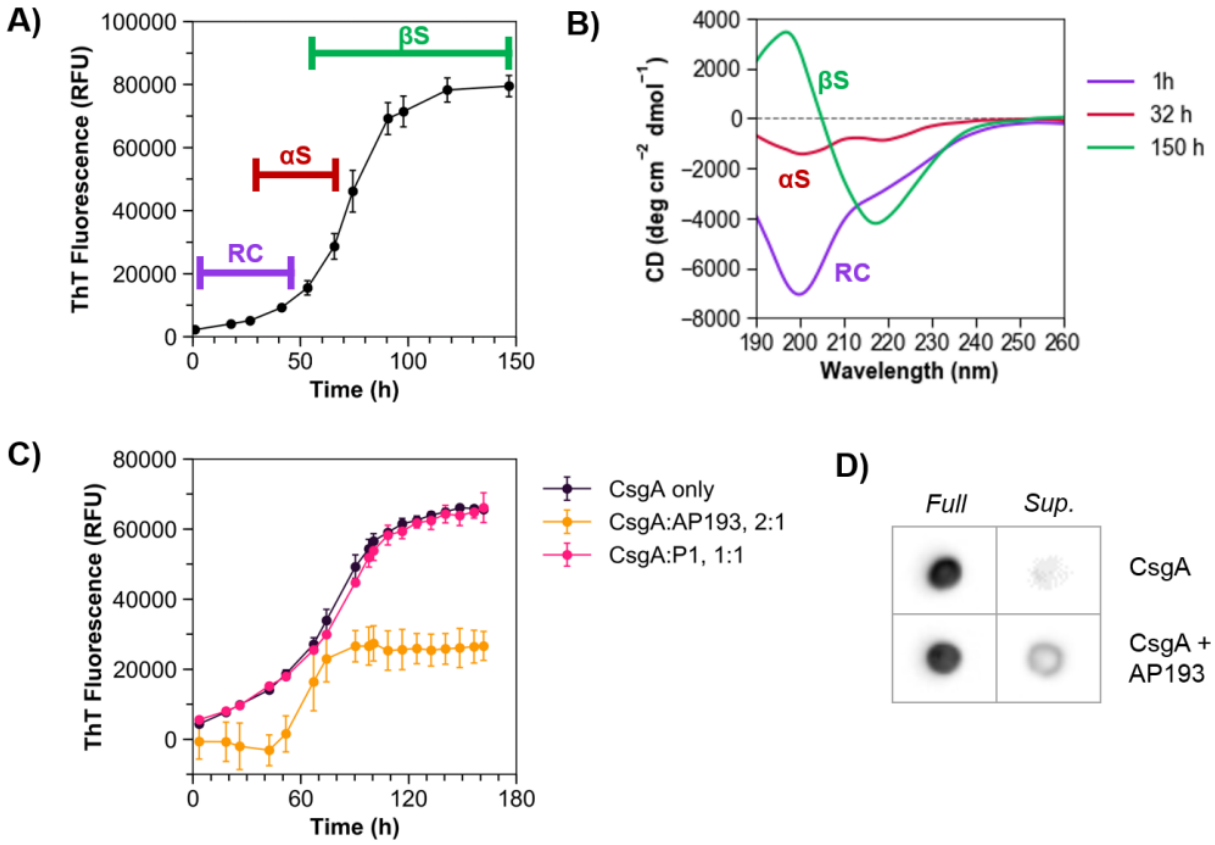


**Figure 6.5. The major curli subunit, CsgA, passes through α-sheet secondary structure on the pathway to amyloid formation.** Aggregation of CsgA at 0.2 mg/mL (~14 μM) in 50 mM KPi, pH 6.2 was monitored with **(A)** ThT fluorescence and **(B)** CD spectroscopy at the given timepoints. At the beginning of the assay (purple bars/lines), CsgA remained soluble and monomeric with random coil (RC) secondary structure. In the middle of the assay (red bars/lines), α-sheet (αS) structure emerged, followed by progression to β-sheet (βS) amyloid fibrils (green bars/lines) at the end of the assay. **C)** AP193 inhibited CsgA aggregation, while P1 did not. In this case, CsgA aggregated at 10 μM and peptides were applied at 5 μM (AP193, 2:1 molar ratio) or 10 μM (P1, 1:1 molar ratio). **D)** Coincubation of CsgA with AP193 suppressed fibril formation and increased the proportion of soluble CsgA in the supernatant (sup.) after centrifugation of endpoint samples. Error bars in **(A)** and **(C)** represent the standard deviation from the mean of at least three replicates.

Additional aggregation assays were carried out to probe the interactions between synthetic α-sheet peptides and their α-sheet-rich CsgA targets. As before, CsgA was desalted and diluted into KPi buffer (10 μM CsgA), but synthetic α-sheet peptides were also added to the mixture (5 μM AP193). As expected, CsgA alone demonstrated a high degree of fibril formation and high ThT fluorescence values. In the presence of AP193, however, CsgA fibril formation was dramatically reduced (**Figure 6.5 C**). Endpoint samples of CsgA with and without AP193 were also analyzed by immunoblotting to determine the amount of soluble CsgA remaining in the supernatant after high gravity centrifugation (**Figure 6.5 D**). CsgA alone converted almost entirely

to insoluble fibrils, as evidenced by a lack of protein in the supernatant. However, coincubation of CsgA with AP193 suppressed fibril formation and increased the proportion of soluble CsgA in the supernatant. These results are in accordance with observations in situ, where synthetic α-sheet peptides promoted a more soluble biofilm phenotype through inhibition of curli formation.

### 6.3.3 *Synthetic α-sheet Peptides Increase Susceptibility to Antibiotics*

The protective coating of the EM shields biofilms from exogenous compounds, reducing susceptibility to antibiotics by several orders of magnitude compared to planktonic microbes[11–13]. Since synthetic α-sheet peptides destabilize the amyloid component of the EM in *E. coli* by interfering with curli assembly, it was hypothesized that α-sheet peptides would induce a corresponding increase in susceptibility to antibiotics. *E. coli* UTI89 WT biofilms were cultivated in the presence of the most potent synthetic α-sheet peptide, AP193, or the unstructured control, P1. Biofilms of UTI89 Δ*csgA* served as positive controls. After 42 h of growth, gentamicin-supplemented (Gm; 300 μg/mL) or antibiotic-free medium was added to the culture and biofilms were incubated for a further 6 h. Biofilms were then harvested and homogenized by ultrasonication, and viable bacteria counts were determined by the drop plate method[250] (**Figure 6.6 A**). In all cases, addition of Gm reduced the number of colony forming units (CFUs) per biofilm, but biofilms grown in the presence of AP193 exhibited lower viability upon addition of antibiotic than P1 or peptide-free controls (**Figure 6.6 B**). Co-treatment with AP193/Gm reduced the CFU counts of UTI89 WT biofilms to those of the matrix-deficient Δ*csgA* strain, demonstrating that destabilization of the curli scaffold leads to improved antibiotic penetration.

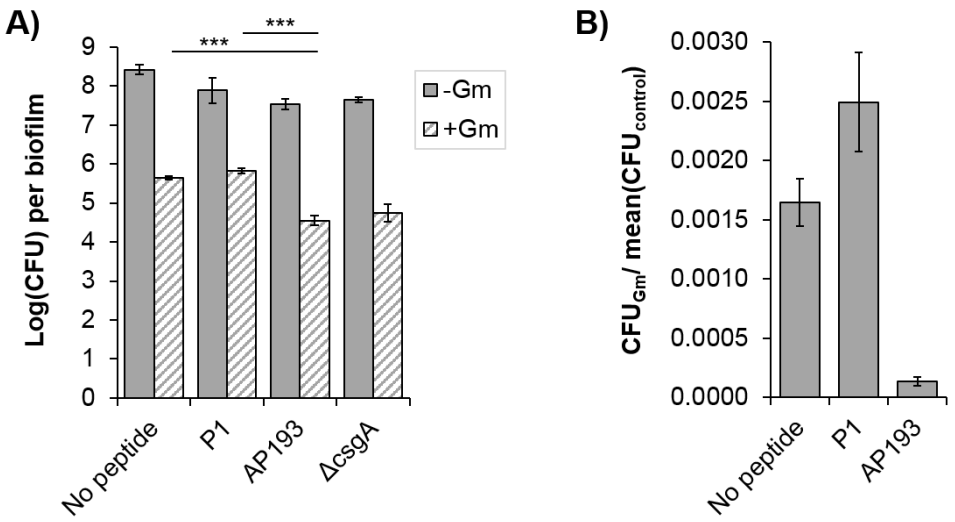


**Figure 6.6. Synthetic α-sheet peptides increase susceptibility of UTI89 biofilms to antibiotics. A)** Colony forming unit (CFU) counts were determined for biofilms with (hashed bars) and without (solid bars) 300 μg/mL gentamicin (Gm) added to the growth medium after 42 h. Addition of AP193 (8 μM) resulted in approximately tenfold fewer viable bacteria than peptide-free controls or P1 (16 μM), and these counts were comparable to those of the curli-deficient strain, Δ*csgA*. **B)** The magnitude of CFU reduction in the presence of Gm was much greater for biofilms grown with AP193 than those without peptide or those with P1. Error bars in both plots represent the standard deviation of six drop counts from three pooled biofilm samples.

### 6.3.4 *Peptide-treated Biofilms are More Vulnerable to Immune Clearance*

When synthetic α-sheet peptides interfere with curli assembly, the EM loses a critical structural reinforcing component, resulting in decreased rigidity and a reduction in the proportion of biofilm-associated bacteria. In addition to improving antibiotic efficacy, it was posited that these structural changes would increase the availability of bacteria for phagocytic clearance by immune cells. To investigate this idea, biofilms were cultivated in microtiter plates with the synthetic α-sheet peptide AP193 added to the growth medium. A fluorescent UTI89 derivative strain (SLC-719, carrying chromosomal vsfGFP) was substituted for these experiments to facilitate visualization[251]. After 48 h, mature biofilms were washed and murine macrophages (RAW 264.7, stained for red fluorescence) were applied to the biofilms for 1 h at a multiplicity of infection (MOI) of ~1:100 (macrophage:bacteria) prior to resuspension of the entire sample. Macrophages were separately co-incubated with planktonic bacteria as a positive control.

Analysis by flow cytometry and fluorescence microscopy revealed a considerable increase in bacterial phagocytosis when biofilms were cultivated in the presence of AP193. Specifically, the rate of phagocytosis (*i.e.*, the proportion of macrophages with internalized bacteria) increased

from 59% in peptide-free biofilm samples to 77% in peptide-treated biofilm samples (**Figure 6.7 A,B**). Addition of synthetic α-sheet peptides increased the availability of dissociated bacteria for phagocytosis by RAW cells, as evidenced by a comparable phagocytosis rate of 73% in planktonic bacteria controls (**Figure 6.7 C**). These measurements correspond to fluorescence microscopy images; when macrophages were co-incubated with peptide-treated biofilms or planktonic bacteria, they easily engulfed the dispersed bacteria, whereas biofilm-associated bacteria were more difficult to access (**Figure 6.7 D-F**). Synthetic α-sheet peptides induce drastic changes in biofilm architecture due to the disruption of curli formation, releasing more bacteria for phagocytosis compared to untreated controls, but macrophages were also examined for phagocytic polarization. Macrophages were also examined for canonical pro-inflammatory (M1) polarization markers. Incubation of RAW 264.7 macrophages with synthetic α-sheet peptides caused a downregulation of iNos and CD86 transcription when measured by RT-qPCR (**Appendix B, Figure B.11**), so increased phagocytosis was largely attributed to changes in biofilm phenotype as opposed to cellular activation. TNFα transcription was upregulated in macrophages incubated with synthetic α-sheet peptides (**Appendix B, Figure B.11**), perhaps due to the fact that phagocytosis requires membrane exocytosis from organelles that also partake in TNF secretion[252].Taken together, the results of this section suggest that synthetic α-sheet peptides induce meaningful changes in biofilm morphology with implications for infection clearance.

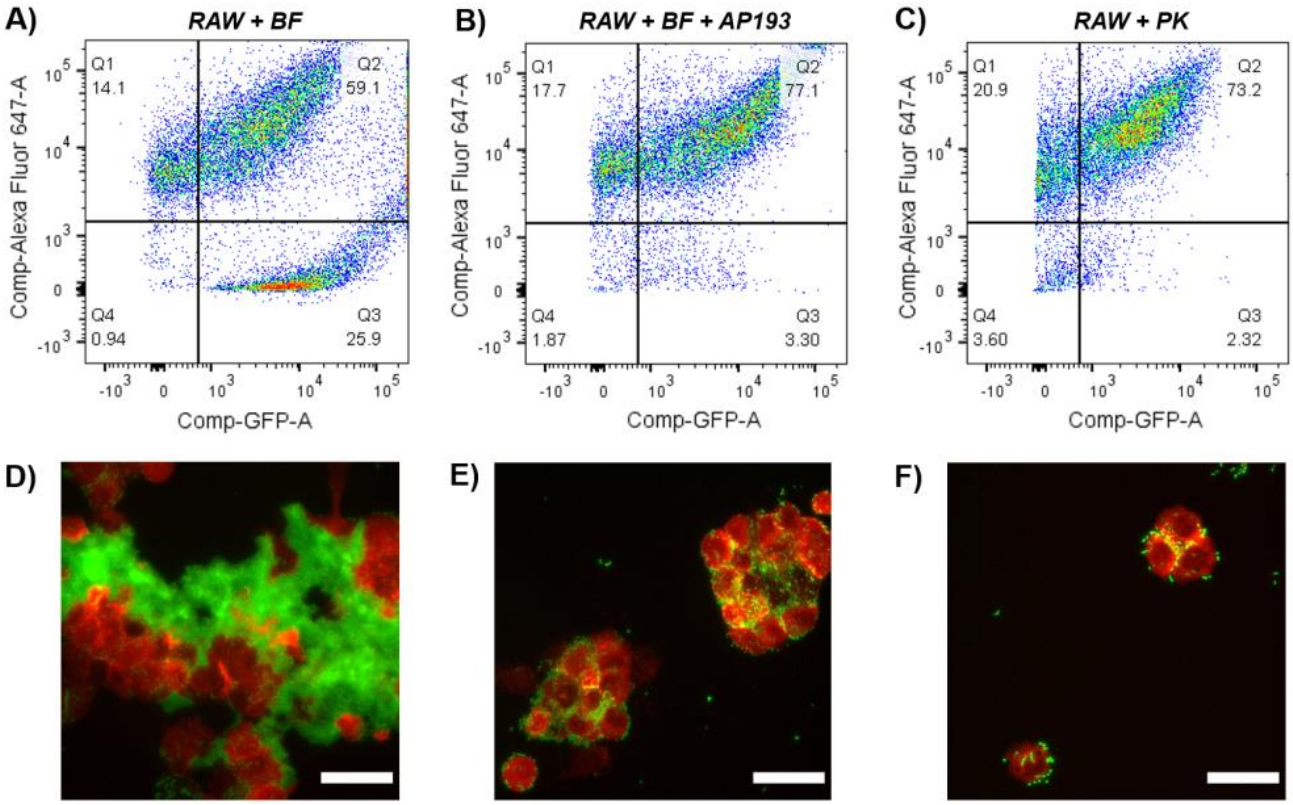


**Figure 6.7. Synthetic α-sheet peptides improve macrophage phagocytosis of UTI89 biofilms.** Flow cytometry and fluorescence microscopy (scale bars = 30 μm) after 1 h coincubation of UTI89 SLC-719 (GFP, green) and RAW 264.7 macrophages (Alexa Fluor 647, red). **A,D)** The rate of phagocytosis for untreated biofilms (RAW + BF) was 59%, and macrophages had difficulty accessing biofilm-associated bacteria. **B,E)** Phagocytosis increased to 77% for biofilms cultivated in the presence of 8 μM AP193 (RAW + BF + AP193), similar to **(C,F)** the 73% rate seen for planktonic cells (RAW + PK). Improved phagocytosis in the presence of AP193 was attributed to improved biofilm solubility and increased availability of individual bacteria.

## 6.4 Discussion

The global threat of antibiotic resistance, coupled with the prevalence of biofilm infections, demands new strategies that specifically target biofilm formation and persistance[253,254]. Current therapies often take one of two approaches to address this problem: *(1)* physical interventions that mechanically disrupt and remove the biofilm (e.g., wound irrigation) or *(2)* chemical tactics that systemically target biofilms or modified implant surfaces that are decorated with or release antibiotics or antimicrobial agents[255]. While these strategies have demonstrated some efficacy in the clinic, they run the risk of dislodging a high load of bacteria for downstream colonization, furthering reliance on antibiotics. Recently, efforts have shifted to target regulatory and structural aspects of biofilm architecture, with the goal of keeping bacteria in the planktonic state and thus

more susceptible to clearance[256–258]. Polysaccharides and nucleic acids serve as important EM scaffold materials in many clinical pathogens, but in UPEC, curli fibrils are one of the most conserved extracellular structures and a widespread contributor to biofilm recalcitrance[241]. Therefore, amyloid fibrils represent a promising target to negate UPEC biofilm formation while avoiding selective pressure for antibiotic resistance. Synthetic α-sheet peptides bind and sequester α-sheet-rich oligomers formed on the pathway to amyloid formation in a variety of systems, both mammalian and bacterial[61,173,183,184,246]. This Chapter illustrates the utility of synthetic α-sheet peptides in a new system, curliated UPEC biofilms.

The UPEC strain UTI89 produces large quantities of curli that reinforce biofilm EM with thick, rigid pellicles that resist dispersion[79]. Conversely, biofilms grown in the presence of synthetic α-sheet peptides displayed a highly soluble phenotype with scant adhesion to surfaces, no fibril structures visible under TEM, and a large proportion of bacteria remaining in the planktonic phase. Indeed, peptide-treated biofilms displayed amyloid fluorescence signals as low as those in curli-deficient Δ*csgA* biofilms, indicating that synthetic α-sheet peptides specifically inhibit curli formation. These dramatic changes in biofilm structure were achieved without any reduction in bacterial viability, mitigating the potential for resistance mutations. Furthermore, curli suppression required remarkably low doses of peptide. Synthetic α-sheet peptides exerted an effect at concentrations as low as 2 μM, and they completely abrogated curli formation at 16 μM – an order of magnitude lower than small-molecule inhibitors previously studied in this system (125 μM FN075 in Cegelski et al.[79]). Additionally, inhibition was achieved at strikingly low ratios of peptide to bacteria, with 8 μM of AP193 equating to just ~0.3 pg peptide per bacterium by the end of the 48 h incubation period.

Dimeric α-sheet peptide designs, AP193 and AP195, were particularly effective in reducing the amyloid content of UTI89 biofilms. The efficiency of these peptides stems from their dimeric design; covalent linkage of two α-sheet hairpins in a single molecule increases the avidity for binding to curli targets (**Figure 4.6**). Dimeric α-sheet peptides also inhibited amyloid formation in an antibiotic-resistant UPEC clinical isolate. The activity of these peptides in situ suggested a broad curli inhibition effect that was subsequently extended to more complex scenarios. First, the most potent synthetic α-sheet peptide, AP193, increased susceptibility of UPEC to antibiotics. As in the fluorescence assay for EM amyloid formation, addition of AP193 increased the gentamicin susceptibility of UTI89 WT biofilms to that of curli-deficient Δ*csgA* biofilms. Biofilms with robust

extracellular matrices show increased tolerance to antibiotic clearance[26], so disrupting the EM scaffold with synthetic α-sheet peptides has important implications for sustaining the efficacy of existing antibiotic drugs and slowing the spread of resistance. The value of suppressing curli formation was further demonstrated in a second test, in which AP193 rendered UPEC more vulnerable to immune clearance by murine macrophages. Independent studies indicate biofilm formation as a widespread mechanism of immune evasion[107,259,260], and extracellular matrix components help maintain the large size of biofilm particles for resistance to phagocytosis[261,262]. Even though the phagocytosis rate in untreated biofilms was greater than zero (59% of macrophages were positive for GFP-expressing bacteria), fluorescence microscopy imaging confirmed the lack of accessibility to large biofilm particles; macrophages crowded around the edges of the biofilm but were unable to break off small pieces (**Figure 6.7 D**). By disrupting the amyloid-enriched EM and forcing bacteria to remain in the planktonic state, synthetic α-sheet peptides represent a promising opportunity to re-engage host defenses against UPEC colonization in the urinary tract.

The specific and potent activity of synthetic α-sheet peptides in UPEC biofilms strongly suggests a role for α-sheet structure in curli assembly. The inhibition was attributed to an interaction between the two components: synthetic α-sheet peptides recognize α-sheet-rich oligomers that arise during aggregation of the curli subunits, sequestering these soluble species and abrogating their further association into fibrils. To test this hypothesis, a series of *in vitro* experiments with the major curli constituent, CsgA, were carried out. CsgA polymerizes to form amyloid fibrils with similar properties to those formed by mammalian amyloids, and previous studies with CD spectroscopy demonstrated conversion of CsgA from largely unstructured monomers to β-sheet-rich fibrils[263,264]. Yet, these spectra failed to capture secondary structure at intermediate time points, i.e., the phase of aggregation with the largest population of oligomers. In this study, secondary structure was tracked by CD throughout incubation, and CsgA converted from its unstructured form to β-sheet-rich amyloid fibrils with α-sheet structure arising in between. The onset of α-sheet structure in CsgA was further confirmed by addition of synthetic α-sheet peptide AP193, which inhibited fibril formation and maintained more soluble CsgA in solution.

## 6.5 Conclusions

Infections of the urinary tract, particularly CAUTI, are of growing concern for hospital hygiene and public health as a whole. Their resistance to antibiotics and their ability to form biofilms make UPEC a major target for molecular engineering approaches to clear these infections, but few current therapies suppress biofilm-specific aspects of virulence. This Chapter describes a unique strategy to prevent formation of curli amyloid fibers, a component of the biofilm EM in clinical UPEC isolates. Synthetic α-sheet peptides are complementary to α-sheet secondary structure formed by CsgA as it aggregates, and these synthetic peptides sequester α-sheet-rich oligomers to block the formation of amyloid fibers. Without amyloid fibers, UPEC biofilms lose a critical structural component and become far more susceptible to antibiotics and immune clearance. These effects have broad implications for improving antibiotic efficacy, reducing the risk of catheterization, and ultimately advancing our ability to combat biofilm infections.

## 6.6 Materials and Methods

### 6.6.1 *Peptide Synthesis and Oxidation*

Synthetic α-sheet peptides were designed *in silico* as described in **Chapter 3** and synthesized via solid-phase peptide synthesis and purified as detailed in **Chapter 4**. Sequences for the three α-sheet designs described in this Chapter (AP193, AP195, and AP5) as well as the unstructured control (P1) are listed in **Table 4.2**. In the case of AP193 and AP195, two monomers were linked together via their Cys residues to form a homodimer. All peptides were lyophilized after purification and stored at -20°C until use.

### 6.6.2 *Biofilm Culturing and Assays*

The *E. coli* strains used in this study are listed in **Appendix A, Table A.2**. Overnight cultures were grown in LB medium for ~18 h. Bacteria were collected by centrifugation at 8000 x*g* for 3 min, resuspended in YESCA broth53 + 4% v/v DMSO, and diluted to an optical density of 0.1 at 600 nm. Peptide stocks were dissolved in water and concentrations were determined by Nanodrop™ (Thermo Scientific). 20 μL of peptide stock and/or sterile ddH2O was added to each well of a sterile 48 well plate such that the final peptide concentration was 0, 2, 4, 10, or 16 μM (0, 1, 2, 5, or 8 μM for dimeric peptides), then 180 μL of diluted bacteria culture was added on

top. Plates were covered, sealed in plastic bags, and incubated at 26°C for 48 h. After growth, planktonic cells and medium were removed and biofilms were rinsed once with 250 μL PBS. Planktonic cells were spun down and resuspended in PBS, and the optical density of both planktonic and rinse samples was determined at 600 nm to estimate cell densities. The PBS solution was removed and biofilms were resuspended in 250 μL PBS + 20 μM ThT. Biofilms were homogenized by vigorous pipetting (30x per well), 1 min sonication, and 1 min on a plate shaker. 100 μL of each biofilm suspension was then transferred to a black-walled, clear-bottom 96 well plate for measurements in a plate reader (PerkinElmer). ThT fluorescence was measured at 438/495 nm as a proxy for amyloid formation, and biofilm absorbance was measured at 600 nm to estimate bacterial cell density. For UTI89 WT, biofilm fluorescence values were normalized to the average value of peptide-free controls, and then the average fluorescence value of UTI89 Δ*csgA* samples was subtracted to account for nonspecific binding. In the case of antibiotic susceptibility tests, biofilms were cultivated in the same manner, but 100 μL YESCA or 100 μL YESCA supplemented with 900 μg/mL Gm was added to wells 6 h before the end of incubation, making the final antibiotic concentration 300 μg/mL. After incubation, planktonic cells and medium were removed and biofilms were rinsed once in sterile PBS. Biofilms were then resuspended in sterile PBS, homogenized by ultrasonication for 5 s on ice, and then diluted in tenfold increments for CFU agar plate counts with the drop plate method[250].

### 6.6.3 *CsgA Expression and Purification*

A synthetic gene corresponding to the *E. coli* K12 CsgA protein, minus its Sec signal sequence, was designed and synthesized by GenScript (Piscataway, NJ). The gene was cloned into the pET30a(+) vector, which added a C-terminal 6x His tag for purification. Plasmids were transformed into *E. coli* BL21 (DE3) cells and protein expression was carried out in 2 L shake flasks at 37°C. Cultures grew to an OD600nm of 0.6-0.8 prior to induction with 1 mM IPTG. After 3-4 hours of additional growth, cells were harvested by centrifugation and resuspended in 30 mL denaturing buffer (8M Gnd HCl, 50 mM NaPi, pH 8.0) and lysed overnight with stirring at 4°C. Insoluble material was removed by centrifugation at 14,000 x*g* for 30 minutes and 15 mL of supernatant was incubated with 5 mL HisPur Ni-NTA beads (Thermo Fisher; Waltham, MA) for 2 h at room temperature with end-over-end rotation. The beads were then washed twice with denaturing buffer, twice again with denaturing buffer plus 15 mM imidazole, and twice again with

denaturing buffer plus 30 mM imidazole. Finally, protein was eluted with denaturing buffer plus 400 mM imidazole. Samples from each step of the purification were precipitated from Gnd HCl by trichloroacetic acid[265] and analyzed by SDS-PAGE. Purified fractions were of high concentration and purity, so they were not purified further prior to aggregation assays.

### 6.6.4 *Aggregation Assays and Analysis*

Immediately prior to use, protein eluents were thawed and desalted according to the Zeba desalting column protocol (Thermo Fisher) into 50 mM KPi, pH 6.2, and kept on ice. Protein concentration was determined by absorption at 280 nm, and the stock was diluted to a working concentration of 0.2 mg/mL (~14 μM) or 10 μM, depending on the assay. ThT stock was added to a concentration of 20 μM, and then CsgA was aliquotted into black-walled, clear-bottom 96 well plates at 100 μL per well. Plates were incubated in the dark at 25°C without shaking, and fluorescence measurements were taken every ~12 h on a plate reader with soft motion robotics to avoid agitation. Every well in the plate was read at every timepoint, regardless of the number of wells containing sample, in order to maintain consistent agitation. In the case of peptide inhibition tests, synthetic α-sheet peptide AP193 was prepared as above and added to the incubation mixture at a concentration of 5 μM (2:1 molar ratio CsgA:peptide). Corrected fluorescence values at each timepoint were calculated by subtracting the fluorescence values of peptide alone from those of CsgA plus peptide. For CsgA solubility tests, endpoint samples (~180 h) were removed from the plate and 2 μL was spotted in triplicate on nitrocellulose membranes. Samples were then centrifuged at 20,000 x*g* for 10 min and the supernatants were spotted in the same manner. Membranes were blocked in PBS + 0.05% v/v Tween-20 + 3% w/v BSA (PBS-T/BSA) for 1 h. Primary antibody (polyclonal anti-CsgA, courtesy of Dr. Matthew Chapman, diluted 1:10,000 in PBS-T/BSA) was applied to the membranes for 1 h. Membranes were then washed three times for 5 min each in PBS-T and secondary antibody was added for 45 min (goat anti-rabbit IgG-horseradish peroxidase (HRP), diluted 1:10,000 in PBS-T/BSA. Santa Cruz Biotechology; Dallas, TX). Membranes were washed three times again and then developed with Pierce ECL substrate (Thermo Fisher) according to the manufacturer's instructions. Chemiluminescence images were captured on an Azure c300 imaging system (Azure Biosystems; Dublin, CA).

### 6.6.5 *Circular Dichroism*

At given timepoints, CsgA samples for CD were transferred directly from microtiter incubation plates to a 1 mm quartz cuvette. CD spectra were recorded on a J-720 spectropolarimeter (Jasco, Inc.; Easton, MD) with the following settings: wavelength 260-195 nm, 0.5 nm data pitch, 1 s integration, 2 nm bandwidth, 25°C, and 6 accumulations. Only data points with detector voltages below 600 V were used. All spectra were corrected by a blank spectrum of relevant buffer and smoothed with a Savitsky-Golay filter at window size 35 and polynomial order 2.

### 6.6.6 *Microscopy*

For adherence tests, UTI89 WT biofilms were grown in 8 well Chamber Slides (Lab-Tek™, Thermo Fisher) for 48 h in YESCA broth + 4% DMSO. Planktonic cells and media were removed, biofilms were rinsed once with PBS, and biofilms were fixed with 4% paraformaldehyde and stained with SYTO 9 (Thermo Fisher) prior to imaging on a Zeiss Axioscope inverted fluorescence microscope using the GFP filter (Carl Zeiss AG). For phagocytosis, samples were prepared as described below for flow cytometry. A portion of each sample was applied to a glass microscope slide using a Cytospin™ centrifuge (Thermo Fisher), and slides were imaged on an Invitrogen (Thermo Fisher) EVOS™ FL upright fluorescent microscope using the GFP and RFP filters. For TEM, UTI89 WT biofilms were cultivated with or without peptide for 48 h in YESCA broth + 4% DMSO. Planktonic cells and media were removed, biofilms were rinsed once with PBS, and biofilms were gently scraped off plates and deposited into 20 μL of sterile PBS. Copper-formvar grids (200 mesh; Ladd Research; Williston, VT) were glow discharged and 3 μL biofilm samples were applied to grids for 2 min in a humidified chamber. Grids were then rinsed five times by touching the grid on a clean drop of water and blotting dry. Samples were stained with 2% uranyl acetate (centrifuged for 5 min at 6000 rpm before use) for 90 s in a humidified chamber, blotted dry, air dried for 5 min, and vacuum dried for 2 min. Images were collected on a Philips (Amsterdam, Netherlands) CMS100 electron microscope at 8 kV with an Olympus Morada digital camera (Olympus; Center Valley, PA) and iTEM Software Version 5.0 (iTEM; Irvine, CA). All image processing and analysis was conducted in the Fiji distribution of ImageJ[266].

### 6.6.7 *Phagocytosis and Flow Cytometry*

Green fluorescent biofilms of *E. coli* UTI89 SLC-719 were grown in YESCA broth + 4% DMSO for 48 h in 48 well polystyrene plates at 26°C. Planktonic cells and media were removed and biofilms were washed once with sterile PBS. RAW 264.7 macrophage cells were grown in complete medium (DMEM + 10% fetal bovine serum + 1X penicillin/streptomycin) to passage 12 ± 2, stained with CellTrace™ Red (Thermo Fisher), and resuspended in FACS buffer (PBS + 5% FBS). For coincubation, 250 μL of stained macrophage suspension was applied on top of each biofilm at a MOI of 1:100 (macrophage:bacteria). Planktonic bacteria and macrophages were coincubated separately at the same ratio. Coincubation proceeded for 1 h at 37°C prior to detachment of cells and biofilm by gentle scraping. Suspensions were collected and centrifuged for 5 min at 800 x*g*. The supernatant was aspirated and pellets were resupended in FACS buffer. 10,000 events per sample gated on single cells were acquired on a BD LSRII flow cytometer (BD Biosciences; Franklin Lakes, NJ) and analyzed using FlowJo software (BD Biosciences). Rate of phagocytosis was calculated as the ratio of AF647/GFP double positive population to AF647 positive population.

### 6.6.8 *RT-qPCR*

For analysis of *csgA* expression in *E. coli* UTI89 WT, biofilms were cultivated in 48 well plates with or without 8 μM AP193, as described above. Biofilm-associated bacteria were collected and normalized to a concentration of $10^8$ cells/mL. Bacteria mixtures were combined with RNAprotect Bacteria Reagent (Qiagen; Hilden, Germany) and lysed. For analysis of macrophage polarization markers, RAW 264.7 cells were seeded in 24 well plates with ~5 x $10^4$ cells per well. After 24 h of growth, the growth medium was aspirated and replaced with medim supplemented with synthetic peptides (5 μM AP193, 5 μM AP195, 10 μM AP5, 10 μM P1), or sterile water in the case of controls. The plate was incubated a further 24 h, and then cells were trypsinized to detach them from the plate, washed, and resuspended in FACS buffer. For all samples, total RNA was extracted and purified with the RNeasy Mini Kit (Qiagen) according to manufacturer instructions. cDNA was synthesized with iScript RT Supermix (BioRad; Hercules, CA) and quantified with the Qubit system (Thermo Fisher). Each RT-qPCR reaction utilized 10 ng of cDNA, 10 μL Power SYBR Green Master Mix (Thermo Fisher), and 0.4 μM each of forward and

reverse primers; samples were prepared in duplicate with appropriate housekeeping gene controls and template-free controls (see primers in **Appendix A**, **Table A.3**). Thermal cycling was carried out on an Applied Biosystems 7900HT Fast Real-Time PCR system (Thermo Fisher) with 40 cycles of 95°C for 15 s and 60°C for 1 min. Data were analyzed in SDS Software v2.4 (Thermo Fisher).

### 6.6.9 *Significance Tests*

Significance tests for bar plots in **Figure 6.2** and **Figure 6.6** are based on *p*-values generated by a two-tailed, homoscedastic Student's t-Test, where * indicates $p < 0.05$, ** indicates $p < 0.01$, *** indicates $p < 0.001$, and *n.s.* indicates $p \geq 0.05$.

# Chapter 7. Polydopamine Coating Enables Conjugation of Synthetic α-sheet Peptides to Medical Implant Materials

## 7.1 Summary

In order to achieve the ultimate goal of deploying synthetic α-sheet peptides as a biofilm control strategy in the clinic, methods are needed to increase their local concentration and thus avoid the complications of systemic administration. This Chapter examines the potential for clinical translation by grafting synthetic α-sheet peptides to the surface of medically relevant materials. Polydopamine (PDA) coating serves as a convenient conjugation strategy to facilitate the display of peptides on a variety of substrates, and the anti-fouling properties of the functional biomaterials are demonstrated with UPEC biofilms as a test organism.

## 7.2 Background and Motivation

The development of modern medical technologies, such as anesthesia and antibiotic therapy, combined with specialized materials manufacturing, has enabled treatment of a wide variety of diseases and disorders via surgery. Unfortunately, the increase in surgical procedures in recent decades has been accompanied by a corresponding increase in HAI, and the majority of these infections can be traced to biofilm formation on or in the surgical site. Upon implantation, medical devices undergo rapid fouling by host proteins and other biopolymers, which in turn provide a substrate for bacterial attachment and biofilm maturation[267]. Indeed, nearly two-thirds of all HAI reported to the Centers for Disease Control and Prevention in 2011-2014 were associated with some type of implanted material, as opposed to a skin or soft tissue infection (SSTI)[18]. Given the life-saving necessity of many implantation procedures, the risk of biofilm infection will remain unless the device materials themselves can be engineered with antimicrobial properties.

Numerous approaches have sought to address this issue. First, modification of the surface itself, through physical changes in microscopic geometry or chemical reformulation of the bulk material, provides a non-lethal means of reducing bacterial colonization, but often these materials succumb to protein deposition from host tissues or protein-independent adhesion by bacteria which renders them inactive[268–271]. Another tactic involves functionalization of standard materials by

coating or impregnating them, as has been intensely studied for a vast array of antimicrobial compounds[255,267]. Many materials incorporate and release bactericidal compounds such as antibiotics, antimicrobial peptides (AMPs), or silver nanoparticles, but these strategies place selective pressure on the microbes they target and resistance has been observed for all three cases[272–277]. Finally, some efficacy has been observed for systemic treatments such as vaccines against specific matrix proteins[278] and matrix-penetrating bacteriophages[279], but these are potential immunogens and therefore pose the threat of complications, which is unacceptable for patients who are already immunocompromised. Surprisingly, even though matrix production is arguably the fundamental hallmark of biofilm formation, very few studies have attempted to incorporate matrix-disrupting compounds into a biomedical coating. Recently, Asker *et al.* engineered covalently-linked glycoside hydrolase coatings to enzymatically degrade the exopolysaccharide Psl in *P. aeruginosa*, preventing colonization and biofilm formation on several substrates[280]. This is a clever strategy that specifically targets a major component of the *P. aeruginosa* biofilm matrix, but it remains to be seen whether hydrolase enzymes retain activity *in vivo*.

Synthetic α-sheet peptides demonstrate great promise as anti-biofilm agents, since their ability to prevent amyloid fibril formation targets a specific mechanism of biofilm virulence and avoids selective pressure for resistance. As discussed in **Chapter 4**, peptides with D-amino acids present many advantages over protein or small molecule inhibitors, including low immunogenicity, high specificity, and resistance to degradation. Thus far, however, synthetic α-sheet peptides have only been studied as inhibitors in solution, and their adaptation to the site of biofilm infection – that is, the surface of medical materials – represents a critical step in translation to clinical settings. In addition to reduced costs and increased potency compared to systemic administration, the presentation of synthetic α-sheet peptides on material surfaces creates an opportunity to combat bacterial colonization immediately after implantation, when the risk of infection is highest. Peptides may be attached to surfaces via a variety of approaches, many of which facilitate conjugation to otherwise incompatible materials[281]. Polydopamine (PDA) coating represents one such approach, and it was chosen here due to its facile implementation, low cost, and versatility.

Over the last decade, PDA surface coatings have become an important method for chemical modification of material surfaces due to their ability to self-polymerize, form thin films, and support grafting of secondary macromolecules. These coatings were originally inspired by the

adhesive proteins secreted by mussels, which are rich in 3,4-dihydroxy-L-phenylalanine (DOPA) and Lys residues[282]. Dopamine, a small molecule, shares these same functional groups (**Figure 7.1 A**), and it polymerizes to form thin, uniform coatings of PDA on a wide variety of substrates[283–285]. Once PDA is deposited on a surface, it displays multiple oxidized quinone forms of its catechol moiety, which can then undergo reactions with amines or thiols to form covalently grafted functional layers[286–288] (**Figure 7.1 B**). Furthermore, PDA itself presents a hydrophilic, non-fouling surface that can impart wettability on even very hydrophobic materials[283]. These collective properties make PDA coating an ideal approach to functionalize medically-relevant substrates with synthetic α-sheet peptides.

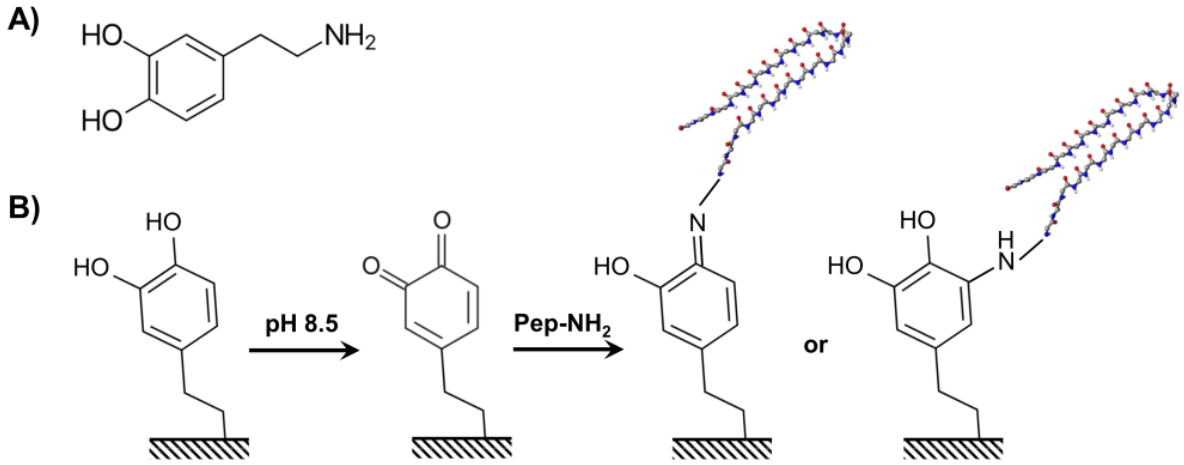


**Figure 7.1. Synthetic α-sheet peptides bind covalently to PDA-coated surfaces. A)** Dopamine displays both DOPA and lysine functional groups. **B)** Reaction scheme to construct PGAPs. At slightly alkaline pH, dopamine undergoes self-polymerization to produce an adherent polydopamine (PDA) coating, accompanied by oxidation of the catechol groups to the quinone form. Synthetic α-sheet peptides contain amino groups (Pep-$NH_2$), which undergo Michael addition or Michael addition/Schiff base reaction to bind covalently to the PDA surface.

In this Chapter, PDA-grafted α-sheet peptides (PGAPs) are presented as a novel anti-biofilm approach that can be applied to a variety of surfaces. Through a simple and effective process, synthetic α-sheet peptides were linked to organic and inorganic material substrates, where they prohibited attachment of uropathogenic *E. coli* in multiple culture models by interfering with curli assembly in the biofilm EM. PGAP materials also possess desirable qualities for medical implants: they are non-toxic to mammalian cells, and they maintain activity over time. To our knowledge, this is the first demonstration of anti-amyloid activity in a material coating, and the results presented here should stimulate further PGAP development, including testing against other

amyloid-forming pathogens, combination with additional material substrates, and examination of performance in animal models.

## 7.3 Results

### 7.3.1 *PDA Enables Covalent Linkage of Synthetic α-sheet Peptides to Surfaces*

Biofilms form on virtually every type of medical device implant, but three materials were chosen as the focus of this work – titanium ($TiO_2$), an inorganic material used for orthopedic implants; polypropylene (PP), an organic material often used in synthetic sutures; and silicone, most commonly used in catheters. Deposition of PDA occurs spontaneously in aqueous solutions at alkaline pH[283]. Submersion of clean substrates in a solution of dopamine HCl (2 mg/mL in 50 mM Tris, pH 8.5) for 24 h with shaking at 300 rpm was sufficient to fully coat the surface in a thin film of PDA, and all surfaces displayed greatly increased hydrophilicity and lower contact angles as reported by others[283,285,289,290]. For peptide grafting, 125 μM synthetic α-sheet peptide solution (AP90 or AP193; P1 and BSA served as controls) was applied to PDA-coated substrates for 4 h at 25°C and then moved to 4°C overnight, for ~18 h total reaction time. Peptide solutions were removed and fully-formed PGAPs (**Figure 7.1 B**) were rinsed thoroughly with sterile water prior to use.

Successful grafting of peptides to the PDA surface was verified by two methods. First, a colorimetric assay (BCA assay; Thermo Fisher) estimated coupling efficiency and surface density. 96 well PP microtiter plates were coated with PDA and incubated with peptide as above, and then the concentration of peptide in solution after grafting was compared to the applied concentration to determine coupling efficiency. AP193 demonstrated higher coupling efficiency (68%) than AP90 at the same concentration (46%), possibly due to the presence of more hydrophobic side chains in the AP193 sequence that promoted its physisorption to the surface. AP193 was therefore chosen as the α-sheet peptide for grafting in all subsequent experiments. The surface coverage of AP193 after coupling was estimated as ~9 μmol/cm$^2$, based on the dimensions of the wells in the PP plate and the mass of peptide bound. Next, the accessibility of AP193 on PGAP surfaces (96 well PP plates) was determined by probing functionalized PGAPs with AlexaFluor®488-conjugated Pac53 antibody, which recognizes one strand of the AP193 hairpin. Immunofluorescence measurements in a plate reader and fluorescence microscopy revealed ample

peptide attachment to the surface (**Figure 7.2 A, B**). It should be noted that AP193 exhibited some nonspecific adsorption to PP surfaces even in the absence of PDA, but pre-coating with PDA substantially increased the amount of peptide bound **(Figure 7.2 A**). This was attributed to the fact that PDA enabled both nonspecific physical adsorption and specific covalent bonding between peptide amine groups and PDA quinones.

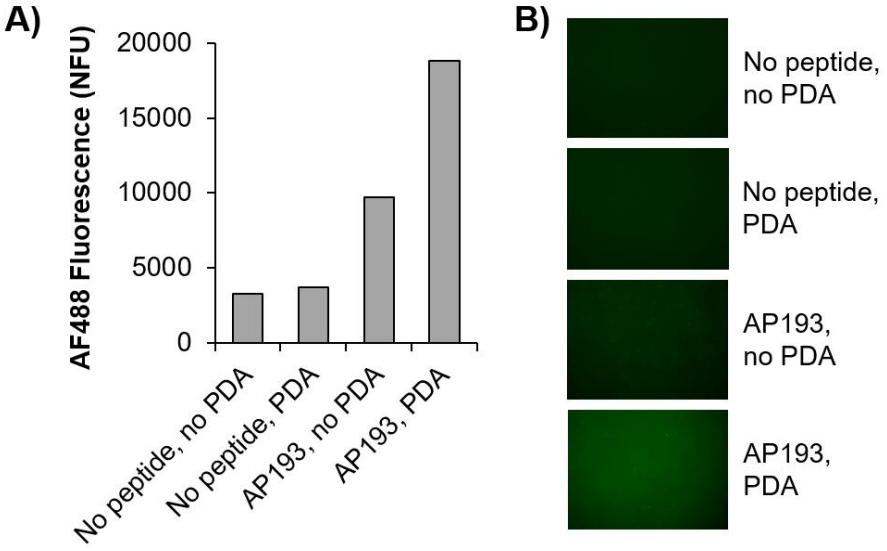


**Figure 7.2. PDA enhances attachment of AP193 to polypropylene substrates.** Polypropylene microtiter plates were prepared according to the PGAP assembly protocol and then probed with Pac53 polyclonal antibody, which recognizes a portion of the AP193 sequence. Pac53 was conjugated to AlexaFluor (AF) 488, which enabled evaluation of AP193 binding by **A)** fluorescence measurements and **B)** fluorescence microscopy (200X magnification).

### 7.3.2 *PGAP Materials Inhibit UPEC Biofilm Formation*

Good attachment and availability of PGAPs on PP surfaces did not necessarily ensure activity of the grafted peptides, so further tests were carried out to determine whether PGAPs could inhibit biofilm formation in a manner similar to synthetic α-sheet peptides in suspension. UPEC biofilms were cultivated on PGAP surfaces for 48 h under conditions known to illicit robust amyloid production in the EM (26°C, YESCA broth + 4% DMSO), and then the degree of biofilm adherence was evaluated by several methods. First, fluorescent *E. c*oli UTI89 (strain SLC-719; **Appendix A, Table A.2**) were cultivated in 96 well PP plates functionalized with PDA/AP193, PDA/P1, PDA alone, or no coating, and the resulting biofilms were evaluated qualitatively with fluorescence microscopy and quantitatively with crystal violet (CV) staining. As shown in **Figure 7.3 A-D**, AP193 PGAPs substantially reduced the fouling of PP surfaces, with very few bacteria

adhered to the plate compared to PDA alone or PDA functionalized with the random coil control peptide, P1. These observations were confirmed by CV staining, which demonstrated significantly less biofilm adherence when AP193 was present in the functional coating (**Figure 7.3 E**) and very little fouling visible to the naked eye (**Figure 7.3 F**). Confocal microscopy revealed similar characteristics for PGAPs displayed on $TiO_2$; these materials exhibited decreased biofilm coverage compared to PDA alone, PDA functionalized with BSA, or uncoated $TiO_2$ (**Figure 7.4**).

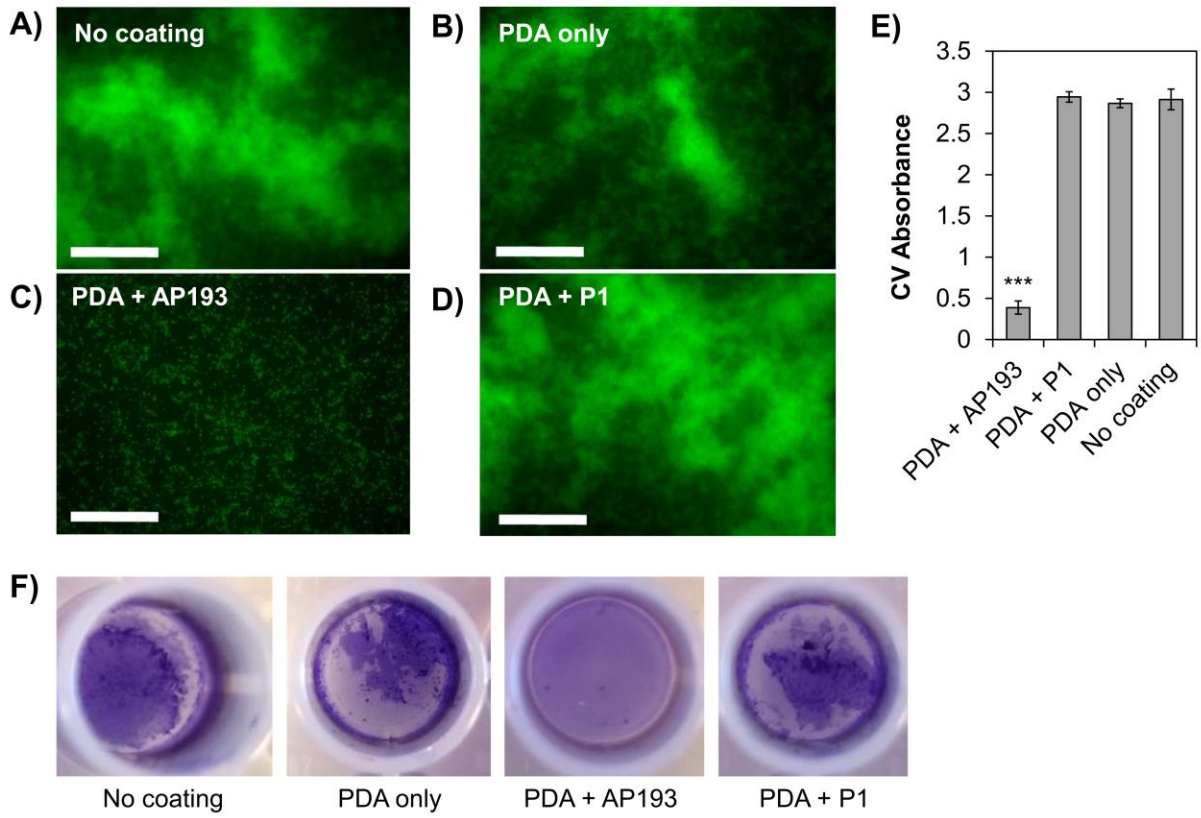


**Figure 7.3. PGAPs prevent formation of *E. coli* biofilms on polypropylene substrates.** Polypropylene PGAPs (96 well microtiter plates) were inoculated with *E. coli* UTI89 SLC-719 and incubated for 48 h at 26°C. The resulting biofilms were visualized by **(A-D)** fluorescence microscopy and **(E-F)** CV staining. Scale bars in **(A-D)** denote 60 μm and error bars in **(E)** represent the standard deviation from the mean of three samples. ***$p < 0.001$, two-tailed Student's t-test.

Healthcare-associated *E. coli* infections typically manifest in the form of CAUTI, which involves biofilm formation on the surface of silicone catheters. Therefore, silicone tubing was implemented as a clinically relevant substrate for evaluation of the PGAP approach and its effect on UPEC biofilm development. Clean, PDA-coated silicone pieces were submerged in cultures of fluorescent *E. coli* UTI89 SLC-719 for 48 h (curli inducing conditions as described above), which encased the silicone in a biofilm. Each piece was then carefully rinsed to remove loosely attached

cells, transferred to a tube of sterile PBS, and sonicated for 1 min to fully detach the adhered biofilm. Fluorescence measurements in a plate reader determined the bacterial density of each biofilm suspension, and biofilms formed on AP193 PGAP silicone were significantly less dense than those on PDA controls or silicone alone (**Figure 7.5 A**). Furthermore, PGAP silicone materials increased biofilms' susceptibility to antibiotics. The same culture conditions were used as in the bacterial density assay, but Gm (300 μg/mL) was added to half of the samples 6 h before the end of incubation. In agreement with the antibiotic susceptibility assay for free-floating peptides in **Section 6.3.3**, antibiotic killing of bacteria increased significantly when biofilms were grown on PGAP silicone as opposed to silicone with PDA alone or no coating (**Figure 7.5 B**). Interestingly, the increases in antibiotic susceptibility were more drastic for PGAPs than freely dispersed peptides at the same dose of Gm, indicating that localized disruption of amyloid assembly at the material surface may have stronger therapeutic implications than those indicated by cell counts or CV staining.

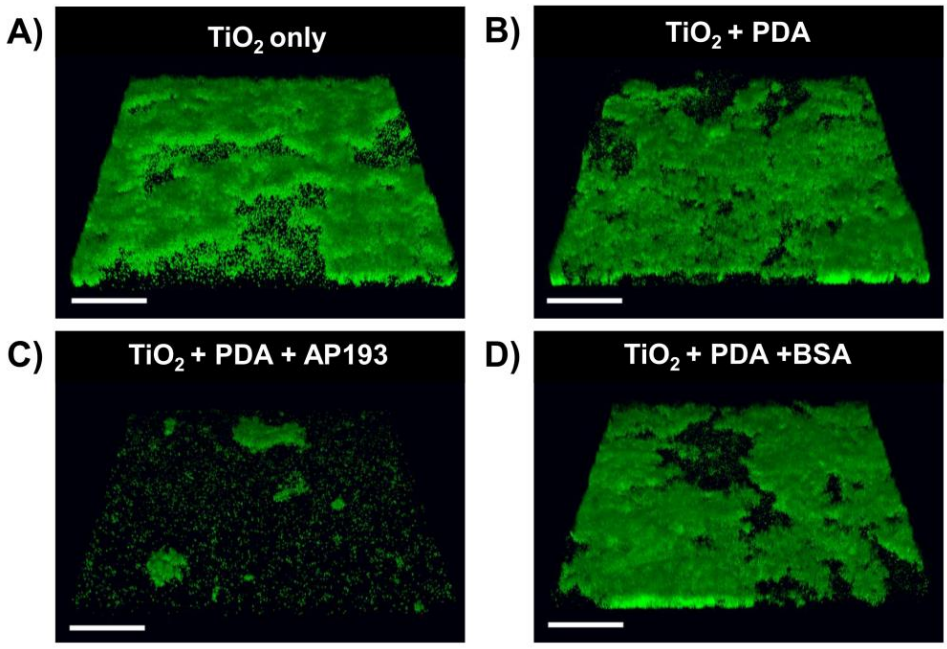


**Figure 7.4. PGAPs prevent formation of *E. coli* biofilms on titanium substrates**. $TiO_2$ disks were functionalized with PGAPs (AP193), inoculated with *E. coli* UTI89 SLC-719 and incubated for 48 h at 26°C. The surfaces were gently washed and imaged by confocal microscopy. Coatings with **(C)** AP193 caused substantial biofilm disruption compared to **(A-B)**, **(D)** controls. Scale bars denote 55 μm.

As a final test of clinical potential, PGAP silicone was probed by immunoassay to determine the accessibility of AP193 after a biofilm had already developed on the material surface.

PGAP silicone pieces from the biofilm density assay (**Figure 7.5 A**) were essentially free of adhered bacteria after the ultrasonication step, but pieces were vortexed for 30 s in fresh PBS to ensure complete detachment. These "spent" materials were then transferred to microcentrifuge tubes, where they were probed with Pac53 primary antibody and anti-IgG-HRP secondary antibody in an ELISA-like manner. Absorbance measurements of the quenched reaction solutions revealed significant AP193 remaining on the surface in PGAP materials compared to controls (**Figure 7.5 C**). The retention of accessible – and presumably, active – α-sheet peptides on the PGAP surface even after the development and removal of a mature biofilm indicates the potential for long-term use of these materials.

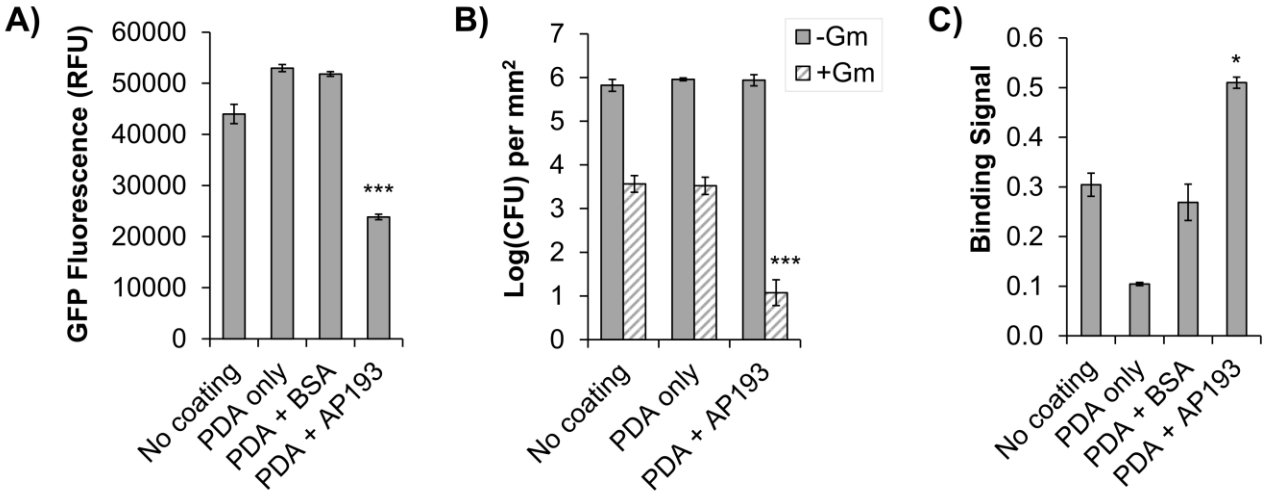


**Figure 7.5. Characterization of silicone PGAPs. A)** Silicone pieces were functionalized with PGAPs (AP193), inoculated with *E. coli* UTI89 SLC-719 and incubated for 48 h at 26°C. After a rinse step, pieces were ultrasonicated to remove adherent biofilms, and then the GFP fluorescence of biofilm suspensions was measured in a plate reader. Coatings with AP193 resulted in a significant decrease in the amount of adhered biofilm (*** $p < 0.0005$). **B)** Colony forming unit (CFU) counts were determined for silicone-associated biofilms with (hashed bars) and without (solid bars) 300 μg/mL Gm challenge. The presence of AP193 on the surface resulted in approximately 100-fold fewer viable bacteria after Gm challenge compared to peptide-free controls. (*** $p < 0.0003$). **C)** Spent silicone pieces were probed with Pac53 antibody in an ELISA-like assay. These PGAP materials still displayed accessible – and presumably, active – AP193 on the surface (* $p < 0.02$). All *p* values were generated by a two-tailed Student's t-test for significance, and error bars indicate the standard deviation from the mean.

### 7.3.3 *PGAP Materials are Non-Toxic*

Finally, the colorimetric MTT (3-(4,5-dimethylthiazol-2-yl)-2,5-diphenyltetrazolium bromide) cell viability assay was applied to determine PGAP compatibility with mouse embryonic fibroblast (3T3) cells. Polystyrene tissue culture plates were coated with PDA as previously and

then AP193 and P1 were grafted to the surface. 3T3 cells were then applied at a fixed dilution to each prepared well in triplicate and allowed to proliferate for 24 h at 37°C prior to application of MTT, cell lysis, and colorimetric measurement (**Appendix B, Figure B.12**). PGAP coatings did not significantly affect the viability of 3T3 cells compared to controls, indicating good compatibility between the functional materials and potential patient hosts.

## 7.4 Conclusions

The results presented in this Chapter demonstrate the efficacy of grafted synthetic α-sheet peptides on medical materials, a promising indication of their adaptability to full-length catheters, titanium implants, or polypropylene devices. PGAP materials depleted the curli content in the EM of UPEC biofilms, leading to a strong anti-fouling effect. Biofilms grown on PGAP surfaces showed poor adhesion and soluble phenotypes like those observed when peptides were incorporated directly into bacterial growth media, but the PDA coating approach afforded anti-amyloid functionality with specificity for the material surface. In addition to their potency, PGAP coatings show potential for multiple improvements over dispersed or systemic administration of synthetic α-sheet peptides. First, the covalent linkage of synthetic α-sheet peptides to PDA stabilizes the surface and prevents clearance of the functional molecule. Second, restriction of PGAP functionality specifically to the material surface reduces the amount of peptide required to achieve a therapeutic effect. Finally, prolonged stability of AP193 peptides following biofilm challenge on silicone PGAPs suggests that these materials may maintain functionality long after their initial implantation. Together, these results provide a foundation for further development of PGAP materials and their extension to other biofilm-forming pathogens in **Chapter 8**.

## 7.5 Materials and Methods

### 7.5.1 *Generation of PGAPs*

Before coating with PDA, all materials were cleaned thoroughly according to previously established protocols[291]. Briefly, titanium disks (medical grade, 1” diameter; Sigma) were cleaned by sonication for 5 min each in acetone, ethanol, and water, and then rinsed thoroughly in distilled water. Silicone tubing was cut by scalpel into ~2 mm x 2 mm pieces and then washed in 70% ethanol for 10 min. 96 well PP plates (Grenier Bio-one; Monroe, NC) were already sterile and not

subjected to further cleaning. To initiate the coating process, 2 mg/mL dopamine HCl (Sigma) was dissolved in 10 mM Tris HCl, pH 8.5, and applied to substrates for 24 h with shaking at 300 rpm. For titanium and silicone, materials were submerged in a petri dish containing dopamine solution, while 96 well plates were coated by filling each well with 165 μL dopamine solution. Incubation lead to polymerization of dopamine, as evidenced by dark coloring of the solutions and deposition of a thin, brown PDA film on all surfaces. Substrates were then rinsed five times with distilled water, air dried, and dried to completion in a vacuum chamber at 30°C for 1 h. Control substrates without PDA were also generated according to the same protocol but with incubation in Tris buffer instead of dopamine solution.

All peptides were synthesized and purified according to protocols in **Section 4.5**, and lyophilized peptides were resuspended in appropriate buffer immediately before use. AP193 dimerization took place in solution using a previously established protocol[292]. Briefly, 0.25 mg of lyophilized AP193 monomer was dissolved in 4 μL DMSO and then diluted in ~300 μL 50 mM sodium carbonate buffer (pH 9.6) to bring the concentration of peptide to 250 μM (monomer concentration). AP193 peptide solution was incubated at 37°C for 2 hours, which allowed complete oxidation of disulfide bonds as evidenced by a lack of absorption at 412 nm by Ellman's reagent (Thermo Fisher). AP90 does not contain disulfide bonds and was therefore resuspended to a concentration of 250 μM in 50 mM potassium phosphate, pH 8.5. Similarly, BSA was diluted from purified 2 mg/mL stock (Thermo Fisher) to 0.3 mg/mL in potassium phosphate buffer. Solutions of peptide (or BSA, where indicated) were applied to clean, PDA-coated substrates for 4 h at 25°C and then continued to react overnight at 4°C for approximately 18 h total reaction time. In the case of 96 well PP plates, 50 μL of peptide solution was aliquoted into each well to initiate coupling. For titanium disks, 20 μL spots of peptide solution were pipetted onto specific regions of the disk and incubation was carried out in a humidified chamber to prevent evaporation. Prepared silicone pieces were submerged in sterile 1.5 mL Eppendorf tubes with 80 μL peptide solution. Peptide solutions were removed, and substrates were washed three times with sterile water. Peptide concentrations (grafting and washes) were compared to the applied concentration using the Pierce BCA Protein Assay Kit (Thermo Fisher) using a simple metric for coupling efficiency:

$$\mathrm{E} = 1 - \left(\frac{\text{concentration removed}}{\text{concentration applied}}\right). \tag{7.1}$$

An anti-AP193 polyclonal antibody (Pac53, from rabbit) was used to verify successful peptide grafting and to determine the stability of PGAPs. For grafting verification, PGAPs on 96 well PP plates were blocked with 3% w/v BSA in PBS-T (PBS + 0.05% v/v Tween-20) for 1 h at room temperature with shaking, and then 100 μL Pac53 solution (1:10,000 in PBS-T + 3% BSA) was applied for 1 h at room temperature with shaking. After three washes, a secondary antibody to rabbit IgG with an AlexaFluor 488 label (Abcam; Cambridge, UK) was applied for 45 min at room temperature with shaking prior to binding evaluation by fluorescence microscopy and plate reader measurement. For stability tests, PGAPs on 96 well PP plates were filled with 100 μL PBS or 100 μL pooled human plasma (50% in PBS; Sigma), covered, and incubated at 37°C without shaking. Every 24 h, PBS and plasma were withdrawn and replaced, for a total of 5 days' incubation. A sandwich ELISA was performed with Pac53 and anti-rabbit IgG secondary antibody (Abcam) to estimate the amount of peptide released from the surface during incubation. Known AP193 concentrations (determined by NanoDrop™) served as standards in the same plate, and colorimetric quantification was performed using 1-Step Ultra TMB ELISA Substrate Solution (ThermoFisher) and 2 M $H_2SO_4$ quenching, followed by absorbance measurements in a plate reader (Perkin Elmer).

For "spent" PGAP silicone pieces, the same antibodies and reagents were used as above. Briefly, spent silicone pieces were vortexed for 30 s in fresh PBS to ensure complete bacterial detachment. They were then transferred to 1.5 mL microcentrifuge tubes, where they were blocked with 200 μL BSA solution overnight (3% w/v in PBS-T), probed 2 h at room temperature with 200 μL Pac53 polyclonal antibody (1:10,000 in PBS-T + 3% w/v BSA), washed three times in 500 μL PBS-T with vortexing, probed 2 h at room temperature with 200 μL secondary antibody to rabbit IgG (Santa Cruz Biotechnology), washed three times in 500 μL PBS-T with vortexing, and then developed for 2 h with 200 μL 1-Step Ultra TMB ELISA Substrate Solution (ThermoFisher). 50 μL of each sample was transferred in duplicate to a microtiter plate and reactions were quenched with 50 μL 2 M $H_2SO_4$ prior to absorbance measurements in a plate reader (PerkinElmer).

### 7.5.2 *Biofilm Challenge Assays*

*E. coli* UTI89 SLC-719 was prepared in YESCA broth + 4% DMSO as described in **Section 6.6.2**. PP plates were inoculated with 120 μL per well of diluted culture, titanium disks were placed in petri dishes and submerged in 5 mL diluted culture, and silicone pieces were placed

in wells of a 48 well polystyrene plate and submerged in 400 μL of diluted culture. All biofilms were grown without shaking for 48 h at 26°C. After growth, planktonic cells and media were removed and biofilms were rinsed once with PBS. PP plates were fixed with 4% paraformaldehyde and imaged on a Zeiss Axio Observer (Carl Zeiss AG) inverted fluorescent microscope, while $TiO_2$ disks were mounted on glass slides with an oiled coverslilp and imaged on a Zeiss LSM 510 confocal laser scanning microscope. For CV assays, 120 μL crystal violet stain solution was applied to each well for 1 h prior to removal, rinsing with PBS, and drying overnight. Dried, CV-stained biofilms were resuspended in 120 μL 30% acetic acid and absorbance measurements at 550 nm served as a crude measure of biofilm biomass. For silicone adherence assays, biofilm-covered silicone pieces were transferred to 1.5 Eppendorf tubes containing 300 μL of sterile PBS and ultrasonicated on ice for 1 min to detach adhered bacteria. Biofilm suspensions were then aliquoted into a black 96 well plate and fluorescence at 488 nm (GFP) served as an estimate of the number of adhered cells. For antibiotic challenge in the silicone adherence assays, biofilm-covered silicone pieces were transferred to wells containing fresh YESCA medium with or without 300 μg/mL Gm during the final 6 h of incubation. Pieces were then rinsed once in 200 μL sterile PBS to remove loosely adhered bacteria, media, and antibiotics, and then pieces were ultrasonicated as above to detach adhered bacteria. Biofilm suspensions were serially diluted in sterile PBS and enumerated on agar plates according to the drop plate method[250]. The number of colonies was back-calculated to determine the total number of bacteria on each silicone piece, and then these counts were normalized according to the surface area of the silicone piece ($CFU/mm^2$).

### 7.5.3 *Cytotoxicity Assessment*

Compatibility of PGAPs with mammalian cells was assessed with the colorimetric MTT assay. Mouse fibroblasts (NIH/3T3 cells; ATCC; Manassas, VA) were cultured in complete medium (DMEM + 10% fetal bovine serum + 1X penicillin/streptomycin) to 70% confluency and then cells were detached by trypsin and counted by hemacytometer. Meanwhile, sterile 96 well polystyrene tissue culture plates were coated with PDA and functionalized with AP193 or BSA as described above. After thorough washing of the prepared plate with sterile water, 150 μL of 3T3 suspension in fresh complete medium ($5 \times 10^4$ cells/mL) was applied to each well, with at least three wells prepared per condition. Serial dilutions ranging from $1 \times 10^6$ to $1 \times 10^3$ cells/mL were also added in triplicate to the same plate to provide a standard curve and determine the linear range

of the assay. After 24 h of growth at 37°C, 37.5 μL MTT solution (3-(4,5-dimethylthiazol-2-yl)-2,5-diphenyltetrazolium bromide; 5 mg/mL in PBS; Sigma) was added to each well and the plate was incubated a further 4 h. Cells were then lysed with a chaotropic buffer (20% SDS, 50% DMF, 1% acetic acid, 0.2% HCl) and incubated overnight to release intracellular oxidoreductase enzymes. These enzymes convert MTT from a yellow color to a dark purple color, which was measured by absorbance on a plate reader at 570 nm; higher absorbance indicated greater cell viability.

# Chapter 8. Related and Continuing Work

## 8.1 Preliminary Evidence for the Role of α-sheet in *P. aeruginosa*

Synthetic α-sheet peptides suppress amyloid formation in the EM of *S. aureus* and *E. coli* biofilms, but initial testing with *P. aeruginosa* strain PAO1 wild-type (WT) did not demonstrate any significant effects. This observation agreed with other studies of *P. aeruginosa* PAO1 reporter strains, which found that constitutive activation of the *fap* promoter did not correlate with increased Fap expression or a strong amyloid phenotype[114]. In other words, PAO1 WT transcribes the *fap* operon but does not necessarily produce large quantities of amyloid fibrils under laboratory growth conditions (37°C, LB medium). Two engineered strains were employed to overcome this issue (**Figure 8.1 A**; **Appendix A, Table A.2**). *P. aeruginosa* PAO1 pFap overexpresses Fap via a recombinant approach – the *fap* operon from PAO1 WT was cloned into a *lac*-inducible expression vector which was then reintroduced into PAO1 for homologous overexpression – while *P. aeruginosa* PAO1 Δ*fap* is unable to express Fap fibrils due to knockout of the operon[114,293]. The use of an overexpressing strain maximizes the potential phenotypic impact of α-sheet peptides, and global protein expression patterns in pFap are actually more representative of disease-associated biofilm (cystic fibrosis) than those in the WT strain[115,294]. Furthermore, the Δ*fap* knockout serves as a negative control with all of the components typically observed in the EM of *P. aeruginosa* biofilms, such as alginate, but no amyloid.

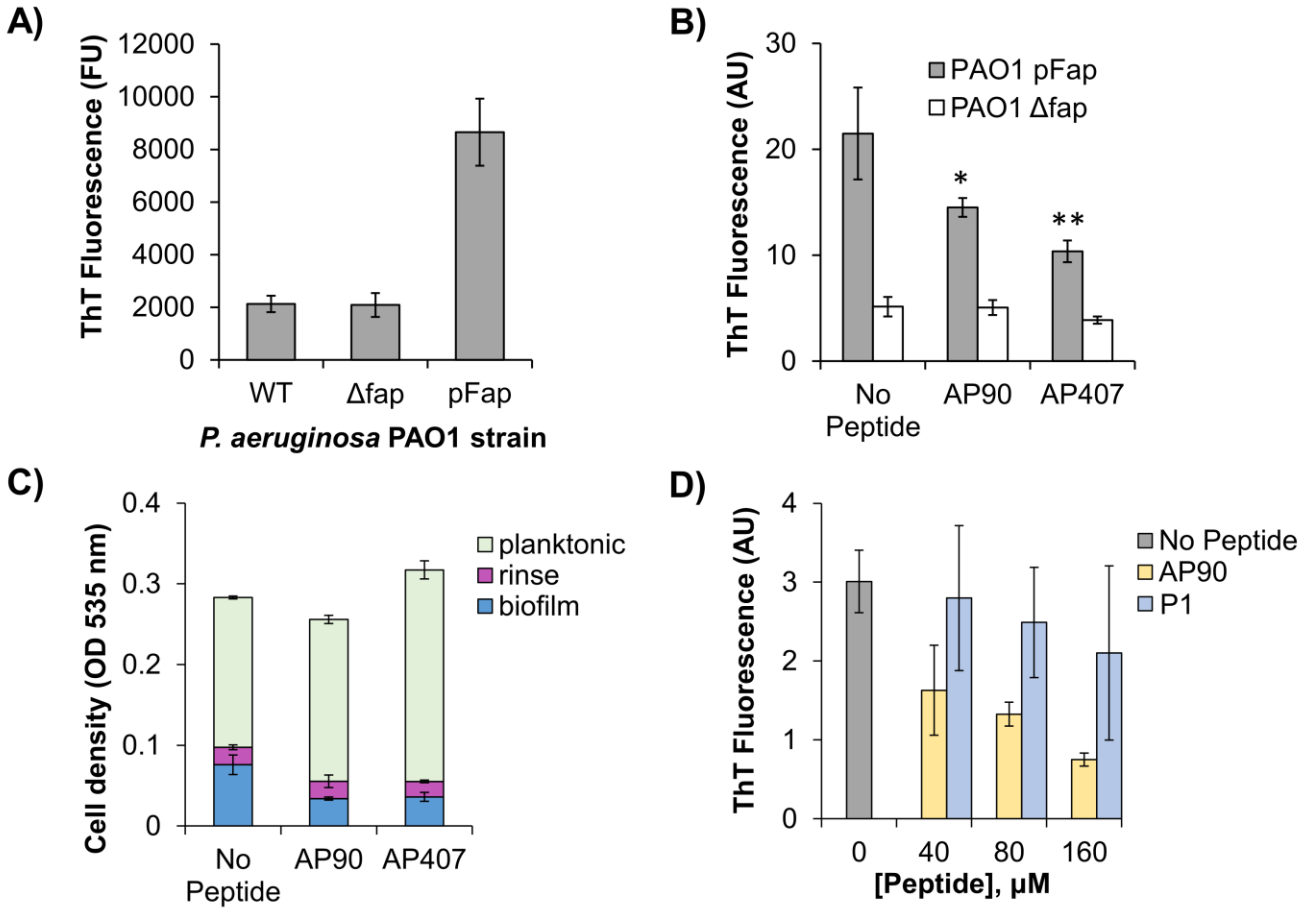


**Figure 8.1. Synthetic α-sheet peptides specifically inhibit amyloid formation in *P. aeruginosa* biofilms. A)** pFap biofilms grown in microtiter plates incorporate substantially higher quantities of amyloid compared to WT or Δ*fap*, as measured by ThT fluorescence. **B)** Both AP90 and AP407 cause a significant decrease in the amyloid content of PAO1 pFap biofilms, but not in the Δfap strain (*p = 0.04, **p = 0.005; two-tailed Student's t-test). **C)** In PAO1 pFap, both AP90 and AP407 reduced the proportion of cells in the biofilm state without reducing the total number of cells. **D)** AP90 reduced the amyloid content of PAO1 pFap biofilms in a dose-dependent manner, but the random-coil control peptide P1 did not have a significant effect. Error bars indicate the standard deviation from the mean of at least three samples.

An *in situ* approach was used to examine whether synthetic α-sheet peptides could suppress amyloid formation in the EM of *P. aeruginosa*. Briefly, overnight cultures from a single colony of freshly transformed PAO1 pFap were used to inoculate 96 well plates in the presence of α-sheet peptides (LB medium). As a control, biofilms of the knockout strain PAO1 Δ*fap* were grown under the same conditions. After 40 h, planktonic cells and media were gently removed, and then the biofilms were rinsed and stained with ThT. Cells from the planktonic and rinse phases were collected and washed for cell density measurements. Stained biofilms were resuspended by pipetting and sonication, and the fluorescence of ThT was measured in a plate reader. For this

assay, leaky expression of cloned *fap* operons was sufficient and no induction by IPTG was used. In agreement with studies in *S. aureus* and *E. coli* biofilms, the synthetic α-sheet peptides AP90 and AP407 caused a significant decrease in the amyloid content of PAO1 pFap biofilms, as measured by ThT (**Figure 8.1 B**; 80 μM peptide). Both peptides also reduced the proportion of cells in the biofilm state without causing a decrease in the total number of bacteria (**Figure 8.1 C**). Thus, synthetic α-sheet peptides fulfill a highly desirable quality for modern antimicrobial designs: they compromise protein scaffolds in the EM without inducing cell death. AP90 and AP407 did not measurably reduce ThT fluorescence or biofilm cell populations when they were applied to PAO1 Δ*fap*, confirming that the inhibitory effect of synthetic α-sheet peptides was amyloid-specific (**Figure 8.1 B**). Furthermore, the amyloid content of PAO1 pFap biofilms was reduced by AP90 in a dose-responsive manner, while the same concentrations of a random-coil control peptide (P1) displayed no significant effect (**Figure 8.1 D**). This preferential response agrees with observations in *E. coli* and *S. aureus*, implying that the efficacy of applied peptides depends on whether they contain α-sheet structure.

Preliminary aggregation tests with the major PAO1 amyloid constituent, FapC, also indicate significant inhibition of fibril formation upon addition of synthetic α-sheet peptides. FapC was expressed and purified as in **Section 2.6.3**, and then it was diluted to a concentration of XX and combined with freshly reconstituted AP90 at a molar ratio of 1:13 (FapC:AP90). ThT was added to the mixture to track amyloid formation by fluorescence, and samples were aliquoted into a 96 well plate. The plate was incubated without shaking at 25°C for 5 days, and then a single fluorescence measurement was used to compare the extent of amyloid formation in FapC alone and in FapC with AP90. In accord with results from PSMα1 and CsgA, addition of synthetic α-sheet peptides to the reaction significantly inhibited amyloid formation in FapC (~25% inhibition, **Figure 8.2**). This finding, combined with the results in PAO1 biofilms, suggests that FapC may develop α-sheet secondary structure as it aggregates.

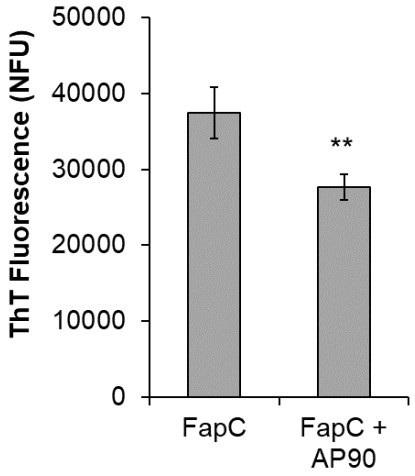


**Figure 8.2. AP90 inhibits amyloid fibril formation by FapC.** Pure FapC (6 μM) was incubated with AP90 (80 μM) in aqueous solution for 5 days prior to ThT fluorescence measurements. **p = 0.0012; two-tailed Student's t-test. Error bars indicate the standard deviation from the mean of at least three samples.

Several studies could be completed in the future to build on the success with synthetic α-sheet peptides in *P. aeruginosa* biofilms and further characterize the role of α-sheet in this system. First, more peptides and combinations could be tested in PAO1 pFap biofilms, and additional characterization such as fluorescence microscopy, TEM, and adhesion assays could shed more light on the mechanism of inhibition. Next, CD spectroscopy could be applied as in Sections 5.3.2 and 6.3.2 to establish the emergence of α-sheet secondary structure in FapC. Finally, ThT-based fibril formation assays with FapC should be carried out with greater time resolution in order to establish the kinetics of polymerization and optimize the dosage of synthetic α-sheet peptides *in vitro*. In combination with the findings reported above, these proposed studies would confirm the presence of α-sheet structure in the EM of *P. aeruginosa* biofilms, adding evidence to support the generality of the α-sheet hypothesis and providing a new therapeutic avenue to combat these infections.

## 8.2 Extension of PGAP Materials to Additional Bacterial Pathogens

The unique conjugation chemistry of PGAP materials bestows a high local concentration of synthetic α-sheet motifs at the surface of biomedically relevant materials, generating a non-fouling surface that also inhibits amyloid formation in the biofilm EM. These effects were demonstrated for *E. coli* in **Chapter 7** through a combination of fluorescence measurements, cell

viability measurements, and visualization by microscopy. PGAPs represent a particularly promising antimicrobial material because they address a specific mechanism of biofilm virulence rather than killing bacteria, and they are non-toxic to mammalian cells. Given the activity of dissolved synthetic α-sheet peptides in multiple bacterial systems, the PGAP surface-anchoring approach should extend to other microbes that produce amyloid, such as *S. aureus* and *P. aeruginosa.* Testing against additional pathogens will further optimize the conjugation chemistry and help anticipate the performance of PGAP materials *in vivo*, since different bacteria tend to form biofilms at specific sites within the body. These clinically relevant materials can then undergo further validation in animal models of infection, with the goal of sustaining their performance for long periods and thereby warding off both initial infections and subsequent threats.

## 8.3 MD Simulations of Dimeric α-sheet Peptides

As discussed in **Chapter 4**, dimerization of synthetic α-sheet peptides presents an opportunity to increase the amount of α-sheet surface area in a given molecule. These peptides were rationally designed using a simple disulfide bond between Cys residues to facilitate dimerization, and the resulting dimers exhibit increased anti-amyloid potency compared to the same dose of monomeric α-sheet peptide. These effects are intriguing and pose several questions regarding the relationship between α-sheet surface area and peptide efficacy that can be answered with MD simulations. First, does the designed increase in α-sheet surface area in dimers retain stability throughout simulation? Second, which interactions between the constituent monomers are important for this stabilization? Finally, how do these effects compare to simulations of the constituent monomer alone?

Several MD simulations have been executed to answer these questions for the most experimentally potent dimeric α-sheet peptide, AP193. The dimeric design was constructed initially using an in-house Python script (algorithm designed for Chimera and implemented in C; developed by Matthew Childers and Timothy Bi), which docked two AP193 hairpin monomers and created a disulfide bond between them. Three different poses were generated to capture the possible orientations of two dimers in three-dimensional space (**Figure 8.3**). Each of these poses was then prepared in triplicate for 50 ns of simulation at 25°C (298 K), using the same minimization and solvation procedures outlined for CsgA in **Section 3.3.2**. A 2 fs timestep was used for both preparation and simulation, and structures were saved every 1 ps for analysis. This

generated a total of 450 ns of simulation data for a single dimeric design. After simulation, trajectories were analyzed for deviation from starting positions (root mean squared deviation, RMSD, and root mean squared fluctuation, RMSF) and secondary structure was determined generally based on backbone hydrogen bonding patterns. Trajectories were also analyzed to determine whether the proposed triple-α-sheet structure was attained, thereby generating increased α-sheet surface area compared to two separate monomers. Interestingly, even though the triple-sheet structures arose occasionally in all three simulation groups (example in **Figure 4.6**), they were rather transient and easily disrupted by steric clashes with side chains or mis-orientation of the disulfide bond. Therefore, the increased potency of α-sheet dimers in experiment likely results from more than one mechanism. Further analyses of the MD trajectories could provide more insight to this phenomenon, and other dimeric designs should also be simulated to examine the effect of alternative side chain chemistries on α-sheet surface area. The AP193 dataset is large and starting poses for AP195 and AP199 have already been generated *in silico*, so future efforts should apply this wealth of data to more specific analyses. Robust metrics for α-sheet surface area must be established, and then these can then be compared between simulation runs and among different designs to draw broader conclusions about dimeric α-sheet stability and its ties to therapeutic efficacy.

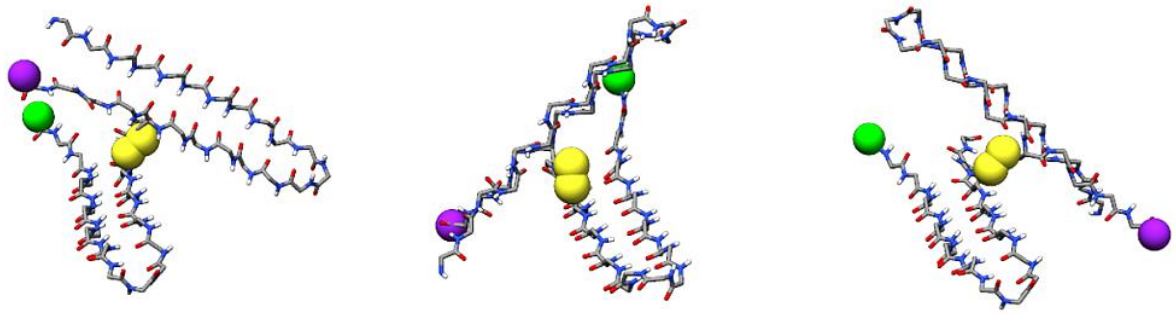

**Figure 8.3. Initial orientations for MD simulations of AP193 dimers.** Each of these three poses was used as the starting structure for triplicate simulations at 298 K. Disulfide bonds in each pair are indicated by yellow spheres. The N-terminal acetyl carbon of the first hairpin (green) and the C-terminal amide nitrogen of the second hairpin (purple) are also designated with spheres to demonstrate the relative orientation of monomers within each pair.

# References


1. Zimlichman, E. *et al.* Health Care–Associated Infections: A Meta-analysis of Costs and Financial Impact on the US Health Care System. *JAMA Intern. Med.* **173**, 2039 (2013).
2. *HCUP Fast Stats: Healthcare Cost and Utilization Project (HCUP)*. (Agency for Healthcare Research and Quality, 2019).
3. Allegranzi, B. *et al.* Burden of endemic health-care-associated infection in developing countries: systematic review and meta-analysis. *The Lancet* **377**, 228–241 (2011).
4. Centers for Disease Control and Prevention. *National and state healthcare associated infections progress report*. (Centers for Disease Control and Prevention, 2016).
5. Magill, S. S. *et al.* Multistate Point-Prevalence Survey of Health Care–Associated Infections. *N. Engl. J. Med.* **370**, 1198–1208 (2014).
6. Klevens, R. M. *et al.* Estimating health care-associated infections and deaths in U.S. hospitals, 2002. *Public Health Rep. Wash. DC 1974* **122**, 160–166 (2007).
7. Bryers, J. D. Medical Biofilms. *Biotechnol. Bioeng.* **100**, 1–18 (2008).
8. Horswill, A. R., Stoodley, P., Stewart, P. S. & Parsek, M. R. The effect of the chemical, biological, and physical environment on quorum sensing in structured microbial communities. *Anal. Bioanal. Chem.* **387**, 371–380 (2007).
9. Hall-Stoodley, L., Costerton, J. W. & Stoodley, P. Bacterial biofilms: from the Natural environment to infectious diseases. *Nat. Rev. Microbiol.* **2**, 95–108 (2004).
10. Flemming, H.-C. & Wingender, J. The biofilm matrix. *Nat. Rev. Microbiol.* **8**, 623 (2010).

11. Tseng, B. S. *et al.* The extracellular matrix protects *Pseudomonas aeruginosa* biofilms by limiting the penetration of tobramycin: Limited tobramycin penetration protects biofilms. *Environ. Microbiol.* **15**, 2865–2878 (2013).

12. Stewart, P. S. Mechanisms of antibiotic resistance in bacterial biofilms. *Int. J. Med. Microbiol.* **292**, 107–113 (2002).

13. Chambless, J. D., Hunt, S. M. & Stewart, P. S. A Three-Dimensional Computer Model of Four Hypothetical Mechanisms Protecting Biofilms from Antimicrobials. *Appl. Environ. Microbiol.* **72**, 2005–2013 (2006).

14. Bagge, N. *et al. Pseudomonas aeruginosa* biofilms exposed to imipenem exhibit changes in global gene expression and beta-lactamase and alginate production. *Antimicrob. Agents Chemother.* **48**, 1175–1187 (2004).

15. Mah, T. F. & O'Toole, G. A. Mechanisms of biofilm resistance to antimicrobial agents. *Trends Microbiol.* **9**, 34–39 (2001).

16. Ma, H. & Bryers, J. D. Non-invasive determination of conjugative transfer of plasmids bearing antibiotic-resistance genes in biofilm-bound bacteria: effects of substrate loading and antibiotic selection. *Appl. Microbiol. Biotechnol.* **97**, 317–328 (2013).

17. Weiner, L. M. *et al. Vital Signs: Preventing Antibiotic-Resistant Infections in Hospitals — United States, 2014*. 235–241 (Centers for Disease Control and Prevention, 2016).

18. Weiner, L. M. *et al.* Antimicrobial-Resistant Pathogens Associated With Healthcare-Associated Infections: Summary of Data Reported to the National Healthcare Safety Network at the Centers for Disease Control and Prevention, 2011–2014. *Infect. Control Hosp. Epidemiol.* **37**, 1288–1301 (2016).

19. Clatworthy, A. E., Pierson, E. & Hung, D. T. Targeting virulence: a new paradigm for antimicrobial therapy. *Nat. Chem. Biol.* **3**, 541–548 (2007).

20. Lewis, K. Platforms for antibiotic discovery. *Nat. Rev. Drug Discov.* **12**, 371–387 (2013).

21. Stewart, P. S. Antimicrobial Tolerance in Biofilms. *Microbiol. Spectr.* **3**, (2015).

22. Felise, H. B. *et al.* An Inhibitor of Gram-Negative Bacterial Virulence Protein Secretion. *Cell Host Microbe* **4**, 325–336 (2008).

23. Moayeri, M. *et al.* Small-Molecule Inhibitors of Lethal Factor Protease Activity Protect against Anthrax Infection. *Antimicrob. Agents Chemother.* **57**, 4139–4145 (2013).

24. Parsek, M. R., Val, D. L., Hanzelka, B. L., Cronan, J. E. & Greenberg, E. P. Acyl homoserine-lactone quorum-sensing signal generation. *Proc. Natl. Acad. Sci. U. S. A.* **96**, 4360–4365 (1999).

25. Åberg, V. & Almqvist, F. Pilicides—small molecules targeting bacterial virulence. *Org Biomol Chem* **5**, 1827–1834 (2007).

26. Billings, N. *et al.* The extracellular matrix Component Psl provides fast-acting antibiotic defense in *Pseudomonas aeruginosa* biofilms. *PLoS Pathog.* **9**, e1003526 (2013).

27. Colvin, K. M. *et al.* The pel polysaccharide can serve a structural and protective role in the biofilm matrix of *Pseudomonas aeruginosa*. *PLoS Pathog.* **7**, e1001264 (2011).

28. Peterson, B. W. *et al.* Viscoelasticity of biofilms and their recalcitrance to mechanical and chemical challenges. *FEMS Microbiol. Rev.* **39**, 234–245 (2015).

29. Carli, A. V. *et al.* Quantification of Peri-Implant Bacterial Load and in Vivo Biofilm Formation in an Innovative, Clinically Representative Mouse Model of Periprosthetic Joint Infection. *J. Bone Joint Surg. Am.* **99**, e25 (2017).

30. Serra, D. O., Richter, A. M., Klauck, G., Mika, F. & Hengge, R. Microanatomy at Cellular Resolution and Spatial Order of Physiological Differentiation in a Bacterial Biofilm. *mBio* **4**, e00103-13 (2013).

31. Smith, A. M. & Scheibel, T. Functional Amyloids Used by Organisms: A Lesson in Controlling Assembly. *Macromol. Chem. Phys.* **211**, 127–135 (2010).

32. Baldwin, A. J. *et al.* Metastability of Native Proteins and the Phenomenon of Amyloid Formation. *J. Am. Chem. Soc.* **133**, 14160–14163 (2011).

33. Fitzpatrick, A. W. P. *et al.* Atomic structure and hierarchical assembly of a cross-amyloid fibril. *Proc. Natl. Acad. Sci.* **110**, 5468–5473 (2013).

34. Nelson, R. *et al.* Structure of the cross-beta spine of amyloid-like fibrils. *Nature* **435**, 773–778 (2005).

35. Tycko, R. & Wickner, R. B. Molecular Structures of Amyloid and Prion Fibrils: Consensus versus Controversy. *Acc. Chem. Res.* **46**, 1487–1496 (2013).

36. Schleeger, M. *et al.* Amyloids: From molecular structure to mechanical properties. *Polymer* **54**, 2473–2488 (2013).

37. Smith, J. F., Knowles, T. P. J., Dobson, C. M., MacPhee, C. E. & Welland, M. E. Characterization of the nanoscale properties of individual amyloid fibrils. *Proc. Natl. Acad. Sci.* **103**, 15806–15811 (2006).

38. Chiti, F. & Dobson, C. M. Protein Misfolding, Amyloid Formation, and Human Disease: A Summary of Progress Over the Last Decade. *Annu. Rev. Biochem.* **86**, 27–68 (2017).

39. Foss, T. R., Wiseman, R. L. & Kelly, J. W. The Pathway by Which the Tetrameric Protein Transthyretin Dissociates. *Biochemistry* **44**, 15525–15533 (2005).

40. Wiseman, R. L., Powers, E. T. & Kelly, J. W. Partitioning conformational intermediates between competing refolding and aggregation pathways: insights into transthyretin amyloid disease. *Biochemistry* **44**, 16612–16623 (2005).

41. Bendor, J. T., Logan, T. P. & Edwards, R. H. The Function of α-Synuclein. *Neuron* **79**, 1044–1066 (2013).

42. Fauvet, B. *et al.* α-Synuclein in Central Nervous System and from Erythrocytes, Mammalian Cells, and *Escherichia coli* Exists Predominantly as Disordered Monomer. *J. Biol. Chem.* **287**, 15345–15364 (2012).

43. Cremades, N. *et al.* Direct Observation of the Interconversion of Normal and Toxic Forms of α-Synuclein. *Cell* **149**, 1048–1059 (2012).

44. Irvine, G. B., El-Agnaf, O. M., Shankar, G. M. & Walsh, D. M. Protein aggregation in the brain: the molecular basis for Alzheimer's and Parkinson's diseases. *Mol. Med. Camb. Mass* **14**, 451–464 (2008).

45. Armen, R. S., Alonso, D. O. V. & Daggett, V. Anatomy of an Amyloidogenic Intermediate: Conversion of β-Sheet to α-Sheet Structure in Transthyretin at Acidic pH. *Structure* **12**, 1847–1863 (2004).

46. Sarkar, B. *et al.* Significant Structural Differences between Transient Amyloid-β Oligomers and Less-Toxic Fibrils in Regions Known To Harbor Familial Alzheimer′s Mutations. *Angew. Chem. Int. Ed.* **53**, 6888–6892 (2014).

47. Cleary, J. P. *et al.* Natural oligomers of the amyloid-β protein specifically disrupt cognitive function. *Nat. Neurosci.* **8**, 79–84 (2005).

48. Sousa, M. M., Cardoso, I., Fernandes, R., Guimarães, A. & Saraiva, M. J. Deposition of transthyretin in early stages of familial amyloidotic polyneuropathy: evidence for toxicity of nonfibrillar aggregates. *Am. J. Pathol.* **159**, 1993–2000 (2001).

49. Lesné, S. E. *et al.* Brain amyloid-β oligomers in ageing and Alzheimer's disease. *Brain J. Neurol.* **136**, 1383–1398 (2013).

50. Lesné, S. *et al.* A specific amyloid-β protein assembly in the brain impairs memory. *Nature* **440**, 352–357 (2006).

51. Laganowsky, A. *et al.* Atomic View of a Toxic Amyloid Small Oligomer. *Science* **335**, 1228–1231 (2012).

52. Kayed, R. *et al.* Common Structure of Soluble Amyloid Oligomers Implies Common Mechanism of Pathogenesis. *Science* **300**, 486–489 (2003).

53. Sebollela, A. *et al.* Elucidating Molecular Mass and Shape of a Neurotoxic Aβ Oligomer. *ACS Chem. Neurosci.* **5**, 1238–1245 (2014).

54. Daggett, V. Alpha-sheet: The toxic conformer in amyloid diseases? *Acc. Chem. Res.* **39**, 594–602 (2006).

55. Glabe, C. G. Structural classification of toxic amyloid oligomers. *J. Biol. Chem.* **283**, 29639–29643 (2008).

56. Petkova, A. T. Self-Propagating, Molecular-Level Polymorphism in Alzheimer's -Amyloid Fibrils. *Science* **307**, 262–265 (2005).

57. Taglialegna, A., Lasa, I. & Valle, J. Amyloid Structures as Biofilm Matrix Scaffolds. *J. Bacteriol.* **198**, 2579–2588 (2016).

58. DePas, W. H. & Chapman, M. R. Microbial manipulation of the amyloid fold. *Res. Microbiol.* **163**, 592–606 (2012).

59. Maury, C. P. J. The emerging concept of functional amyloid. *J. Intern. Med.* **265**, 329–334 (2009).

60. Chapman, M. R. *et al.* Role of *Escherichia coli* curli operons in directing amyloid fiber formation. *Science* **295**, 851–855 (2002).

61. Bleem, A., Francisco, R., Bryers, J. D. & Daggett, V. Designed α-sheet peptides suppress amyloid formation in *Staphylococcus aureus* biofilms. *Npj Biofilms Microbiomes* **3**, (2017).

62. Schwartz, K., Syed, A. K., Stephenson, R. E., Rickard, A. H. & Boles, B. R. Functional Amyloids Composed of Phenol Soluble Modulins Stabilize *Staphylococcus aureus* Biofilms. *PLoS Pathog.* **8**, e1002744 (2012).

63. Taglialegna, A. *et al.* Staphylococcal Bap Proteins Build Amyloid Scaffold Biofilm Matrices in Response to Environmental Signals. *PLOS Pathog.* **12**, e1005711 (2016).

64. Dueholm, M. S. *et al.* Functional amyloid in *Pseudomonas*. *Mol. Microbiol.* **77**, 1009–1020 (2010).

65. Hammer, N. D., Schmidt, J. C. & Chapman, M. R. The curli nucleator protein, CsgB, contains an amyloidogenic domain that directs CsgA polymerization. *Proc. Natl. Acad. Sci. U. S. A.* **104**, 12494–12499 (2007).

66. Evans, M. L. & Chapman, M. R. Curli biogenesis: Order out of disorder. *Biochim. Biophys. Acta BBA - Mol. Cell Res.* **1843**, 1551–1558 (2014).

67. Evans, M. L. *et al.* The Bacterial Curli System Possesses a Potent and Selective Inhibitor of Amyloid Formation. *Mol. Cell* **57**, 445–455 (2015).

68. Goyal, P. *et al.* Structural and mechanistic insights into the bacterial amyloid secretion channel CsgG. *Nature* **516**, 250–253 (2014).

69. Brombacher, E. The curli biosynthesis regulator CsgD co-ordinates the expression of both positive and negative determinants for biofilm formation in *Escherichia coli*. *Microbiology* **149**, 2847–2857 (2003).

70. Rouse, S. L. *et al.* Purification, crystallization and characterization of the *Pseudomonas* outer membrane protein FapF, a functional amyloid transporter. *Acta Crystallogr. Sect. F Struct. Biol. Commun.* **72**, 892–896 (2016).

71. Bieler, S. *et al.* Amyloid formation modulates the biological activity of a bacterial protein. *J. Biol. Chem.* **280**, 26880–26885 (2005).

72. Romero, D., Aguilar, C., Losick, R. & Kolter, R. Amyloid fibers provide structural integrity to *Bacillus subtilis* biofilms. *Proc. Natl. Acad. Sci.* **107**, 2230–2234 (2010).

73. Dueholm, M. S. *et al.* The Tubular Sheaths Encasing *Methanosaeta thermophila* Filaments are Functional Amyloids. **290**, 20590–20600 *J. Biol. Chem.* (2015).

74. Claessen, D. A novel class of secreted hydrophobic proteins is involved in aerial hyphae formation in *Streptomyces coelicolor* by forming amyloid-like fibrils. *Genes Dev.* **17**, 1714–1726 (2003).

75. Erskine, E., MacPhee, C. E. & Stanley-Wall, N. R. Functional Amyloid and Other Protein Fibers in the Biofilm Matrix. *J. Mol. Biol.* **430**, 3642–3656 (2018).

76. Seviour, T. *et al.* Functional Amyloids Keep Quorum-sensing Molecules in Check. *J. Biol. Chem.* **290**, 6457–6469 (2015).

77. Stenvang, M. *et al.* Epigallocatechin Gallate Remodels overexpressed Functional Amyloids in *Pseudomonas aeruginosa* and Increases Biofilm Susceptibility to Antibiotic Treatment. **291**, 26540–26553 *J. Biol. Chem.* (2016).

78. Sellstedt, M. Development of 2-Pyridone–Based Central Fragments – Affecting the Aggregation of Amyloid Proteins. (Umea University, 2012).

79. Cegelski, L. *et al.* Small-molecule inhibitors target *Escherichia coli* amyloid biogenesis and biofilm formation. *Nat. Chem. Biol.* **5**, 913–919 (2009).

80. Romero, D., Sanabria-Valentín, E., Vlamakis, H. & Kolter, R. Biofilm Inhibitors that Target Amyloid Proteins. *Chem. Biol.* **20**, 102–110 (2013).

81. Maurer-Stroh, S. *et al.* Exploring the sequence determinants of amyloid structure using position-specific scoring matrices. *Nat. Methods* **7**, 237–242 (2010).

82. Thompson, M. J. *et al.* The 3D profile method for identifying fibril-forming segments of proteins. *Proc. Natl. Acad. Sci.* **103**, 4074–4078 (2006).

83. Gasior, P. & Kotulska, M. FISH Amyloid – a new method for finding amyloidogenic segments in proteins based on site specific co-occurence of aminoacids. *BMC Bioinformatics* **15**, 54 (2014).

84. Conchillo-Solé, O. *et al.* AGGRESCAN: a server for the prediction and evaluation of 'hot spots' of aggregation in polypeptides. *BMC Bioinformatics* **8**, 65 (2007).

85. Fernandez-Escamilla, A.-M., Rousseau, F., Schymkowitz, J. & Serrano, L. Prediction of sequence-dependent and mutational effects on the aggregation of peptides and proteins. *Nat. Biotechnol.* **22**, 1302–1306 (2004).

86. Walsh, I., Seno, F., Tosatto, S. C. E. & Trovato, A. PASTA 2.0: an improved server for protein aggregation prediction. *Nucleic Acids Res.* **42**, W301–W307 (2014).

87. Tartaglia, G. G. & Vendruscolo, M. The Zyggregator method for predicting protein aggregation propensities. *Chem. Soc. Rev.* **37**, 1395 (2008).

88. Kuhlman, B. & Baker, D. Native protein sequences are close to optimal for their structures. *Proc. Natl. Acad. Sci.* **97**, 10383–10388 (2000).

89. Goldschmidt, L., Teng, P. K., Riek, R. & Eisenberg, D. Identifying the amylome, proteins capable of forming amyloid-like fibrils. *Proc. Natl. Acad. Sci.* **107**, 3487–3492 (2010).

90. Childers, M. C. & Daggett, V. Insights from molecular dynamics simulations for computational protein design. *Mol. Syst. Des. Eng.* **2**, 9–33 (2017).

91. Alder, B. J. & Wainwright, T. E. Studies in Molecular Dynamics. I. General Method. *J. Chem. Phys.* **31**, 459–466 (1959).

92. Armen, R. S., Bernard, B. M., Day, R., Alonso, D. O. V. & Daggett, V. Characterization of a possible amyloidogenic precursor in glutamine-repeat neurodegenerative diseases. *Proc. Natl. Acad. Sci. U. S. A.* **102**, 13433–13438 (2005).

93. Armen, R. S., DeMarco, M. L., Alonso, D. O. V. & Daggett, V. Pauling and Corey's α-pleated sheet structure may define the prefibrillar amyloidogenic intermediate in amyloid disease. *Proc. Natl. Acad. Sci.* **101**, 11622–11627 (2004).

94. Steward, R. E., Armen, R. S. & Daggett, V. Different disease-causing mutations in transthyretin trigger the same conformational conversion. *Protein Eng. Des. Sel.* **21**, 187–195 (2008).

95. Towse, C.-L., Hopping, G., Vulovic, I. & Daggett, V. Nature versus design: the conformational propensities of D-amino acids and the importance of side chain chirality. *Protein Eng. Des. Sel.* **27**, 447–455 (2014).

96. Childers, M. C., Towse, C.-L. & Daggett, V. The effect of chirality and steric hindrance on intrinsic backbone conformational propensities: tools for protein design. *Protein Eng. Des. Sel.* **29**, 271–280 (2016).

97. Towse, C.-L., Rysavy, S. J., Vulovic, I. M. & Daggett, V. New Dynamic Rotamer Libraries: Data-Driven Analysis of Side-Chain Conformational Propensities. *Structure* **24**, 187–199 (2016).

98. Beck, D. A. C., Alonso, D. O. V., Inoyama, D. & Daggett, V. The intrinsic conformational propensities of the 20 naturally occurring amino acids and reflection of these propensities in proteins. *Proc. Natl. Acad. Sci. U. S. A.* **105**, 12259–12264 (2008).

99. Gellatly, S. L. & Hancock, R. E. W. *Pseudomonas aeruginosa* : new insights into pathogenesis and host defenses. *Pathog. Dis.* **67**, 159–173 (2013).

100. Bjarnsholt, T. *et al.* The in vivo biofilm. *Trends Microbiol.* **21**, 466–474 (2013).

101. Williams, B. J., Dehnbostel, J. & Blackwell, T. S. *Pseudomonas aeruginosa*: Host defence in lung diseases. *Respirology* **15**, 1037–1056 (2010).

102. Boisvert, A.-A., Cheng, M. P., Sheppard, D. C. & Nguyen, D. Microbial Biofilms in Pulmonary and Critical Care Diseases. *Ann. Am. Thorac. Soc.* **13**, 1615–1623 (2016).

103. Bjarnsholt, T. *et al. Pseudomonas aeruginosa* biofilms in the respiratory tract of cystic fibrosis patients. *Pediatr. Pulmonol.* **44**, 547–558 (2009).

104. Pritt, B., O'Brien, L. & Winn, W. Mucoid *Pseudomonas* in Cystic Fibrosis. *Am. J. Clin. Pathol.* **128**, 32–34 (2007).

105. Lee, K. & Yoon, S. S. *Pseudomonas aeruginosa* Biofilm, a Programmed Bacterial Life for Fitness. *J. Microbiol. Biotechnol.* **27**, 1053–1064 (2017).

106. Leid, J. G. *et al.* The exopolysaccharide alginate protects *Pseudomonas aeruginosa* biofilm bacteria from IFN-gamma-mediated macrophage killing. *J. Immunol. Baltim. Md 1950* **175**, 7512–7518 (2005).

107. Jones, C. J. & Wozniak, D. J. Psl Produced by Mucoid *Pseudomonas aeruginosa* Contributes to the Establishment of Biofilms and Immune Evasion. *mBio* **8**, e00864-17, /mbio/8/3/e00864-17.atom (2017).

108. Jennings, L. K. *et al.* Pel is a cationic exopolysaccharide that cross-links extracellular DNA in the *Pseudomonas aeruginosa* biofilm matrix. *Proc. Natl. Acad. Sci.* **112**, 11353–11358 (2015).

109. Wei, Q. & Ma, L. Biofilm Matrix and Its Regulation in *Pseudomonas aeruginosa*. *Int. J. Mol. Sci.* **14**, 20983–21005 (2013).

110. O'Toole, G. A. & Kolter, R. Flagellar and twitching motility are necessary for *Pseudomonas aeruginosa* biofilm development. *Mol. Microbiol.* **30**, 295–304 (1998).

111. Reichhardt, C., Wong, C., Passos da Silva, D., Wozniak, D. J. & Parsek, M. R. CdrA Interactions within the *Pseudomonas aeruginosa* Biofilm Matrix Safeguard It from Proteolysis and Promote Cellular Packing. *mBio* **9**, (2018).

112. Zeng, G. *et al.* Functional bacterial amyloid increases *Pseudomonas* biofilm hydrophobicity and stiffness. *Front. Microbiol.* **6**, (2015).

113. Rouse, S. L., Matthews, S. J. & Dueholm, M. S. Ecology and Biogenesis of Functional Amyloids in *Pseudomonas*. *J. Mol. Biol.* **430**, 3685–3695 (2018).

114. Dueholm, M. S. *et al.* Expression of Fap amyloids in *Pseudomonas aeruginosa* , *P. fluorescens,* and *P. putida* results in aggregation and increased biofilm formation. *MicrobiologyOpen* **2**, 365–382 (2013).

115. Herbst, F.-A. *et al.* Major Proteomic Changes Associated with Amyloid-Induced Biofilm Formation in *Pseudomonas aeruginosa* PAO1. *J. Proteome Res.* **14**, 72–81 (2015).

116. Dueholm, M. S., Otzen, D. & Nielsen, P. H. Evolutionary Insight into the Functional Amyloids of the Pseudomonads. *PLoS ONE* **8**, e76630 (2013).

117. Barnhart, M. M. & Chapman, M. R. Curli Biogenesis and Function. *Annu. Rev. Microbiol.* **60**, 131–147 (2006).

118. Rouse, S. L. *et al.* A new class of hybrid secretion system is employed in *Pseudomonas* amyloid biogenesis. *Nat. Commun.* **8**, (2017).

119. Bleem, A. *et al.* Protein Engineering Reveals Mechanisms of Functional Amyloid Formation in *Pseudomonas aeruginosa* Biofilms. *J. Mol. Biol.* **430**, 3751–3763 (2018).

120. Trainor, K., Broom, A. & Meiering, E. M. Exploring the relationships between protein sequence, structure and solubility. *Curr. Opin. Struct. Biol.* **42**, 136–146 (2017).

121. Sievers, F. *et al.* Fast, scalable generation of high-quality protein multiple sequence alignments using Clustal Omega. *Mol. Syst. Biol.* **7**, 539 (2011).

122. Hilpert, K., Winkler, D. F. H. & Hancock, R. E. W. Peptide arrays on cellulose support: SPOT synthesis, a time and cost efficient method for synthesis of large numbers of peptides in a parallel and addressable fashion. *Nat. Protoc.* **2**, 1333–1349 (2007).

123. Gade Malmos, K. *et al.* ThT 101: a primer on the use of thioflavin T to investigate amyloid formation. *Amyloid* **24**, 1–16 (2017).

124. Sarroukh, R., Goormaghtigh, E., Ruysschaert, J.-M. & Raussens, V. ATR-FTIR: A “rejuvenated” tool to investigate amyloid proteins. *Biochim. Biophys. Acta BBA - Biomembr.* **1828**, 2328–2338 (2013).

125. Klein, S. *et al.* Adaptation of *Pseudomonas aeruginosa* to various conditions includes tRNA-dependent formation of alanyl-phosphatidylglycerol. *Mol. Microbiol.* **71**, 551–565 (2009).

126. Jones, E. M., Cochrane, C. A. & Percival, S. L. The Effect of pH on the Extracellular Matrix and Biofilms. *Adv. Wound Care* **4**, 431–439 (2015).

127. Pezzulo, A. A. *et al.* Reduced airway surface pH impairs bacterial killing in the porcine cystic fibrosis lung. *Nature* **487**, 109–113 (2012).

128. Foderà, V. *et al.* Thioflavin T Hydroxylation at Basic pH and Its Effect on Amyloid Fibril Detection. *J. Phys. Chem. B* **112**, 15174–15181 (2008).

129. Steinmann, J., Buer, J., Pietschmann, T. & Steinmann, E. Anti-infective properties of epigallocatechin-3-gallate (EGCG), a component of green tea: Anti-infective effects of EGCG. *Br. J. Pharmacol.* **168**, 1059–1073 (2013).

130. Yang, L., Liu, Y., Sternberg, C. & Molin, S. Evaluation of Enoyl-Acyl Carrier Protein Reductase Inhibitors as *Pseudomonas aeruginosa* Quorum-Quenching Reagents. *Molecules* **15**, 780–792 (2010).

131. Hudson, S. A., Ecroyd, H., Kee, T. W. & Carver, J. A. The thioflavin T fluorescence assay for amyloid fibril detection can be biased by the presence of exogenous compounds: Exogenous compounds can bias thioflavin T assays. *FEBS J.* **276**, 5960–5972 (2009).

132. Palhano, F. L., Lee, J., Grimster, N. P. & Kelly, J. W. Toward the Molecular Mechanism(s) by Which EGCG Treatment Remodels Mature Amyloid Fibrils. *J. Am. Chem. Soc.* **135**, 7503–7510 (2013).

133. Lendel, C. *et al.* On the Mechanism of Nonspecific Inhibitors of Protein Aggregation: Dissecting the Interactions of α-Synuclein with Congo Red and Lacmoid. *Biochemistry* **48**, 8322–8334 (2009).

134. Feng, B. Y. *et al.* Small-molecule aggregates inhibit amyloid polymerization. *Nat. Chem. Biol.* **4**, 197–199 (2008).

135. Kaplan, B., Shtrasburg, S. & Pras, M. Micropurification techniques in the analysis of amyloid proteins. *J. Clin. Pathol.* **56**, 86–90 (2003).

136. Meisl, G. *et al.* Molecular mechanisms of protein aggregation from global fitting of kinetic models. *Nat. Protoc.* **11**, 252–272 (2016).

137. Arosio, P., Knowles, T. P. J. & Linse, S. On the lag phase in amyloid fibril formation. *Phys. Chem. Chem. Phys.* **17**, 7606–7618 (2015).

138. Michaels, T. C. T. *et al.* Chemical Kinetics for Bridging Molecular Mechanisms and Macroscopic Measurements of Amyloid Fibril Formation. *Annu. Rev. Phys. Chem.* **69**, 273–298 (2018).

139. Cohen, S. I. A., Vendruscolo, M., Dobson, C. M. & Knowles, T. P. J. From Macroscopic Measurements to Microscopic Mechanisms of Protein Aggregation. *J. Mol. Biol.* **421**, 160–171 (2012).

140. Heras, B. *et al.* DSB proteins and bacterial pathogenicity. *Nat. Rev. Microbiol.* **7**, 215–225 (2009).

141. Arts, I. S. *et al.* Dissecting the Machinery That Introduces Disulfide Bonds in *Pseudomonas aeruginosa*. *mBio* **4**, e00912-13-e00912-13 (2013).

142. Otzen, D. Functional amyloid: Turning swords into plowshares. *Prion* **4**, 256–264 (2010).

143. Paul, K. R. *et al.* Effects of Mutations on the Aggregation Propensity of the Human Prion-Like Protein hnRNPA2B1. *Mol. Cell. Biol.* **37**, e00652-16 (2017).

144. Hee, J. S., Mitchell, S. M., Liu, X. & Leonhardt, R. M. Melanosomal formation of PMEL core amyloid is driven by aromatic residues. *Sci. Rep.* **7**, 44064 (2017).

145. Carpentier, G. Protein Array Analyzer for ImageJ. in (eds. ImageJ User and Developer Conference & Centre de Recherche Public Henri Tudor) (Centre de Recherche Public Henri Tudor, 2008).

146. Gasteiger, E. *et al.* Protein Identification and Analysis Tools on the ExPASy Server. in *The Proteomics Protocols Handbook* 571–607 (Humana Press Inc., 2005).

147. Morris, R. J. *et al.* Mechanistic and environmental control of the prevalence and lifetime of amyloid oligomers. *Nat. Commun.* **4**, 1891 (2013).

148. Schneider, C. A., Rasband, W. S. & Eliceiri, K. W. NIH Image to ImageJ: 25 years of image analysis. *Nat. Methods* **9**, 671–675 (2012).

149. Tugyi, R. *et al.* Partial d-amino acid substitution: Improved enzymatic stability and preserved Ab recognition of a MUC2 epitope peptide. *Proc. Natl. Acad. Sci. U. S. A.* **102**, 413–418 (2005).

150. Kuhlman, B. Design of a Novel Globular Protein Fold with Atomic-Level Accuracy. *Science* **302**, 1364–1368 (2003).

151. Sawaya, M. R. *et al.* Atomic structures of amyloid cross-β spines reveal varied steric zippers. *Nature* **447**, 453–457 (2007).

152. Conway, P., Tyka, M. D., DiMaio, F., Konerding, D. E. & Baker, D. Relaxation of backbone bond geometry improves protein energy landscape modeling: Relaxation of Backbone Bond Geometry. *Protein Sci.* **23**, 47–55 (2014).

153. Sievers, S. A. *et al.* Structure-based design of non-natural amino-acid inhibitors of amyloid fibril formation. *Nature* **475**, 96–100 (2011).

154. Raveh, B., London, N. & Schueler-Furman, O. FLEXPEPDOCK - Sub-angstrom modeling of complexes between flexible peptides and globular proteins. *Proteins Struct. Funct. Bioinforma.* NA-NA (2010). doi:10.1002/prot.22716

155. O'Meara, M. J. *et al.* Combined Covalent-Electrostatic Model of Hydrogen Bonding Improves Structure Prediction with Rosetta. *J. Chem. Theory Comput.* **11**, 609–622 (2015).

156. Leaver-Fay, A., Kuhlman, B. & Snoeyink, J. An adaptive dynamic programming algorithm for the side chain placement problem. *Pac. Symp. Biocomput. Pac. Symp. Biocomput.* 16–27 (2005).

157. Andreasen, M. *et al.* Physical Determinants of Amyloid Assembly in Biofilm Formation. *mBio* **10**, (2019).

158. Taylor, J. D. *et al.* Electrostatically-guided inhibition of Curli amyloid nucleation by the CsgC-like family of chaperones. *Sci. Rep.* **6**, 24656 (2016).

159. Klementieva, O. *et al.* Pre-plaque conformational changes in Alzheimer's disease-linked Aβ and APP. *Nat. Commun.* **8**, 14726 (2017).

160. Fenwick, R. B., Esteban-Martín, S. & Salvatella, X. Understanding biomolecular motion, recognition, and allostery by use of conformational ensembles. *Eur. Biophys. J.* **40**, 1339–1355 (2011).

161. Beck, D. A. C., Alonso, D. O. V. & Daggett, V. *In lucem molecular mechanics (ilmm)*. (2000).

162. Levitt, M., Hirshberg, M., Sharon, R. & Daggett, V. Potential energy function and parameters for simulations of the molecular dynamics of proteins and nucleic acids in solution. *Comput. Phys. Commun.* **91**, 215–231 (1995).

163. Levitt, M., Hirshberg, M., Sharon, R., Laidig, K. E. & Daggett, V. Calibration and Testing of a Water Model for Simulation of the Molecular Dynamics of Proteins and Nucleic Acids in Solution. *J. Phys. Chem. B* **101**, 5051–5061 (1997).

164. Pauling, L. & Corey, R. B. The Pleated Sheet, A New Layer Configuration of Polypeptide Chains. *Proc. Natl. Acad. Sci.* **37**, 251–256 (1951).

165. Tian, P. *et al.* Structure of a Functional Amyloid Protein Subunit Computed Using Sequence Variation. *J. Am. Chem. Soc.* **137**, 22–25 (2015).

166. Jones, D. T., Buchan, D. W. A., Cozzetto, D. & Pontil, M. PSICOV: precise structural contact prediction using sparse inverse covariance estimation on large multiple sequence alignments. *Bioinformatics* **28**, 184–190 (2012).

167. Marks, D. S. *et al.* Protein 3D Structure Computed from Evolutionary Sequence Variation. *PLoS ONE* **6**, e28766 (2011).

168. Remmert, M., Biegert, A., Hauser, A. & Söding, J. HHblits: lightning-fast iterative protein sequence searching by HMM-HMM alignment. *Nat. Methods* **9**, 173–175 (2012).

169. Shewmaker, F. *et al.* The Functional Curli Amyloid Is Not Based on In-register Parallel β-Sheet Structure. *J. Biol. Chem.* **284**, 25065–25076 (2009).

170. Irbäck, A. & Mohanty, S. PROFASI: A Monte Carlo simulation package for protein folding and aggregation. *J. Comput. Chem.* **27**, 1548–1555 (2006).

171. DeBenedictis, E. P., Ma, D. & Keten, S. Structural predictions for curli amyloid fibril subunits CsgA and CsgB. *RSC Adv* **7**, 48102–48112 (2017).

172. Beck, D. A. C. & Daggett, V. Methods for molecular dynamics simulations of protein folding/unfolding in solution. *Methods San Diego Calif* **34**, 112–120 (2004).

173. Hopping, G. *et al.* Designed α-sheet peptides inhibit amyloid formation by targeting toxic oligomers. *eLife* **3**, e01681 (2014).

174. Towse, C.-L., Vymetal, J., Vondrasek, J. & Daggett, V. Insights into Unfolded Proteins from the Intrinsic ϕ/ψ Propensities of the AAXAA Host-Guest Series. *Biophys. J.* **110**, 348–361 (2016).

175. Childers, M. C., Towse, C.-L. & Daggett, V. Molecular dynamics-derived rotamer libraries for D -amino acids within homochiral and heterochiral polypeptides. *Protein Eng. Des. Sel.* **31**, 191–204 (2018).

176. Sato, A. K., Viswanathan, M., Kent, R. B. & Wood, C. R. Therapeutic peptides: technological advances driving peptides into development. *Curr. Opin. Biotechnol.* **17**, 638–642 (2006).

177. Mcgregor, D. Discovering and improving novel peptide therapeutics. *Curr. Opin. Pharmacol.* **8**, 616–619 (2008).

178. Ladner, R. C., Sato, A. K., Gorzelany, J. & de Souza, M. Phage display-derived peptides as therapeutic alternatives to antibodies. *Drug Discov. Today* **9**, 525–529 (2004).

179. Arnesen, T. Towards a Functional Understanding of Protein N-Terminal Acetylation. *PLoS Biol.* **9**, e1001074 (2011).

180. Kim, K.-H. & Seong, B. L. Peptide amidation: Production of peptide hormonesin vivo andin vitro. *Biotechnol. Bioprocess Eng.* **6**, 244–251 (2001).

181. Wallace, R. J. Acetylation of peptides inhibits their degradation by rumen micro-organisms. *Br. J. Nutr.* **68**, 365–372 (1992).

182. Gao, X., Ma, Q. & Zhu, H. Distribution, industrial applications, and enzymatic synthesis of D-amino acids. *Appl. Microbiol. Biotechnol.* **99**, 3341–3349 (2015).

183. Shea, D. *et al.* α-Sheet secondary structure in amyloid β-peptide drives aggregation and toxicity in Alzheimer's disease. *Proc. Natl. Acad. Sci.* **116**, 8895–8900 (2019).

184. Kellock, J., Hopping, G., Caughey, B. & Daggett, V. Peptides Composed of Alternating L- and D-Amino Acids Inhibit Amyloidogenesis in Three Distinct Amyloid Systems Independent of Sequence. *J. Mol. Biol.* **428**, 2317–2328 (2016).

185. Calero, M. & Gasset, M. Featuring Amyloids with Fourier Transform Infrared and Circular Dichroism Spectroscopies. in *Amyloid Proteins* (eds. Sigurdsson, E. M., Calero, M. & Gasset, M.) **849**, 53–68 (Humana Press, 2012).

186. Gobeaux, F. & Wien, F. Reversible Assembly of a Drug Peptide into Amyloid Fibrils: A Dynamic Circular Dichroism Study. *Langmuir* **34**, 7180–7191 (2018).

187. Micsonai, A. *et al.* Accurate secondary structure prediction and fold recognition for circular dichroism spectroscopy. *Proc. Natl. Acad. Sci.* **112**, E3095–E3103 (2015).

188. Whitmore, L. & Wallace, B. A. Protein secondary structure analyses from circular dichroism spectroscopy: Methods and reference databases. *Biopolymers* **89**, 392–400 (2008).

189. Holzwarth, G. & Doty, P. The Ultraviolet Circular Dichroism of Polypeptides. *J. Am. Chem. Soc.* **87**, 218–228 (1965).

190. Greenfield, N. J. Using circular dichroism spectra to estimate protein secondary structure. *Nat. Protoc.* **1**, 2876–2890 (2007).

191. Venyaminov, S. Y., Baikalov, I. A., Shen, Z. M., Wu, C. S. C. & Yang, J. T. Circular Dichroic Analysis of Denatured Proteins: Inclusion of Denatured Proteins in the Reference Set. *Anal. Biochem.* **214**, 17–24 (1993).

192. Whitmore, L., Miles, A. J., Mavridis, L., Janes, R. W. & Wallace, B. A. PCDDB: new developments at the Protein Circular Dichroism Data Bank. *Nucleic Acids Res.* **45**, D303–D307 (2017).

193. Cochran, A. G., Skelton, N. J. & Starovasnik, M. A. Tryptophan zippers: Stable, monomeric -hairpins. *Proc. Natl. Acad. Sci.* **98**, 5578–5583 (2001).

194. Maris, N. L., Shea, D., Bleem, A., Bryers, J. D. & Daggett, V. Chemical and Physical Variability in Structural Isomers of an α-Sheet Peptide Designed To Inhibit Amyloidogenesis. *Biochemistry* **57**, (2018).

195. Torii, H. Amide I Infrared Spectral Features Characteristic of Some Untypical Conformations Appearing in the Structures Suggested for Amyloids. *J. Phys. Chem. B* **112**, 8737–8743 (2008).

196. Hayden, E. Y., Conovaloff, J. L., Mason, A., Bitan, G. & Teplow, D. B. Preparation of Pure Populations of Amyloid β-Protein Oligomers of Defined Size. in *Amyloid Proteins* (eds. Sigurdsson, E. M., Calero, M. & Gasset, M.) **1779**, 3–12 (Springer New York, 2018).

197. Groenning, M. *et al.* Study on the binding of Thioflavin T to β-sheet-rich and non-β-sheet cavities. *J. Struct. Biol.* **158**, 358–369 (2007).

198. Fields, G. B. & Stawikowski, M. Introduction to Peptide Synthesis. in *Current Protocols in Protein Science* (eds. Coligan, J. E., Dunn, B. M., Speicher, D. W. & Wingfield, P. T.) 18.1.1-18.1.9 (John Wiley & Sons, Inc., 2001).

199. Albericio, F. *et al.* Preparation and application of the 5-(4-(9-fluorenylmethyloxycarbonyl)aminomethyl-3,5-dimethoxyphenoxy)-valeric acid (PAL) handle for the solid-phase synthesis of C-terminal peptide amides under mild conditions. *J. Org. Chem.* **55**, 3730–3743 (1990).

200. David, M. Z. & Daum, R. S. Community-Associated Methicillin-Resistant *Staphylococcus aureus*: Epidemiology and Clinical Consequences of an Emerging Epidemic. *Clin. Microbiol. Rev.* **23**, 616–687 (2010).

201. Enright, M. C. *et al.* The evolutionary history of methicillin-resistant *Staphylococcus aureus* (MRSA). *Proc. Natl. Acad. Sci. U. S. A.* **99**, 7687–7692 (2002).

202. Klevens, R. M. Invasive Methicillin-Resistant *Staphylococcus aureus* Infections in the United States. *JAMA* **298**, 1763 (2007).

203. Arciola, C. R., Campoccia, D., Speziale, P., Montanaro, L. & Costerton, J. W. Biofilm formation in *Staphylococcus* implant infections. A review of molecular mechanisms and implications for biofilm-resistant materials. *Biomaterials* **33**, 5967–5982 (2012).

204. Mack, D. *et al.* The intercellular adhesin involved in biofilm accumulation of *Staphylococcus epidermidis* is a linear beta-1,6-linked glucosaminoglycan: purification and structural analysis. *J. Bacteriol.* **178**, 175–183 (1996).

205. Rohde, H. *et al.* Polysaccharide intercellular adhesin or protein factors in biofilm accumulation of *Staphylococcus epidermidis* and *Staphylococcus aureus* isolated from prosthetic hip and knee joint infections. *Biomaterials* **28**, 1711–1720 (2007).

206. Otto, M. Staphylococcal Infections: Mechanisms of Biofilm Maturation and Detachment as Critical Determinants of Pathogenicity. *Annu. Rev. Med.* **64**, 175–188 (2013).

207. Foster, T. J., Geoghegan, J. A., Ganesh, V. K. & Höök, M. Adhesion, invasion and evasion: the many functions of the surface proteins of *Staphylococcus aureus*. *Nat. Rev. Microbiol.* **12**, 49–62 (2014).

208. Peschel, A. & Otto, M. Phenol-soluble modulins and staphylococcal infection. *Nat. Rev. Microbiol.* **11**, 667–673 (2013).

209. Chatterjee, S. S. & Otto, M. How can *Staphylococcus aureus* phenol-soluble modulins be targeted to inhibit infection? *Future Microbiol.* **8**, 693–696 (2013).

210. Cheung, G. Y. C., Joo, H.-S., Chatterjee, S. S. & Otto, M. Phenol-soluble modulins – critical determinants of staphylococcal virulence. *FEMS Microbiol. Rev.* **38**, 698–719 (2014).

211. Wang, R. *et al.* Identification of novel cytolytic peptides as key virulence determinants for community-associated MRSA. *Nat. Med.* **13**, 1510–1514 (2007).

212. Queck, S. Y. *et al.* Mobile Genetic Element-Encoded Cytolysin Connects Virulence to Methicillin Resistance in MRSA. *PLoS Pathog.* **5**, e1000533 (2009).

213. Qi, R. *et al.* Increased in vitro phenol-soluble modulin production is associated with soft tissue infection source in clinical isolates of methicillin-susceptible *Staphylococcus aureus*. *J. Infect.* **72**, 302–308 (2016).

214. Khorasani, M. R., Zamanzad, B., Rostami, S. & Gholipour, A. High prevalence of SCC mec-associated Phenol-soluble modulin gene in clinical isolates of methicillin-resistant. *Staphylococcus aureus*. *Ann. Ig. Med. Prev. E Comunita* **31**, 148–155 (2019).

215. Berlon, N. R. *et al.* Clinical MRSA isolates from skin and soft tissue infections show increased in vitro production of phenol soluble modulins. *J. Infect.* **71**, 447–457 (2015).

216. Wang, R. *et al. Staphylococcus epidermidis* surfactant peptides promote biofilm maturation and dissemination of biofilm-associated infection in mice. *J. Clin. Invest.* **121**, 238–248 (2011).

217. Periasamy, S. *et al.* How *Staphylococcus aureus* biofilms develop their characteristic structure. *Proc. Natl. Acad. Sci.* **109**, 1281–1286 (2012).

218. Marinelli, P., Pallares, I., Navarro, S. & Ventura, S. Dissecting the contribution of *Staphylococcus aureus* α-phenol-soluble modulins to biofilm amyloid structure. *Sci. Rep.* **6**, 34552 (2016).

219. Rostagno, A. & Ghiso, J. Isolation and Biochemical Characterization of Amyloid Plaques and Paired Helical Filaments. *Current Protocols in Cell Biology*. John Wiley & Sons, Inc., 2009.

220. Schwartz, K., Ganesan, M., Payne, D. E., Solomon, M. J. & Boles, B. R. Extracellular DNA facilitates the formation of functional amyloids in *Staphylococcus aureus* biofilms. *Mol. Microbiol.* **99**, 123–134 (2016).

221. Lee, C. C., Walters, R. H. & Murphy, R. M. Reconsidering the Mechanism of Polyglutamine Peptide Aggregation. *Biochemistry* **46**, 12810–12820 (2007).

222. Chen, S., Ferrone, F. A. & Wetzel, R. Huntington's disease age-of-onset linked to polyglutamine aggregation nucleation. *Proc. Natl. Acad. Sci.* **99**, 11884–11889 (2002).

223. Gorman, P. M., Yip, C. M., Fraser, P. E. & Chakrabartty, A. Alternate Aggregation Pathways of the Alzheimer β-Amyloid Peptide: Aβ Association Kinetics at Endosomal pH. *J. Mol. Biol.* **325**, 743–757 (2003).

224. Tayeb-Fligelman, E. *et al.* The cytotoxic *Staphylococcus aureus* PSMα3 reveals a cross-α amyloid-like fibril. *Science* **355**, 831–833 (2017).

225. Tacconelli, E. & Magrini, N. *Global priority list of antibiotic-resistant bacteria to guide research, discovery, and development of new antibiotics*. 7 (World Health Organization, 2017).

226. Hollenbeak, C. S. & Schilling, A. L. The attributable cost of catheter-associated urinary tract infections in the United States: A systematic review. *Am. J. Infect. Control* **46**, 751–757 (2018).

227. Spaulding, C. & Hultgren, S. Adhesive Pili in UTI Pathogenesis and Drug Development. *Pathogens* **5**, 30 (2016).

228. Jacobsen, S. M., Stickler, D. J., Mobley, H. L. T. & Shirtliff, M. E. Complicated Catheter-Associated Urinary Tract Infections Due to *Escherichia coli* and *Proteus mirabilis*. *Clin. Microbiol. Rev.* **21**, 26–59 (2008).

229. Flores-Mireles, A. L., Walker, J. N., Caparon, M. & Hultgren, S. J. Urinary tract infections: epidemiology, mechanisms of infection and treatment options. *Nat. Rev. Microbiol.* **13**, 269–284 (2015).

230. Hooton, T. M. *et al.* Diagnosis, prevention, and treatment of catheter-associated urinary tract infection in adults: 2009 International Clinical Practice Guidelines from the Infectious Diseases Society of America. *Clin. Infect. Dis. Off. Publ. Infect. Dis. Soc. Am.* **50**, 625–663 (2010).

231. Hammar, M., Arnqvist, A., Bian, Z., Olsén, A. & Normark, S. Expression of two *csg* operons is required for production of fibronectin- and congo red-binding curli polymers in *Escherichia coli* K-12. *Mol. Microbiol.* **18**, 661–670 (1995).

232. Wang, X. & Chapman, M. R. Sequence Determinants of Bacterial Amyloid Formation. *J. Mol. Biol.* **380**, 570–580 (2008).

233. Schubeis, T. *et al.* Structural and functional characterization of the Curli adaptor protein CsgF. *FEBS Lett.* (2018). doi:10.1002/1873-3468.13002

234. Newman, S. L., Will, W. R., Libby, S. J. & Fang, F. C. The curli regulator CsgD mediates stationary phase counter-silencing of *csgBA* in *Salmonella* Typhimurium. *Mol. Microbiol.* **108**, 101–114 (2018).

235. Klein, R. D. *et al.* Structure-Function Analysis of the Curli Accessory Protein CsgE Defines Surfaces Essential for Coordinating Amyloid Fiber Formation. *mBio* **9**, (2018).

236. Cao, B. *et al.* Structure of the nonameric bacterial amyloid secretion channel. *Proc. Natl. Acad. Sci.* **111**, E5439–E5444 (2014).

237. Kai-Larsen, Y. *et al.* Uropathogenic *Escherichia coli* Modulates Immune Responses and Its Curli Fimbriae Interact with the Antimicrobial Peptide LL-37. *PLoS Pathog.* **6**, e1001010 (2010).

238. Hollenbeck, E. C. *et al.* Phosphoethanolamine cellulose enhances curli-mediated adhesion of uropathogenic *Escherichia coli* to bladder epithelial cells. *Proc. Natl. Acad. Sci.* **115**, 10106–10111 (2018).

239. Hung, C., Marschall, J., Burnham, C.-A. D., Byun, A. S. & Henderson, J. P. The Bacterial Amyloid Curli Is Associated with Urinary Source Bloodstream Infection. *PLoS ONE* **9**, e86009 (2014).

240. Tükel, Ç. *et al.* Toll-like receptors 1 and 2 cooperatively mediate immune responses to curli, a common amyloid from enterobacterial biofilms: TLR2 interacts with TLR1 to recognize curli. *Cell. Microbiol.* **12**, 1495–1505 (2010).

241. Schiebel, J. *et al.* Genotypic and Phenotypic Characteristics Associated with Biofilm Formation by Human Clinical *Escherichia coli* Isolates of Different Pathotypes. *Appl. Environ. Microbiol.* **83**, (2017).

242. Frömmel, U. *et al.* Adhesion of Human and Animal Escherichia coli Strains in Association with Their Virulence-Associated Genes and Phylogenetic Origins. *Appl. Environ. Microbiol.* **79**, 5814–5829 (2013).

243. Cordeiro, M. A., Werle, C. H., Milanez, G. P. & Yano, T. Curli fimbria: an *Escherichia coli* adhesin associated with human cystitis. *Braz. J. Microbiol.* **47**, 414–416 (2016).

244. Hadjifrangiskou, M. *et al.* Transposon Mutagenesis Identifies Uropathogenic *Escherichia coli* Biofilm Factors. *J. Bacteriol.* **194**, 6195–6205 (2012).

245. Bemporad, F. & Chiti, F. Protein Misfolded Oligomers: Experimental Approaches, Mechanism of Formation, and Structure-Toxicity Relationships. *Chem. Biol.* **19**, 315–327 (2012).

246. Paranjapye, N. & Daggett, V. De Novo Designed α-Sheet Peptides Inhibit Functional Amyloid Formation of *Streptococcus mutans* Biofilms. *J. Mol. Biol.* **430**, 3764–3773 (2018).

247. Lim, J. Y., May, J. M. & Cegelski, L. Dimethyl sulfoxide and ethanol elicit increased amyloid biogenesis and amyloid-integrated biofilm formation in *Escherichia coli*. *Appl. Environ. Microbiol.* **78**, 3369–3378 (2012).

248. Römling, U. Characterization of the rdar morphotype, a multicellular behaviour in *Enterobacteriaceae*. *Cell. Mol. Life Sci.* **62**, 1234–1246 (2005).

249. Bi, T. M. & Daggett, V. The Role of α-sheet in Amyloid Oligomer Aggregation and Toxicity. *Yale J. Biol. Med.* **91**, 247–255 (2018).

250. Herigstad, B., Hamilton, M. & Heersink, J. How to optimize the drop plate method for enumerating bacteria. *J. Microbiol. Methods* **44**, 121–129 (2001).

251. Eshaghi, M., Mehershahi, K. & Chen, S. Brighter Fluorescent Derivatives of UTI89 Utilizing a Monomeric vGFP. *Pathogens* **5**, 3 (2016).

252. Arango Duque, G. & Descoteaux, A. Macrophage Cytokines: Involvement in Immunity and Infectious Diseases. *Front. Immunol.* **5**, (2014).

253. Hall, C. W. & Mah, T.-F. Molecular mechanisms of biofilm-based antibiotic resistance and tolerance in pathogenic bacteria. *FEMS Microbiol. Rev.* **41**, 276–301 (2017).

254. Totsika, M. Disarming pathogens: benefits and challenges of antimicrobials that target bacterial virulence instead of growth and viability. *Future Med. Chem.* **9**, 267–269 (2017).

255. Koo, H., Allan, R. N., Howlin, R. P., Stoodley, P. & Hall-Stoodley, L. Targeting microbial biofilms: current and prospective therapeutic strategies. *Nat. Rev. Microbiol.* **15**, 740–755 (2017).

256. Christensen, L. D. *et al.* Clearance of *Pseudomonas aeruginosa* Foreign-Body Biofilm Infections through Reduction of the Cyclic Di-GMP Level in the Bacteria. *Infect. Immun.* **81**, 2705–2713 (2013).

257. Baker, P. *et al.* Exopolysaccharide biosynthetic glycoside hydrolases can be utilized to disrupt and prevent *Pseudomonas aeruginosa* biofilms. *Sci. Adv.* **2**, e1501632 (2016).

258. Novotny, L. A., Jurcisek, J. A., Goodman, S. D. & Bakaletz, L. O. Monoclonal antibodies against DNA-binding tips of DNABII proteins disrupt biofilms in vitro and induce bacterial clearance *in vivo*. *EBioMedicine* **10**, 33–44 (2016).

259. Thurlow, L. R. *et al. Staphylococcus aureus* Biofilms Prevent Macrophage Phagocytosis and Attenuate Inflammation *In Vivo*. *J. Immunol.* **186**, 6585–6596 (2011).

260. Le, K. Y., Park, M. D. & Otto, M. Immune Evasion Mechanisms of *Staphylococcus epidermidis* Biofilm Infection. *Front. Microbiol.* **9**, 359 (2018).

261. Mishra, M. *et al. Pseudomonas aeruginosa* Psl polysaccharide reduces neutrophil phagocytosis and the oxidative response by limiting complement-mediated opsonization: Psl and the innate immune response towards *P. aeruginosa*. *Cell. Microbiol.* **14**, 95–106 (2012).

262. Stewart, P. S. Biophysics of biofilm infection. *Pathog. Dis.* **70**, 212–218 (2014).

263. Wang, X., Smith, D. R., Jones, J. W. & Chapman, M. R. *In Vitro* Polymerization of a Functional *Escherichia coli* Amyloid Protein. *J. Biol. Chem.* **282**, 3713–3719 (2006).

264. Dueholm, M. S. *et al.* Fibrillation of the Major Curli Subunit CsgA under a Wide Range of Conditions Implies a Robust Design of Aggregation. *Biochemistry* **50**, 8281–8290 (2011).

265. Arnold, U. & Ulbrich-Hofmann, R. Quantitative Protein Precipitation from Guanidine Hydrochloride-Containing Solutions by Sodium Deoxycholate/Trichloroacetic Acid. *Anal. Biochem.* **271**, 197–199 (1999).

266. Schindelin, J. *et al.* Fiji: an open-source platform for biological-image analysis. *Nat. Methods* **9**, 676–682 (2012).

267. Khatoon, Z., McTiernan, C. D., Suuronen, E. J., Mah, T.-F. & Alarcon, E. I. Bacterial biofilm formation on implantable devices and approaches to its treatment and prevention. *Heliyon* **4**, e01067 (2018).

268. Zeng, G., Ogaki, R. & Meyer, R. L. Non-proteinaceous bacterial adhesins challenge the antifouling properties of polymer brush coatings. *Acta Biomater.* **24**, 64–73 (2015).

269. Falde, E. J., Yohe, S. T., Colson, Y. L. & Grinstaff, M. W. Superhydrophobic materials for biomedical applications. *Biomaterials* **104**, 87–103 (2016).

270. May, R. M. *et al.* An engineered micropattern to reduce bacterial colonization, platelet adhesion and fibrin sheath formation for improved biocompatibility of central venous catheters. *Clin. Transl. Med.* **4**, (2015).

271. Gilabert-Porres, J. *et al.* Design of a Nanostructured Active Surface against Gram-Positive and Gram-Negative Bacteria through Plasma Activation and in Situ Silver Reduction. *ACS Appl. Mater. Interfaces* **8**, 64–73 (2016).

272. Campoccia, D., Montanaro, L., Speziale, P. & Arciola, C. R. Antibiotic-loaded biomaterials and the risks for the spread of antibiotic resistance following their prophylactic and therapeutic clinical use. *Biomaterials* **31**, 6363–6377 (2010).

273. Gruenheid, S. & Moual, H. Resistance to antimicrobial peptides in Gram-negative bacteria. *FEMS Microbiol. Lett.* **330**, 81–89 (2012).

274. Banerjee, I., Pangule, R. C. & Kane, R. S. Antifouling Coatings: Recent Developments in the Design of Surfaces That Prevent Fouling by Proteins, Bacteria, and Marine Organisms. *Adv. Mater.* **23**, 690–718 (2011).

275. Qin, H. *et al.* In vitro and in vivo anti-biofilm effects of silver nanoparticles immobilized on titanium. *Biomaterials* **35**, 9114–9125 (2014).

276. Forier, K. *et al.* Lipid and polymer nanoparticles for drug delivery to bacterial biofilms. *J. Controlled Release* **190**, 607–623 (2014).

277. Silver, S., Phung, L. T. & Silver, G. Silver as biocides in burn and wound dressings and bacterial resistance to silver compounds. *J. Ind. Microbiol. Biotechnol.* **33**, 627–634 (2006).

278. Flores-Mireles, A. L., Pinkner, J. S., Caparon, M. G. & Hultgren, S. J. EbpA vaccine antibodies block binding of *Enterococcus faecalis* to fibrinogen to prevent catheter-associated bladder infection in mice. *Sci. Transl. Med.* **6**, 254ra127-254ra127 (2014).

279. Lu, T. K. & Collins, J. J. Dispersing biofilms with engineered enzymatic bacteriophage. *Proc. Natl. Acad. Sci.* **104**, 11197–11202 (2007).

280. Asker, D., Awad, T. S., Baker, P., Howell, P. L. & Hatton, B. D. Non-eluting, surface-bound enzymes disrupt surface attachment of bacteria by continuous biofilm polysaccharide degradation. *Biomaterials* **167**, 168–176 (2018).

281. Goddard, J. M. & Hotchkiss, J. H. Polymer surface modification for the attachment of bioactive compounds. *Prog. Polym. Sci.* **32**, 698–725 (2007).

282. Waite, J. H. & Qin, X. Polyphosphoprotein from the Adhesive Pads of *Mytilus edulis*. *Biochemistry* **40**, 2887–2893 (2001).

283. Lee, H., Dellatore, S. M., Miller, W. M. & Messersmith, P. B. Mussel-Inspired Surface Chemistry for Multifunctional Coatings. *Science* **318**, 426–430 (2007).

284. Orishchin, N. *et al.* Rapid Deposition of Uniform Polydopamine Coatings on Nanoparticle Surfaces with Controllable Thickness. *Langmuir* **33**, 6046–6053 (2017).

285. Kang, S. M. *et al.* One-Step Modification of Superhydrophobic Surfaces by a Mussel-Inspired Polymer Coating. *Angew. Chem. Int. Ed.* **49**, 9401–9404 (2010).

286. Ding, Y. H., Floren, M. & Tan, W. Mussel-inspired polydopamine for bio-surface functionalization. *Biosurface Biotribology* **2**, 121–136 (2016).

287. Lee, Y. B. *et al.* Polydopamine-mediated immobilization of multiple bioactive molecules for the development of functional vascular graft materials. *Biomaterials* **33**, 8343–8352 (2012).

288. Xu, L. Q., Yang, W. J., Neoh, K.-G., Kang, E.-T. & Fu, G. D. Dopamine-Induced Reduction and Functionalization of Graphene Oxide Nanosheets. *Macromolecules* **43**, 8336–8339 (2010).

289. Lim, K. *et al.* Development of a catheter functionalized by a polydopamine peptide coating with antimicrobial and antibiofilm properties. *Acta Biomater.* **15**, 127–138 (2015).

290. Yang, K. *et al.* Polydopamine-mediated surface modification of scaffold materials for human neural stem cell engineering. *Biomaterials* **33**, 6952–6964 (2012).

291. Jiang, L. *et al.* Surface characteristics of mussel-inspired polydopamine coating on titanium substrates. *J. Wuhan Univ. Technol.-Mater Sci Ed* **29**, 197–200 (2014).

292. Tam, J. P., Wu, C. R., Liu, W. & Zhang, J. W. Disulfide bond formation in peptides by dimethyl sulfoxide. Scope and applications. *J. Am. Chem. Soc.* **113**, 6657–6662 (1991).

293. Choi, K.-H. & Schweizer, H. P. An improved method for rapid generation of unmarked Pseudomonas aeruginosa deletion mutants. *BMC Microbiol.* **5**, 30 (2005).

294. Hoboth, C. *et al.* Dynamics of Adaptive Microevolution of Hypermutable *Pseudomonas aeruginosa* during Chronic Pulmonary Infection in Patients with Cystic Fibrosis. *J. Infect. Dis.* **200**, 118–130 (2009).

295. Newman, J. R. & Fuqua, C. Broad-host-range expression vectors that carry the L-arabinose-inducible *Escherichia coli* araBAD promoter and the araC regulator. *Gene* **227**, 197–203 (1999).

296. Yang, H., Yang, S., Kong, J., Dong, A. & Yu, S. Obtaining information about protein secondary structures in aqueous solution using Fourier transform IR spectroscopy. *Nat. Protoc.* **10**, 382–396 (2015).

# Appendix A: Sequences, Strains, and Primers

## Table A.1. Sequence analysis of GVNXAA hexapeptides in *P. aeruginosa* PAO1 FapC.

| Strain | NCBI Reference | R1 motif | %ID to PAO1 (GVNVAA) | R2 motif | %ID to PAO1 (GVNVAA) | R3 motif | %ID to PAO1 (GVNIAA) |
|---|---|---|---|---|---|---|---|
| *Pseudomonas aeruginosa* PAO1 | NP_250644.1 | GVNVAA | | GVNVAA | | GVNIAA | |
| *Pseudomonas putida* GB-1 | WP_012272553.1 | GINVAA | 83.33 | GINIAG | 50 | GVNVAA | 83.33 |
| *Pseudomonas putida* F1 | WP_012052566.1 | GINVAA | 83.33 | GINVAG | 66.67 | GVNVAA | 83.33 |
| *Pseudomonas putida* BIRD-1 | WP_014591276.1 | GINVAA | 83.33 | GINVAG | 66.67 | GVNVAA | 83.33 |
| *Pseudomonas putida* KT2440 | NP_745000.1 | GINVAA | 83.33 | GINVAG | 66.67 | GVNVAA | 83.33 |
| *Pseudomonas entomophila* L48 | WP_011534103.1 | GVNVAA | 100 | GINIAG | 50 | GVNVAA | 83.33 |
| *Pseudomonas putida* W619 | WP_012314614.1 | GVNVAA | 100 | GINVAG | 66.67 | GVNVAA | 83.33 |
| *Pseudomonas sp.* UK4 | EEP64551.1 | GANIAA | 66.67 | GVNVAA | 100 | GVNVAA | 83.33 |
| *Pseudomonas fluorescens* A506 | WP_003190893.1 | GVNAQS | 50 | GYNGQA | 50 | GVNLQS | 50 |
| *Pseudomonas fluorescens* SBW25 | WP_012723889.1 | GVNVQA | 83.33 | GYNGQA | 50 | GVNLQS | 50 |
| *Pseudomonas fluorescens* WH6 | ZP_07775110.1 | GVNVQA | 83.33 | GYNGQA | 50 | GVNLQS | 50 |
| *Pseudomonas synxantha* BG33R | ZP_10141134.1 | GVNVQS | 66.67 | GYNGQS | 33.33 | GVNLQS | 50 |
| *Pseudomonas sp.* S9 | ZP_09711309.1 | GINVVA | 66.67 | GANVAA | 83.33 | GVNVAA | 83.33 |
| *Pseudomonas aeruginosa* 2192 | ZP_04933660.1 | GVNVAA | 100 | GVNVAA | 100 | GVNIAA | 100 |
| *Pseudomonas aeruginosa* C3719 | ZP_04928363.1 | GVNVAA | 100 | GVNVAA | 100 | GVNIAA | 100 |
| *Pseudomonas aeruginosa* LESB58 | WP_003113480.1 | GVNVAA | 100 | GVNVAA | 100 | GVNIAA | 100 |
| *Pseudomonas aeruginosa* PACS2 | ZP_01365301.1 | GVNVAA | 100 | GVNVAA | 100 | GVNIAA | 100 |
| *Pseudomonas putida* S16 | WP_013972458.1 | GVNVAA | 100 | GINIAG | 50 | GVNVAA | 83.33 |
| *Pseudomonas aeruginosa* 39016 | ZP_07797129.1 | GVNVAA | 100 | GVNVAA | 100 | GVNIAA | 100 |
| *Pseudomonas aeruginosa* DK2 | WP_003088317.1 | GVNVAA | 100 | GVNVAA | 100 | GVNIAA | 100 |
| *Pseudomonas aeruginosa* NCGM2.S1 | WP_003088317.1 | GVNVAA | 100 | GVNVAA | 100 | GVNIAA | 100 |
| *Pseudomonas aeruginosa* PAb1 | ZP_06879114.1 | GVNVAA | 100 | GVNVAA | 100 | GVNIAA | 100 |
| *Pseudomonas aeruginosa* UCBPP-PA14 | WP_003088317.1 | GVNVAA | 100 | GVNVAA | 100 | GVNIAA | 100 |
| *Pseudomonas sp.* 2_1_26 | ZP_09055487.1 | GVNVAA | 100 | GVNVAA | 100 | GVNIAA | 100 |
| *Pseudomonas aeruginosa* M18 | WP_003121980.1 | GVNVAA | 100 | GVNVAA | 100 | GVNIAA | 100 |
| *Pseudomonas sp.* M47T1 | ZP_10148953.1 | GVNVAG | 83.33 | GINVTS | 50 | GANVAS | 50 |
| *Pseudomonas fluorescens* Pf0-1 | WP_011334011.1 | GMNNTA | 50 | GVNNSA | 66.67 | GYNNAA | 66.67 |
| *Pseudomonas brassicacearum* NFM421 | WP_003202372.1 | GANIAA | 66.67 | GINVTA | 66.67 | GANVSA | 50 |
| *Pseudomonas fluorescens* F113 | WP_014338150.1 | GANIAA | 66.67 | GINVTA | 66.67 | GANVSA | 50 |
| *Pseudomonas chlororaphis* O6 | ZP_10175099.1 | GANVAA | 83.33 | GINVTA | 66.67 | GANVSA | 50 |
| *Pseudomonas protegens* Pf-5 | WP_011061407.1 | GANVAA | 83.33 | GINVTA | 66.67 | GANVSA | 50 |
| **AVERAGE %ID to PAO1** | | | **85.5** | | **75.6** | | **78.9** |

**Table A.2. Bacterial strains and mammalian cell lines**

| **Bacterial strains** | | |
|---|---|---|
| *Strain* | *Relevant traits* | *Source* |
| *P. aeruginosa* PAO1 WT | Wild-type; no mutation | - |
| *P. aeruginosa* PAO1 pFap | PAO1 with pMMB90Tc-PAO1fap plasmid encoding *fapA-fapF*, Tet resistant | Dueholm et al. (2013) |
| *P. aeruginosa* PAO1 *Δfap* | PAO1 with knockout of the *fap* operon, Gm resistant | Dueholm et al. (2013) |
| *P. aeruginosa* PAO1 pJN105fap | PAO1 with pJN105-PAO1fap plasmid encoding *fapA-fapF*, Gm resistant | This work |
| *S. aureus* SH1000 (WT) | Laboratory strain, *rsbU*$^{+}$ | Horsburgh et al. (2002) |
| *S. aureus* MN8 | Clinically relevant strain; urogenital tract | - |
| *S. aureus* MN8 + *mCherry* | Transcriptional fusion of RFP to the P3 promoter of strain MN8 | B. Boles (2015) |
| *E. coli* UTI89 WT | UPEC strain; cystitis isolate | Mulvey et al., 2001 |
| *E. coli* UTI89 Δ*csgA* | UPEC strain; cystitis isolate with chromosomal deletion of *csgA* gene | Cegelski et al., 2009 |
| *E. coli* UTI89 SLC-719 | Derivative of UTI89 expressing chromosomal vsfGFP | Eshaghi et al., 2016 |
| *E. coli* GERB 319 | Clinical isolate from pediatric UTI; resistant to gentamicin and ciprofloxacin | Evgeni Sokurenko |

| **Mammalian cell lines** | | |
|---|---|---|
| *Cells* | *Relevant traits* | *Source* |
| RAW 264.7 | Murine macrophage | ATCC |
| 3T3 | Murine embryonic fibroblasts | ATCC |

**Table A.3. Primers.** [c] F = forward primer; R = reverse primer. * Indicates housekeeping gene.

**qPCR primer sequences**

| *Gene* | *Oligonucleotide sequence[c], 5'-3'* | *Amplicon size (bp)* | *Source* |
|---|---|---|---|
| *csgA* | F: GATCTGACCCAACGTGGCTTCG<br>R: GATGAGCGGTCGCGTTGTTACC | 178 | Silva et al., 2014 |
| *gapA** | F: GATTACATGGCATACCTG<br>R: CAGACGAACGTTCAGGTCAA | 244 | Silva et al., 2014 |
| *iNOS* | F: GCCACCTTGGTGAAGGGACT<br>R: ACGTTCTCCGTTCTCTTGCAGT | 111 | This work |
| *TNFα* | F: GTCCCCAAAGGGATGAGAAGT<br>R: TTTGCTACGACGTGGGCTAC | 124 | This work |
| *CD86* | F: AACTTACGGAAGCACCCACG<br>R: CTCCACGGAAACAGCATCTGAG | 101 | This work |
| *PPIA** | F: GTCTCCTTCGAGCTGTTTGC<br>R: GCGTGTAAAGTCACCACCCT | 150 | This work |

**PCR primer sequences**

| *Gene* | *Oligonucleotide sequence[c], 5'-3'* | *Amplicon size (bp)* | *Source* |
|---|---|---|---|
| *csgA* | F: GGCCCAAATTCTGAGCTGAAC<br>R: ATGAGCGGTCGCGTTGTTA | 330 | This work |
| *fapC ΔCys* | F: CCGGGCCGCTGCTGCTACC<br>R: CGGGTGGTGAAAGCCTGG | 261 | This work |

**Gibson assembly primer sequences**

| *Fragment* | *Oligonucleotide sequence[c], 5'-3'* | *Source* |
|---|---|---|
| *fap* | F: CGTTTTTTTGGGCTAGCGCCCCTCAGAAGTAG<br>R: CTATAGGGCGAATTGGAGCTCATCATGTCGGGGAGTTC | This work |
| *pJN105* | F: AGCTCCAATTCGCCCTATAG<br>R: CGCTAGCCCAAAAAAACG | This work |

# Appendix B: Supplemental Figures

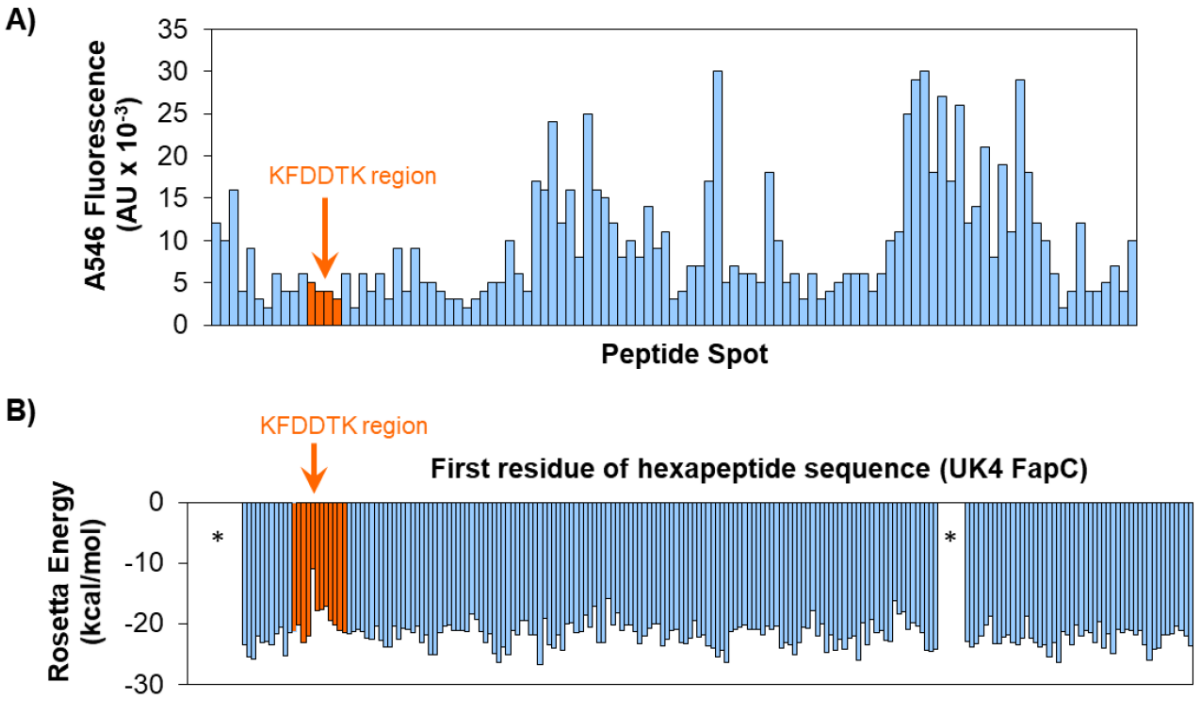


**Figure B.1. Selection of FapC mutation sequence with peptide array and ZipperDB data. A)** Relative fluorescence intensity of A546-labeled UK4 FapC on cellulose peptide array, plotted against each spot peptide sequence of UK4 FapC. Bars highlighted in orange indicate peptide spots containing the KFDDTK sequence. **B)** Rosetta energies for each hexapeptide segment of the UK4 FapC sequence. Candidate sequences were taken from the area shaded in orange, and the sequence KFDDTK was ultimately selected for PAO1 FapC mutations due to its combination of relatively high Rosetta energy (low amyloid propensity) and net neutral charge. *Proline residues are incompatible with the 3D profile method in ZipperDB; hexapeptides with prolines are therefore unscored.

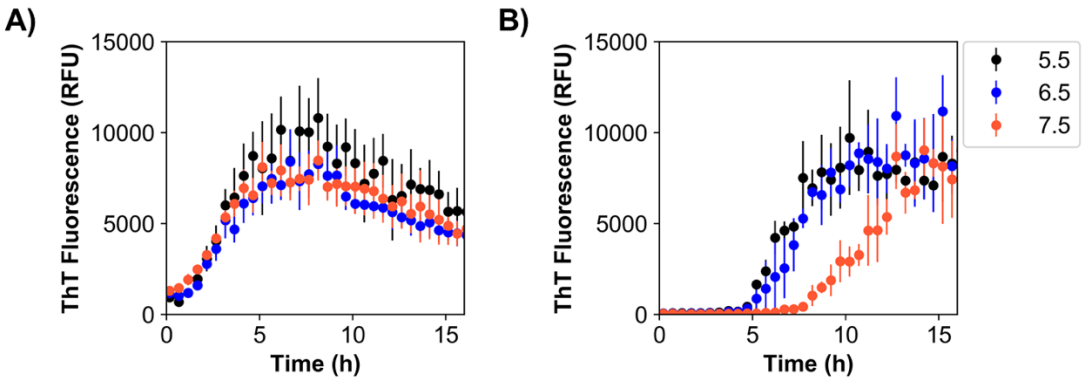


**Figure B.2. FapC fibril formation under different pH conditions. A)** FapC WT and **B)** FapC R3 mutant were incubated with shaking at 37°C in 10 mM Tris buffer, pH 5.5 (black), 6.5 (blue), and 7.5 (orange). ThT fluorescence indicates amyloid fibril formation, and error bars represent the standard deviation from the mean of three replicates.

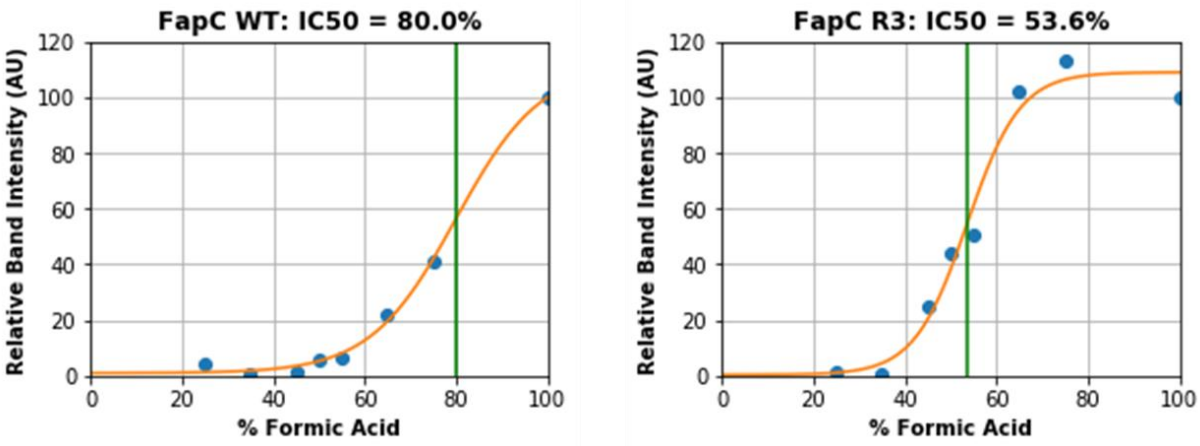


**Figure B.3. Least squares regression of FapC dissolution data.** The sigmoidal fit (orange lines) took the form of Equation 2.1. The parameter $x_0$ defines an "IC50", i.e. the concentration of FA at which relative band intensity reached half-maximum (green vertical lines).

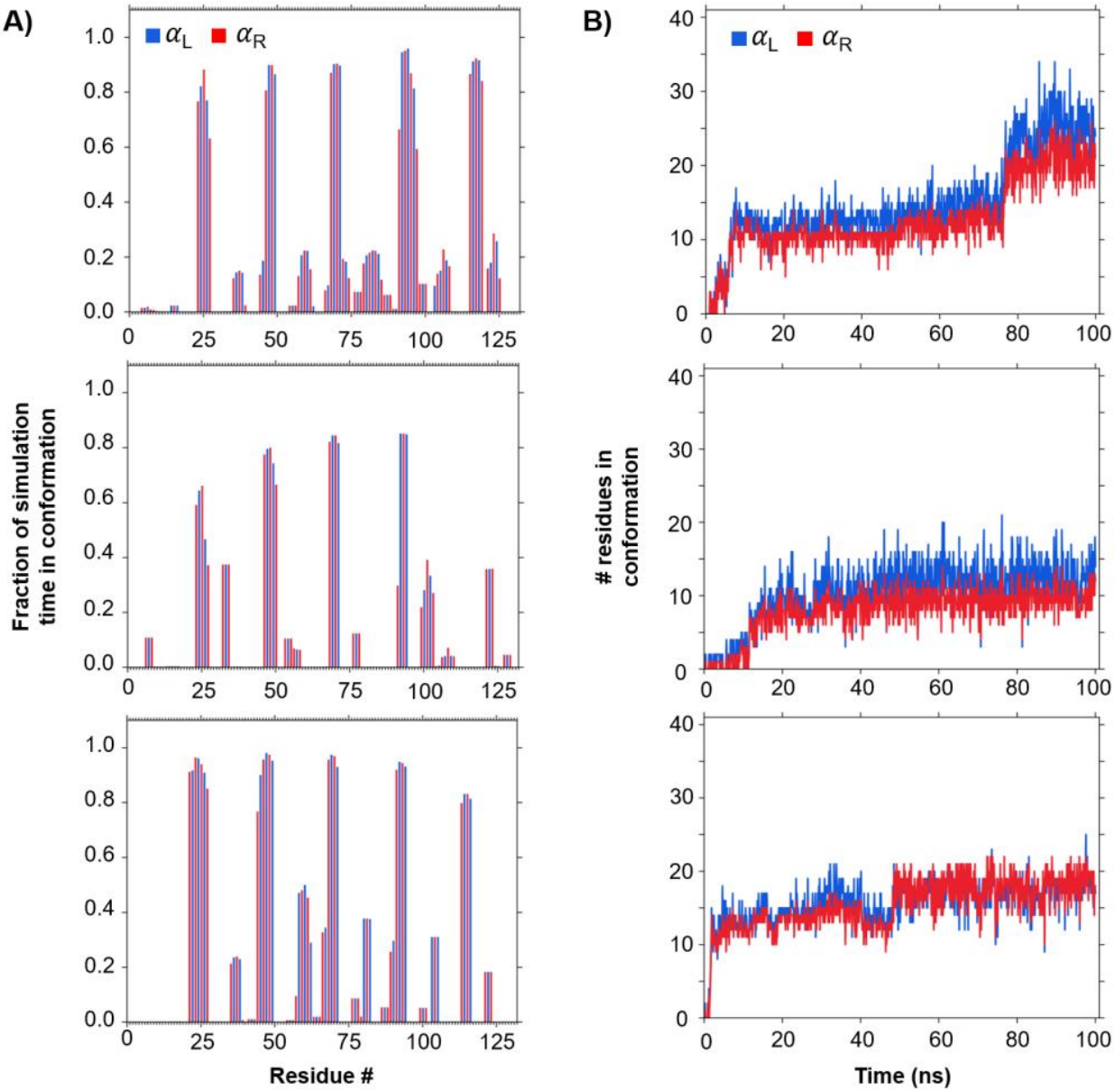


**Figure B.4. MD simulation data for α-strand formation in CsgA at low pH. A)** as a function of residue number and **B)** as a function of time. Top = Run 1; middle = Run 2; bottom = Run 3. Most α-sheet formation was localized to a single face of the CsgA helix, as reflected by clusters of bars in **(A)**. In Run 1, some additional α-strands formed on the other side of the helix, as indicated by the sudden increase in α-conformation residues at ~80 ns in **(B)**.

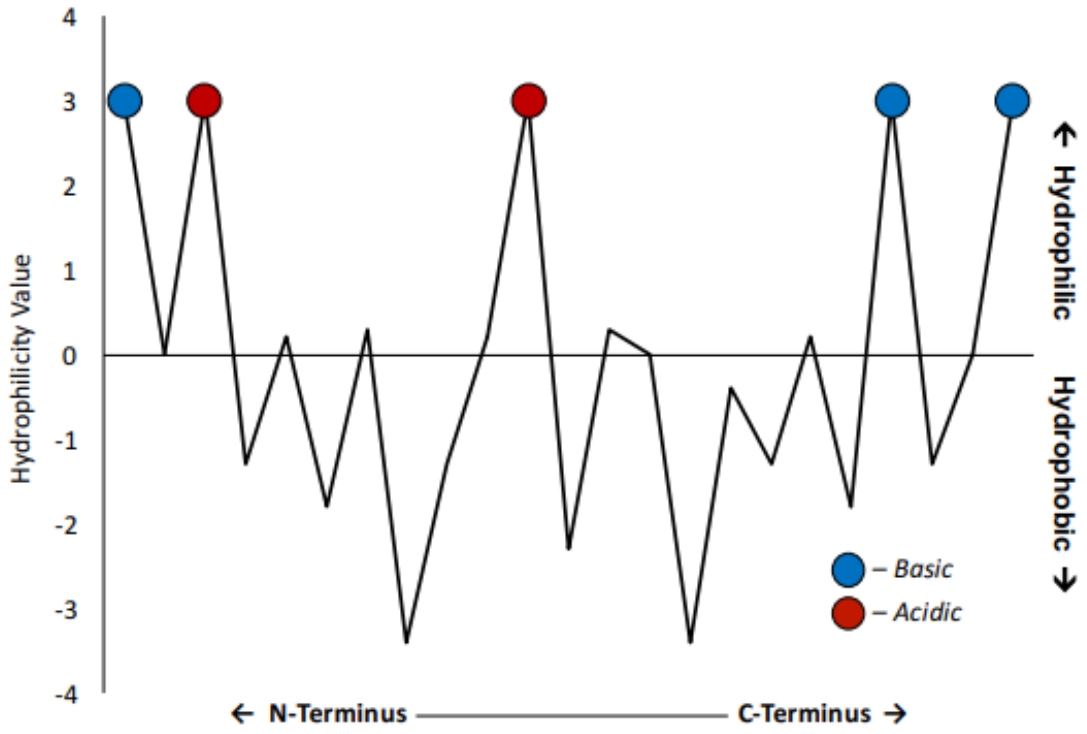


**Figure B.5. Hopp-Woods hydrophilicity plot of the AP90/P90 sequence.** Blue circles indicate basic residues, and red indicate acidic residues. The majority of amino acids in the sequence possess a near-zero (neutral) or negative (hydrophobic) hydrophilicity value.

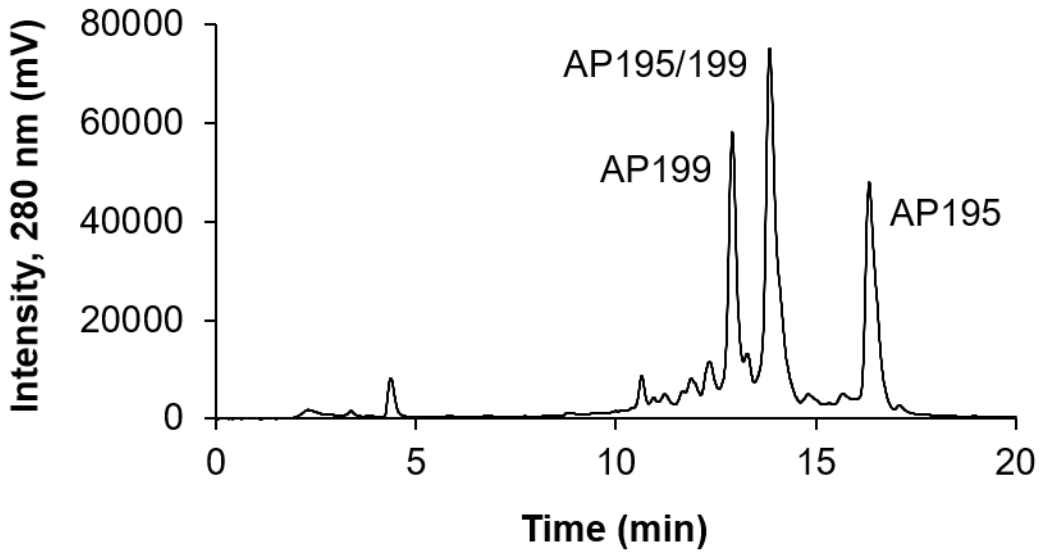


**Figure B.6. RP-HPLC for resolution of AP199 and AP195 oxidation reactions.** Peak 1 = AP199 homodimer, peak 2 = AP195/199 heterodimer, peak 3 = AP195 homodimer. Data shown is for the gradient elution portion of the run (no wash step). Separations were performed with a 5 µM C12 100 Å column and a gradient of acetonitrile in water.

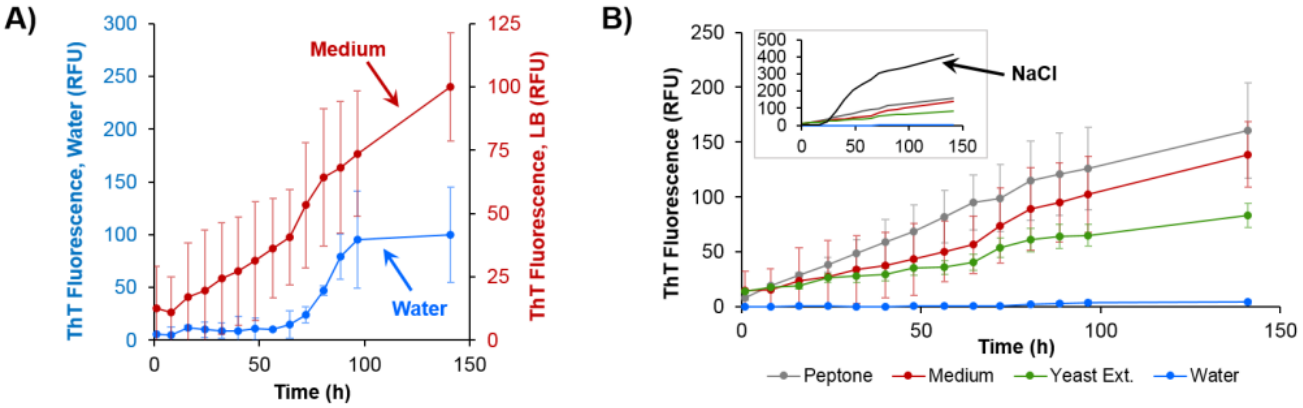


**Figure B.7. A)** ThT fluorescence curves monitoring the aggregation kinetics of PSMα1 under the two different solvent conditions in **Figure 5.4A** (blue = water; red = LB medium). **B)** The contribution of individual LB medium components (10 g/L peptone, 5 g/L yeast extract, and 85 mM NaCl) to PSMα1 aggregation kinetics. Fluorescence in NaCl solution was quite high, so that curve is shown as an inset. All solutions contained 0.34% DMSO for solubilization of PSMα1. Values are averages of 3 samples, corrected by blanks without PSMα1, with error bars to represent the standard deviation of the mean.

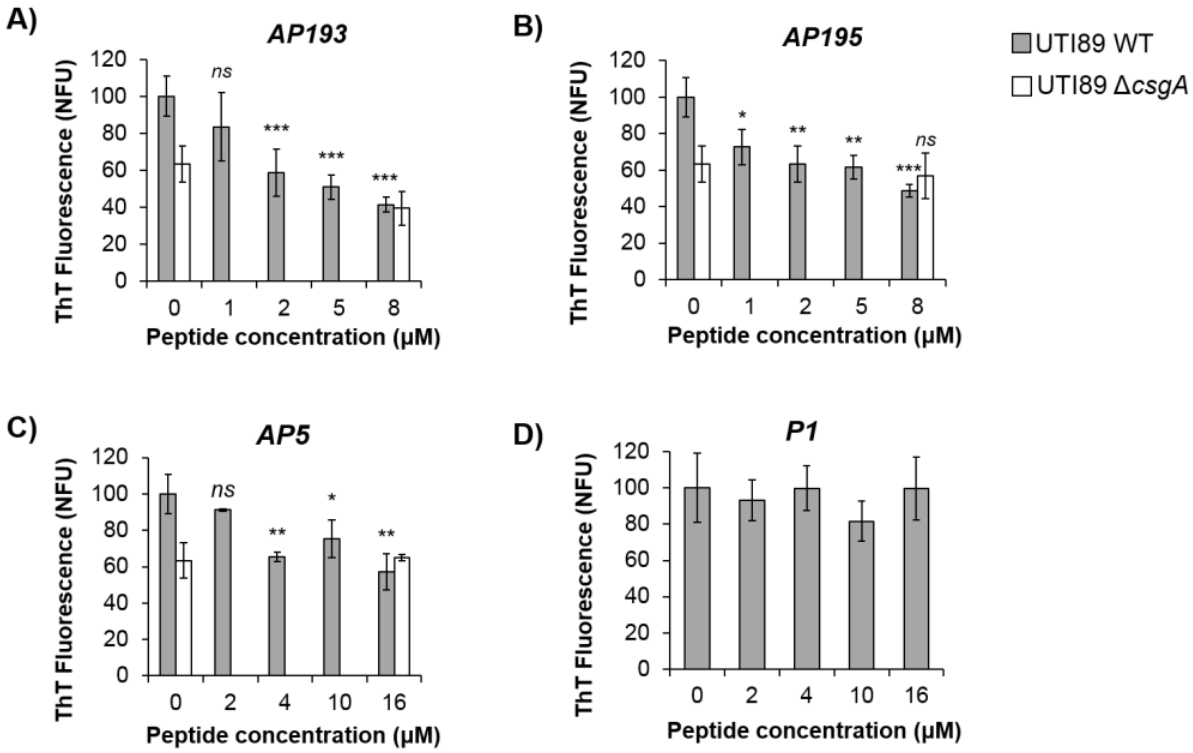


**Figure B.8.** Synthetic α-sheet peptides **(A)** AP193, **(B)** AP195, and **(C)** AP5 caused dose-dependent reductions in ThT fluorescence, while the unstructured control peptide **(D)** P1 had no effect. At the highest dose, all three synthetic α-sheet peptide designs reduced the ThT fluorescence of UTI89 WT biofilms to that of the ΔcsgA strain.

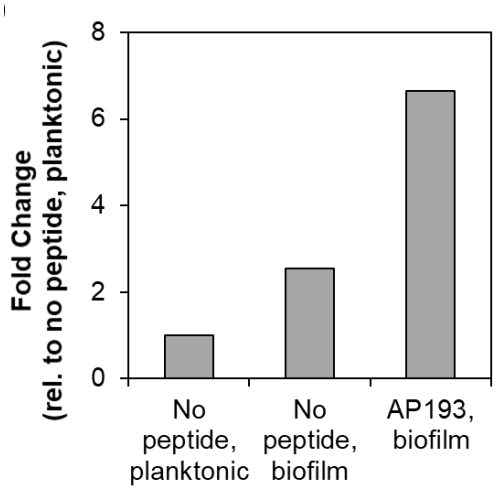


**Figure B.9.** *E. coli* UTI89 WT biofilms grown in the presence of AP193 did not exhibit significant changes in *csgA* transcription when compared to untreated controls.

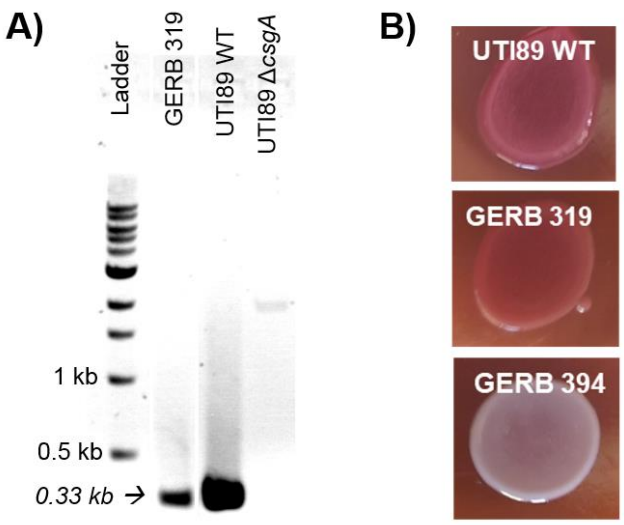


**Figure B.10.** Antibiotic-resistant *E. coli* strain GERB 319 demonstrates a strong curliated phenotype, as demonstrated by the presence of both **A)** the *csgA* gene (330 bp target amplified by PCR from genomic DNA) and **B)** "rdar" colony morphotype. A non-curliated strain, GERB 394, is shown in **(B)** for comparison.

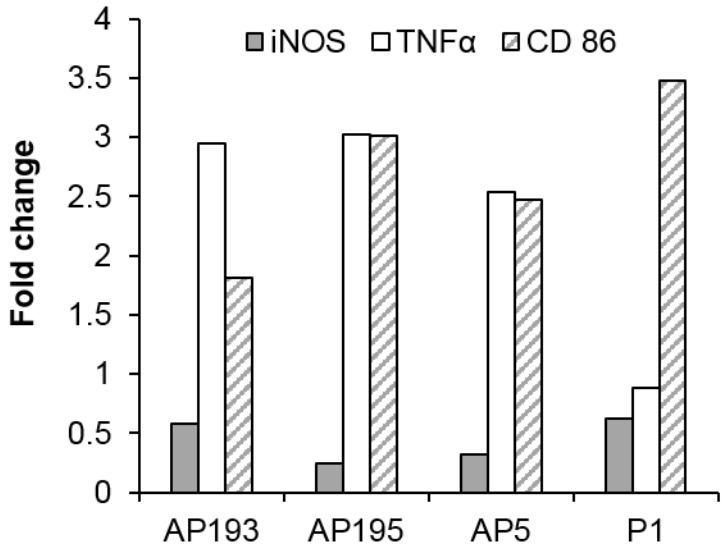


**Figure B.11. Mixed polarization of RAW 264.7 cells in the presence of synthetic α-sheet peptides.** Macrophages were grown on 24 well polystyrene tissue culture plates with the indicated peptides for 24 h, and then expression of pro-inflammatory ("M1") markers was evaluated by RT-qPCR. Expression of TNFα and CD 86 increased compared to peptide-free controls, but expression of iNOS decreased.

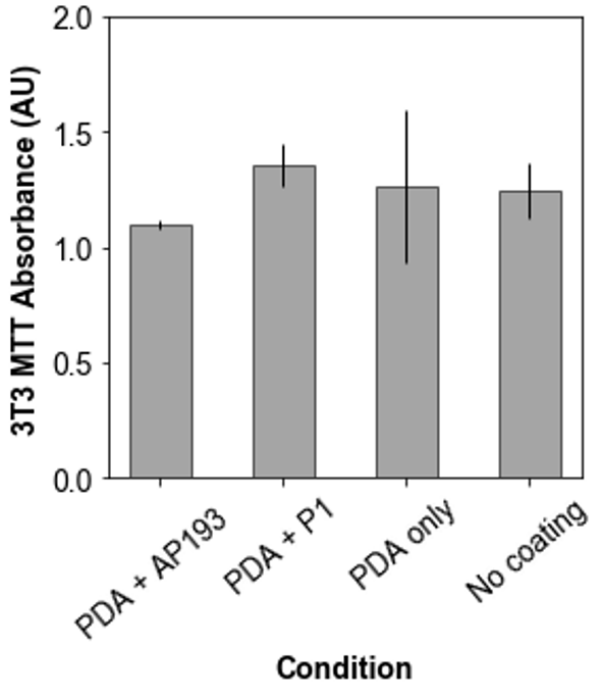


**Figure B.12. PGAP coatings do not affect cell viability.** Mouse 3T3 fibroblasts were grown on 96 well polystyrene tissue culture plates with the indicated coatings for 24 h, and then cell viability was determined by MTT assay. Absorbance readings indicated no significant difference between samples. Error bars indicate standard deviation from the mean of three replicates.

# Appendix C: Supplementary Information

## C.1 Tunable Expression of *fap* with an Arabinose-Inducible Vector

Overexpression of the *fap* operon in *P. aeruginosa* PAO1 pFap is controlled by a promoter derived from the *lac* promoter. Constitutive expression of *lac* in *Pseudomonas* makes it difficult to sync bacterial growth with plasmid-driven *fap* overexpression. Induction of *fap* by an exogenous metabolite, such as L-arabinose, can help overcome this issue. The vector pJN105 (donated by Morten Dueholm) utilizes the PBAD promoter to induce expression according to the level of L-arabinose present in the growth medium[295], so the *fap* operon was cloned into this vector via Gibson assembly. Genomic DNA was extracted from *P. aeruginosa* PAO1 WT and the *fap* operon was amplified by primers with Gibson assembly tags (**Appendix A, Table A.3**). The pJN105 vector was also amplified with the same tags, and then the two fragments were joined with Gibson Assembly® Master Mix (New England Biolabs; Ipswitch, MA) according to manufacturer protocols, and the purified plasmid product was amplified in *E. coli* DH5α. The resulting construct, called pJN105-PAO1fap, was then transformed into *P. aeruginosa* PAO1 WT for homologous overexpression. The induction of pJN105-PAO1fap by L-arabinose was verified in two ways. First, liquid cultures of *P. aeruginosa* pJN105-PAO1fap were grown in shake flasks to an optical density (600 nm) of 0.6, and then they were induced with 0%, 0.05%, 0.1%, or 0.5% w/v L-arabinose and allowed to grow another 12 h. Cells were harvested by centrifugation and lysed by repeated sonication in 6 M urea, while the biofilms adhered to the empty flasks were stained with Crystal Violet (**Figure 2.1 A**). Protein concentrations of the cell lysates were normalized, and these were blotted on a nitrocellulose membrane and probed with an anti-FapC polyclonal antibody (Morten Dueholm). Development of the blot with a HRP-conjugated secondary antibody confirmed that the FapC concentration increased as L-arabinose concentration increased.

## C.2 FTIR and NMR of Synthetic α-sheet Peptides

FTIR spectroscopy uses infrared radiation to excite vibrational transitions in molecules. In proteins, the vibrations between 1700 and 1600 $cm^{-1}$ (amide I) are most sensitive to changes in backbone conformation, because these result from C=O stretching of the amide group[296]. Density functional theory calculations[195] predict strong FTIR absorbance peaks for α-sheet at ~1640 and

1675-1685 $cm^{-1}$, since the amide groups are aligned in α-sheet backbone conformations. In accordance with these theoretical predictions, the synthetic α-sheet peptides AP90, AP193, and AP407 exhibit strong absorbance bands at 1640 and weaker bands at 1675-1680 $cm^{-1}$ in dry film FTIR[173] and microfluidic modulation spectroscopy (MMS; a liquid-phase FTIR technique)[183] . These measurements provide additional corroboration for the presence of α-sheet secondary structure observed by CD. Finer detail has also been provided for AP90 and AP407 in the form of NMR spectra. In AP90, strong sequential $d_{NN}$ Nuclear Overhauser Effect (NOE) crosspeaks indicated alignment of amide groups on one side of the chain[173]. Later NMR experiments yielded far more NOEs between protons, and these data were combined with chemical shifts to generate structural models of AP407 that accurately reflect the α-sheet backbone design set forth *in silico*[183]. Together, these studies provide additional evidence for atypical secondary structure in synthetic α-sheet peptides and indicate successful translation of the computationally designed structures to real peptide material. Moreover, these studies in combination with CD spectra lay the foundation for new peptide designs to further optimize the α-sheet structure.

# Copyright Permissions

**Chapter 1** reproduced in part with permission from:

Bleem, A. and Daggett, V. “Structural and functional diversity among amyloid proteins: Agents of disease, building blocks of biology, and implications for molecular engineering.” *Biotechnol. Bioeng.* **114**, 7-20 (2017). Copyright 2017 John Wiley and Sons.

**Chapter 2** reproduced in part from:

Bleem, A., *et al*. "Protein engineering reveals mechanisms of functional amyloid formation in *Pseudomonas aeruginosa* biofilms." *J. Mol. Biol.* **430**, 3751-3763 (2018).

**Chapter 3** reproduced in part with permission from:

Maris, N. L., *et al*. “Chemical and physical variability in structural isomers of an L/D α-sheet peptide designed to inhibit amyloidogenesis.” *Biochemistry.* **57**, 507-510 (2018). Copyright 2018 American Chemical Society.

**Chapter 5** reproduced in part from:

Bleem, A., *et al*. "Designed α-sheet peptides suppress amyloid formation in *Staphylococcus aureus* biofilms." *npj Biofilms and Microbiomes.* **3**, 16 (2017).

# VITA

Alissa Catherine Bleem was born and grew up in Fort Collins, Colorado. She received her Bachelor of Science in Chemical Engineering in 2014 from Montana State University in Bozeman, Montana. In 2019, she earned her Doctor of Philosophy from the University of Washington in the Department of Bioengineering. Her publications include:

**Bleem, A.**, Chen, R., Hady, T., Li, J., Ott, A., Hwang, B., Bryers, J. D., and Daggett, V. (2019). Synthetic α-sheet peptides disrupt uropathogenic *Escherichia coli* biofilms by inhibiting curli fibril formation. In Preparation.

**Bleem, A.**, Daggett, V., and Bryers, J. D (2019). Polydopamine-grafted α-sheet peptides prevent biofilm formation on medial implant materials. In Preparation.

**Bleem, A.**, Christiansen, G., Madsen, D. J., Maric, H., Strømgaard, K., Bryers, J. D., Daggett, V., Meyer, R. L, and Otzen, D. E. (2018). Protein engineering reveals mechanisms of functional amyloid formation in *Pseudomonas aeruginosa* biofilms. Journal of Molecular Biology, *430,* 3751-3763.

Maris, N. L., Shea, D., **Bleem, A.**, Bryers, J. D., and Daggett, V. (2018). Chemical and physical variability in structural isomers of an L/D α-sheet peptide designed to inhibit amyloidogenesis. Biochemistry, *57,* 507-510.

**Bleem, A.**, Francisco, R., Bryers, J. D., and Daggett, V. (2017). Designed alpha-sheet peptides suppress amyloid formation in *Staphylococcus aureus* biofilms. Nature Biofilms and Microbiomes, *3,* 16.

**Bleem, A.** and Daggett, V. (2017). Structural and functional diversity among amyloid proteins: Agents of disease, building blocks of biology, and implications for molecular engineering. Biotechnology and Bioengineering *114*, 7-20.

Beck, A. E., Pintar, K., Schepens, D., Schrammeck, A., Johnson, T., **Bleem, A.**, Bernstein, H. C., Gedeon, T., Heys, J. J., and Carlson, R. P. (2019). Fighting acid with acid: Emergent properties of co-metabolism in *Escherichia coli*. In Preparation.